UNIVERSIDADE FEDERAL DO CEARÁ
TECHNOLOGY CENTER
DEPARTMENT OF METALLURGICAL AND MATERIALS ENGINEERING
POSTGRADUATE PROGRAM IN MATERIALS SCIENCES AND ENGINEERING
DOCTORAL COURSE IN MATERIALS SCIENCE AND ENGINEERING

GERBSON DE QUEIROZ CAETANO

PROCESSING, MICROSTRUCTURE, MECHANICAL PROPERTIES AND CORROSION SUSCEPTIBILITY OF FERRITIC/AUSTENITIC DISSIMILAR WELDS PRODUCED BY FSW

FORTALEZA-CE
2022

GERBSON DE QUEIROZ CAETANO

PROCESSING, MICROSTRUCTURE, MECHANICAL PROPERTIES AND CORROSION SUSCEPTIBILITY OF FERRITIC/AUSTENITIC DISSIMILAR WELDS PRODUCED BY FSW

Thesis Submitted to Postgraduate Program in Materials Sciences and Engineering at the Technology Center of the Universidade Federal do Ceará, in partial fulfilment of the requirements for the Degree of Doctor in Materials Sciences and Engineering. Concentration Area: Physical Properties and Mechanics of Materials.

Advisor: Prof. Dr. Cleiton Carvalho Silva.

FORTALEZA

2022

Dados Internacionais de Catalogação na Publicação
Universidade Federal do Ceará
Sistema de Bibliotecas
Gerada automaticamente pelo módulo Catalog, mediante os dados fornecidos pelo(a) autor(a)

C131p Caetano, Gerbson de Queiroz.
Processing, microstructure, mechanical properties and corrosion susceptibility of ferritic/austenitic dissimilar welds produced by fsw / Gerbson de Queiroz Caetano. – 2022.
332 f. : il. color.

Tese (doutorado) – Universidade Federal do Ceará, Centro de Tecnologia, Programa de Pós-Graduação em Engenharia e Ciência de Materiais, Fortaleza, 2022.
Orientação: Prof. Dr. Cleiton Carvalho Silva.

1. Welding. 2. FSW. 3. Stainless Steel. 4. Microstructure. 5. Properties. I. Título.

CDD 620.11

GERBSON DE QUEIROZ CAETANO

PROCESSING, MICROSTRUCTURE, MECHANICAL PROPERTIES AND CORROSION SUSCEPTIBILITY OF FERRITIC/AUSTENITIC DISSIMILAR WELDS PRODUCED BY FSW

Thesis Submitted to Postgraduate Program in Materials Sciences and Engineering at the Technology Center of the Universidade Federal do Ceará, in partial fulfilment of the requirements for the Degree of Doctor in Materials Sciences and Engineering. Concentration Area: Physical Properties and Mechanics of Materials.

Approved on:

EXAMINATION BOARD

Prof. Dr. Cleiton Carvalho Silva (Advisor)
Universidade Federal do Ceará (UFC)

Prof. Dr. Jorge Fernandez dos Santos
Helmholtz-Zentrum Geesthacht (HZG)

Prof. Dr. Marcelo Ferreira Motta
Universidade Federal do Ceará (UFC)

Prof. Dr. Hamilton Ferreira Gomes de Abreu
Universidade Federal do Ceará (UFC)

Prof. Dr. Edmilson Otoni Corrêa
Universidade Federal de Itajubá/ (UNIFEI)

ACKNOWLEDGEMENTS

To my parents, especially my mother for all their love and dedication so that I had access to the best schools and universities.

To my maternal and paternal grandparents for having lived this dream with me.

To my brother and sister, as well as my brother-in-law and sister-in-law, for all the encouraging words.

I would like to thank all my friends and family for all their support and encouragement.

I would like to thank my supervisor Professor Dr. Cleiton Carvalho Silva for guiding me through all these years and for believing that I could be a researcher.

I would like to thank all the professors at LPTS, especially Prof. Dr. Helio Miranda, for the initial opportunity given to me and guidance in the first years of my academic life.

I would like to thank the Federal University of Ceará in particular to the Professors of the Department of Engineering and Materials Science, for all the knowledge transmitted.

I would like to thank the ANP/PETROBRAS by the funding of all resources need to this thesis and the funding agencies that give support to department like CAPES, CNPq and FUNCAP system.

I also would like to thank the HZG (Helmholtz-Zentrum Geesthacht - Zentrum Für Material - Und Küstenforschung) by support in the manufacture of the samples used in this studied.

I am grateful to LPTS (Laboratório de Pesquisa e Tecnologia em Soldagem), LPC (Laboratório de Pesquisa em Corrosão), GPTA (Grupo de Pesquisa em Termofluidodinâmica Aplicada) and Central Analítica/ UFC for the support of laboratory facilities.

ABSTRACT

This study aimed to investigate the dissimilar welding of ferritic and austenitic stainless steels, through different joint configurations AISI 410S / 304L and AISI 444 / 316L, by the friction stir welding process (FSW), evaluating operational and metallurgical aspects. The FSW welding of different joints in this study was performed at the Helmholtz-Zentrum Geesthacht (Germany) due to establishing a cooperation agreement with the Universidade Federal do Ceará. The welding parameters range on setting was based on the best parameters found on the FSW similar welding for these steels. Changes in the parameters were performed to determine an acceptable combination of surface finish, absence of cracks and good penetration. The better welding conditions for each welded joint configuration were subjected to mechanical evaluation through the tensile, bending, and microhardness tests. In the same way, for samples from the better welding conditions were extracted for corrosion resistance evaluation through DL-EPR, Salt Spray and Immersion Oil tests. In these conditions, microstructural analysis was performed by optical microscopy (OM) and scanning electron microscopy (SEM). The electron backscatter diffraction (EBSD) with inverse pole figure (IPF) map and Kernel Average Misorientation (KAM) was also used in some conditions to help understand recrystallised fraction and grain orientation. The results from microscopy techniques allow the correlation between process parameters and microstructure with the mechanical properties and corrosion resistance. For the AISI 410S/304L dissimilar welds, it was possible to observe a grain size refinement and increase in microhardness values in HAZ, TMAZ and SZ, with better results in the tensile test concerning the base metal of the AISI 410S steel and low sensitisation levels and corrosion rates in the salt spray test. AISI 444 / 316L dissimilar welded joints were produced with excellent grain refinement, absence of defects and undesirable phases, high cohesion between the two materials and good results in the yield and tensile strength, without loss of the intergranular corrosion resistance of the joints. Therefore, based on the corrosion resistance and mechanical testing, it is possible to conclude that AISI 410S/304L and AISI 444/316L stainless steel dissimilar welds can be successfully performed by the FSW process with enhanced microstructural features.

K**eywords**: Welding, FSW, Steel, Stainless Steel, Microstructure, Properties.

RESUMO

Este trabalho teve como objetivo investigar a soldagem dissimilar de aços inoxidáveis ferríticos e austeníticos, através de diferentes configurações de juntas AISI 410S / 304L e AISI 444 / 316L, pelo processo Friction Stir Welding (FSW), avaliando aspectos operacionais e metalúrgicos. A soldagem FSW das diferentes juntas neste estudo foi realizada na Helmholtz-Zentrum Geesthacht (Alemanha) devido ao estabelecimento de um acordo de cooperação com a Universidade Federal do Ceará. Os ajustes na faixa de parâmetros de soldagem foram baseados nos melhores parâmetros encontrados na soldagem FSW similar para esses aços. Mudanças nos parâmetros foram realizadas para determinar uma combinação entre acabamento superficial aceitável, ausência de trincas e boa penetração. As melhores condições de soldagem para cada configuração de junta soldada foram submetidas à avaliação mecânica através dos ensaios de dobramento, tração e microdureza. Da mesma forma, para as melhores condições de soldagem foram extraídas amostras para avaliação da resistência à corrosão através dos testes EPR-DL, Névoa Salina e Imersão em Óleo. Nestas condições, análise microestrutural foi realizada por microscopia óptica (MO) e microscopia eletrônica de varredura (MEV). A difração de elétrons retroespalhados (EBSD) com mapas de figura de polo inversa (IPF) e desorientação média de kernel (KAM) também foram usadas em algumas condições para ajudar a entender a fração recristalizada e orientação de grãos. Os resultados das técnicas de microscopia permitiram uma correlação entre os parâmetros do processo e a microestrutura com as propriedades mecânicas e resistência à corrosão. Para as soldas dissimilares AISI 410S/304L, foi possível observar um refinamento do tamanho de grão e aumento nos valores de microdureza em ZAC, ZTMA e ZM, com melhores resultados no ensaio de tração em relação ao metal base do aço AISI 410S e baixos níveis de sensitização e taxas de corrosão no teste de névoa salina. Foram produzidas juntas dissimilares AISI 444 / 316L com excelente refinamento de grão, ausência de defeitos e fases indesejáveis, alta coesão entre os dois materiais e bons resultados no limite de escoamento e resistência à tração, sem prejuízo da resistência à corrosão intergranular das juntas. Portanto, com base na resistência à corrosão e testes mecânicos, é possível concluir que soldas dissimilares de aço inoxidável AISI 410S/304L e AISI 444/316L podem ser realizadas com sucesso pelo processo FSW com aprimoradas características microestruturais.

Palavras-chave: Soldagem, FSW, Aços, Inoxidáveis, Microestrutura, Propriedades.

LIST OF FIGURES

LIST OF TABLES

CONTENTS

1 CHAPTER 1: Overview of the problematics concerning dissimilar welding of ferritic and austenitic stainless steels by the friction stir welding (FSW) process

1.1 Introduction

Among stainless steels, the ferritic group is characterized by having an essentially ferritic microstructure at room temperature, thus having a body-centred cubic (BCC) crystal structure. Its chromium content can vary from 11 to 30%, and it can also contain the addition of Mo, Nb, Ti and others. Austenitic stainless steel (ASS) is the most used commercially due to its high mechanical and corrosion resistance. It has a face-centred cubic (CFC) crystal structure thanks to the Ni addition, which stabilizes this phase. Compared to the austenitic, ferritic steels can provide approximately the same corrosion resistance but have lower ductility and weldability (SMITH, W. F. 1993). Ferritic stainless steels (FSS) can be used in various applications when pitting corrosion resistance and stress corrosion cracking resistance is more required than mechanical strength (LIPPOLD; KOTECKI, 2005). Another great advantage of ferritic stainless steels is the absence of Ni in their composition, since Ni is one of the most expensive alloying elements, with an intense price fluctuation and increase trend in the international market, which considerably raises the cost of austenitic stainless steels compared to ferritic stainless steels.

Thus, the good corrosion resistance associated with the low cost of FSS have attracted the attention of numerous industrial sectors, such as the automotive industry, railway and subway industries, oil and gas, petrochemicals, naval industry, pharmaceuticals, food, beverages, household appliances, kitchenware, civil construction and architecture, among others, as noted by SINGH et al. (2022). SILVA et al. (2013) point out that different industrial segments use dissimilar welding as an economical option to join different metals to bring together different properties, minimise costs, maximising the performance of equipment and machinery with different welding processes. The potentialities of stainless steels, especially in Brazil, are the most interesting, including cost reduction and increased competitiveness provided by the optimised choice of ferritic stainless steels in place of austenitic ones, depending on application and corrosion resistance requirements. Currently, as observed in studies of

WU; HU and SHEN (2015), ferritic stainless steels have found strong use in replacing carbon steels and have also been used industrially to replace different austenitic stainless steels, as analysed by RAJPUT et al. (2020) and SINGH et al. (2022). MUKHERJEE and PAL (2012) claim that the dissimilar joints between ferritic and austenitic stainless steels are efficient for prolonging metals' service life due to improved toughness, mechanical strength, and corrosion resistance. As highlighted by KUMAR et al. 2015, the need for structures with a good relationship between strength and low cost led to the need to integrate different types of materials into a single structure; however, the assembly of these components made of different materials in terms of chemical, thermal, physical and mechanical properties, became a significant challenge.

As noted by LI et al. (2021) and ZHANG et al. (2019) in fusion welding process, a big gap to be filled regarding the expansion of applications of ferritic and austenitic stainless steels in dissimilar joints is related to their different behaviour at high temperatures and their high sensitivity to thermal welding cycles. Grain growth stands out among these metallurgical problems that compromise the weldability of these materials, which causes a decrease in toughness. The precipitation of chromium nitrides and carbides causes embrittlement and intergranular corrosion. The formation of undesirable phases such as the σ-phase and the χ-phase can have a detrimental effect on the material's mechanical and corrosion resistance properties. These recurring metallurgical problems in the welding of ASS and FSS can be observed by BARROS, (2013) and MACHADO et al. (2006) in research carried out in the Laboratório de Pesquisa e Tecnologia em Soldagem (LPTS).

In recent decades, Friction Welding (FSW), a solid-state welding process developed by THOMAS et al. (1991) in The Welding Institute (TWI) in Cambridge, England, has revolutionised the joining of materials considered non-weldable or difficult to weld. MISHRA and MA (2005) reported that this process uses a non-consumable tool that rotates and penetrates the joint, resulting in heating and plastic deformation of the materials to be joined and heated to temperatures below those experienced in fusion welding. According to JACQUIN and GUILLEMOT (2021), among the advantages commonly attributed to the FSW process, the following stand out: good strength and ductility of welds, minimal residual stress and distortion, absence of defects related to material melting, smaller heat-affected zone and microstructure with refined grains, which increase tensile strength and fatigue life, as proposed by BILGIN and MERAN,

(2012), DEBROY and BHADESHIA, (2013) and SATHIYA et al. (2006). In the FSW process, rotational speed and axial force are the two parameters directly related to heat generation. A combination of welding speed, axial force and rotational speed are the critical factors in achieving a balanced set of welding parameters. As noted by HEIDARZADEH et al. (2021), correct adjustment of these parameters can result in significant microstructural evolution in certain aspects, including grain size, grain boundaries, dissolution and hardening of precipitates, dissolution and redistribution of dispersoids, as well as the modification of the crystallographic texture.

The critical advance in creating welding tools for joining high-temperature melting point materials, various FSW examinations have been devoted to joining different steels as shown by FUJII et al. (2006) and CHUNG et al. (2010) specifically, for the stainless steels. The applications of the FSW process in similar welds of austenitic stainless steel show that although the formation of deleterious phases is predicted in the stir zone, as proved by KOKAWA et al. (2005) and PARK et al. (2003). The intense grain refining resulting from dynamic recrystallisation shows that the application of the FSW process is promising from the point of view of mechanical properties, as observed by WANG et al. (2014). Low heat input and high welding speed are recommended for ferritic stainless steels to minimise ferritic grain growth and form a refined microstructure. CAETANO et al. (2018) and BILGIN e MERAN (2012) showed that such characteristics could be achieved using the FSW process.

Despite significant progress on issues related to the application of the FSW process in dissimilar joints of aluminium alloys and other light alloys, in studies like Raju et al. (2022) and KADIAN and BISWAS, (2018) and these alloys with steels as shown RAMIREZ et al. (2011) and KASAI et al. (2015), studies with the exploration of process parameters required the dissimilar joining of different steels, such as those carried out by WANG et al. (2019), are still developing and more detailed information about the influence of process parameters and the phenomena involved in microstructural evolution and their correlation with mechanical properties and corrosion resistance, becomes a topic of strong scientific and technological appeal. Within this context, this thesis intends to investigate the dissimilar welding between austenitic stainless steels and ferritic stainless steel, through FSW joints formed by the steels AISI 410S/304L and AISI 444/316L, evaluating the microstructural evolution, mechanical properties and corrosion resistance

of the produced joints, through the establishment of a cooperation work between the Federal University of Ceará (Brazil) and the Helmholtz-Zentrum Geesthacht (Germany).

1.2 Objectives

This study aims to investigate the dissimilar welding between ferritic and austenitic stainless steels by the friction stir welding (FSW) process, evaluating operational and metallurgical aspects for the production of joints with good mechanical properties and high corrosion resistance.

1.2.1 Specific Objectives

- Evaluate the effects of the main FSW welding parameters for producing dissimilar joints without defects.
- Investigate the metallurgical characteristics of the different zones produced in the dissimilar FSW welding between AISI 410S/AISI 304L and AISI 444/AISI 316L steels, especially in relation to recrystallisation grain refinement, and phase transformations.
- Determine the mechanical behaviour of dissimilar joints produced by FSW associated with the metallurgical alterations resulting from the process.
- Evaluate the corrosion resistance of dissimilar joints welded by the FSW process through DL-EPR, salt spray and oil immersion tests.

1.3 Thesis organization

This thesis was split into eleven main chapters, addressing the analysis of welding parameters, microstructural characterisation, mechanical properties evaluation and corrosion resistance assessment of AISI 410S / 304L and AISI 444 / 316L FSW dissimilar joints, aiming to complete the proposed objectives and fulfil all requirements as part of the doctorate's requisites in Materials Science and Engineering.

In this Chapter 1, in addition to the structure of the thesis, an overview of the problematics concerning dissimilar welding of ferritics and austenitic stainless steels by the friction stir welding (FSW) process is portrayed in the introduction, as well as the main objectives of this work.

Chapter 2 consists of a comprehensive review of the literature, which was performed aiming to cover metallurgical aspects of the materials to be studied, an overview of the FSW process, including general aspects, the main welding parameters, and the tools, a brief comment on different kinds of weld defects and their relationship with the procedure and parameters.

Chapter 3 aims to evaluate the effect of joint configuration and welding parameters, such as axial force, on the production of FSW dissimilar joints between austenitic stainless steel AISI 304L and ferritic stainless steel AISI 410S with an excellent surface appearance and no defects. In this chapter, an initial study was carried out on the proper positioning of the steels between the advancing and retreating sides and the influence of axial force and rotational speed on heat generation and defects formation.

In Chapter 4 evaluated the effect of different FSW welding parameters in the microstructural evolution of dissimilar joints between AISI 304L austenitic stainless steel and AISI 410S ferritic stainless steel. In this chapter, for a more detailed investigation of the possible precipitates and the constitution of the interfaces between the AISI 304L/410S steels, analyses were performed by scanning electron microscopy (SEM) in an FEI Quanta 250 microscope with an Oxford Nordlys EDS system coupled. The electron backscatter diffraction (EBSD) was also used in some conditions to help understand recrystallised fraction, inverse pole figure (IPF) map and Kernel Average Misorientation (KAM).

Chapter 5 seeks to evaluate the effect of FSW welding parameters on the mechanical properties of dissimilar joints between AISI 304L austenitic stainless steel and AISI 410S ferritic stainless steel, evaluating the performance of welded joints through bending, microhardness and uniaxial tensile tests. Thereby, mechanical tests were performed in order to determine the mechanical properties and correlate them with the microstructural characteristics observed along the joints.

Chapter 6 was addressed to evaluate the corrosion resistance of FSW dissimilar joints between the AISI 304L austenitic stainless steel and the AISI 410S ferritic stainless steel through a non-destructive and quantitative technique called the double loop electrochemical potentiokinetic reactivation (DL-EPR) technique to determine the degree of sensitisation of stainless steel and accelerated laboratory test provides a controlled corrosive in salt spray environment. Thus, Chapters 3, 4, 5 and 6 are intended to analyse

parameters, microstructure, and mechanical and corrosion resistance properties of dissimilar FSW joints of AISI 410S and AISI 304L steels.

Chapter 7 determine the effect of different FSW welding parameters, such as rotation speed, axial force, torque, thickness, and joint configuration, in the production of dissimilar welds between austenitic stainless steel AISI 316L and ferritic stainless steel AISI 444, evaluating aspects such as the effects of these parameters on the plasticisation process and consequently on the formation of defects.

Chapter 8 evaluate the effect of different FSW welding parameters in the microstructural evolution of dissimilar joints between AISI 316L austenitic stainless steel and AISI 444 ferritic stainless steel. Detailing macro and microstructural aspects along the different zones formed and the main differences observed between the butt joint welded conditions about the overlap joint welded conditions.

Chapter 9 evaluated the effect of FSW welding parameters on the mechanical properties of dissimilar joints between austenitic stainless steel AISI 316L and ferritic stainless steel AISI 444, evaluating the mechanical performance of welded joints through bending, microhardness tests, uniaxial traction tests for butt joint weld conditions and shear tests for the conditions welded in an overlap joint.

Chapter 10 evaluated the corrosion resistance of dissimilar FSW joints between the austenitic stainless steel AISI 316L and the ferritic stainless steel AISI 444, evaluating the corrosion resistance of welded joints through a non-destructive and quantitative technique called the double loop electrochemical potentiokinetic reactivation (DL-EPR) technique to determine the degree of sensitisation of stainless steels, even as, the behaviour of these dissimilar FSW joints when in contact with high salinity oil at high temperature and pressure. Therefore, Chapters 7, 8, 9 and 10 are intended to analyse parameters, microstructure, mechanical properties and corrosion resistance of dissimilar FSW joints of AISI 444 and AISI 316L steels. Finally, in Chapter 11, the main conclusions were listed.

Figure 1.1- Flowchart of this study.

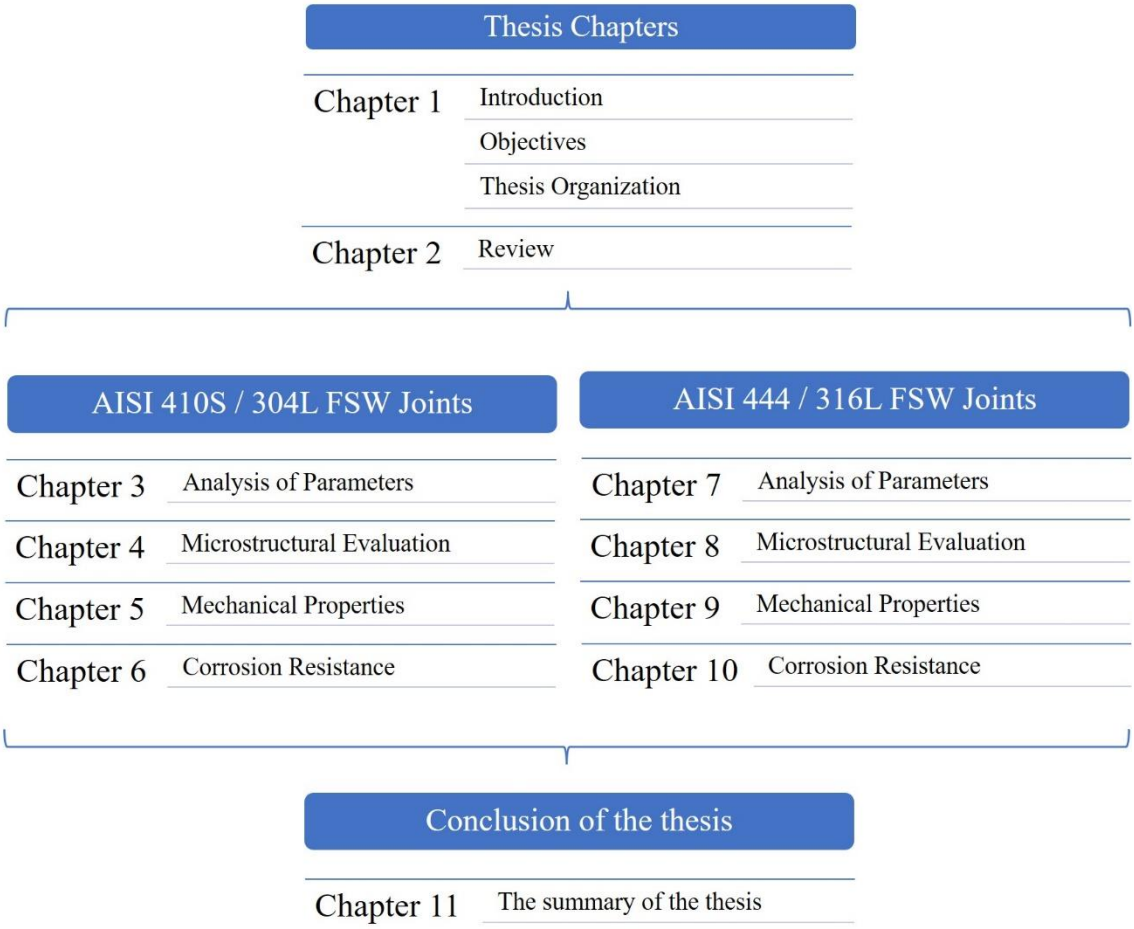

Source: The author

1.4 References

BARROS, I. F. DE. **Soldagem dissimilar do aço inoxidável ferrítico AISI 444 e do aço inoxidável austenítico AISI 316L por meio do processo TIG autógeno utilizando corrente pulsada**. 2013. Dissertação de Mestrado, Universidade Federal do Ceará, Fortaleza, 2013.

BILGIN, M. B.; MERAN, C. The effect of tool rotational and traverse speed on friction stir weldability of AISI 430 ferritic stainless steels. **Materials & Design**, [s.l.], v. 33, p. 376–383, jan. 2012.

CAETANO, G. DE Q. et al. Influence of rotation speed and axial force on the friction stir welding of AISI 410S ferritic stainless steel. **Journal of Materials Processing Technology**, v. 262, p. 430–436, 1 dez. 2018.

CAETANO, G. Q. **Soldagem Similar de aços Inoxidaveis Ferríticos e Austenícios pelo Processo "Friction Stir Welding"**. 2016. Dissertação de Mestrado, Universidade Federal do Ceará, Fortaleza, 2016.

CHUNG, Y. D. et al. Friction stir welding of high carbon steel with excellent toughness and ductility. **Scripta Materialia**, [s.l.], v. 63, n. 2, p. 223–226, 1 jul. 2010.

DEBROY, T.; BHADESHIA, H. Friction stir welding of dissimilar alloys–a perspective. **Science and Technology of Welding & Joining**, [s.l.]: [s.n.], 2013.

FUJII, H. et al. Friction stir welding of carbon steels. **Materials Science and Engineering: A**, [s.l.], v. 429, n. 1, p. 50–57, 15 ago. 2006.

HEIDARZADEH, A. et al. Friction stir welding/processing of metals and alloys: A comprehensive review on microstructural evolution. **Progress in Materials Science**, [s.l.], v. 117, p. 100752, 1 abr. 2021.

JACQUIN, D.; GUILLEMOT, G. A review of microstructural changes occurring during FSW in aluminium alloys and their modelling. **Journal of Materials Processing Technology**, [s.l.], v. 288, p. 116706, 1 fev. 2021.

KADIAN, A. K.; BISWAS, P. The study of material flow behaviour in dissimilar material FSW of AA6061 and Cu-B370 alloys plates. **Journal of Manufacturing Processes**, [s.l.], v. 34, p. 96–105, 1 ago. 2018.

KASAI, H.; MORISADA, Y.; FUJII, H. Dissimilar FSW of immiscible materials: Steel/magnesium. **Materials Science and Engineering: A**, [s.l.], v. 624, p. 250–255, 29 jan. 2015.

KOKAWA, H. et al. Microstructures in Friction Stir Welded 304 Austenitic Stainless Steel. **Welding in the World**, [s.l.], v. 49, n. 3, p. 34–40, 1 mar. 2005.

KUMAR, N.; YUAN, W.; MISHRA, R. S. Chapter 2 - A Framework for Friction Stir Welding of Dissimilar Alloys and Materials. Em: KUMAR, N.; YUAN, W.; MISHRA, R. S. (Eds.). **Friction Stir Welding of Dissimilar Alloys and Materials**. Friction Stir Welding and Processing. [s.l.] Butterworth-Heinemann, 2015. p. 15–33.

LI, X. et al. Characterization and formation mechanism of ultra-fine ferrite grains in dissimilar metal weld between austenitic stainless steel and low alloy ferritic steel. **Materials Characterization**, [s.l.], v. 171, p. 110777, 1 jan. 2021.

LIPPOLD, J. C.; KOTECKI, D. J. **Welding metallurgy and weldability of stainless steels**. New Jersey, USA: John Wiley & Sons, 2005.

MACHADO, J. P. S. E. et al. Effect of temperature on the level of corrosion caused by heavy petroleum on AISI 304 and AISI 444 stainless steel. **Materials Research**, [s.l.], v. 9, n. 2, p. 137–142, 2006.

MISHRA, R. S.; MA, Z. Y. Friction stir welding and processing. **Materials Science and Engineering: R: Reports**, [s.l.], v. 50, n. 1–2, p. 1–78, 31 ago. 2005.

MUKHERJEE, M.; PAL, T. K. Influence of Heat Input on Martensite Formation and Impact Property of Ferritic-Austenitic Dissimilar Weld Metals. **Journal of Materials Science & Technology**, [s.l.], v. 28, n. 4, p. 343–352, 1 abr. 2012.

PARK, S. H. C. et al. Rapid formation of the sigma phase in 304 stainless steel during friction stir welding. **Scripta Materialia**, [s.l.], v. 49, n. 12, p. 1175–1180, dez. 2003.

R, S. R. et al. Predication of temperature distribution and strain during FSW of dissimilar Aluminum alloys using Deform 3D. **Materials Today: Proceedings**, [s.l.], v. 59, p. 1760–1767, 2022. Trabalho apresentado no Second International Conference on Materials and Technologies, [s.l.], 2022.

RAJPUT, S. K. et al. Investigation of microstructural behavior and mechanical properties of dissimilar weld joints of austenitic-ferritic stainless steel. **Materials Today: Proceedings**, Greater Noida, India, v. 25, p. 778–784, 2019. Trabalho apresentado no 2nd

International Conference on Computational and Experimental Methods in Mechanical Engineering, 2019, Greater Noida, India.

RAMIREZ, A. J. et al. Effect of Tool Offset on Dissimilar Cu-AISI 316 Stainless Steel Friction Stir Welding. *In*: The Twenty-first International Offshore and Polar Engineering Conference, 2011, [s.l.]. **Anais**...International Society of Offshore and Polar Engineers, 2011. Disponível em: <https://www.onepetro.org/conference-paper/ISOPE-I-11-103>. Acesso em: 6 dez. 2016.

SATHIYA, P.; ARAVINDAN, S.; HAQ, A. N. Effect of friction welding parameters on mechanical and metallurgical properties of ferritic stainless steel. **The International Journal of Advanced Manufacturing Technology**, [s.l.], v. 31, n. 11–12, p. 1076–1082, 21 jan. 2006.

SILVA, C. C. et al. Microstructural characterization of the HAZ in AISI 444 ferritic stainless steel welds. **Materials Characterization**, [s.l.], v. 59, n. 5, p. 528–533, maio 2008.

SILVA, C. C. et al. Austenitic and ferritic stainless steel dissimilar weld metal evaluation for the applications as-coating in the petroleum processing equipment. **Materials & Design**, [s.l.], v. 47, p. 1–8, 1 maio 2013.

SINGH, B. et al. Dissimilar joining of different grades of ferritic stainless steel: A review. **Materials Today: Proceedings**, [s.l.], v. 62, p. 4386–4391, 2022. Trabalho apresentado no International Conference on Materials, Processing & Characterization (13th ICMPC), [s.l.], 2022.

SMITH, W. F. **Structure and Properties of Engineering Alloys**. n. 2, [s.l.], McGraw-Hill (New York), 1993.

THOMAS, W. M. et al. **Friction stir butt welding**. Cambridge, TWI, 1991.

WANG, D. et al. Microstructural evolution and mechanical properties of friction stir welded joint of Fe–Cr–Mn–Mo–N austenite stainless steel. **Materials & Design**, [s.l.], v. 64, p. 355–359, 2014.

WANG, H. et al. Microstructure and mechanical properties of dissimilar friction stir welded type 304 austenitic stainless steel to Q235 low carbon steel. **Materials Characterization**, [s.l.], v. 155, p. 109803, 1 set. 2019.

WU, W.; HU, S.; SHEN, J. Microstructure, mechanical properties and corrosion behavior of laser welded dissimilar joints between ferritic stainless steel and carbon steel. **Materials & Design (1980-2015)**, [s.l.], v. 65, p. 855–861, 1 jan. 2015.

ZHANG, X. et al. Effects of melting-mixing ratio on the interfacial microstructure and tensile properties of austenitic–ferritic stainless steel joints. **Journal of Materials Research and Technology**, [s.l.], v. 8, n. 3, p. 2649–2661, 1 maio 2019.

2 CHAPTER 2: A fundamental literature review to begin the study

2.1 Stainless Steels

Stainless steels are iron-based alloys containing at least 10.5% chromium (PECKNER et al., 1977). This composition allows the formation of a surface film of chromium oxide that is highly adherent to the metal surface, of the order of 3 to 5 μm, preventing the action of aggressive agents, providing a superior corrosion resistance to other steels and elements such as nickel, molybdenum, copper, titanium, aluminium and niobium can also be added to improve their properties (LIPPOLD; KOTECKI, 2005).

Initially, stainless steels were named according to the levels of chromium and nickel in the alloy. The first types developed, which contained 18% Cr and 8% Ni, were called 18-8 stainless steels. As new stainless steel alloys were developed, this nomenclature became unfeasible. This led AISI (The American Iron and Steel Institute) to establish a classification system for stainless steels (SILVA et al., 2011). According to AISI, stainless steels can be classified into five categories according to the predominant constituent phase in its microstructure, in addition to the chemical composition and hardening mechanisms, which confer their own characteristics, referring to mechanical properties and corrosion resistance. Thus, we have austenitic, ferritic, martensitic, duplex and precipitation hardened stainless steels.

The most common stainless steels are the 300 series, essentially Fe-Cr-Ni alloys. The presence of Ni considerably improves corrosion resistance at high temperatures, aiding in the formation of the chromium oxide layer. The Ni element is a primary stabiliser for austenite and Cr for ferrite, so the correct proportion between these elements will define the balance between the phases. Four solid phases are present in this system: austenite, delta ferrite, alpha ferrite and sigma phase. The different microstructures of stainless steels exist depending on the amount of alloying elements present. There are mainly two groups of alloying elements: those that stabilise the ferrite phase (Cr, Si, Mo, Ti and Nb); and those that stabilise the austenite phase (Ni, C, N and Mn). Thus, alloying elements with similar characteristics were grouped based on their phase stabilisation potential, in terms of chromium equivalent (Cr_{eq}) and nickel equivalent (Ni_{eq}). From this grouping, the Schaeffler diagram presented in Fig. 2.1 was built, which relates the stainless steel microstructure with its chemical composition (DAVIS, 1994).

Analysing the Schaeffler diagram, the presence of three distinct regions corresponding to the austenite, ferrite and martensite phases can be seen. This diagram also shows regions with the formation of two and even three phases, giving stainless steels different properties according to the quantity and characteristics of each phase. Among the steels mentioned, the most consumed are austenitic, especially AISI 304. However, due to factors such as the rise in nickel prices, there is an increasing substitution of these by ferritic stainless steels. Especially in conditions where resistance to pitting or stress corrosion is more required than mechanical strength.

Figure 2.1 - Schaeffler diagram for stainless steels.

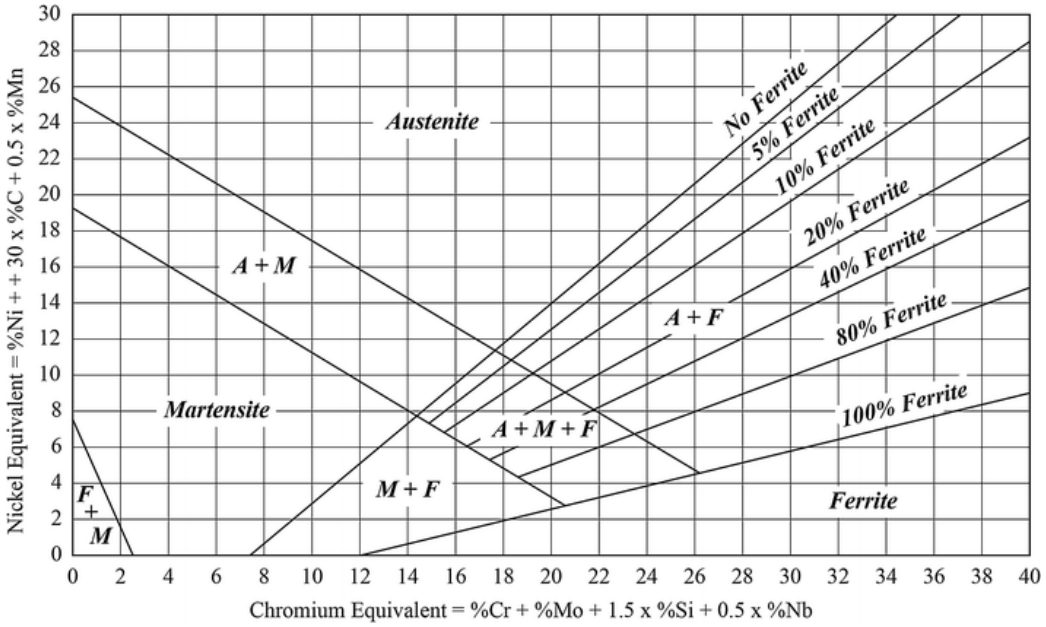

Source: DAVIS, (1994).

2.1.1 Ferritic Stainless Steels

Ferritic stainless steels have an essentially ferritic microstructure, thus having a body-centred cubic (BCC) crystal structure at room temperature. In addition to chromium, it may contain other ferrite-stabilizing elements, such as aluminium, niobium, molybdenum and titanium. These materials are less used than austenitic materials, as they have lower ductility and weldability (SMITH, W. F., 1993).

However, these steels have received considerable attention due to their excellent resistance to stress corrosion cracking and to lower cost than austenitic stainless steels (KRISHNAN et al., 2022). In addition to low cost, they also have high thermal conductivity, low linear expansion, and better resistance to stress corrosion in

environments containing chloride and atmospheric corrosion and oxidation than austenitic stainless steels (SHAN et al., 2011).

Fully ferritic structures have their toughness and ductility affected when precipitation with interstitial elements, such as carbon and nitrogen, and grain growth co-occur (LIPPOLD; KOTECKI, 2005). As ferritic stainless steels have low solubility to nitrogen and carbon in the ferritic phase, the appearance of precipitates is favoured (GORDON et al., 1996). Thus, one of the ways to avoid or minimise the appearance of precipitates in the structure is to stabilise these steels by adding niobium or titanium to their structure, which in turn will combine with carbon and nitrogen so that there is no formation of chromium carbides (GORDON et al., 1996; SELLO et al., 2010).

The most popular of the ferritic stainless steels is AISI 430, with more than 16% chromium; being one material with excellent corrosion resistance (CARBÓ, 2001). The most significant limitation for using the 430 steel is its weldability, as the welds in this steel are fragile and less resistant to corrosion (SUNNY; KORRA, 2021). AISI 410S ferritic stainless steel is a variation of martensitic stainless steel 410, with a lower carbon content and lower content of other austenitising alloying elements, containing 10.5-12.5% Cr and less than 1% Ni. These differences give the steel a lower capability to stabilise austenite at high temperatures and, consequently, lower potential for martensitic transformation, resulting in softer steel when cooled quickly. (SANDMEYER STEEL, 2014).

The precipitation of chromium carbides, and the excessive growth of the grain size in the welded regions are the main causes that lead to the poor performance of this material in welding. So, typically to this material is added stabilising elements such as titanium and niobium, as can be seen in Fig. 2.2, which have a tremendous chemical affinity with carbon and nitrogen, forming carbides and nitrides. This mainly prevents the precipitation of chromium carbonitrides and the formation of martensite. As carbon and nitrogen are austenitizing elements, which when dissolved in the matrix can cause the formation of austenite at the grain boundary of the ferrite, which after high cooling rates can lead to the martensitic transformation. (SEDRICKS, 1996). Among the stabilised ferritic stainless steels, the AISI 444 can be highlighted by its advantages in terms of corrosion performance and lower cost, thanks to their 18 wt.% of chromium and approximately 2 wt.% of molybdenum, small addition of Ti or Nb, and absence of Ni.

Figure 2.2 - Flowchart of composition variations from AISI 430 ferritic stainless steel, aiming at better properties.

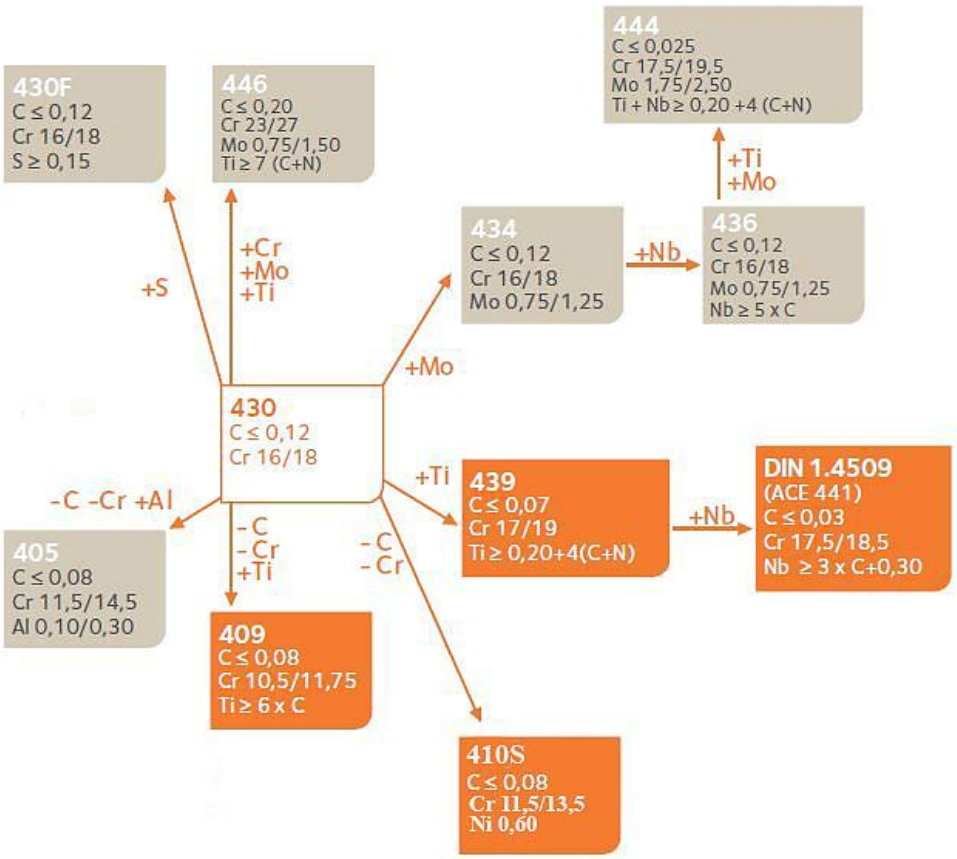

Source: CARBÓ, (2001).

2.1.2 Austenitic Stainless Steels

Austenitic stainless steels have a predominantly austenitic microstructure at room temperature, thanks to the addition of nickel as the primary austenitising elements. As presented by MICHLER (2016), even though only about 10.5% chromium is needed to make stainless alloys, austenitic stainless steels always include at least 15% chromium, which is coupled with nitrogen, carbon, manganese, and nickel to maintain the fcc structure. These steels are characterised by their high corrosion resistance, high tensile strength, and good elongation, offering the best properties for cold working (CHIAVERINI, 1998). Furthermore, this type of stainless steel cannot be hardened by heat treatment, but its hardness and tensile strength can be increased by work hardening.

Austenitic steel also has good ductility and resistance to high and low temperatures, good workability and weldability. (SUNNY; KORRA, 2021).

These materials are the most used commercially due to their combination of good mechanical properties with corrosion resistance and are responsible for approximately 70% of the production of stainless steels. These applications range from working at high temperatures, around 1150 °C, to very low temperatures (cryogenic conditions), generating a series of alternatives that are difficult to achieve with other materials, as highlighted by WAS and UKAI (2019) and CARBÓ, (2001).

Among the austenitic steels, AISI 304, also known as 18-8 (18%Cr and 8%Ni), is a general-purpose steel widely used in the industry. This is because it presents an excellent combination of resistance to corrosion and oxidation, good conformation, proper weldability, good ductility and impact resistance, even at temperatures of approximately -180°C. Additions of other alloying elements such as molybdenum can improve the corrosion resistance of these steels in several media, for example, the AISI 316, in which the addition of 2 wt.% of Mo makes it more resistant to stress corrosion cracking and pitting corrosion compared to AISI 304 (DILLON, 1995; SOURMAIL, 2001). The reduction of carbon in austenitic stainless steels AISI 304 and 316 to reduce the sensitisation phenomenon, how will it be dealt with later, gives rise to AISI 304L and 316L steels, as can be seen in Fig. 2.3.

AISI 304L steel has a chemical composition very similar to 304, with 304L being a variation with lower carbon content. This improves weldability and reduces the risk of intergranular corrosion. However, 304L has a yield strength and tensile strength slightly lower than type 304. These steels are widely used in different industrial sectors, from food and beverage processing to petrochemical industries. 316L steel has application in the same type of industries where AISI 304 and 304L steels are used. It is mainly intended for application in environments containing chlorides prone to pitting and crevice corrosion, as AISI 316L steel is more resistant than AISI 304L under these conditions. Thus, in alcohol distilleries, in the first distillation column, which operates at higher temperature and with higher levels of chlorides, the use of 316L steel becomes necessary. (PADILHA et al., 2002).

Figure 2.3 - Flowchart of composition variations from 304 austenitic stainless steel, aiming at better properties.

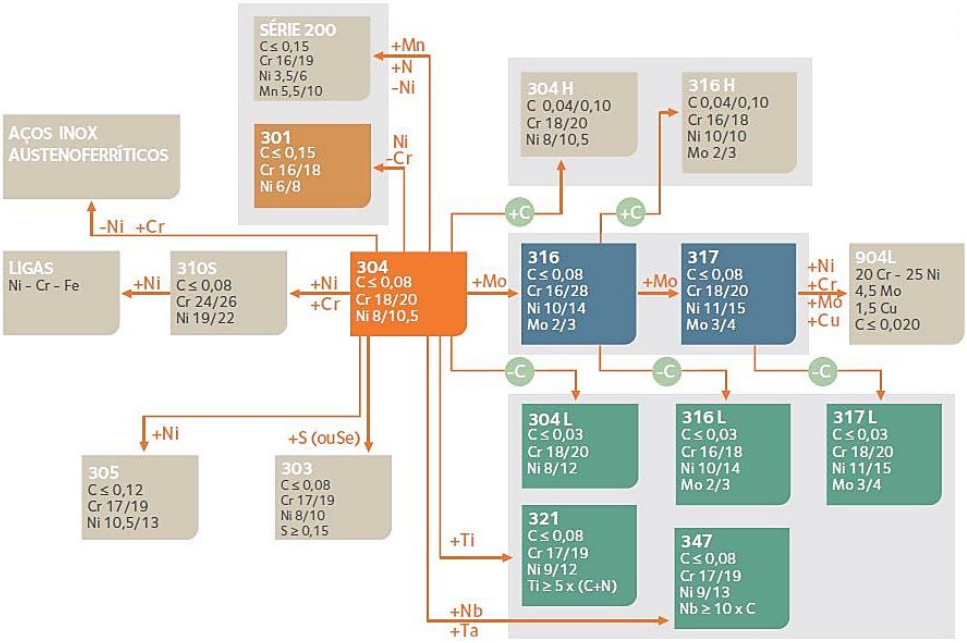

Source: CARBÓ, (2001).

2.1.3 Weldability of stainless steels

The weldability of stainless steels varies depending on the steel or combination of steels to be welded. Each type of stainless steel has a particularity regarding the embrittlement phenomena associate with its specific microstructural feature. In the fusion welding processing of ferritic stainless steels, their strength and ductility can be altered as a function of the excessive grain growth in the molten zone (MZ) and/or in the heat-affected zone (HAZ), due to direct solidification from the liquid phase to the ferrite phase, without any intermediate phase transformation during cooling. To minimise grain growth in these alloys, it is recommended that welding be performed using low energy and high speed. (MOHANDAS et al., 1999; VILLAFUERTE et al., 1990).

However, the degradation of mechanical properties in ferritic steels is not strictly related to grain growth, may also contribute to the intergranular precipitation of Cr-rich nitrides and carbides, which come from rapid cooling. (FRANKENTHAL; PICKERING, 1973) To overcome the problems of low ductility, new ferritic stainless steels with low

carbon and nitrogen contents have been developed, which also improve weldability. (LIPPOLD; KOTECKI, 2005).

Although austenitic stainless steels are considered materials of good weldability, in addition to sensitisation, which is the precipitation of chromium carbides in the intergranular spaces of the matrix, causing a decrease in corrosion resistance and mechanical properties, these steels are also subject to problems with distortion in the welds due to their high coefficient of thermal expansion. (HALL; BRIANT, 1984).

Another problem that austenitic stainless steels are subject to is associated with solidification cracking. This type of crack is associated with the presence of tensions combined with the presence of segregations that lead to the formation of intergranular liquid films in a coarse-grained structure, in the final stages of solidification. The ferrite content contained in the filler metal must be different from that contained in the base metal and must be well controlled to avoid the formation of a fully austenitic structure, which favours the appearance of solidification cracks. Typically, this problem is minimised in fusion welding processes by using a filler metal that leads to the formation of an austenitic-ferritic structure and the adoption of welding procedures that reduce the stresses in the weld (TAKALO; SUUTALA; MOISIO, 1979).

According to SAI RAKESH SINGH et al. (2022), to the criteria of strength, reduced investment cost and service standards, dissimilar welding between stainless steels became necessary, requiring the combination of different steels. An effective dissimilar welding should guarantee a mechanical resistance superior to the material of lesser resistance in the welded region. Such joints can be welded using a variety of welding methods. The main challenges in expanding the application of dissimilar joints between ferritic and austenitic stainless steels occur due of the highly inhomogeneous nature of these joints in terms of their microstructure, mechanical, thermal and fracture properties. The negative points of materials can be enhanced, such as hot cracking in austenitic steel and excessive grain growth in ferritic steel. (KUMAR et al., (2018) In solid state welding, some advantages can be achieved in these dissimilar joints, such as the absence of porosities, undercuts, and hot cracks, which can be avoided. However, these advantages depend primarily on the correct choice of parameters and the proper use of the welding procedure. (MISHRA et al., 2005). Despite the advantages, in solid-state welding of stainless steels, sigma phase formation and sensitisation are still recurrent problems, and the interference of welding parameters in the formation of defects, as well

as the phenomena involved in the recrystallisation process, are still aspects that need further research.

2.2 Friction stir welding (FSW)

In recent decades, Friction Welding (FSW), a solid-state welding process, was developed by THOMAS et al. (1991) in The Welding Institute (TWI) in Cambridge, England, derived from conventional friction welding techniques allowing the use of the advantages of solid-state welding to produce butt and lap joints. Widespread benefits have resulted from applying FSW in joining aluminium components in the aerospace, shipbuilding, automotive and rail industries. (MISHRA; MA, 2005; NANDAN; DEBROY; BHADESHIA, 2008). FSW process may causes less distortions and reduces residual stresses associated with the welding process. The intense plastic deformation can result in dynamic recrystallisation and grain refinement and FSW joints can be free of defects and failures such as cracks, hydrogen fissures, solid inclusions and lack of fusion (MAHAKUR et al., 2021)

The FSW process uses a rotating tool consisting of a cylindrical shoulder and a pin forced into the seam. This occurs under conditions where the friction between the material and the tool promotes heating to a temperature below the melting point of the metal, and the material is plastically deformed during the process. Localised heating softens the material around the pin, and the combination of tool rotation and the translation of the material from the front of the pin to the back of the pin leads to the movement necessary for developing the weld. The rotation and displacement of the tool produce a flow of material around the tool, which varies with the tool's geometry and with the traverse and rotational speed, allowing solid phase bonding between the two pieces. In contrast to conventional melting processes, surface cleaning, consumable electrodes and a shielding gas are not required. In essence, FSW is a straightforward process, and its main features are presented in Fig. 2.4. (MISHRA; MA, 2005).

Figure 2.4 - Schematic illustration of the FSW process.

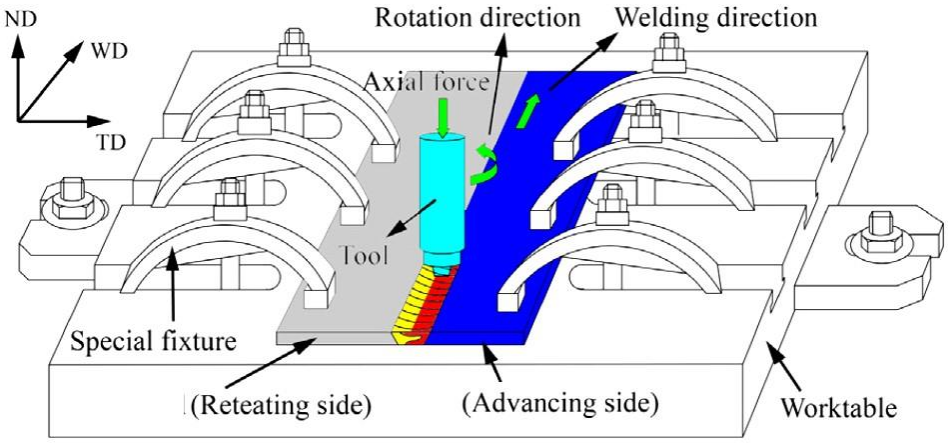

Source: Adapted from WANG, H. et al. (2019).

2.2.1 FSW process parameters

2.2.1.1 Tool Geometry

The quality of FSW joints and the success of the process depend on the correct setting of the parameters. Thus, understanding and optimising process parameters is essential for an efficient FSW process, as highlighted by RANI et al. (2022). The tool and its geometry play a critical role in the process, as they are responsible for heating the parts, moving and subsequent material flow. According to UDAY et al. (2010), the tool's primary function is to create localised heating. During the start of tool immersion, friction between the pin and the workpiece generates heat, softening the material. Due to friction between them, most of the heat is supplied when the tool shoulder is touching the workpiece (UDAY et al., 2010). The shoulder must also contain the volume of heated and plasticised material to avoid loss of softened material in the plasticised zone and to avoid forming plasticised pores or tunnel defects.

The tool's geometry has evolved significantly, intending to achieve better results such as reduced force, easier penetration of the pin, increased interface between the pin and the plasticised material, more regular material flows, among others (GIBSON *et al.*, 2014). Depending on the taper of the tool, the presence or absence of threads, the pitch and direction of these threads, the length of the pin and the diameter of the shoulder,

among others, there may be more heat, more friction and more deformation of the material and the flow of the material can be more complex or more intense. (MISHRA et al., 2005).

As noted by GHANGAS and SINGHAL, (2018) the lower profile of the shoulder has the mechanical function of forging material, in turn, it also has responsibility for the flash production generated during the process. Thus, tools with negative recesses were developed, in which the material in the plastic flow state assumes this negative volume of the support, causing less material to be expelled out of the face contact region, which improves weld bead closure and reduces flash production.

Low melting point materials are welded by the friction stir welding process with tools produced from hardened tool steels, which have a low manufacturing cost. Tool steels provide sufficient hardness and abrasion resistance for FSW welding of aluminum alloys and other low melting point materials. High melting temperature materials, such as carbon steel, stainless steel, nickel-based alloys, among others, were not initially applied to the FSW process, mainly due to the limitation of the materials that constituted the first tools. Those made of refractory alloys containing tungsten, hafnium, rhenium, molybdenum, niobium and zirconium had high melting temperatures but lacked hardness and abrasion resistance to weld steels because, during FSW welding with this tool, contamination by these alloying elements occurred in the stir zone (STEEL, et al, 2014).

However, friction welding of ferrous and non-ferrous alloys with a high melting point is now possible thanks to developments in material technology as well as FSW equipment specifically designed for these alloys. Successful FSW welding of high melting temperature materials requires careful control of process variables (STEEL et al., 2014). Thus, a tool coupling system was designed with a tool holder with liquid cooling and shielding gas and a precise system for measuring temperature and process variables, as shown in Fig. 2.5.

Figure 2.5 - (a) Tool system required to friction stir weld ferrous alloys (b) FSW tool with PCBN tip, locking collar and tungsten carbide shank.

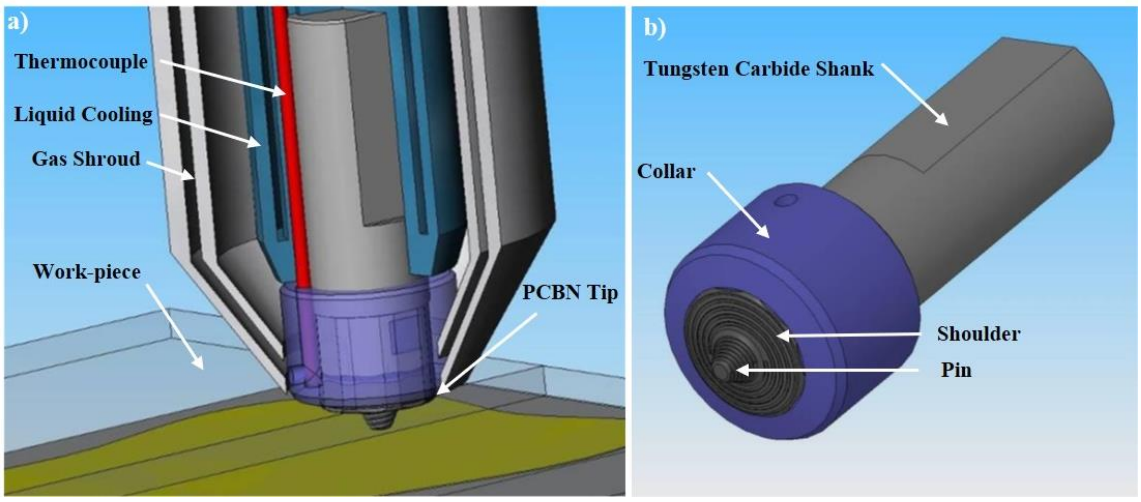

Source: Adapted from STEEL et al. (2014).

As FSW welding of ferrous and non-ferrous metals requires a tool that can withstand temperatures of approximately 900°C and 1000°C and high loads during the welding process, a tool has been developed to produce welds at these temperatures while maintaining high abrasion resistance. This tool is made of polycrystalline cubic boron nitride (PCBN), and numerous studies prove the high efficiency of using this tool for FSW welding with stainless steels, even using high rotation and welding speeds and, thus, withstanding high temperatures. In the study developed by WANG *et al.* (2014) with AISI 304 austenitic stainless steel, using 800 rpm and 100 mm/min, joints with similar mechanical strength to the base metal were produced. As well as the analyses carried out by AHN *et al.* (2012) using AISI 409L ferritic stainless steel, with 700 rpm and 60 mm/min, which also obtained welds with mechanical properties and resistance to intergranular corrosion similar to the base metal.

2.2.1.2 Rotation Speed

Rotation speed is the parameter related to the friction force and friction at the interface between the material and the tool and is closely linked to the heat generated during the welding process, as the frictional coupling of the tool surface with the joint governs the heating mechanism and the rotation of the tool results in agitation and stir of the material around the pin, as highlighted KUMAR et al. (2022). The higher the rotation

speed, the higher the temperature reached in the process due to the increase in frictional heating (MISHRA et al., 2005).

Evaluating the microstructure and mechanical properties of aluminium alloys using the FSW process, it is possible to verify that, as the rotation speed increases, the hardness in the stir zone gradually increases due to the increase in dislocation density. The ultimate tensile strength increases as the rotation speed increases from 600 rpm to 800 rpm, reaching stabilisation over a wide rpm range. Then, with rotation speeds of 1400 rpm, a noticeable decrease is observed in the tensile strength limit due to the formation of voids with the high heat input. At high rotational speeds, defect-free FSW joints of aluminium alloys tend to displace the fracture into the heat-affected zone (HAZ) (ZHANG et al., 2011).

In the study of LAKSHMINARAYANAN et al. (2013) on the application of different rotation speeds for ferritic stainless steel in FSW welds, varying the rotation from 800 rpm to 1200 rpm, it was possible to observe that the best result of tensile strength limit was for the rotation speed of 840 rpm, similar to the range in which the stabilisation of the best tensile strength results occurred in the aluminium alloy evaluated by ZHANG et al. (2011).

2.2.1.3 Welding speed

The tool travel speed or welding speed influences the dynamic conditions of the material flow around the pin and the process's heat generation, since it increases or decreases the time the material is exposed to tool friction. Thus, low welding speeds imply more significant heat input during the process. According to LAKSHMINARAYANAN et al. (2013), for stainless steels, welding speed is the factor that has the most significant influence on the tensile and impact strength limit, followed by rotation speed and shoulder diameter, as the material's microstructure is substantially altered by temperature elevation and intense plastic deformation, the welding speed being the most influential parameter in these factors.

The variation of the welding speed implies considerably in the mechanical properties and the size and shape of the different zones in magnesium alloys, as observed in the study of ABBASI GHARACHEH *et al.* (2006), as well as in the grain size of aluminum alloys (HIRATA et al., 2007). The higher the welding speed, the higher the

cooling rates, restricting grain growth and decreasing the thermomechanically affected zones (TMAZ) and heat-affected zone (HAZ).

2.2.1.4 Tool tilt angle

Tool tilt plays an essential role in FSW welding, as it assists in moving material from front to back of the pin and also in the consolidation of the plasticised material after its passage due to the higher pressure in the stir region (CAPELARI, 2006). Increasing the tool angle results in a greater immersion of the tool in the material and an increase in the stability of the FSW process (GIBSON *et al.*, 2013). The increase in penetration as a function of tool angle change (α) is exemplified by Fig. 2.6.

Figure 2.6 - Increase in penetration as a function of tool angle change.

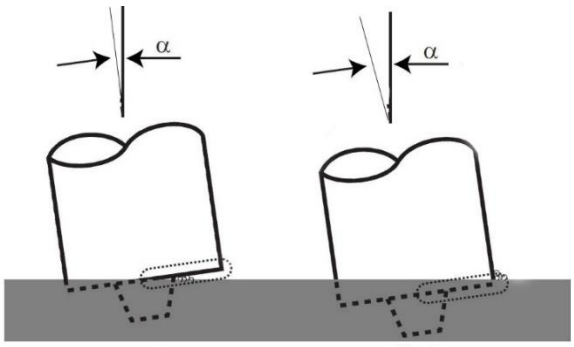

Source: SHULTZ *et al.* (2010).

2.2.1.5 Tool penetration

Tool penetration is a function of the length of the pin, and the angle of inclination adopted and defines the pressure exerted on the material at the back of the tool during welding (MAHAKUR et al., 2021). When the pin is excessively long, the tool shoulder has little contact with the sheet to be welded. This lowers the weld temperature and reduces back shoulder pressure on the sheet, often resulting in faulty welds. This is because the friction between the shoulder and the sheet surface is the main heat source for welding. (ZHU et al., 2004). The ideal pin dimension avoids contact with the clamping bracket below the sheet and, for a given angle of inclination, allows sufficient shoulder pressure on the sheet to result in a full penetration weld.

2.2.1.6 Axial force

The axial force has a considerable influence on the distribution and flow of material along the welded joint, in addition to its participation in generating heat during welding. According to KIM *et al.*, (2006), for each axial force, there is an appropriate rotational that results in a defect-free weld. A high axial force results in a greater amount of flash production, and losses in the stability of its application imply the formation of volumetric defects. (KIM et al., 2006).

2.2.2 Microstructural Profile

The typical microstructure of FSW has some differences from the microstructure of conventional solder joints. During the FSW process, the temperature and the plastic deformation generated by an input of energy supplied mainly by the friction between the tool and the material resulting in significant microstructural evolution in certain aspects, including grain size, grain boundary, dissolution and hardening of precipitates, dissolution and redistribution of dispersoids, as well as texture modification. (GENEVOIS et al., 2006).

Visualising the cross-section of a FSW joint, it is possible to observe an asymmetrical arrangement of the different zones formed. The welding side where the direction of travel is the same as the direction of rotation of the tool is called the "advancing side". Likewise, the side where the directions are opposite is called the "retreating side". TWI established a convention many years ago that the direction of tool rotation is by default clockwise on TWI equipment, so the advancing side is almost always the right side of cross-sectional macrographs (THREADGILL, 2007).

By classifying weld zones produced by friction stir welding, it is possible to visualise microstructural zones that are rarely similar to those found in other materials. However, the classification system must be able to accommodate all materials. Thus, the cross-section of FSW welded joints is divided into four main regions as indicated in Fig. 2.7. Area "A" is the base metal (MB) region not affected by the heat or strain rate induced by the welding tool during the FSW process. In this region, the grains deform according to the processing and heat treatment of the alloy manufacturing. Area "B" is the heat-affected zone (HAZ), a region affected by the thermal cycle during welding, which leads to microstructural and mechanical properties modification, but without residual plastic deformation in the microstructure. Area "C" is affected by both heat, and plastic

deformation called the thermomechanically affected zone (TMAZ), in which the material was plastically deformed by the tool and the resulting heat flow exerted some sort of influence on the material, resulting in recovery and recrystallisation of the material. (THREADGILL, 2007).

The fourth area, "D" extends to the center between the advancing and retreating sides, corresponding to the tool's shoulder width. The stir zone (SZ), also called “nugget”, corresponds to the central region of the weld in which original grains and subgrain boundaries favour the formation of refined equiaxed grains, from recrystallisation, due to the combined action of the support and tool pin as sources of heat by friction and plastic deformation simultaneously, resulting in changes in the mechanical properties of the material. (FRATINI et al., 2005)

Figure 2.7- Perfil schematic of a transverse cross-section showing different zones of a friction stir weld. A, BM; B, HAZ; C, TMAZ; and D, SZ or Nugget.

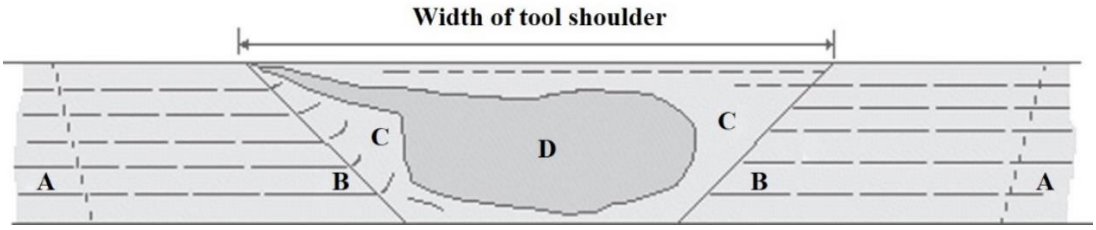

Source: MISHRA et al. (2016)

The different regions in the FSW welded joint is determined by the degree of deformation, and the maximum temperature reached resulting from the process parameters. However, another critical element in forming these regions is the stacking fault energy (SFE) of the material to be welded, as it determines the tendency of the metal to recover or recrystallize dynamically.

Recrystallisation is the generation of new grains from the deformed metal by the formation and migration of high-angle grain boundaries (HAGB), promoted by the energy stored in the material during deformation in the form of dislocations. According to KOU, 2003, the recrystallisation phenomenon, for most metal alloys, occurs at a temperature around 40% to 50% of the melting temperature, but this recrystallisation temperature can be affected by the amount of plastic deformation and the composition of the alloy. While recovery is any softening process that occurs in the deformed metal without involving the migration of HAGB. The driving force for this transformation is the reduction of the

energy accumulated during deformation through the rearrangement of dislocations, which leads to the formation of low-angle grain boundaries (LAGB) (PORTER et al., 2009).

2.2.3 Defects Formation in FSW

FSW has been described as a solid state welding process with flux progressing through metallurgical processing zones with initial deformation, extrusion, forging and cooling. (ARBEGAST et al., 2003). According to ARBEGAST (2008), these zones and flow patterns are observed in all metallic and thermoplastic materials, with only the volume and direction of the material in each zone being different. However, the interactions of tool geometry, material properties and the effects of process parameters on defect formation are complex.

MISHRA and MAHONEY (2007) highlight that the characteristic defects of the FSW process can be identified as those related to the flow and the tool geometry. The lack of penetration defect occurs due to the inadequate penetration depth of the tool pin, which is related, among other factors, to the geometry of the pin. Flow-related defects occur outside the acceptable processing window with parameters considered too hot or too cold. Under hot processing, excessive material flow results in flash formation, surface galling and nugget collapse. Under cold processing, insufficient flowing material results in surface lack of fill, wormhole, or lack of consolidation defects on the advancing side, as can be seen in Fig. 2.8.

Figure 2.8 - Characteristic defect types in friction stir welds.

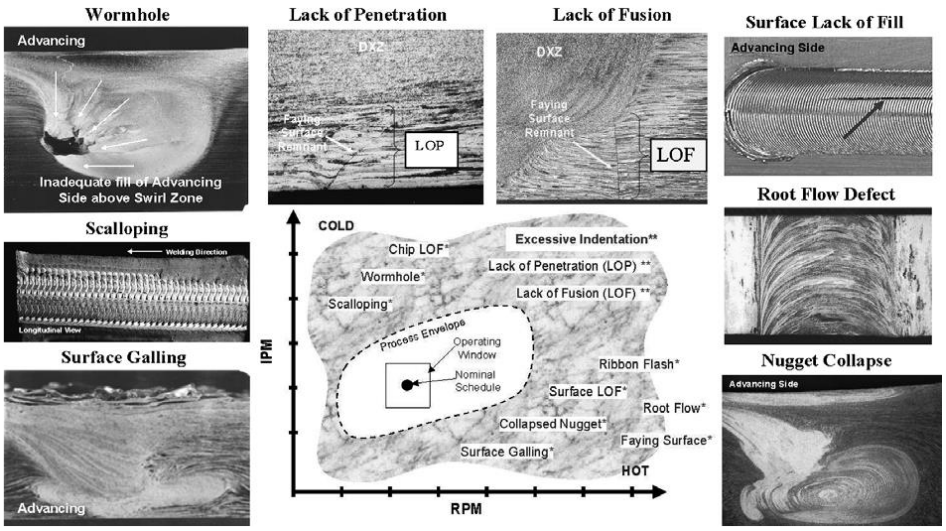

Source: MISHRA and MAHONEY, (2007)

However, few studies focus on quantifying these defects and their effect on the service life of FSW joints. Despite recent studies performed by MAHTO, KUMAR and PAL (2020), the dependence between the welding process parameters and the resulting number of defects is highlighted. In the case of dissimilar FSW joints, IORDACHE et al., (2021) highlights that the analysis of defects within this welding configuration is one of the most critical points, because the heat generated by the friction between the shoulder and the tool pin and the dissimilar plates is not always evenly distributed between the plates. In addition, the values of the mechanical and thermal properties of the sheets to be welded are different. Therefore, it is necessary to choose the joining parameters (welding speed, rotation speed and axial force) in order to obtain an optimal welding temperature in the mixing zone, suitable for the different welded materials.

2.3 Application of the FSW Process in Dissimilar Materials

The importance of joining dissimilar materials increases as engineers strive to reduce weight and improve component performance. Over the years, the FSW process has been widely adopted for joining aluminum alloys in the automotive, railway, aerospace and shipbuilding industries (DAWOOD; MOHAMMED; RAJAB, 2014). As highlighted by KUMAR and BALASUBRAMANIAN (2020), the combination of different materials, such as aluminium and steel, aluminum and magnesium, steel and nickel superalloy, allows an optimal exploitation of the best properties of both materials. However, a barrier placed in the welding of these different materials is the formation of intermetallic compounds, which reduces the mechanical resistance and corrosion, compromising the integrity of the welded structure. Efforts to eliminate the formation of these harmful compounds have been carried out, among other ways, by the use of the FSW process. They have led to the implementation and production of structures of dissimilar materials for industrial applications. (KUMAR et al., 2015).

A better understanding of the behaviour of materials in the FSW process requires establishing a precise relationship between the input variables (tool rotation speed, tool travel speed, axial force, torque, etc.) and the output process variables. (temperature, precipitates, etc.). Among the key factors for optimising the FSW process in dissimilar joints are heat generation and material flow. Together these determine the temperature history, material flow pattern and resulting microstructure.

2.3.1 Heat Generation and Temperature Distribution

Analytical estimation of heat generation in similar FSW welds is relatively more accessible, as we have only one type of material in contact with the tool. However, the phenomenon becomes quite complicated regarding heat generation and temperature distribution in dissimilar FSW welds. Different materials, in general, have different thermal properties and different flow characteristics. These factors affect heat generation, temperature distribution and material flow.

In similar FSW welding, the position of the tool's axis of rotation relative to the weld centerline does not affect heat generation. However, it becomes important to consider the proportion of the tool surface in contact with each material for different materials. Studies show that in dissimilar FSW welding between aluminum and steel alloys, if the tool is dipped to the side of the high melting point material, the heat generation is so excessive that it causes the lower melting point material to melt therefore an appropriate strategy needs to be adopted (MURR, 2010).

During the FSW process, frictional heating between the tool and the workpiece is an important component of the total heat generated. In similar welds, the tool is in contact with the same type of material along its entire length. However, as shown schematically in Fig. 2.9, in dissimilar FSW joints during each rotation, one part of the tool is in contact with one type of material and the rest with another. Thus, depending on the position of the tool in relation to the centre of the weld, the friction coefficient of the materials and the amount of heat generated can vary significantly. (KUMAR et al., 2015b).

Figure 2.9 - A schematic of the transverse cross-section of the dissimilar weld showing asymmetrically located FSW tool.

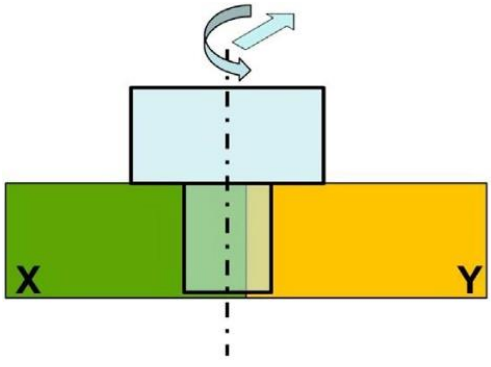

Source: KUMAR et al. (2015).

In similar welding, for all practical purposes, the thermal profile can be considered symmetrical concerning the weld centerline. However, during dissimilar welding, the significant difference in the thermal diffusivity of the materials will lead to the establishment of a highly asymmetrical thermal field. Thermal profiles for a given set of processing parameters are schematically shown for similar welding in Fig. 2.10 (a), showing the existence of symmetry in the temperature distribution in the weld cross-section. However, as shown in Fig. 2.10 (b), an asymmetrical temperature distribution should be noted due to differences in thermal and physical properties of both materials (BARBINI et al., 2017).

Figure 2.10 - Temperature contours showing (a) symmetric profile in similar welding and (b) asymmetric profile in dissimilar welding.

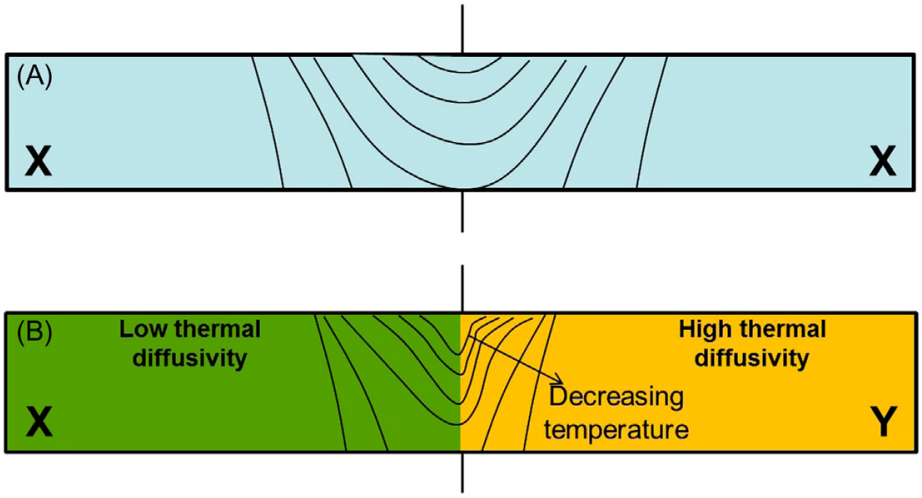

Source: KUMAR et al. (2015).

2.3.2 Material flow

The same material flow model developed to understand the flow of materials around the tool during similar FSW welding can be used to understand material flow in dissimilar welding. As GUERRA et al., (2002) proposed, the front metal is removed to the back side of the tool. With each new rotation, a new material makes contact with the tool on the advancing side (AS). With each new rotation, a new amount of material is directed to the material already deposited on the retreating side (RS), and this increases the thickness of the shear layer on the retreating side, as shown in Fig. 2.11(a). This value can be modified for dissimilar welding and is shown in Fig. 2.11 (b), which shows that

up to point B, only material X is removed in the tool from the advancing side to the retreating side. From point B onwards, material Y begins to pass over material X, accumulated during tool rotation between points A and B. (KUMAR et al., 2015c).

Figure 2.11 – (a) Visualization of material flow during the FSW process (AS, advancing side; RS, retreating side). (b) Visualisation of material flow in dissimilar metal welding during FSW (AS, advancing side; RS, retreating side).

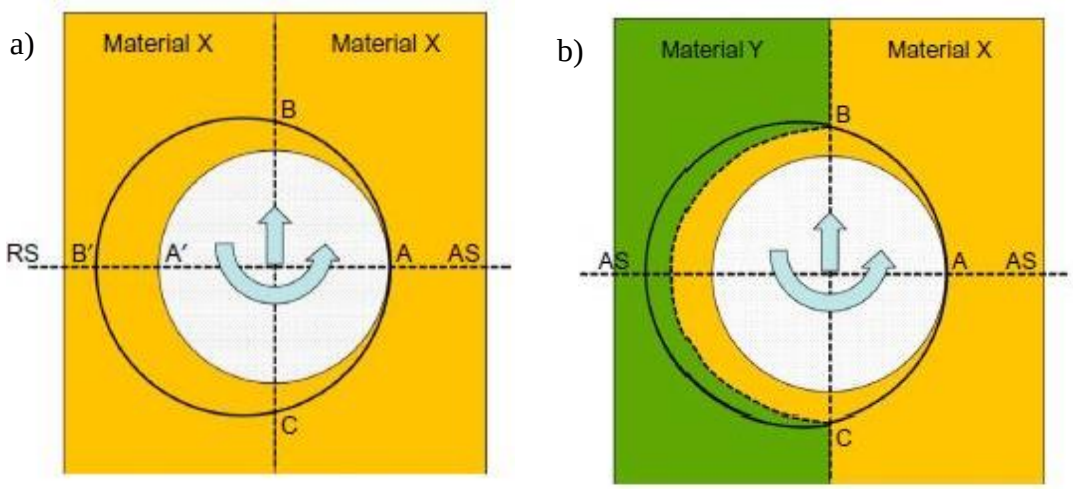

Fonte: KUMAR et al. (2015).

In this description of the material flow around the tool, at point B, the weld center line is present, which coincides with the linear path of the tool movement. However, the weld centerline can be tilted to AS or RS. These arrangements will impact the material flow around the tool and the flow pattern developed in the stir zone. It is also recognised from the material flow study that, in general, the material present in front of the tool towards the AS has a different flow than that towards the RS, therefore the level of stir between materials X and Y also depend on which material is located on the advancing side and on the retreating side. In addition to the position of the tool concerning the weld interface, other parameters such as rotational speeds and welding speed play an important role in determining the level of a stir between the two materials. (KUMAR et al., 2015c).

2.3.3 Challenges for Friction Stir Welding of Dissimilar Materials

The FSW process has shown great potential in the union of several alloys with different physical characteristics and chemical properties, as shown by SHANKAR et al. (2022) and GOTAWALA and SHRIVASTAVA (2020). The industrial implementation of the FSW process in different materials has shown considerable benefits in design flexibility and weight reduction for structures. However, as highlighted by EMAMI et al. (2020) the differences in physical, mechanical, and metallurgical properties of the metals make the FSW dissimilar welding more complex when compared with the welding of similar metals. Thus, the control of process parameters on forming defects and metallurgical transformations resulting from the dissimilar FSW process becomes a challenge with strong scientific and technological appeal. Among the main challenges in expanding the FSW process of dissimilar materials is the investment in research on reliability and durability through careful analysis of the mechanical performance and corrosion resistance of welded joints.

2.4 References

ABBASI GHARACHEH, M. et al. The influence of the ratio of "rotational speed/traverse speed" (ω/v) on mechanical properties of AZ31 friction stir welds. **International Journal of Machine Tools and Manufacture**, [s.l.], v. 46, n. 15, p. 1983–1987, dez. 2006.

AHN, B. W. et al. Microstructures and properties of friction stir welded 409L stainless steel using a Si3N4 tool. **Materials Science and Engineering: A**, [s.l.], v. 532, p. 476–479, 15 jan. 2012.

ARBEGAST, W. J. et al. Hot deformation of aluminum alloys III. **TMS, Warrendale, Pa**, p. 313–327, 2003.

ARBEGAST, W. J. A flow-partitioned deformation zone model for defect formation during friction stir welding. **Scripta Materialia**, Viewpoint set no. 43 "Friction stir processing". [s.l.], v. 58, n. 5, p. 372–376, 1 mar. 2008.

BARBINI, A.; CARSTENSEN, J.; DOS SANTOS, J. F. Influence of a non-rotating shoulder on heat generation, microstructure and mechanical properties of dissimilar AA2024/AA7050 FSW joints. **Journal of Materials Science & Technology**, 1 nov. 2017.

CAPELARI, T. V. **Avaliação do desempenho de ferramentas na soldagem de alumínio AA 5052 pelo processo FSW**. 2006. Dissertação de Mestrado, Universidade Federal do Rio Grande do Sul, Porto Alegre, 2006.

CARBÓ, H. M. **Aço Inoxidável:** Aplicações e Especificações. São paulo: Acesita, 2001.

CHIAVERINI, V. **Aços e Ferros Fundidos**, v. 1, n. 7, Associação Brasileira de Metalurgia e Materiais, Brasil, 1988.

DAVIS, J. R. **Stainless Steels**. [s.l.] ASM International, 1994.

DAWOOD, H. I.; MOHAMMED, K. S.; RAJAB, M. Y. Advantages of the Green Solid State FSW over the Conventional GMAW Process. **Advances in Materials Science and Engineering**, [s.l.], v. 2014, p. e105713, 28 maio 2014.

DILLON, C. P. **Corrosion Resistance of Stainless Steels**. [s.l.] CRC Press, 1995.

EMAMI, S. et al. Dissimilar friction stir welding of AISI 430 ferritic and AISI 304L austenitic stainless steels. **Archives of Civil and Mechanical Engineering**, [s.l.], v. 20, n. 4, p. 131, 18 out. 2020.

FRANKENTHAL, R. P.; PICKERING, H. W. Intergranular Corrosion of a Ferritic Stainless Steel. **Journal of The Electrochemical Society**, [s.l.], v. 120, n. 1, p. 23, 1973.

FRATINI, L.; BUFFA, G. CDRX modelling in friction stir welding of aluminium alloys. **International Journal of Machine Tools and Manufacture**, [s.l.], v. 45, n. 10, p. 1188–1194, ago. 2005.

GENEVOIS, C. et al. On the coupling between precipitation and plastic deformation in relation with friction stir welding of AA2024 T3 aluminium alloy. **Materials Science and Engineering: A**, [s.l.], v. 441, n. 1–2, p. 39–48, 15 dez. 2006.

GHANGAS, G.; SINGHAL, S. Effect of tool pin profile and dimensions on mechanical properties and microstructure of friction stir welded armor alloy. **Materials Research Express**, [s.l.], v. 5, n. 6, p. 066555, jun. 2018.

GIBSON, B. T. et al. Friction stir welding: Process, automation, and control. **Journal of Manufacturing Processes**, [s.l.], v. 16, n. 1, p. 56 – 73, 2014

GORDON, W.; VAN BENNEKOM, A. Review of stabilisation of ferritic stainless steels. **Materials Science and Technology**, [s.l.], v. 12, n. 2, p. 126–131, 1 fev. 1996.

GOTAWALA, N.; SHRIVASTAVA, A. Analysis of material distribution in dissimilar friction stir welded joints of Al 1050 and copper. **Journal of Manufacturing Processes**, v. 57, p. 725–736, 1 set. 2020.

HALL, E. L.; BRIANT, C. L. Chromium depletion in the vicinity of carbides in sensitized austenitic stainless steels. **Metallurgical Transactions A**, [s.l.], v. 15, n. 5, p. 793–811, maio 1984.

HIRATA, T. et al. Influence of friction stir welding parameters on grain size and formability in 5083 aluminum alloy. **Materials Science and Engineering: A**, [s.l.], v. 456, n. 1–2, p. 344–349, 15 maio 2007.

HUNTER, G. B.; EAGAR, T. W. Ductility of stabilized ferritic stainless steel welds. **Metallurgical transactions A**, [s.l.], v. 11, n. 2, p. 213–218, 1980.

IORDACHE, M. D. et al. A numerical strategy to identify the FSW process optimal parameters of a butt-welded joint of quasi-pure copper plates: modeling and experimental validation. **The International Journal of Advanced Manufacturing Technology**, [s.l.], v. 115, n. 7–8, p. 2505–2520, ago. 2021.

KIM, Y. G. et al. Three defect types in friction stir welding of aluminum die casting alloy. **Materials Science and Engineering: A**, [s.l.], v. 415, n. 1, p. 250–254, 2006.

KOU, S. **Welding metallurgy**. New Jersey. USA: John Wiley & Sons, 2003.

KRISHNAN, T. M. et al. Influence of arc duration on microstructure and tensile behavior of magnetically impelled arc butt welded AISI 409 ferritic stainless steel tubes. **Materials Science and Engineering: A**, [s.l.], v. 831, p. 142257, 13 jan. 2022.

KUMAR, K. P. V.; BALASUBRAMANIAN, M. Analyzing the Effect of FSW Process Parameter on Mechanical Properties for a Dissimilar Aluminium AA6061 and Magnesium AZ31B Alloy. **Materials Today: Proceedings**, Vellore, India, v. 22, p. 2883–2889, 2019. Trabalho apresentado no 2nd International Conference on Materials Manufacturing and Modelling, ICMMM – 2019, VIT University, 2019, Vellore, India.

KUMAR, N.; YUAN, W.; MISHRA, R. S. A Framework for Friction Stir Welding of Dissimilar Alloys and Materials. **Friction Stir Welding of Dissimilar Alloys and Materials**. Friction Stir Welding and Processing. [s.l.] Butterworth-Heinemann, 2015a. p. 15–33.

KUMAR, N.; YUAN, W.; MISHRA, R. S. Tool Design for Friction Stir Welding of Dissimilar Alloys and Materials. **Friction Stir Welding of Dissimilar Alloys and Materials**. Friction Stir Welding and Processing. [s.l.] Butterworth-Heinemann, 2015b. p. 35–42.

KUMAR, N.; YUAN, W.; MISHRA, R. S. Modeling and Simulation of Friction Stir Welding of Dissimilar Alloys and Materials **Friction Stir Welding of Dissimilar Alloys and Materials**. Friction Stir Welding and Processing. [s.l.] Butterworth-Heinemann, 2015c. p. 115–121.

KUMAR, R. et al. Effect of FSW process parameters on mechanical properties and microstructure of dissimilar welded joints of AA2024 and AA6082. **Materials Today: Proceedings**, Phagwara, India, v. 50, p. 1435–1441, 2021. Trabalho apresentado no 2nd International Conference on Functional Material, Manufacturing and Performances (ICFMMP-2021), 2021, Phagwara, India.

KUMAR, S. R. et al. Investigation on Microstructural behavior and Mechanical Properties of plasma arc welded dissimilar butt joint of austenitic- ferritic stainless steels. **Materials Today: Proceedings**, Tiruchirappalli, India, v. 5, n. 2, Part 2, p. 8008–8015. Trabalho apresentado no International Conference on Emerging Trends in Materials and Manufacturing Engineering (IMME17), 2017, Tiruchirappalli, India.

LAKSHMINARAYANAN, A. K.; BALASUBRAMANIAN, V. Process Parameters Optimisation for Friction Stir Welding of AISI 409M Grade Ferritic Stainless Steel. **Experimental Techniques**, [s.l.], v. 37, n. 5, p. 59–73, 2013.

LIPPOLD, J. C.; KOTECKI, D. J. **Welding metallurgy and weldability of stainless steels**. New Jersey, USA: John Wiley & Sons, 2005.

MAHAKUR, V. K. et al. A Review on Advancement in Friction Stir Welding Considering the Tool and Material Parameters. **Arabian Journal for Science and Engineering**, [s.l.], v. 46, n. 8, p. 7681–7697, 1 ago. 2021.

MAHTO, R. P.; KUMAR, R.; PAL, S. K. Characterizations of weld defects, intermetallic compounds and mechanical properties of friction stir lap welded dissimilar alloys. **Materials Characterization**, [s.l.], v. 160, p. 110115, fev. 2020.

MICHLER, T. Austenitic Stainless Steels. Em: **Reference Module in Materials Science and Materials Engineering**. [s.l.] Elsevier, 2016. p. B9780128035818025000.

MISHRA, R. et al. **Friction stir welding and processing VII**. [s.l.] Springer, 2016.

MISHRA, R. S.; MA, Z. Y. Friction stir welding and processing. **Materials Science and Engineering: R: Reports**, [s.l.], v. 50, n. 1–2, p. 1–78, 31 ago. 2005.

MISHRA, R. S.; MAHONEY, M. W. (EDS.). **Friction stir welding and processing**. Materials Park, Ohio: ASM International, 2007.

MURR, L. E. A Review of FSW Research on Dissimilar Metal and Alloy Systems. **Journal of Materials Engineering and Performance**, [s.l.], v. 19, n. 8, p. 1071–1089, 1 nov. 2010.

NANDAN, R.; DEBROY, T.; BHADESHIA, H. K. D. H. Recent advances in friction-stir welding – Process, weldment structure and properties. **Progress in Materials Science**, [s.l.], v. 53, n. 6, p. 980–1023, ago. 2008.

PECKNER, D.; BERNSTEIN, I. M. **Handbook of stainless steels**. New York, NY: McGraw-Hill, 1977.

PORTER, D. A.; EASTERLING, K. E.; SHERIF, M. **Phase Transformations in Metals and Alloys,** (Revised Reprint). [s.l.] CRC press, 2009.

RANI, P. et al. Multi-objective parametric optimization of FSW for mechanical properties of AA5083 joint. **Materials Today: Proceedings**, 12 jul. 2022.

SAI RAKESH SINGH, S. et al. Welding, mechanical properties and microstructure of different grades of austenitic stainless steels: A review. **Materials Today: Proceedings**, Telangana, India, v. 62, p. 3675–3680. Trabalho apresentado no International Conference on Materials, Processing & Characterization (13th ICMPC), 2022, Telangana, India.

SANDMEYER STEEL. **Alloy 410S Ferritic Stainless Steel**. [s.l: s.n.]. Disponível em: <http://www.sandmeyersteel.com/410s.html>. Acesso em: 4 set. 2015.

SEDRICKS, A. J. **Corrosion of stainless steel**. New York, USA: Wiley Intersciense Publications, 1996.

SELLO, M. P.; STUMPF, W. E. Laves phase embrittlement of the ferritic stainless steel type AISI 441. **Materials Science and Engineering: A**, [s.l.], v. 527, n. 20, p. 5194–5202, 25 jul. 2010.

SHAN, Y. et al. Mechanisms of Solidification Structure Improvement of Ultra Pure 17 wt% Cr Ferritic Stainless Steel by Ti, Nb Addition. **Journal of Materials Science & Technology**, [s.l.], v. 27, n. 4, p. 352–358, abr. 2011.

SHANKAR, S. et al. Dissimilar friction stir welding of Al to non-Al metallic materials: An overview. **Materials Chemistry and Physics**, [s.l.], v. 288, p. 126371, 1 set. 2022.

SHULTZ, E. F. et al. Effect of compliance and travel angle on friction stir welding with gaps. **Journal of Manufacturing Science and Engineering**, [s.l.], v. 132, n. 4, p. 041010, 2010.

SILVA, A. L. C.; MEI, P. R. **Aços e Ligas Especiais**. 3. ed. [s.l.] EDGARD BLUCHER, 2011.

SMITH, W. F. **Structure and Properties of Engineering Alloys**. n. 2, [s.l.], McGraw-Hill (New York), 1993.

SOURMAIL, T. Precipitation in creep resistant austenitic stainless steels. **Materials Science and Technology**, [s.l.], v. 17, n. 1, p. 1–14, 1 jan. 2001.

STEEL, R. J.; JENKINS, A.; FLECK, D. **Friction Stir Welding of High Melting Temperature Materials - Equipment Requirements**. [s.l.] Mega Stir, 2014.

SUNNY, K. T.; KORRA, N. N. A systematic review about welding of super austenitic stainless steel. **Materials Today: Proceedings**, FRESM'21. [s.l.], v. 47, p. 4378–4381, 1 jan. 2021.

TAKALO, T.; SUUTALA, N.; MOISIO, T. Austenitic solidification mode in austenitic stainless steel welds. **Metallurgical Transactions A**, [s.l.], v. 10, n. 8, p. 1173–1181, ago. 1979.

THOMAS, W. M. et al. **Friction stir butt welding**. Cambridge, TWI, 1991.

THREADGILL, P. L. Terminology in friction stir welding. **Science and Technology of Welding and Joining**, [s.l.], v. 12, n. 4, p. 357–360, 1 maio 2007.

UDAY, M. B. et al. Advances in friction welding process: a review. **Science and Technology of Welding & Joining**, [s.l.], v. 15, n. 7, p. 534–558, 2010.

WANG, D. et al. Microstructural evolution and mechanical properties of friction stir welded joint of Fe–Cr–Mn–Mo–N austenite stainless steel. **Materials & Design**, [s.l.], v. 64, p. 355–359, 2014.

WANG, H. et al. Microstructure and mechanical properties of dissimilar friction stir welded type 304 austenitic stainless steel to Q235 low carbon steel. **Materials Characterization,** [s.l.], v. 155, p. 109803, 1 set. 2019.

WAS, G. S.; UKAI, S. Chapter 8 - Austenitic Stainless Steels. Em: ODETTE, G. R.; ZINKLE, S. J. (Eds.). **Structural Alloys for Nuclear Energy Applications**. Boston: Elsevier, 2019. p. 293–347.

ZHANG, H. J.; LIU, H. J.; YU, L. Microstructure and mechanical properties as a function of rotation speed in underwater friction stir welded aluminum alloy joints. **Materials & Design**, [s.l.], v. 32, n. 8, p. 4402–4407, 2011.

ZHU, X. K.; CHAO, Y. J. Numerical simulation of transient temperature and residual stresses in friction stir welding of 304L stainless steel. **Journal of materials processing technology**, [s.l.], v. 146, n. 2, p. 263–272, 2004.

3 CHAPTER 3: Assessment of joint configuration and welding parameters for the dissimilar joining of AISI 304L and AISI 410S stainless steels by the friction stir welding

3.1 Abstract

The FSW process parameters for dissimilar welding of AISI 410S and 304L steels were varied to provide a combination of good surface finish, no voids, and full tool penetration. Preliminary tests to analyze the proper position of the steels between the advancing and retreating sides were performed. In welding, axial forces from 25 to 40 kN were applied, keeping the rotational speed constant at 450 rpm and the welding speed at 1 mm/s. Due to the differences between the physical and chemical properties of welded steels, a reduction in flash production and void formation along the stir zone is observed with the positioning of ferritic stainless steel AISI 410S on the advancing side. As the axial force increases, there is an increase in flash production, being more intense in the advancing side than on the retreating side. However, this increase in axial force decreases the size of the materials insertions and nullifies the root flaws on the joints. It is possible to produce dissimilar joints between AISI 410S / 304L steels by the FSW process with good surface finish and no defects in the stir zone.

Key-words: Friction stir welding; Stainless Steel; Axial Force; Rotation Speed; Defects.

3.2 Introduction

Stainless steels are Fe-based alloys with a chromium content of 11 to 30% and may contain Mo, Nb, Ti additions, among others. Their chemical composition may result in different microstructures, giving rise to their classification, as shown FOLKHARD (1988) and KOTECKI (2005). Austenitic stainless steels have a crystalline structure face-centered cubic (FCC), is the most commercially used due to their high mechanical and corrosion resistance, and have a predominantly austenitic microstructure at room temperature. Ferritic stainless steels, on the other hand, are characterized by having an essentially ferritic microstructure with a body centered cubic structure (BCC). SMITH,

W. F., (1993) has noted that ferritic stainless steels supply approximately the same corrosion resistance but have lower ductility, toughness, and weldability when equated to austenitic stainless steels. However, LIPPOLD and KOTECKI, (2005) have shown that ferritic stainless steels can be used in various applications where resistance to pitting and/or stress corrosion cracking is more critical than mechanical strength. Another benefit of ferritic stainless steel is that it usually does not contain nickel in its composition, as nickel is one of the costliest alloying elements and considerably increases the price of austenitic stainless steels over ferritic stainless steels as reported by SILVA et al. (2007).

The lower application of ferritic stainless steels in the industry is related to the metallurgical problems arising from these steels' fusion welding. When subjected to welding thermal cycles, these materials go through metallurgical changes, which compromise their weldability and the mechanical and/or corrosion response of welds. The toughness is significantly affected as it is directly related to grain growth in the heat-affected zone and melting zone for autogenous welds, as shown by SILVA et al. (2008). Besides, some secondary phases may be formed in the weld, affecting corrosion resistance. SILVA et al. (2006) evaluated the changes in the HAZ of the AISI 410S ferritic stainless steel, submitted to different heat input levels in a fusion welding process. The authors have reported that there were zones with excessive grain growth in addition to martensite formation, which causes a compromises mechanical strength and toughness. Another problem was the precipitation of chromium nitrides and finely dispersed carbides in the HAZ, which cause embrittlement and intergranular corrosion.

In recent decades, Friction Welding (FSW), a solid-state welding process developed by THOMAS et al. (1991) in The Welding Institute (TWI) in Cambridge, England, has revolutionised the joining of materials considered of low weldability. MISHRA and MA (2005) reported that this process uses a non-consumable tool that rotates and penetrates the joint, resulting intense plastic deformation of the materials to be joined, resulting in dynamic recrystallisation. Benefits commonly attributed to the FSW process include good weld strength and ductility, minimal residual stress and distortion, absence of melt-related defects, and fine-grained microstructure that increase resistance to traction and fatigue life as proposed by BILGIN and MERAN, (2012), DEBROY and BHADESHIA, (2013) and SATHIYA et al., (2006). LIU et al., (2018) reports that compared to traditional fusion welding, FSW steel welding has significant advantages because of the efficient control of welding temperature and/or cooling rate. This control avoids unfavorable phase

transformation that usually occurs during traditional welding, and favorable phase fractions can be kept in the weld zone, thus avoiding the degradation of typical properties associated with fusion welding.

The applications of the FSW process in similar austenitic stainless steel welds show that although the formation of deleterious phases is expected in the stir zone, as proved by KOKAWA et al., (2005) and PARK et al., (2003), an essential aspect for the success of the welds produced is the intense grain refining resulting from dynamic recrystallization, as observed by WANG et al., (2014). However, ÇAM, (2011) mentions that in the application of the FSW process in ferritic stainless steels, there is some difficulty in recrystallization and grain refining, although studies show promising applications from the point of view of mechanical properties. However, the combination of these aspects in dissimilar FSW welding between ferritic and austenitic stainless steel is still incipient. More detailed information about the influence of process parameters and the phenomena involved in producing faultless and good quality welds becomes a subject of strong scientific and technological appeal.

In the FSW process, rotational speed and axial force are the two main parameters directly related to heat generation, as shown by CAETANO et al., (2019) and MISHRA; MA, (2005). A proper combination of welding speed, axial force, and rotational speed is critical in achieving a balanced set of welding parameters. Correct adjustment of these parameters allows the joining of metals, especially those with lower weldability when other welding processes are applied, as noted by SILVA et al., (2008). For ferritic stainless steels, low heat input and high welding speed are recommended to minimize ferritic grain growth and form a refined microstructure. CAETANO et al., (2018) and BILGIN e MERAN, (2012) showed that such characteristics could very well be achieved using the FSW process.

Different industrial segments use dissimilar welding joints of different metals to bring together different properties, seek to minimize costs, and maximize the performance of equipment and machinery with different welding processes. SILVA et al. (2013) point out to be promising to join different stainless steels in dissimilar joints in the petroleum distillation towers in the gas and petroleum industries through fusion welding processes. MUKHERJEE and PAL (2012) claim that the dissimilar joints between ferritic and austenitic stainless steels are efficient for prolonging metals' service life due to improved toughness, mechanical strength, and corrosion resistance.

CHEN et al. (2019) show that the development and improvement of the FSW process parameters for different metal alloys made it possible to apply them to dissimilar joints. The obtaining of promising results ranges from the union of different aluminum alloys as shown MURR, (2010), the joining of aluminum alloys with copper and magnesium alloys as studied by CARLONE et al. (2015) and ABDOLLAHZADEH et al., (2019). Thus, recent studies carried out by LI et al. (2020) show satisfactory results for the application of the FSW process in the dissimilar joining between Mg/Ti alloys.

Among the FSW process parameters evaluated over time and which were necessary for the progress of the dissimilar joining of these materials, stands out the influence of plate position, tool offset and tool rotational speed, as noted by SAHU et al. (2016), as well as the behavior of the material flow and stir zone consolidation with the rotation speed, observed by GERLICH et al., (2008) and the influence of axial force on heat generation.

However, since the analyzes carried out by WATANABE et al. (2006), in the dissimilar joining between aluminum alloys and steels by the FSW process, studies with the exploration of process parameters required the dissimilar joining of different steels, such as those carried out by WANG et al., (2019), are still incipient, requiring a more detailed exploration of the impact of these parameters on the origin and defects formation. Thus, this work aims to evaluate the effect of joint configuration and welding parameters, as axial force, on the production of FSW dissimilar joints between austenitic stainless steel AISI 304L and ferritic stainless steel AISI 410S with the excellent surface appearance and no defects.

3.3 Materials and Methods

The welds were made using 4-mm-thick plates of AISI 410S ferritic stainless steel and AISI 304L austenitic stainless. The materials' chemical composition was determined by optical emission spectroscopy (Shimadzu model PA7000 Japan) and is presented in Table 3.1.

Table 3.1. Chemical composition of the base metals (% weight).

Material	Elements											
	C	Si	Mn	P	S	Cr	Ni	Mo	Cu	Co	N	Fe
410S	0.025	0.37	0.30	0.023	<0.010	12.8	0.21	0.01	0.21	0.02	0.033	Bal.
304L	0.026	0.32	1.21	0.029	<0.010	18.5	7.24	0.29	0.34	0.15	0.058	Bal.

Source: The author.

The FSW process joined the samples at Helmholtz-Zentrum Geesthacht (HZG) in Germany. All welds were made using the HZG Gantry System with a butt joint configuration, as shown in Fig. 3.1. An inert gas (Ar) injection system was used to protect the material during the process as at temperatures above 535 °C; these stainless steels react with the atmosphere. Welds were performed in load control mode with an integrated system to record process data such as penetration depth, rotational speed, torque, tool forces, and tool position over time.

The welds were made with a tool of polycrystalline cubic boron nitride (PCBN). The tool had a conical diameter of 25 mm with a conical pin with a 9.2 mm diameter and a length of 3.7 mm. The pin had a conical surface with negative recesses, which were in the form of a spiral concerning the tool's axis of symmetry.

Figure 3.1 - Dissimilar butt joint configuration between AISI 410S and AISI 304L steels.

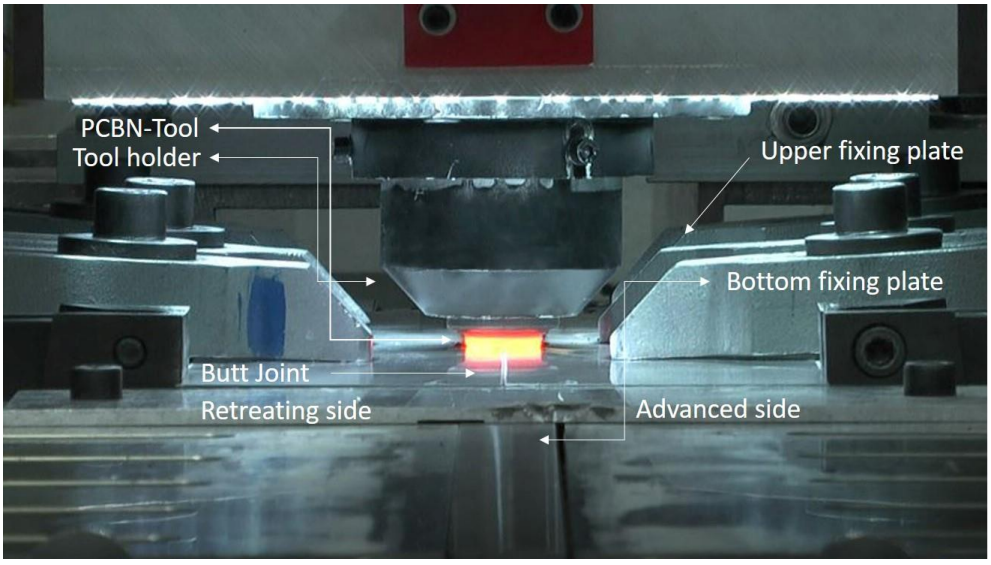

Source: CAETANO et al. (2019).

Preliminary tests were performed to evaluate the behavior of steels to the effects of different phenomena between the advancing side, where the direction of travel is the same as the direction of rotation of the tool, and the retreating side that has these opposite directions in the FSW welding. For these tests, the best parameter settings found by CAETANO et al., (2018) on the FSW similar welding for AISI 410S ferritic stainless steel. Thus, in the preliminary tests, the rotational speed was kept constant at 450 rpm, the welding speed at 1 mm/s and the tool inclination angle at 0º, varying the axial force between 25 kN and 30 kN and concerning to the position of the AISI 304L and AISI 410S steels between the advancing and retreating sides, as shown in Table 3.2.

Table 3.2. Parameters Test for Dissimilar FSW Butt Welding of AISI 410S/304L Steels.

Test	Rotation Speed (rpm)	Axial Force (kN)	Advancing Side	Retreating Side
1	450	25	304L	410S
2	450	30	304L	410S
3	450	25	410S	304L
4	450	30	410S	304L

Source: The author.

After choosing the appropriate steel for the FSW joint's advancing and retreating side, four welding conditions were analyzed to evaluate the influence of process parameters on heat generation and defect formation. Under these conditions, the axial force was varied from 25 to 40 kN, maintaining the rotational speed at 450 rpm, the tool angle at 0º, and the welding speed at 1 mm/s, as shown in Table 3.3.

Table 3.3. Welding Parameters for Dissimilar FSW Butt Welding of AISI 410S/304L Steels

Condition	Rotation Speed (rpm)	Axial Force (kN)
1	450	25
2	450	30
3	450	35
4	450	40

Source: The author.

These parameters were related to the heat input generated during FSW welding. Equation 1 shows the equivalent heat input total required for the joint consolidation among the different ways to calculate the heat generated during the FSW process. The

coefficient of friction of the material, the pressure exerted by the tool, the rotational speed, and the geometry of the tool used in welding are the inputs needed to determine that heat input and are calculated according to the equation formulated by DEQING et al., (2004):

$$E_t = \pi \,.\, \mu \,.\, Ps \,.\, Vr \,.\, \frac{D^2 + D\,.d + d^2}{45\,.(D+d)} \quad (1)$$

Where E_t is the equivalent total heat input (kJ/mm), μ is the coefficient of friction of the material, Ps is the pressure exerted by the tool on the material (Pa), Vr is the speed of rotation (rad/s), D is the shoulder diameter and d is the pin diameter (m). Another way to calculate the heat input to the FSW process is by using Equation 2 to determine the equivalent heat input per unit length per second, proposed by LIENERT et al., (2002):

$$E_l = \eta \,.\, \frac{T\,.Vr}{Vs} \quad (2)$$

Where E_l is the heat input per unit length (kJ/mm), η is the efficiency of the FSW process for steels, T the Torque (Nm), Vr the rotational speed (rad/s), and Vs the welding speed. (mm/s).

3.4 Results and Discussions

3.4.1 Setting the joint configuration based on the position of the steel.

Due to the differences in physical and chemical properties between AISI 410S and AISI 304L steels, preliminary testing was required to choose the most suitable steel for the FSW joint's advancing and retreating side. In previous work, MUTHUKUMARAN and MUKHERJEE (2006) observed that metal flow in FSW welds is caused by metal extrusion around the tool pin and the frictional heat generated between the tool shoulder and the sample. SINHA et al. (2008) showed that as the friction intensity between the tool shoulder and the workpiece is one of the main factors responsible for defect elimination. Thus, parameters such as axial force and speed of rotation directly affect this metallic flow.

In this study, such as thermal conductivity and elastic modulus are different between welded steels, an asymmetry in heat input, deformation, and flow of materials were

observed between the advancing side and retreating side. Through the Fig. 3.2, it can be seen that in Tests 1 and 2, in which the AISI 410S ferritic stainless steel was placed on the retreating side, with the tool travel direction opposite to the tool rotation direction, a large production of flash was observed, which were more intense for Test 2, which was welded with greater axial force. However, in Tests 3 and 4, where AISI 304L austenitic stainless steel was placed on the retreating side, a better surface finish was found with a considerable decrease in flash production.

Figure 3.2 - Surface finishing of dissimilar welding tests of AISI 410S/304L steels by FSW process.

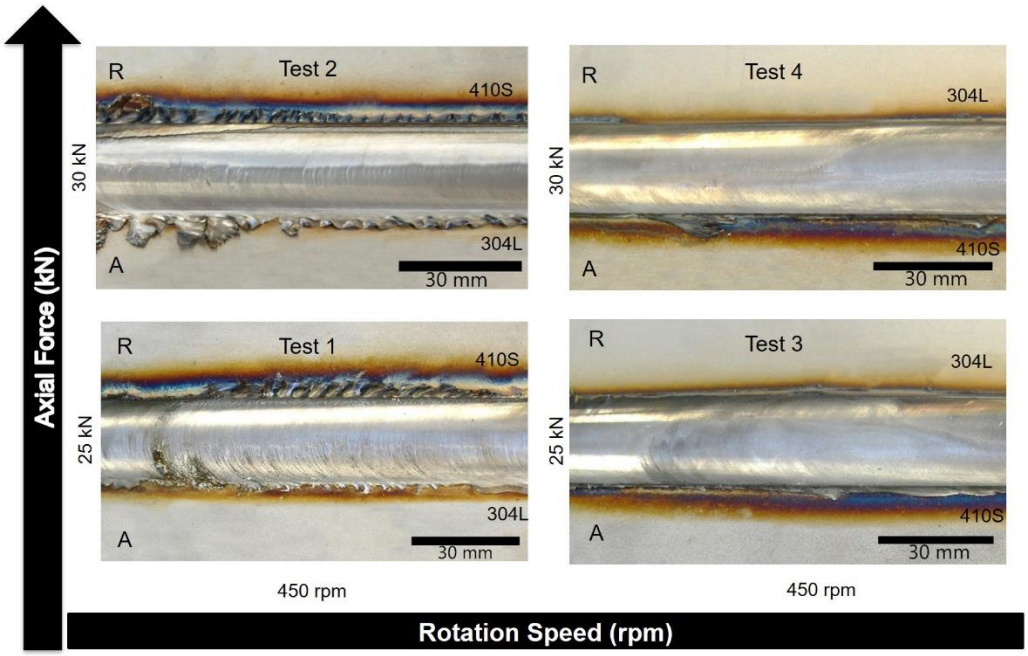

Source: The author.

Analyzing the cross-sectional macrographs of the dissimilar stainless steel welded joints produced by the FSW process, it is possible to observe that besides the higher flash production in Tests 1 and 2, the presence of voids and a smaller stir between the steels is noticeable. In the other tests, in which the AISI 410S ferritic stainless steel is positioned on the advancing side, the tool travel direction is the same direction of rotation and the highest temperatures being reached; the best results were achieved. The joint configuration of Test 3 and 4, which were welded with the low-strength metal on the advancing side, provided a more massive flow of elastoplastic material from the advancing side directed to the retreating side, generating more significant participation of

the AISI 410S steel in the formation of the stir zone. This behavior avoids the formation of voids and the consequent instabilities responsible for excessive flash production, as shown in Fig. 3.3. WANG et al. (2019), analyzing welded dissimilar joints of AISI 304 austenitic stainless steel and low carbon steel by FSW process, also proved beneficial effects positioning the low-strength steel on the advancing side. In this joint configuration, the authors reached material flow sufficient to fill up the cavities and other defects, getting good results. According to JAFARZADEGAN et al. (2013), the austenitic stainless steels have relatively high elevated temperature flow stress and low thermal diffusivity compared to carbon steels, compromising an adequate material flow when this steel is positioned on the advancing side in the FSW process.

Figure 3.3 - Cross-section macrograph of AISI 410S/304L dissimilar welding tests performed by the FSW process.

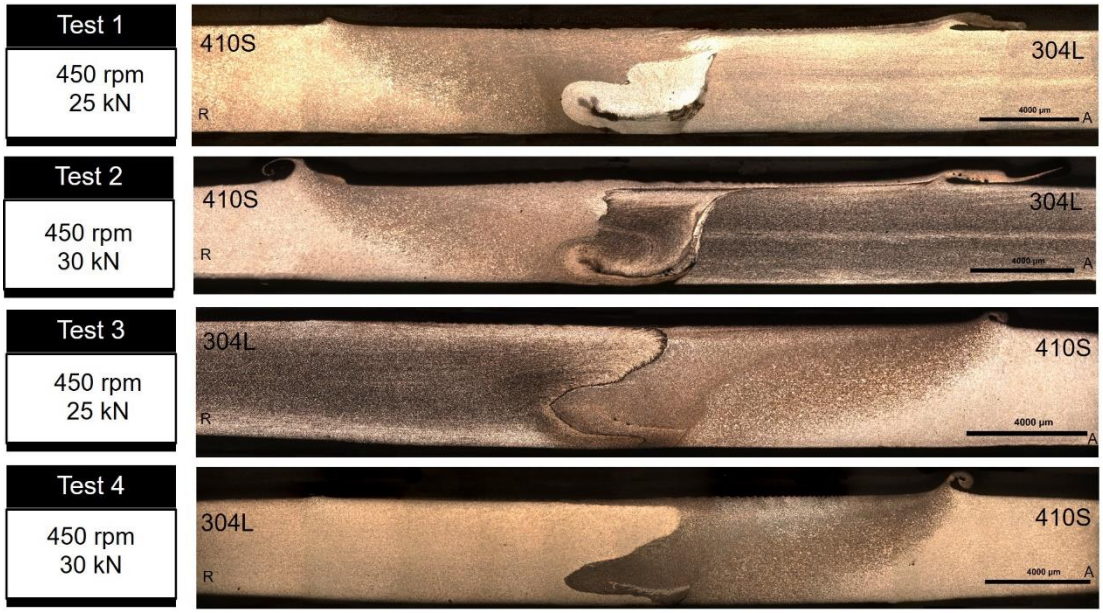

Source: The author.

Thus, based on these results, it was demonstrated that improvements in surface finish and elimination of voids in the stir zone were achieved when the AISI 410S ferritic stainless steel was placed on the advancing side and the AISI 304L austenitic stainless steel was on the retreating side of the butt joint. After this set of experiments, four different conditions following the parameters indicated in Table 3.3 were additionally tested. These conditions were welded to evaluate further the interference of rotation speed, axial force, and torque on surface finish and defect formation.

3.4.2 Axial Force

Axial force has a considerable influence on the distribution and flow of material along the welded joint and its participation in heat generation during welding. According to KIM et al. (2006), there is an appropriate rotation and forward speed for each applied axial force that results in defect-free welds. It is possible to observe through the analysis of the axial force over the welding time that significant interference was not observed after stabilization, and its application in none of the welded conditions resulted in the instability of the process, as shown in Fig. 3.4. KIM et al., (2006) reported in their study that the instability in the application of axial force results in a lack of forging necessary to ensure the consolidation of the welded joint and, consequently, leads to the formation of volumetric defects.

Figure 3.4 - Axial force variation during the AISI 410S/304L steels dissimilar welding by the FSW process.

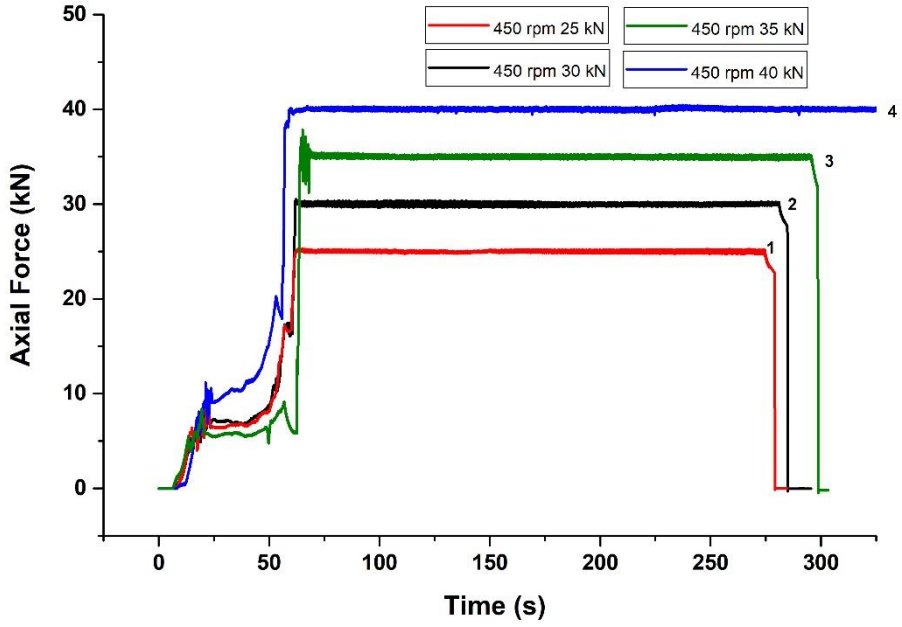

Source: The author.

The four axial force curves over time initially displayed similar behaviour. During the initial stage of the process, a pressure gradient emerged along the penetration channel. This variation occurs due to the different levels of contact between the tool and the joint surface and, consequently, the area's variation at the force application. Increased pressure

is counterbalanced by increased axial force. After the tool reaches the desired penetration depth, the pressure gradient decreases to a stable state. After reaching equilibrium, any new sudden changes in the axial force versus time curve characterize a non-uniformity in applying force, compromising the material flow and resulting in defect formation. However, in the welded conditions tested in this study, after the equilibrium to be established, no changes were observed in the application of axial force, resulting in adequate material flow, as observed by CAETANO et al., (2018) in similar welding of AISI 410S steel plates.

3.4.3 Torque

An analysis of the parameters for the dissimilar welding of AISI 410S/304L stainless steels by the FSW process shows that the torque exerted by the tool increases with increasing axial force. Fig. 3.5 shows that the torque for condition 4, with an axial force of 40 kN, is greater than the torque for condition 1, with an axial force of 25 kN. Therefore, the higher the force, the higher the tool pressure on the material, and the higher torque required for tool rotation. In previous work, BUCHIBABU et al. (2017) noted that in FSW welding, the torque is influenced by changes in axial force and increases with increasing welding speed for different rotational speeds. Rotational speed also causes torque changes due to the greater or lesser degree of plasticity of the base metal, caused by changes in heat input. Thus, the rotational speed, the welding speed and the applied axial force determine factors for the torque evolution during the FSW process, as reported by LEITAO et al., (2012).

Figure 3.5 - Torque variation during the AISI 410S/304L steels dissimilar welding by the FSW process.

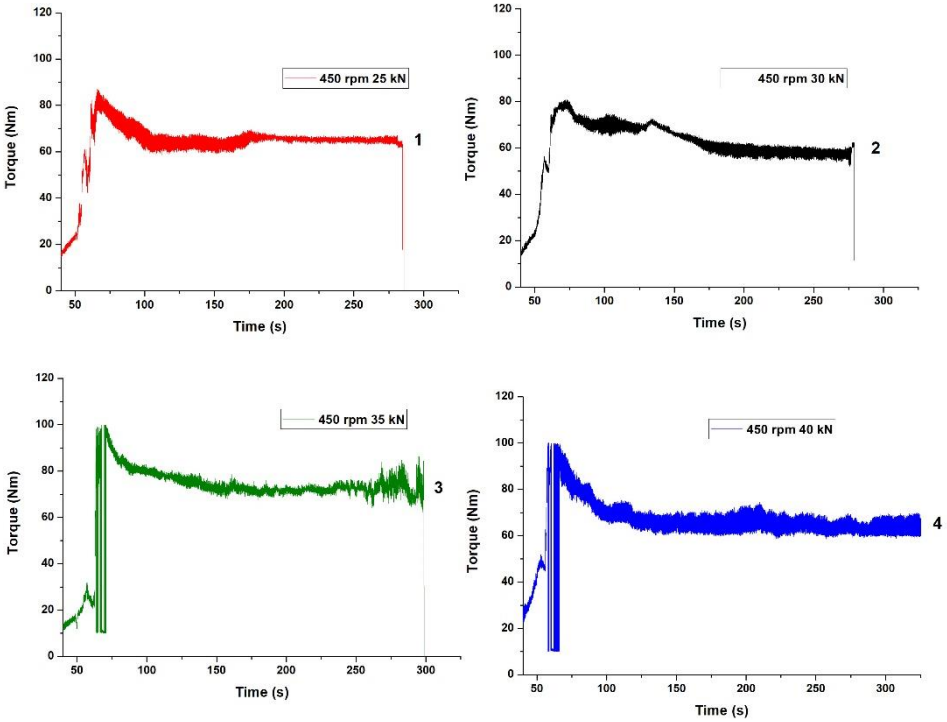

Source: The author.

3.4.4 Heat Generation

The process parameters directly affect the heat input, which strongly influences the heating and cooling rates of the thermal cycle and, consequently, the resulting microstructure. However, the heat input calculated based on the process parameters corresponds to equivalent heat input and not precisely to the heat input produced during the process, since there are losses that are not considered, being the main ones by conduction and convection in the weld region.

The rotational speed is the main parameter related to the friction force at the interface between the base metals and the tool. It is directly linked to heat generation during the welding process, as reported by BILGIN e MERAN, (2012) and LAKSHMINARAYANAN and BALASUBRAMANIAN, (2013). Frictional coupling of the tool surface with the base metal governs the heating mechanism and tool rotation, thereby allowing the stirring and mixing the material around the pin. Thus, the higher the rotational speed, the higher the process temperature, and this is due to increased friction heating as proposed by COLEGROVE et al. (2007), SHIRI et al. (2013), and UDAY et al. (2010).

The strong influence of the rotational speed on heat generation was observed among similar welds of AISI 410S ferritic stainless steel produced by FSW, as pointed out by CAETANO et al. (2018), which observed that the reduction in rotational speed from 800 to 450 rpm generates a drop-in equivalent heat input total and equivalent heat input per unit length around 0.4 kJ/mm, keeping the axial force constant. Observing the Fig. 3.6, for the FSW dissimilar welding between ferritic and austenitic stainless steels, when the constant rotational speed is maintained at 450 rpm, and the axial force is changed from 25 kN to 40 kN, it can be inferred that the 5 kN force increase between conditions 1, 2, 3 and 4, also produce a more significant amount of heat in the process. Therefore, this increase in axial force will help raise the temperature and increase the material's softening degree. However, the axial force has less influence on the heat generation than other parameters such as the rotation speed due, among other factors, to its lower influence on the frictional heat generated during the FSW process.

Figure 3.6 - Equivalent heat input per unit length and total heat input calculated for the different conditions of AISI 410S/304L steels dissimilar welding performed by the FSW process.

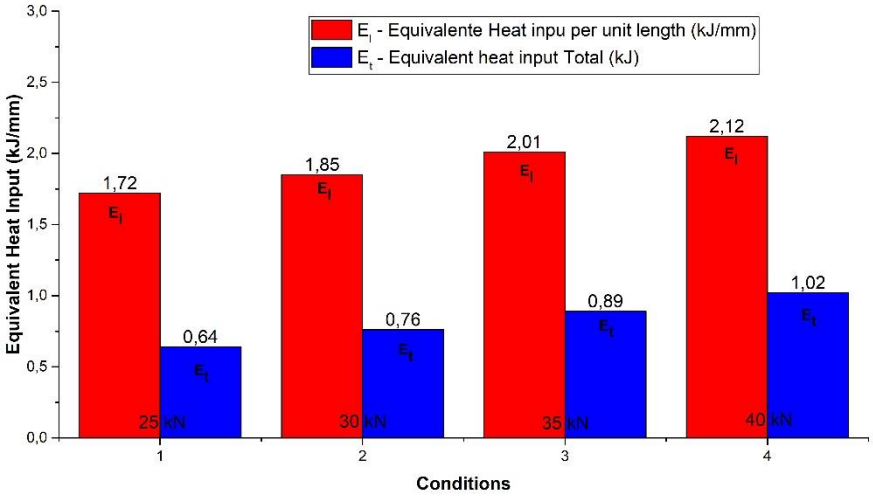

Source: The author.

3.4.5 Surface Finishing

Surface analysis of the dissimilar joints for the AISI 410S/304L steels obtained by the FSW process in this work shows that the flash produced is directly related to the axial

force increase. As pointed out by TRUEBA et al. (2015), increases in axial force cause an increase in heat input, thereby allowing higher FSW welding temperatures, causing a decrease in viscosity and displacement of a more considerable amount of material through the tool pin. However, as the material flow is enhanced, the plasticized material's contention by the shoulder of the tool becomes more difficult. When the metal's viscosity reaches such low values, which are enough to allow the plasticized material displaced by the shoulder of the tool to flow out of the weld nugget, large flashes will be formed, as observed in Fig. 7.

Fig. 3.7 shows in detail that the number of flash increases as the axial force increases from 25 to 40 kN, and these flashes are more critical for the advancing than the retreading side. According to BOGAARD et al. (1993) and MANDAL et al. (2009), the austenitic stainless steel has relatively low thermal diffusivity and high flow stress in elevated temperature in relation the ferritic stainless steel. Thus, as the axial force increases and the temperature rises, there is a greater material flow in the elastoplastic state of AISI 410S steel on the advancing side. Thus, due to the lack of tool shoulder restraint, a more significant amount of steel is available to scape around the tool, generating the larger flashes in this region. According to the analysis of defects in FSW welds performed by THREADGILL (2007), flash production can occur either by high heat input or by instabilities in the application of axial force, generating an irregular flow of material with the formation of voids and loss of plasticized material.

Figure 3.7 - The surface finish of dissimilar welding of AISI 410S/304L steels by FSW process in a function of rotational speed and axial force applied.

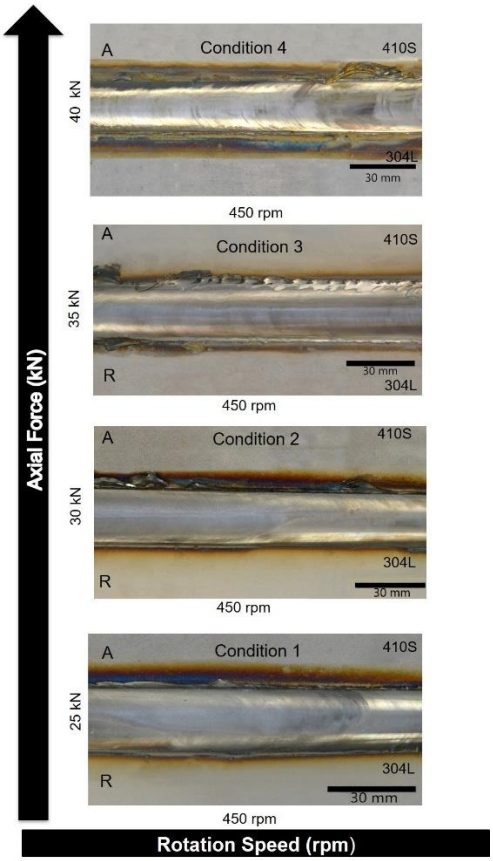

Source: The author.

In the evaluated conditions, no surface cavities were observed despite the presence of superficial depressions due to the intense pressure exerted by the tool shoulder on the welded material, under conditions 3 and 4, which were welded with the highest axial forces. These surface cavities are associated with a lack of heat or excess heat in the material during the welding process. Even under conditions with lower axial force and, consequently, lower heat input, the amount of heat generated in the region near the tool and shoulder was sufficient to give the material a suitable viscosity and plasticity. Despite the presence of dissimilar alloys in the joint formation, there was uniformity in the surface finish with onion rings patterns being formed, a fact not always achieved in dissimilar joints, as shown by SHANKAR et al. (2019) regarding FSW welding between Al and Cu and by KASAI et al., (2015) on the FSW dissimilar joining between steel and magnesium.

3.4.6 Defect Analysis

The cross-sectional analysis of AISI 410S/304L stainless steel dissimilar joints produced by the FSW process is shown in Fig. 3.8. It was verified that the joints' consolidation without internal voids for Conditions 2, 3, and 4, welded with axial forces of 30, 35, and 40 kN, respectively. It shows that the material flow reached an adequate plasticization state due to the intensity of heat obtained by combining the parameters used. However, for Condition 1, welded with an axial force of 25 kN, the presence of small voids in the stir zone in a region closer to the weld root was observed.

This behavior was noted by TONGNE et al., (2015), which attributed it to a lower interaction between the tool and material due to the low axial force. Consequently, a reduction in frictional force and insufficient heat is observed, making it difficult to reach a plasticizer state suitable for material flow during the FSW process. Second DOUDE et al. (2015), these voids in the stir zone in regions close to the weld root, as noted in Condition 1, indicate the use of parameters below the recommended ideal set for consolidation of a defect-free FSW joint. It is due to the low rotation speed combined with a low axial force. Therefore, the combination of rotation speed at 450 rpm, axial force at 25 kN, and welding speed at 1 mm/s was an inadequate condition, with low quality to dissimilar FSW joint between AISI 410S and AISI 304L steels.

Figure 3.8 - Transverse macrographs of the different dissimilar welding conditions of AISI 410S/304L stainless steels by the FSW process.

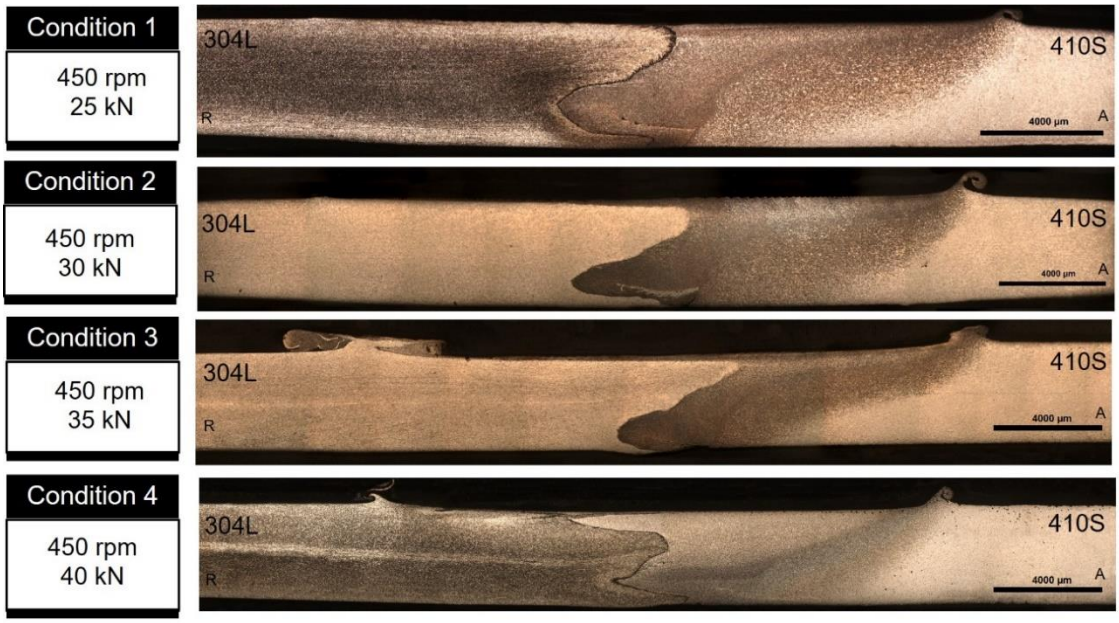

Source: The author.

In welds analyzed as the axial force increases under conditions 2, 3, and 4, it is possible to observe a more significant contact between the two steels in the stir zone, with the formation of larger inserts of AISI 304L austenitic stainless steel towards AISI 410S ferritic stainless steel and from this to AISI 304L austenitic stainless steel. While for Condition 1 only two large inserts of AISI 304L steel and one of AISI 410S steel were observed in the formation of the contact region between the two steels, in the stir zone for Condition 4, three AISI 304L steel inserts and three AISI 410S steel inserts were observed in the contact region. Therefore, it is possible to observe that the application of a more intense axial force strongly influences the contact zone between the two steels.

The macrographs' evaluation, along the cross-section of the FSW welds, also shown the increase in the flash production as the axial force increases. The flash formation is higher in the advancing side concerning the retreading side, as observed between Condition 2 and Condition 4, where keeping the rotational speed at 450 rpm and increasing the axial force from 30 to 40 kN, it is clearly observed the occurrence of such effects as can be seen in the Fig. 3.9.

Figure 3.9 - Micrograph of the tool/steel contact boundary. (a) Small flash production on the retreading side of Condition 2. (100x) (b) Larger flash on the advancing side of Condition 2 (100x). (c) Larger flash production on the retreading side of Condition 4 relative to Condition 2. (100x) and (d). Flash production on the advancing side of Condition 4 larger than the retreading side. (100x)

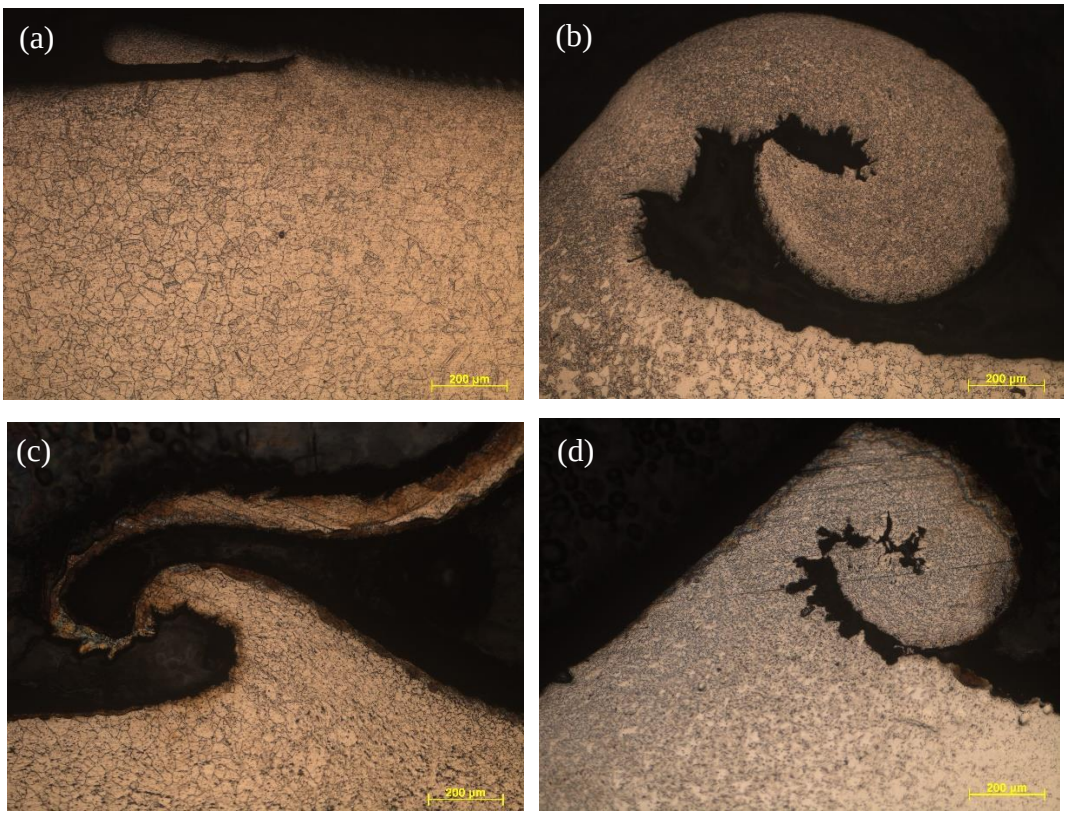

Source: The author

In both Condition 1 and Condition 2, welded with axial forces of 25 and 30 kN, respectively, root flaws were found, as can be seen in Fig. 3.10 (a). These defects are observed a line relative to the interface between the two plates of the butt joints and a lack of cohesion between the two steels forming a discontinuity in the root of the joint. EDWARDS and RAMULU (2015), reported that this defect is associated with insufficient tool penetration. However, as the axial force increases to 35 and 40 kN, the remaining line of the interface between the butt joint materials is still noticeable, but without evidence of joint root recess, as can be seen in Fig. 3.10 (b). KUMAR and KAILAS (2013) studied the material flow in dissimilar joints of aluminum alloys welded by the FSW process. The authors have also observed the formation of this remnant line in the weld root. Their results shown that an attenuation regarding the defects formation

have occurred, due to the displacement of the tool to advancing side. According to the authors, this uncentered configuration of the butt joint has intensified the plastic deformation. However, the same study also has shown that the remaining line's presence does not change the material's mechanical strength properties.

CAETANO et al. (2018) observed that there are different root flaws morphologies. They attributed this behavior to the distinct mechanisms of the formation of these defects. This defect can be formed either by the excess or lack of axial force. When an excessive axial force is applied, the tool pin will penetrate the plate a lot. Thus, it will promote an excess heat generated at the bottom of the plate, leading to the welding between the plate and the counter plate, thus affecting the material flow in this region. However, the root flaws observed in Conditions 1 and 2 can be formed due to a reduction in axial force. In this case, the defects are attributed to a lesser interaction between the tool and the material, consequently reducing frictional force and heat generation, both necessary to achieve a proper state of plasticization of the material flow. This improper plasticization hinders material movement around the tool. This behavior makes it challenging to consolidate the stir zone during the FSW process.

Figure 3.10 - (a) Root flaws due to lack of penetration in Condition 2. (200x) (b) No root flaws in Condition 4 (200x).

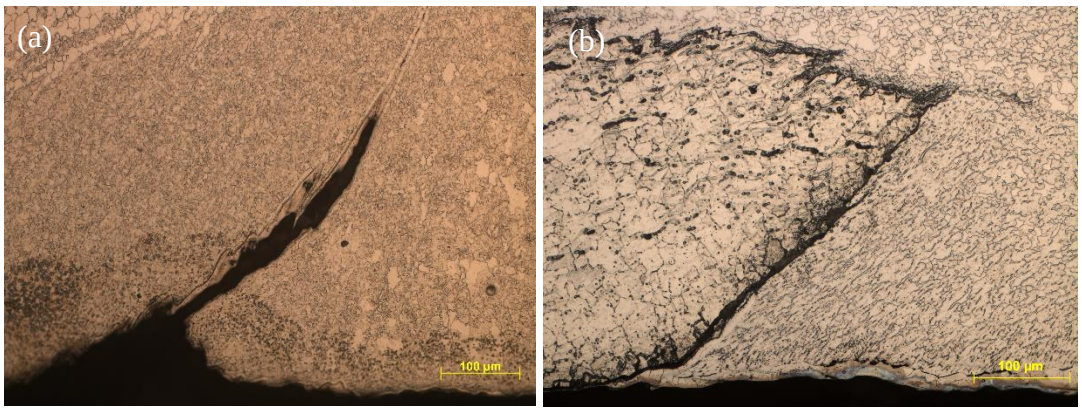

Source: The author.

The occurrence of root flaws due high and low penetration demonstrates that the production of FSW joints without root failures must be accomplished not only with an increase or decrease in axial force but also with an appropriate balance between axial force and tool angle, which allows a greater immersion of the pin in the joint, as reported by SHULTZ et al., (2010). The correct balance between tool angle and axial force is a

way to consolidate FSW joints without defects in the root. This behavior can also be achieved with the correct balance between axial force and rotational speed, without having to vary the tool's angle, as occurred in Condition 4. For this condition, although the remaining line refers to the interface between the different butt joint materials, no discontinuities that characterize the formation of a root defect was observed.

Among the welded conditions, the macroscopic analysis confirmed the presence of small voids in AISI 410S steel, in a region close to the interface with AISI 304L steel and close to the joint's root in the stir zone of Condition 1, as shown in Figure 3.11. This lack of fill or tunnel defect consists of the weld joint's internal regions without material, forming voids along the weld length. According to MISHRA and MA (2005), this defect is caused by the lack of heat produced by cold parameters, such as low rotational speeds and low axial forces, which generate less friction or shorter tool time residence in the material. KUMAR and KAILAS (2008) state that, in addition to low heat, the lack of tool shoulder pressure on the material also unsettles the flow, precluding it from filling the entire weld region.

Figure 3.11. Voids present in the stir zone in a region near the root. (a) (100x) (b) (500x).

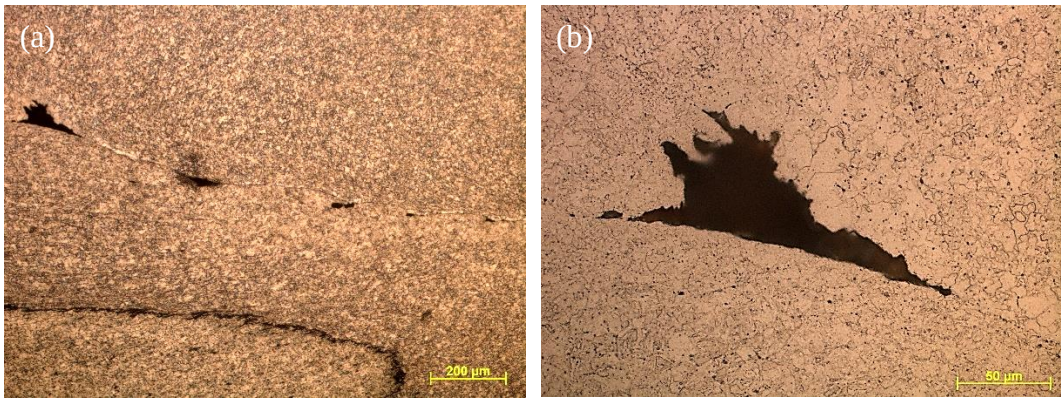

Source: The author.

Therefore, the different welded conditions' analysis shows that it is possible to produce dissimilar joints between AISI 410S ferritic stainless steel and AISI 304L austenitic stainless steel by the FSW process with good surface finish and no stir zone defects. This behavior is possible, using parameters that ensure a suitable heat intensity to plasticize the material flow, which can be obtained by increasing the axial force around 40 kN at the constant rotational speed at 450 rpm because, despite flash production,

condition 4 is free of voids and root recesses that characterize the formation of joint root flaws.

3.5 Conclusions

Based on the experimental results of the FSW process parameters and their implications on the formation of defects for dissimilar welding between AISI 410S ferritic stainless steel and AISI 304L austenitic stainless steel, it was possible to conclude that:

1. With the right combination of welding parameters, a dissimilar joint can be successfully welded between AISI 410S ferritic stainless steel and AISI 304L austenitic stainless steel, producing a stable and defect-free joint.
2. Due to the differences in the steels' physical and chemical properties and the different phenomena that occur on the advancing and retreating side, the reduction in flash production and voids in the stir zone occurs when AISI 410S ferritic stainless steel is placed on the advancing side.
3. By analyzing axial force over the welding time, it is possible to observe that in none of the welded conditions, significant fluctuation in applying axial force was observed, allowing in some conditions, the formation of the stir zone without defects.
4. The torque exerted by the tool increases with increasing applied force because the more significant the friction resulting from the application of force, the higher the tool pressure on the material, and the higher the torque required to consolidate the tool rotation.
5. The flash production increases with increasing axial force, and it is larger for the advancing side. In this region, higher temperatures are found and allow more material in the elastoplastic state. The lack of restraint by the tool shoulder of this larger amount of material generates larger flash production on the advancing side.
6. The dissimilar joints' production between the AISI 410S/304L stainless steels welded by the FSW process without root flaws was achieved, keeping the

rotational speed at 450 rpm and increasing the axial force to 40 kN, consolidating an appropriate balance between rotation speed, axial force, and tool angle.

3.6 Acknowledgments

The authors are grateful for the support given by the following Institutions: Universidade Federal do Ceará, Laboratório de Pesquisa e Tecnologia em Soldagem (LPTS), in Brazil, and the Solid State Joining Processes, Helmholtz-Zentrum Geesthacht (HZG), in Germany. As well as the Brazilian funding agencies CNPq (Universal 472185/2011-0), and FUNCAP and CAPES (Project CI1-0050-00049.01.00/11 – International Cooperation) for financial support and CAPES for the Ph.D. scholarship.

3.7 References

ABDOLLAHZADEH, A. et al. In-situ nanocomposite in friction stir welding of 6061-T6 aluminum alloy to AZ31 magnesium alloy. **Journal of Materials Processing Technology**, [s.l.], v. 263, p. 296–307, 1 jan. 2019.

BILGIN, M. B.; MERAN, C. The effect of tool rotational and traverse speed on friction stir weldability of AISI 430 ferritic stainless steels. **Materials & Design**, [s.l.], v. 33, p. 376–383, jan. 2012.

BOGAARD, R. H. et al. Thermophysical properties of stainless steels. **Thermochimica Acta**, [s.l.], v. 218, p. 373–393, 3 maio 1993.

BUCHIBABU, V.; REDDY, G. M.; DE, A. Probing torque, traverse force and tool durability in friction stir welding of aluminum alloys. **Journal of Materials Processing Technology**, [s.l.], v. 241, p. 86–92, 2017.

CAETANO, G. DE Q. et al. Influence of rotation speed and axial force on the friction stir welding of AISI 410S ferritic stainless steel. **Journal of Materials Processing Technology**, [s.l.], v. 262, p. 430–436, 1 dez. 2018.

CAETANO, G. DE Q. et al. Intergranular corrosion evaluation of friction stir welded AISI 410S ferritic stainless steel. **Journal of Materials Research and Technology**, fev. 2019.

ÇAM, G. Friction stir welded structural materials: beyond Al-alloys. **International Materials Reviews**, [s.l.], v. 56, n. 1, p. 1–48, 1 jan. 2011.

CARLONE, P. et al. Microstructural aspects in Al–Cu dissimilar joining by FSW. **The International Journal of Advanced Manufacturing Technology**, [s.l.], v. 79, n. 5, p. 1109–1116, 1 jul. 2015.

CHEN, K.; LIU, X.; NI, J. A review of friction stir–based processes for joining dissimilar materials. **The International Journal of Advanced Manufacturing Technology**, [s.l.], v. 104, n. 5, p. 1709–1731, 1 out. 2019.

COLEGROVE, P. A.; SHERCLIFF, H. R.; ZETTLER, R. Model for predicting heat generation and temperature in friction stir welding from the material properties. **Science and Technology of Welding and Joining**, [s.l.], v. 12, n. 4, p. 284–297, 1 maio 2007.

DEBROY, T.; BHADESHIA, H. Friction stir welding of dissimilar alloys–a perspective. **Science and Technology of Welding & Joining**, [s.l.]: [s.n.], 2013.

DEQING, W.; SHUHUA, L.; ZHAOXIA, C. Study of friction stir welding of aluminum. **Journal of materials science**, [s.l.], v. 39, n. 5, p. 1689–1693, 2004.

DOUDE, H. et al. Optimizing weld quality of a friction stir welded aluminum alloy. **Journal of Materials Processing Technology**, [s.l.], v. 222, p. 188–196, 2015.

EDWARDS, P. D.; RAMULU, M. Material flow during friction stir welding of Ti-6Al-4V. **Journal of Materials Processing Technology**, [s.l.], v. 218, p. 107–115, 2015.

FOLKHARD, E. **Welding Metallurgy of Stainless Steels, Texto original**. Wien: Springer-Verlag, 1988.

GERLICH, A. et al. Material flow and intermixing during dissimilar friction stir welding. **Science and Technology of Welding and Joining**, [s.l.], v. 13, n. 3, p. 254–264, 1 abr. 2008.

JAFARZADEGAN, M. et al. Microstructure and Mechanical Properties of a Dissimilar Friction Stir Weld between Austenitic Stainless Steel and Low Carbon Steel. **Journal of Materials Science & Technology**, [s.l.], v. 29, n. 4, p. 367–372, 1 abr. 2013.

KASAI, H.; MORISADA, Y.; FUJII, H. Dissimilar FSW of immiscible materials: Steel/magnesium. **Materials Science and Engineering: A**, [s.l.], v. 624, p. 250–255, 29 jan. 2015.

KIM, Y. G. et al. Three defect types in friction stir welding of aluminum die casting alloy. **Materials Science and Engineering: A**, [s.l.], v. 415, n. 1, p. 250–254, 2006.

KOKAWA, H. et al. Microstructures in Friction Stir Welded 304 Austenitic Stainless Steel. **Welding in the World**, [s.l.], v. 49, n. 3, p. 34–40, 1 mar. 2005.

KUMAR, K.; KAILAS, S. V. The role of friction stir welding tool on material flow and weld formation. **Materials Science and Engineering: A**, [s.l.], v. 485, n. 1, p. 367–374, 2008.

KUMAR, K.; KAILAS, S. V. Positional dependence of material flow in friction stir welding: analysis of joint line remnant and its relevance to dissimilar metal welding. **Science and Technology of Welding & Joining**, 2013.

LAKSHMINARAYANAN, A. K.; BALASUBRAMANIAN, V. Process Parameters Optimisation for Friction Stir Welding of AISI 409M Grade Ferritic Stainless Steel. **Experimental Techniques**, [s.l.], v. 37, n. 5, p. 59–73, 2013.

LEITAO, C.; LOURO, R.; RODRIGUES, D. M. Using torque sensitivity analysis in accessing Friction Stir Welding/Processing conditions. **Journal of Materials Processing Technology**, [s.l.], v. 212, n. 10, p. 2051–2057, 2012.

LI, Q. et al. Effective joining of Mg/Ti dissimilar alloys by friction stir lap welding. **Journal of Materials Processing Technology**, [s.l.], v. 278, p. 116483, 1 abr. 2020.

LIENERT, T. J.; STELLWAG JR, W.; LEHMAN, L. Comparison of heat inputs: friction stir welding vs. arc welding. **American Welding Society**, p. 1–3, 2002.

LIPPOLD, J. C.; KOTECKI, D. J. **Welding metallurgy and weldability of stainless steels**. New Jersey, USA: John Wiley & Sons, 2005a.

LIPPOLD, J. C.; KOTECKI, D. J. **Welding Metallurgy and Weldability of Stainless Steels**. 1 edition ed. Hoboken, NJ: Wiley-Interscience, 2005b.

LIU, F. C. et al. A review of friction stir welding of steels: Tool, material flow, microstructure, and properties. **Journal of Materials Science & Technology**, [s.l.], v. 34, n. 1, p. 39–57, 1 jan. 2018.

MANDAL, S. et al. Constitutive equations to predict high temperature flow stress in a Ti-modified austenitic stainless steel. **Materials Science and Engineering: A**, [s.l.], v. 500, n. 1, p. 114–121, 25 jan. 2009.

MISHRA, R. S.; MA, Z. Y. Friction stir welding and processing. **Materials Science and Engineering: R: Reports**, [s.l.], v. 50, n. 1–2, p. 1–78, 31 ago. 2005.

MUKHERJEE, M.; PAL, T. K. Influence of Heat Input on Martensite Formation and Impact Property of Ferritic-Austenitic Dissimilar Weld Metals. **Journal of Materials Science & Technology**, [s.l.], v. 28, n. 4, p. 343–352, 1 abr. 2012.

MURR, L. E. A Review of FSW Research on Dissimilar Metal and Alloy Systems. **Journal of Materials Engineering and Performance**, [s.l.], v. 19, n. 8, p. 1071–1089, 1 nov. 2010.

MUTHUKUMARAN, S.; MUKHERJEE, S. K. Two modes of metal flow phenomenon in friction stir welding process. **Science and Technology of Welding and Joining**, [s.l.], v. 11, n. 3, p. 337–340, 2006.

PARK, S. H. C. et al. Rapid formation of the sigma phase in 304 stainless steel during friction stir welding. **Scripta Materialia**, [s.l.], v. 49, n. 12, p. 1175–1180, dez. 2003.

SAHU, P. K. et al. Influence of plate position, tool offset and tool rotational speed on mechanical properties and microstructures of dissimilar Al/Cu friction stir welding joints. **Journal of Materials Processing Technology**, [s.l.], v. 235, p. 55–67, 1 set. 2016.

SATHIYA, P.; ARAVINDAN, S.; HAQ, A. N. Effect of friction welding parameters on mechanical and metallurgical properties of ferritic stainless steel. **The International Journal of Advanced Manufacturing Technology**, [s.l.], v. 31, n. 11–12, p. 1076–1082, 21 jan. 2006.

SHANKAR, S. et al. Joint strength evaluation of friction stir welded Al-Cu dissimilar alloys. **Measurement**, 8 jul. 2019.

SHIRI, S. G. et al. Diffusion in FSW Joints by Inserting the Metallic Foils. **Journal of Materials Science & Technology**, [s.l.], v. 29, n. 11, p. 1091–1095, 1 nov. 2013.

SHULTZ, E. F. et al. Effect of compliance and travel angle on friction stir welding with gaps. **Journal of Manufacturing Science and Engineering**, [s.l.], v. 132, n. 4, p. 041010, 2010.

SILVA, C. C. et al. Alterações Microestruturais na ZAC do aço inoxidável ferrítico 410S-Efeitos sobre a resistência à corrosão. **Soldagem & Inspeção**, [s.l.], v. 11, 2006.

SILVA, C. C. et al. High-temperature hydrogen sulfide corrosion on the heat-affected zone of the AISI 444 stainless steel caused by Venezuelan heavy petroleum. **Journal of Petroleum Science and Engineering**, [s.l.], v. 59, n. 3–4, p. 219–225, nov. 2007.

SILVA, C. C. et al. Microstructural characterization of the HAZ in AISI 444 ferritic stainless steel welds. **Materials Characterization**, [s.l.], v. 59, n. 5, p. 528–533, maio 2008.

SILVA, C. C. et al. Austenitic and ferritic stainless steel dissimilar weld metal evaluation for the applications as-coating in the petroleum processing equipment. **Materials & Design**, [s.l.], v. 47, p. 1–8, 1 maio 2013.

SINHA, P.; MUTHUKUMARAN, S.; MUKHERJEE, S. K. Analysis of first mode of metal transfer in friction stir welded plates by image processing technique. **Journal of Materials Processing Technology**, [s.l.], v. 197, n. 1, p. 17–21, 2008.

SMITH, W. F. **Structure and Properties of Engineering Alloys**. n. 2, [s.l.], McGraw-Hill (New York), 1993.

THOMAS, W. M. et al. **Friction stir butt welding**. Cambridge, TWI, 1991.

THREADGILL, P. L. Terminology in friction stir welding. **Science and Technology of Welding and Joining**, [s.l.], v. 12, n. 4, p. 357–360, 1 maio 2007.

TONGNE, A. et al. Banded structures in friction stir welded Al alloys. **Journal of Materials Processing Technology**, [s.l.], v. 221, p. 269–278, 2015.

TRUEBA, L. et al. Effect of tool shoulder features on defects and tensile properties of friction stir welded aluminum 6061-T6. **Journal of Materials Processing Technology**, [s.l.], v. 219, p. 271–277, 2015.

UDAY, M. B. et al. Advances in friction welding process: a review. **Science and Technology of Welding & Joining**, [s.l.], v. 15, n. 7, p. 534–558, 2010.

WANG, D. et al. Microstructural evolution and mechanical properties of friction stir welded joint of Fe–Cr–Mn–Mo–N austenite stainless steel. **Materials & Design**, [s.l.], v. 64, p. 355–359, 2014.

WANG, H. et al. Microstructure and mechanical properties of dissimilar friction stir welded type 304 austenitic stainless steel to Q235 low carbon steel. **Materials Characterization**, [s.l.], v. 155, p. 109803, 1 set. 2019.

WATANABE, T.; TAKAYAMA, H.; YANAGISAWA, A. Joining of aluminum alloy to steel by friction stir welding. **Journal of Materials Processing Technology**, [s.l.], v. 178, n. 1, p. 342–349, 14 set. 2006.

4 CHAPTER 4: Microstructure evolution of dissimilar AISI 304L and AISI 410S stainless steel joints by the friction stir welding

4.1 Abstract

The present study investigated the main microstructural characteristics of dissimilar welding between AISI 304L and AISI 410S stainless steel. In the welds, axial forces from 25 to 40 kN were applied, keeping the rotation speed constant at 450 rpm and the welding speed of 1 mm/s, with AISI 304L steel on the retreating side and AISI 410S steel on the advancing side. As the axial force increases, it is possible to observe a refinement in ferritic grain size in the HAZ and the TMAZ of AISI 410S and an increase in ferrite-δ intensity in HAZ and TMAZ of AISI 304L. In all conditions, in the SZ an intense and higher grain refining compared to TMAZ and HAZ can be observed. An interface zone between the two steels, increasing the application of axial force, not only increases the number of inserts of steels but also modifies the morphology of the interface between the two materials because the inserts stop being in a format longer rounded to submit a more pointed shape with the formation of secondary insertions, improving FSW joint consolidation between welded stainless steels.

Keywords: Friction stir welding; Stainless Steel; Microstructure

4.2 Introduction

The Friction Stir Welding (FSW) process developed by The Welding Institute (TWI) by THOMAS et al. (1991) in Cambridge, England, is a solid-state welding process that uses a non-consumable tool, which rotates and penetrates the joint, resulting in heating and plastic deformation of the materials to be joined. MISHRA and MA (2005) claim that there are significant differences in the microstructure of the joints welded by the FSW process compared to conventional processes. As noted by ÇAM et al. (2017) and MOHAN and WU, (2021) , during the FSW process, the temperature and the plastic deformation generated, mainly by the friction between the tool and the material, resulted in significant microstructural evolution in certain aspects, including grain size, grain

boundaries, dissolution and hardening of precipitates, dissolution and redistribution of dispersoids, as well as the modification of the crystallographic texture.

As highlighted by LIU et al. (2018), even in similar FSW joints, it is possible to observe an asymmetrical arrangement of the different zones formed because we have the welding side where the displacement direction is the same tool rotation direction called “advancing side” and the side where the directions are opposite, called the “retreating side”. Thus, FSW welds present asymmetries in temperature distribution and strain intensity both transversely and longitudinally. Second THREADGILL, (2007) the cross-section of FSW welded joints is divided into four main regions: the base metal (BM), which is the region not affected by heat and which does not suffer deformation rate induced by tool rotation; the heat-affected zone (HAZ), being the region affected by the thermal cycle during welding, but without residual plastic deformation in the microstructure; the thermomechanically affected zone (TMAZ), in which the material was plastically deformed by the tool, and the resulting heat flow exerted some influence on the material; and the zone that extends to the centre corresponding to the shoulder width of the tool which is called the stir zone (SZ). According to FRATINI and BUFFA, (2005), the arrangement of these zones along the cross-section of FSW joints varies depending on the maximum temperature reached, the degree of deformation, and the stacking fault energy (SFE) of each material to be welded, as this determines the metal’s tendency to dynamically recover or recrystallize. The FSW procedure frequently gives fine dynamically recrystallized (DRX) grains in the stir zone (SZ) and outstanding mechanical properties.

With the critical advance in creating welding tools for joining high-temperature melting point materials, various FSW examinations have been devoted to joining different steels, as shown by FUJII et al. (2006) and CHUNG et al. (2010) specifically, for the stainless steels as presented in the studies of CAETANO et al. (2018) and HAJIZADEH; EMAMI and SAEID, (2020). The applications of the FSW process in austenitic stainless steel (ASS) welds appears in an attempt to solve problems like solidification cracking, weld decay, knife-line attack, and hot cracking in the weld region, and these problems are recurrent in the welded region, which experiences high thermal cycles during the fusion welding processes. In FSW of ASS, although the formation of deleterious phases is expected in the stir zone, as proved by KOKAWA et al, (2005) and PARK et al, (2003), an essential aspect for the success of the welds produced is the intense grain refining

resulting from dynamic recrystallization, as observed by WANG et al., (2014). The peak temperature primarily influences the microstructural properties at the weld SZ during FSW. According to JOHNSON and MURUGAN, (2020), apart from peak temperature, two different mechanisms, namely the pace of heat generation and the rate of material deformation, also govern microstructure evolution. An increase in heat generation results in grain coarsening, whereas the increase in deformation rate results reduction in grain size due to recrystallization contribution. Despite the lower temperatures experienced in FSW welds of ASS, some researchers, as KOKAWA et al. (2005) and PARK et al, (2003) have reported the precipitation of the sigma phase during FSW of ASS AISI 304. The authors speculate that the sigma phase precipitation was due to the emergence of δ-ferrite at higher welding temperatures experiencing severe strain in the material during frictional stirring, which subsequently led to decomposition of delta ferrite to sigma phase during the thermal cooling cycle.

12 % Cr ferritic stainless steel (FSS) has been widely applied in the transportation, construction, and power industries due to its low-cost fabrication, excellent mechanical properties, and good corrosion resistance. Conventional 12 % Cr FSS with a fully ferritic structure, for instance, 410S, has widely been used in applications that do not require welding owing to its very poor weldability. In recent years, with the emergence of advanced steel-making technologies, modified 12 % Cr FSS has been developed by controlling carbon and nitrogen at shallow levels and adding stabilizing elements such as Al, Ti, and Nb as reported by ZHENG et al. (2010). This group of materials can undergo a ferrite–austenite transformation upon heating, leading to the generation of martensite on cooling. This can lead to significantly improved welding performance. However, problems in fusion welding of these steels were observed by SILVA et al. (2006) that evaluated the changes in the HAZ of an AISI 410S ferritic stainless steel subjected to different heat inputs in SMAW fusion welding and observed that in addition to the formation of martensite, there were zones with excessive growth of ferritic grains, which causes a decrease in hardness and compromises mechanical strength. Similar microstructural changes are reported for AISI 410S steel when welded by other processes such as plasma and laser, as highlighted by KÖSE and TOPAL, (2019a) and (2019b). ÇAM, (2011) mentions that in applying the FSW process in FSS, there is some difficulty in recrystallization and grain refining, although studies show promising applications from the point of view of mechanical properties. However, AHN et al. (2012). analyzed the

microstructural features of a FSW 409L FSS joint. They concluded that equiaxed ferrite grains were generated in the SZ due to dynamic recrystallization (DRX). LAKSHMINARAYANAN and BALASUBRAMANIAN, (2010) investigated the microstructure and mechanical properties in an FSW of 409 M FSS at a rotational speed of 1000 r/min and a welding speed of 50 mm/min. It was concluded that the stir zone (SZ) of the weld consisted of a duplex microstructure of ferrite and martensite, and the joint exhibited acceptable ductility and impact toughness. For FSS, low heat input and high welding speed are recommended to minimize ferritic grain growth and form a refined microstructure. CAETANO et al., (2018) and HAN et al. (2022) showed that such characteristics could very well be achieved using the FSW process.

Different industrial segments use dissimilar welding joints of different metals to bring together different properties, minimize costs, and maximize the performance of equipment and machinery with different welding processes. SILVA et al. (2013) point out to be promising to join different stainless steels in dissimilar joints in the petroleum distillation towers in the gas and petroleum industries through fusion welding processes. Some industrial applications need the joining of austenitic stainless steels (ASSs) to ferritic stainless steels (FSSs). As observed by EMAMI et al. (2020), such a combination of dissimilar materials is commonly found in high-temperature applications such as energy conversion systems. For example, central power stations include boiler sections made from ferritic stainless steel operating at low temperatures. The section is usually connected with another section made from austenitic stainless steel, which operates at higher temperatures. Therefore, the transition occurs through a dissimilar weld between these two materials. MUKHERJEE and PAL (2012) claim that the dissimilar joints between ferritic and austenitic stainless steels are efficient for prolonging metals' service life due to improved toughness, mechanical strength, and corrosion resistance.

In this regard, some fusion and solid-state welding techniques were used to produce dissimilar joints of Austenitic/Ferritic (A/F) stainless steels. AGUILAR; TABARES and SERNA, (2013) studied the metallurgical transformations that occurred during the SMAW welding of AISI 316L austenitic stainless steel with AISI 430 ferritic stainless steel. They evaluated the influence of heat input and usage of two different electrodes on the microstructural evolution of the heat-affected and the fusion zone; in the results, the heat-affected zone of the ferritic side showed grain coarsening. BARROS (2013) welded AISI 316L and AISI 444 in dissimilar joints by TIG welding autogenous (without filler

metal) with pulsed current, although the use of pulse frequency is effective in reducing the grain size in the HAZ and the molten zone of the welded samples, this refining was not efficient in ensuring good tenacity of the produced joints. According to KOU (2003), grain growth in ferritic stainless steels, which can occur both in the molten zone and in the HAZ when subjected to arc welding, is mainly responsible for compromising the mechanical performance with a decrease in hardness, ductility and tenacity.

According to MURR, (2010), when the FSW process is applied to the weld of dissimilar joints, the asymmetry between the retreating and advancing sides is intensified because we have in HAZ, TMAZ e SZ different behaviours concerning thermal conductivity and plastic deformation due to differences in the physical and chemical properties of the materials involved, which support in the asymmetry of heat generation and material flow. Over the last few years significant progress on issues related to the application of the FSW process in dissimilar joints of aluminium alloys and other light alloys, in studies like BARBINI et al. (2017) and KADIAN and BISWAS, (2018) and these alloys with steels as shown RAMIREZ et al. (2011) and KASAI et al. (2015). In the application of the FSW process in the dissimilar welding of stainless steels, EMAMI et al. (2020) analysed the dissimilar joining of AISI 430 ferritic and AISI 304L austenitic stainless steels managed to obtain a joint free of defects and with mechanical properties superior to ferritic steel. GUO et al. (2021) evaluating the microstructure of friction stir welded dissimilar austenite–ferrite stainless steels joints, the results indicated that when the 304 plate was placed on advancing side, the weld metal showed superior flow characteristics and better material mixing compared to the weld when the 304 plate was placed on retreating side, showing that the positioning of the steels in the FSW dissimilar joint has a strong connection with the formation of defects. Despite recent advances, the understanding of flow and microstructural evolution in dissimilar FSW joints involving the wide variety of existing stainless steels, relating aspects such as phase transformations, intensity and type of recrystallisation, grain size, deformation intensity and defect formation along the different zones formed are still incipient. Thus, this work aims to evaluate the effect of different FSW welding parameters in the microstructural evolution of dissimilar joints between AISI 304L austenitic stainless steel and AISI 410S ferritic stainless steel.

4.3 Materials and Methods

The welds were made using 4-mm-thick plates of AISI 410S ferritic stainless steel and AISI 304L austenitic stainless. The materials' chemical composition was determined by optical emission spectroscopy (Shimadzu model PA7000 Japan) and is presented in Table 4.1.

Table 4.1 - Chemical composition of the base metals (% weight).

Material	Elements											
	C	Si	Mn	P	S	Cr	Ni	Mo	Cu	Co	N	Fe
410S	0.025	0.37	0.30	0.023	<0.010	12.8	0.21	0.01	0.21	0.02	0.033	Bal.
304L	0.026	0.32	1.21	0.029	<0.010	18.5	7.24	0.29	0.34	0.15	0.058	Bal

Source: The author.

The FSW process joined the samples at Helmholtz-Zentrum Geesthacht (HZG) in Germany. All welds were made using the HZG Gantry System with a butt joint configuration, as shown in Fig. 4.1. An inert gas (Ar) injection system was used to protect the material during the process as at temperatures above 535 °C; these stainless steels react with the atmosphere. Welds were performed in load control mode with an integrated system to record process data such as penetration depth, rotational speed, torque, tool forces, and tool position over time. The welds were made with a tool of polycrystalline cubic boron nitride (PCBN). The tool had a conical diameter of 25 mm with a conical pin with a 9.2 mm diameter and a length of 3.7 mm. The pin had a conical surface with negative recesses, which were in the form of a spiral concerning the tool's axis of symmetry.

Figure 4.1 – Dissimilar butt joint configuration between AISI 410S and AISI 304L steels.

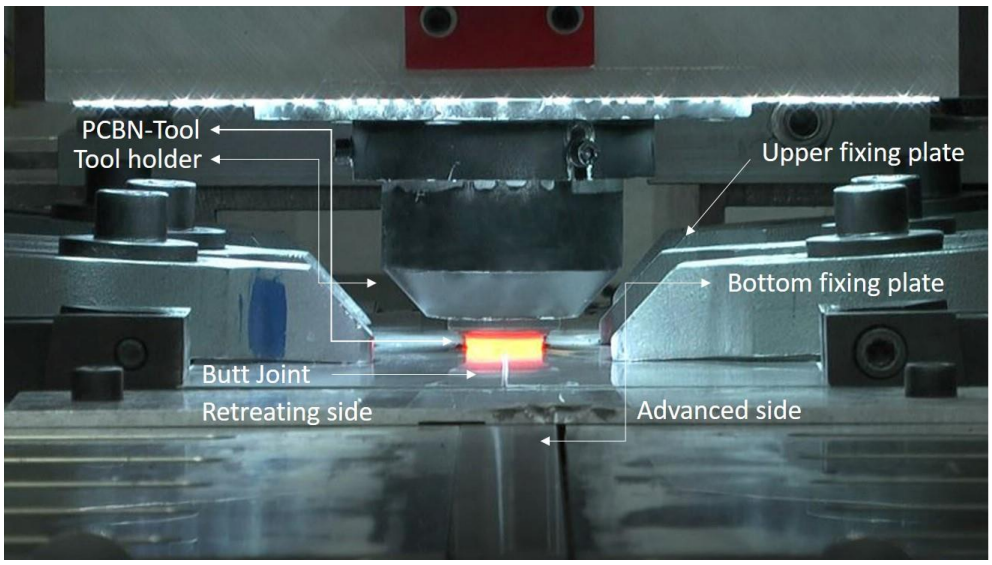

Source: CAETANO et al. (2019).

To determine the best set of the welding parameters, a previous study was carried out by CAETANO et al. (2018) in FSW welding similar to AISI 410S ferritic stainless steel. Thus, four welding conditions were analyzed to assess the influence of process parameters in the extension, formation and morphology of the different zones existing in the dissimilar FSW welds of the AISI 304L and AISI 410S steels. In these conditions, the axial force was varied from 25 to 40 kN, keeping the rotation speed at 450 rpm, the tool inclination angle at 0º and the welding speed at 1.0 mm/s, as shown in Table 4.2.

As the stainless steels used in this study have different physical, mechanical and chemical properties, such as stacking-fault energy (SFE), thermal conductivity, modulus of elasticity and flow stress, the correct side placing is essential to perform a good weld without defects. These differences also contribute to an asymmetry in heat generation, deformation and flow of welded materials, preliminary tests were carried out in Chapter 02 to evaluate the behaviour of steels to the effects of different phenomena that occurred between the advancing side, where the displacement direction is the same as the tool rotation direction and the retreating side that has these opposite directions in FSW welding. Thus, considering the preliminary tests under the four conditions welded in this study, the AISI 304L austenitic stainless steel was located on the retreating side, and AISI 410S ferritic stainless steel on the advancing side of the butt joint.

Table 4.2 – Welding Parameters for Dissimilar FSW Butt Welding of AISI 410S/304L Steels.

Condition	Rotation Speed (rpm)	Axial Force (kN)	Advancing Side	Retreating Side
1	450	25	410S	304L
2	450	30	410S	304L
3	450	35	410S	304L
4	450	40	410S	304L

Source: The author.

In the analyze, the temperature achieved during the FSW process were used 24 thermocouples divided into four different zones separate by 110 mm, with three thermocouples positioned on the advancing side and 3 positioned on the retreating side in each zone. For microscopic analysis, the welds were initially cut with a diamond abrasive disc on a Struers Discotom-6 cutter. Sandpapers with a grain size between 120 and 2500 mesh were used for grinding. The polishing step was performed in a Struers universal polishing machine with 3μ, 1μ and 1/4μ diamond pastes and a rotation speed of 150 rpm. As the butt joints are composed of AISI 304L and AISI 410S steels, a combination of reagents was necessary. After several tests, Vilella and 10% Chromic Acid reagents were chosen for the adequate production of contrasts between the phases and microconstituents present in the sample, enabling a complete analysis of its microstructure. Optical microscopy (OM) analysis was performed using a Carl Zeiss optical microscope integrated with the AxioVision SE64 software to assess the layout and characteristics of the different zones. However, for a more detailed investigation of the possible precipitates and the constitution of the interfaces between the AISI 304L/410S steels, analyses were performed by scanning electron microscopy (SEM) in an FEI Quanta 250 microscope with an Oxford Nordlys EDS system coupled. The electron backscatter diffraction (EBSD) with inverse pole figure (IPF) map and Kernel Average Misorientation (KAM) was also used in some conditions to help understand recrystallised fraction and grain orientation. Samples for this analysis were conventionally prepared by metallography following the same route described previously and including a final polishing step with OPS colloidal silica. Finally, further thermodynamic simulations were carried out to enrich the metallurgical discussion. All simulations were performed using ThermoCalc® and JmatPro® softwares.

4.4 Results and Discussions

4.4.1 Macrostructural Analysis

An analysis of the cross-section of the AISI 304L/410S stainless steel dissimilar FSW welded joints is presented in Fig. 4.2. It shows that increasing the applied axial force from 25 kN to 30 kN, 35 kN and 40 kN, keeping the rotation speed at 450 rpm, allows the material flow to reach a better plasticization state, eliminating the presence of internal voids and providing more significant interaction of the two steels in the stir zone. This better plasticization state can be attributed to the higher heat intensity obtained by combining the parameters used with, the higher axial forces.

In Condition 1, welded with an axial force of 25 kN, the presence of small voids in the stir zone in a region closer to the weld root has been observed. This behaviour, as noted by TONGNE et al. (2015), was attributed to less interaction between the tool and the material due to low axial force and consequent reduction in friction force and sufficient heat to achieve a plasticizer state suitable for material flow during the FSW process. Second DOUDE et al. (2015), these voids in the stir zone in regions close to the weld root, as noted in Condition 1, indicate the use of parameters with values below the ideal set recommended for consolidation of a defect-free FSW joint, and this is partly due to the use of low rotational speed and/or low axial force.

Figure 4.2 - Transverse macrographs of the different dissimilar welding conditions of AISI 410S/304L stainless steels by the FSW process. (a) Condition 1 (b) Condition 2 (c) Condition 3 and (d) Condition 4.

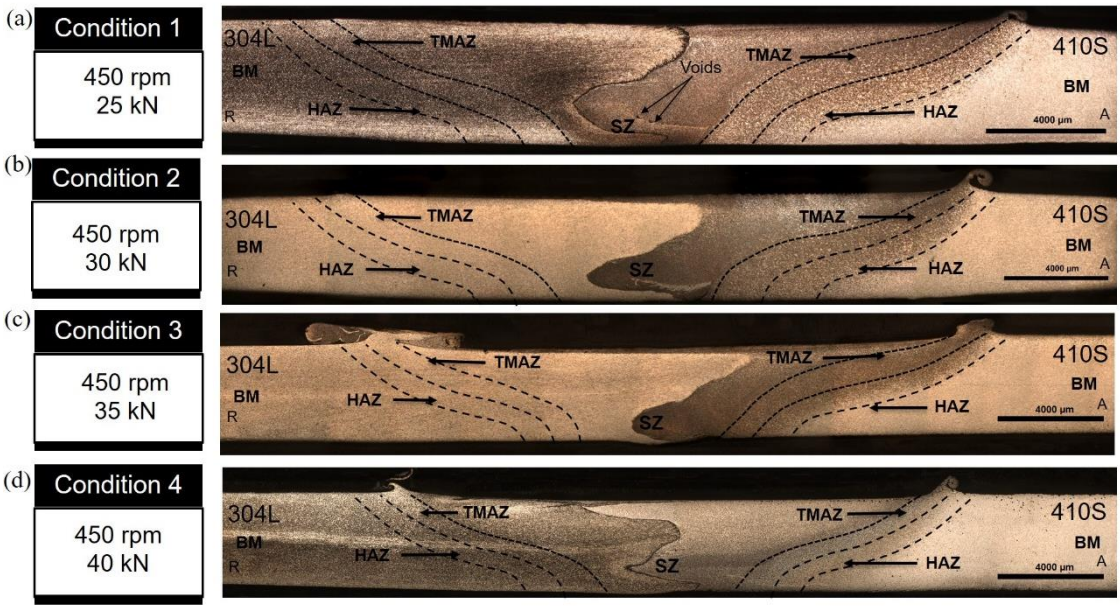

Source: The author.

According to DEBROY and BHADESHIA (2013), the main difference between similar and dissimilar FSW welds is the discontinuity in physical and chemical properties found on the interface between the two materials, as well as the morphology of this contact influenced by the adopted welding parameters and, consequently, of the flow of these materials in the stir zone. In the analyzed welds, as the axial force increases in conditions 2, 3 and 4, it is possible to observe a more significant contact between the two steels in the stir zone, with the formation of larger inserts of AISI 304L austenitic stainless steel in AISI 410S ferritic stainless steel and this in AISI 304L austenitic stainless steel.

While for Condition 1, only two large AISI 304L steel inserts and one of AISI 410S steel are observed in the formation of the contact region between the two steels in the stir zone. For Condition 4, three AISI 304L steel inserts and three AISI 410S steel inserts are observed in the contact region. In Condition 4, the increase in axial force increases the participation of steels in the formation of the interface zone. With the increase in axial force, in addition to the increase in the number of inserts, it is possible to observe that these inserts no longer present the profile rounded as shown in the Fig. 4.3 (b), but a more pointed shape, with the formation of secondary inserts, allowing a greater stir between the two steels, as can be seen in the Fig. 4.3 (c).

Figure 4.3 – (a) Cross-section macrograph of the Condition 1 (b), Inserts rounded profile in the interface zone of the Condition 1, welded with 25 kN axial force (200x) (b) Inserts pointed shape, with the formation of secondary inserts in the interface zone of the Condition 4, welded with 40 kN axial force (200x). (d) Cross-section macrograph of Condition 4.

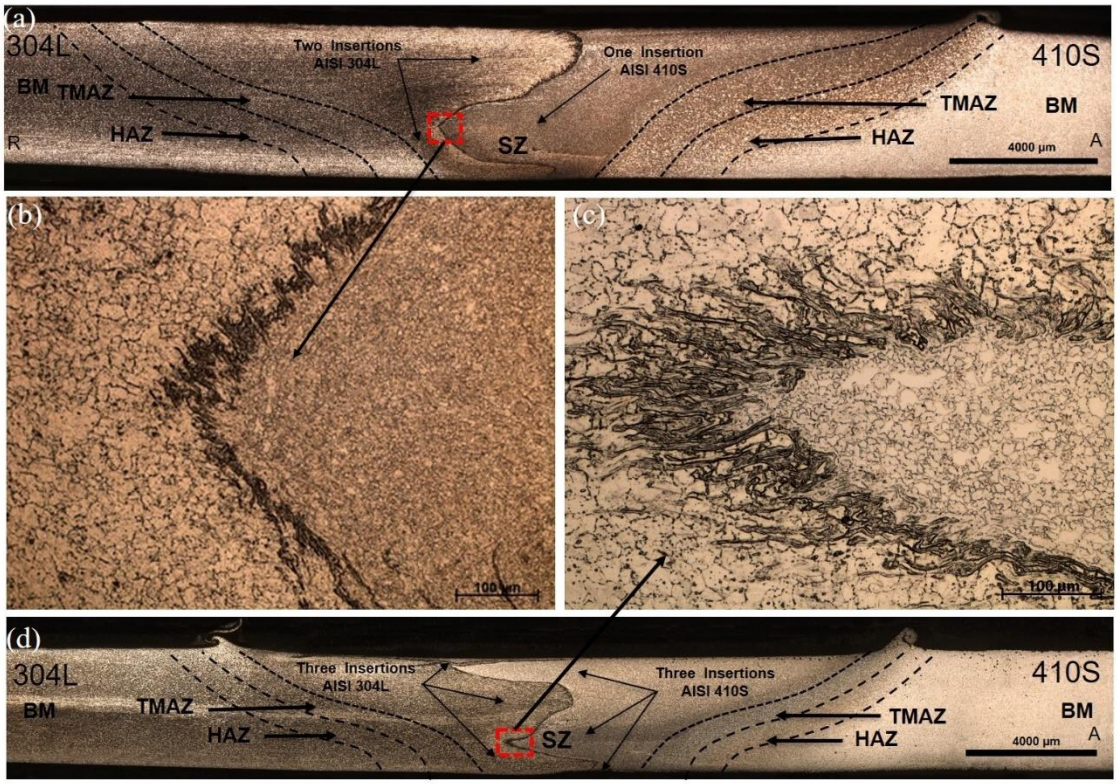

Source: The author.

4.4.2 Microstructural Analysis

4.4.2.1 Retreating Side – AISI 304L Austenitic Stainless Steel

Microstructural characterization results for Conditions 1, 2, 3 and 4 concerning the AISI 304L austenitic stainless steel, located on the retreating side of the dissimilar joint, in which the tool's travel direction is opposite to the tool's rotation direction, is presented below. A detailed analysis among the base metal (BM), heat-affected zone (HAZ) and thermomechanically-affected zone (TMAZ) was made. It was verified that for all conditions the BM presents metallurgical characteristics of austenitic stainless steels submitted to the hot rolling process, showing equiaxed austenite grains with residual δ-ferrite parallel to the rolling direction. The microstructure also exhibits crystal twinning

of annealing, a two-dimensional crystalline defect characteristic of FCC materials with low stacking fault energy (SFE), where the slipping of atomic planes is more difficult to be activated. However, in the heat-affected zone (HAZ) there are few microstructural changes in relation to the base metal (MB). DU et al. (2014) noted that for AISI 304 austenitic stainless steel, there are many similarities between BM and HAZ, except for the apparent reduction in deformation macle density and slightly larger grains, as can be seen for Condition 1 in Fig. 4.4 (b) and Fig. 4.4 (c) and for Condition 4 in Fig. 4.4 (d) and Fig. 4.4 (e).

Figure 4.4 – (a) Cross-section macrograph of the Condition 1 (b) BM of AISI 304L steel, Condition 1, welded with an axial force of 25 kN (500x). (c) HAZ of AISI 304L steel, Condition 1, welded with an axial force of 25 kN (500x). (d) BM of AISI 304L steel, Condition 4, welded with an axial force of 40 kN (500x). (e) HAZ of AISI 304L steel, Condition 4, welded with an axial force of 40 kN (500x). (f) Cross-section macrograph of the Condition 4.

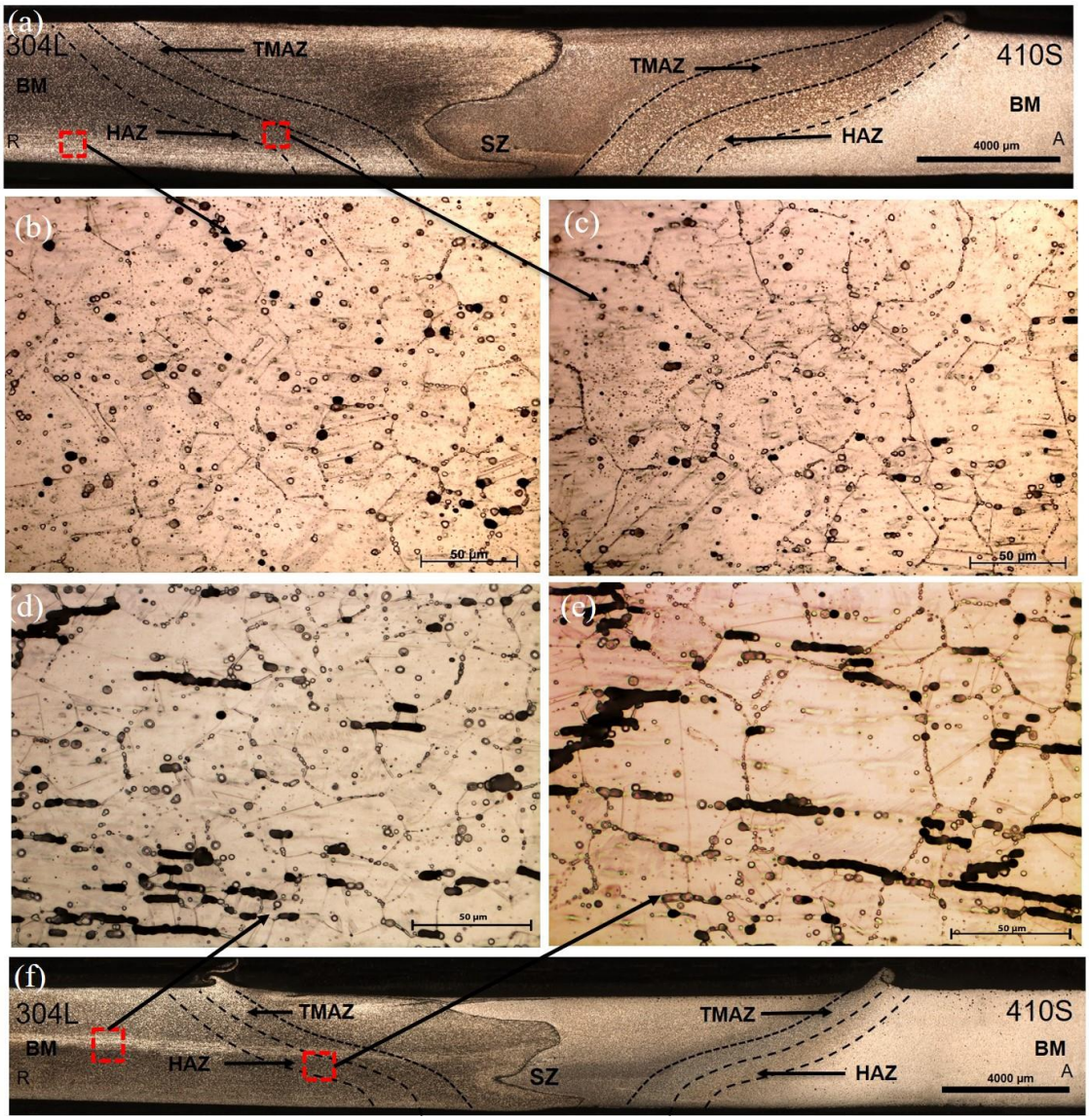

Source: The author.

In the thermomechanically affected zone (TMAZ), due to the grains of this region being affected by both the heat and strain rate induced by the rotation and tool friction during the FSW process, austenitic grains no longer are presented equiaxed with grain boundaries faceted. However, they present a microstructure with serrated and deformed

austenitic grains following the direction of material flow around the tool, as shown in Fig. 4.5 (b) and Fig. 4.5 (c), for Condition 1 and Condition 4, respectively. JAFARZADEGAN et al. (2012) also observed similar behaviour on the TMAZ retreating side of AISI 304 steel and attributed it to the effects of plastic deformation and dynamic recovery to which the material was submitted. The main difference for the welded conditions evaluated is the applied axial force that increases from 25 kN to 30 kN, 35 kN and 40 kN, whichleads to an increase in heat input and consequently results in an δ-ferrite increase in HAZ and TMAZ. This increase is critical for Condition 4, welded with an axial force of 40 kN, as seen in Fig. 4.4 (e) and Fig. 4.5 (c). In principle, austenitic stainless steels are formulated and thermomechanically processed to present an austenitic microstructure. However, ferrite-δ is the result of the participation of "ferrite promoting" elements, usually Cr, during solidification and thermomechanical processing, as shown LIPPOLD and KOTECKI, (2005).

Figure 4.5 – (a) Cross-section macrograph of the Condition 1 (b) TMAZ of AISI 304L steel, Condition 1, welded with an axial force of 25 kN (500x). (c) TMAZ of AISI 304L steel, Condition 4, welded with an axial force of 40 kN (500x). (d) Cross-section macrograph of Condition 4.

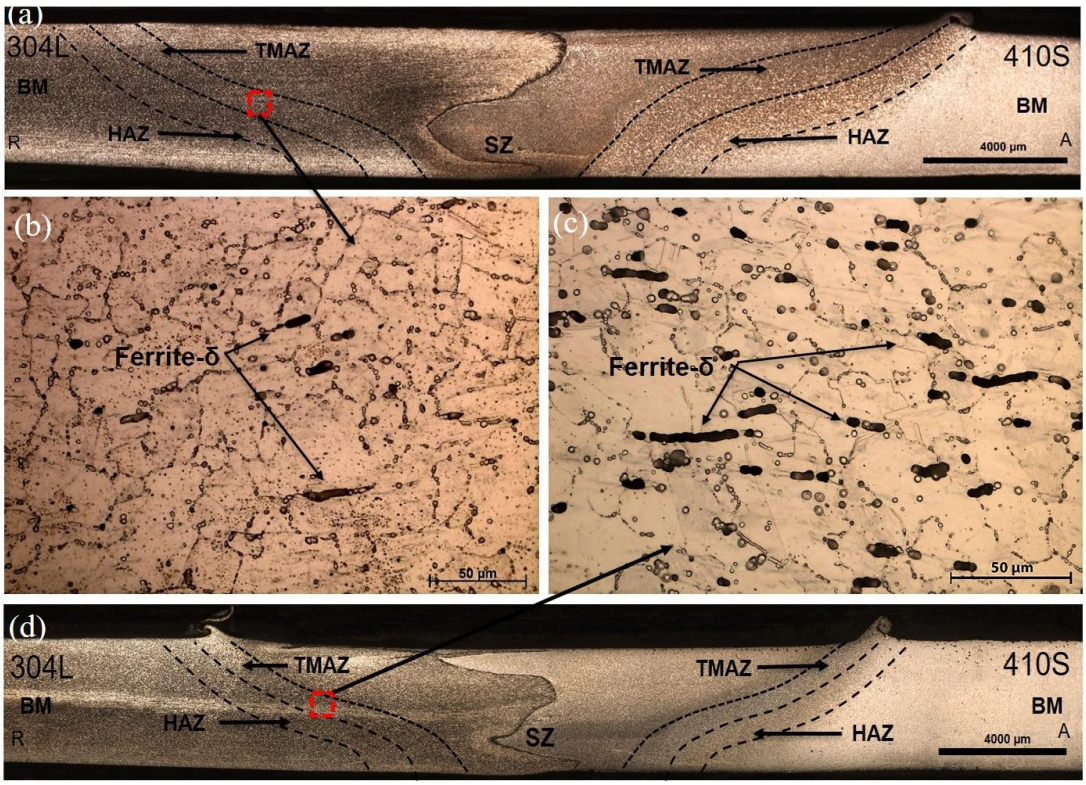

Source: The author.

MA et al. (2016) noted that in the high-temperature solidification of austenitic stainless steels, δ-ferrite is easily formed by element segregation, such as Cr, Mo, Ni, and Mn. This higher incidence of ferrite-δ in Condition 4 occurs due to a range of temperatures, which this condition is submitted during the FSW process, showing temperature peaks average of 600° C, as shown in the thermal analysis of Fig. 4.6. However, the measured temperatures are positioned 15 mm from the centre of the weld joint, and the temperatures reached in the stir zone are higher than in other regions. In temperatures above 600° C, the formation of ferrite-δ is predicted by the equilibrium phase diagram for AISI 304L austenitic stainless steel shown in Fig. 4.7 (a). In this diagram, the horizontal axis corresponds to temperature, and the vertical axis denotes the molar fraction of the formed phases (NPM). Although the phase transformations resulting from the heating and cooling cycles in welding occur outside equilibrium conditions, this can result in changes in the effective temperatures at which these transformations occur and may even partially or entirely suppress some transformation. Still, this diagram is handy, helping to understand the likely changes in structures based on an approach considering thermodynamic equilibrium conditions.

Although some studies highlight the harmful effects of ferrite-δ, which generally leads to detrimental effects on the high-temperature workability and corrosion resistance on mechanical properties and corrosion resistance, WANG et al. (2020) report that the uniformly distributed δ-ferrite improve the fatigue life of austenitic stainless steel. XU et al. (2019) affirm that in this steels the stress corrosion cracking (SCC) retardation is observed because the presence of δ-ferrite changes the direction of the SCC propagation and increases the lengths of the SCC propagation pathways. Although sigma phase precipitation and carbides and nitrides are predicted in the TTT (Transformation–Time–Temperature) diagram for AISI 304L austenitic stainless steel in Fig. 4.7 (b), through optical microscopy analysis, these precipitates were not identified. However, TSENG et al. (1994), on the ageing of austenitic stainless steel containing delta-ferrite, reported that $M_{23}C_6$ carbide was first precipitated along δ/γ boundaries in the temperature range between 500 and 900 °C.

Figure 4.6 - Thermal analysis for the four different zones on the retreating side showing to the temperature peaks of AISI 304L austenitic stainless steel.

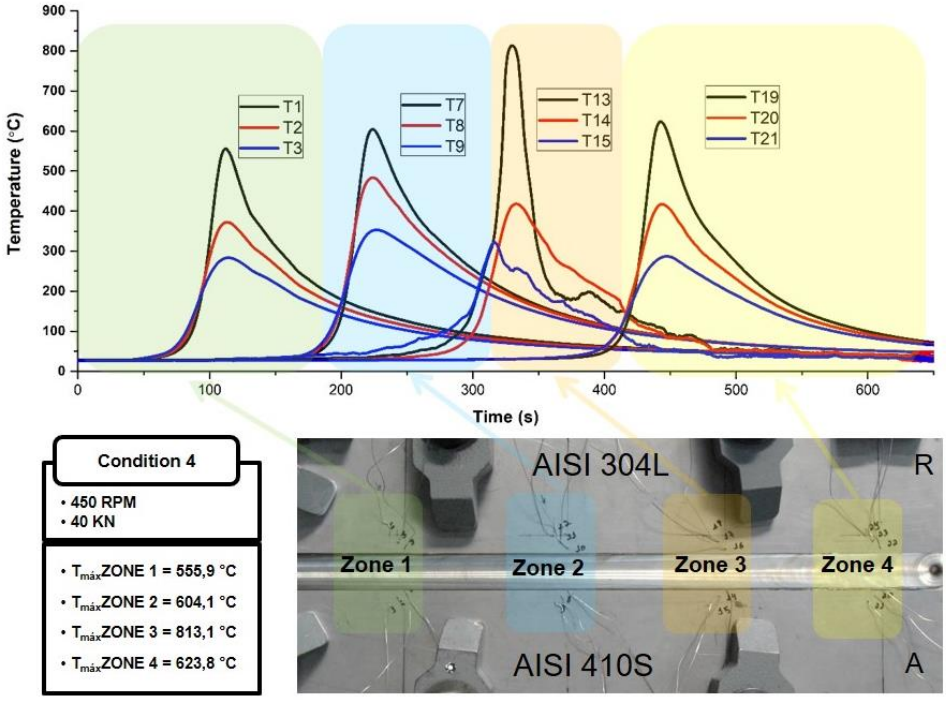

Source: The author.

Figure 4.7 – (a) Equilibrium phase diagram for AISI 304L austenitic stainless steel simulated using the Thermo-Calc software. NPM – molar fraction of the phases. (b) TTT (Transformation–Time–Temperature) diagram for AISI 304L austenitic stainless steel simulated using the JmatPro software.

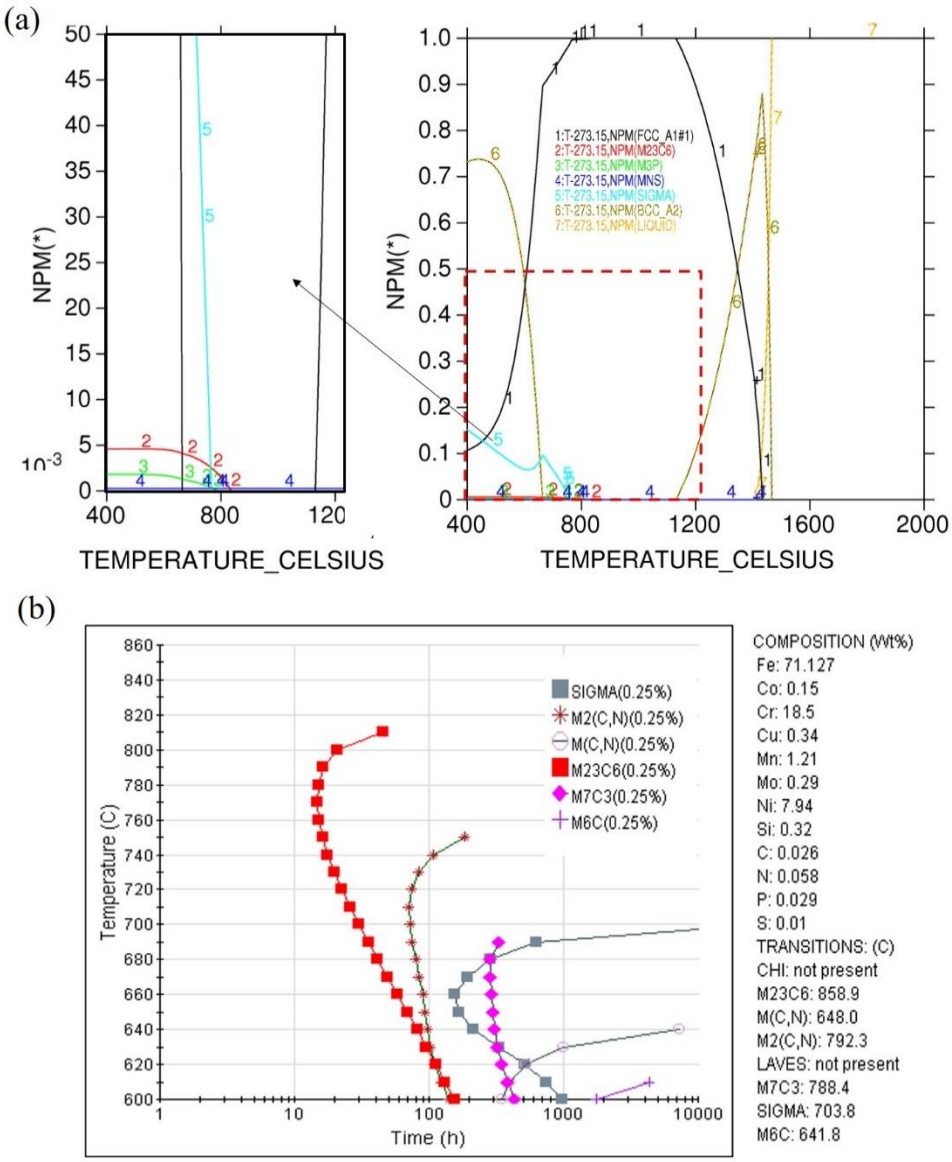

Source: The author.

4.4.2.2 Advancing Side - AISI 410S Ferritic Stainless Steel

On the advancing side of the dissimilar joint, where the direction of travel is the same as the direction of the rotation tool, the base metal (BM), the heat-affected zone (HAZ) and the thermomechanically affected zone (TMAZ) of the AISI 410S ferritic

stainless steel are shown. For all evaluated conditions in the base metal (MB), as it is not affected by the heat input or deformation induced by tool rotation during the FSW process, only equiaxed ferritic grains are observed, as shown in Fig. 4.8 (c) and Fig. 4.8 (e). However, in the heat affected zone (HAZ), due to the interference of the thermal welding cycle, the presence of equiaxed ferritic grains surrounded by martensite is observed, as can be seen in the Fig. 4.8 (b) and Fig. 4.8 (d). As noted by CAETANO et al. (2019) In the welding of AISI 410S steel by the FSW process, when subjected to temperature peaks superior than 800 °C, the partial transformation of ferrite into austenite occurs, whose nucleation occurs along the grain boundaries of the ferrite. This austenite formed on heating, transforms into martensite on subsequent cooling, giving rise to the biphasic microstructure observed in the HAZ of the AISI 410S steel.

The temperature analysis produced by using 24 thermocouples divided into 4 four different zones of condition 4, welded with the highest axial force, shown in Fig. 4.9, proved the thermal asymmetry between the advancing and retreating sides of the dissimilar FSW joints AISI 304L/410S. It can be seen that on average, the temperatures on the advancing side are 60° higher than those observed on the retreating side, despite a measurement error in zone 3, showed shown in Fig. 4.6, due to the contact of the flash produced during the process with the thermocouple number 13, show a peak temperature of 813°C for the retreating side. However, these e temperature measurements were taken ed from 15 mm from the centre of the stir zone, and the temperatures reached from the interface region between the two materials at the centre of the weld are higher than those observed in the thermal analysis.

In the modelling and simulation of austenitic and ferritic stainless steel joints by the FSW process, SILVA (2021) report that from conditions with a rotation speed of 450 rpm and axial force of 35 kN, keeping the welding speed at 1.0 mm/s, some tests reached in the stir zone temperatures above 85% of the melting point, indicating a possible overheating caused by the excessive application heat input when an inadequate combination of axial force and rotation speed was taken.

Figure 4.8 - (a) Cross-section macrograph of the Condition 1 (b) HAZ of AISI 410S steel, Condition 1, welded with an axial force of 25 kN (200x). (c) MB of AISI 410S steel, Condition 1, welded with an axial force of 25 kN (200x). (d) HAZ of AISI 410S steel, Condition 4, welded with an axial force of 40 kN (200x). (e) MB of AISI 410S steel, Condition 4, welded with an axial force of 40 kN (200x). (f) Cross-section macrograph of Condition 4.

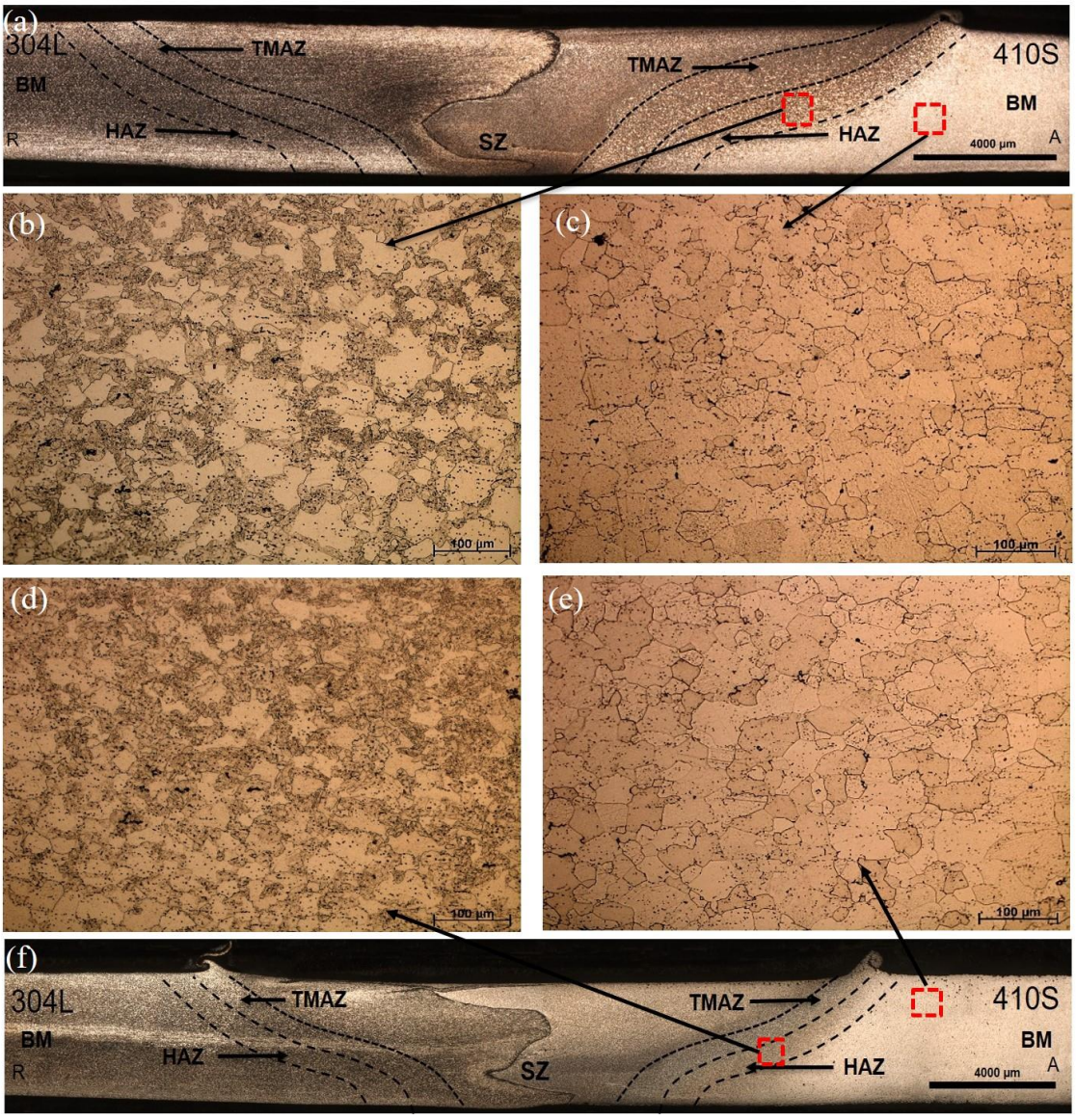

Source: The author.

Figure 4.9 - Thermal analysis for the four different zones on the retreating side showing to the temperature peaks of AISI 410S ferritic stainless steel.

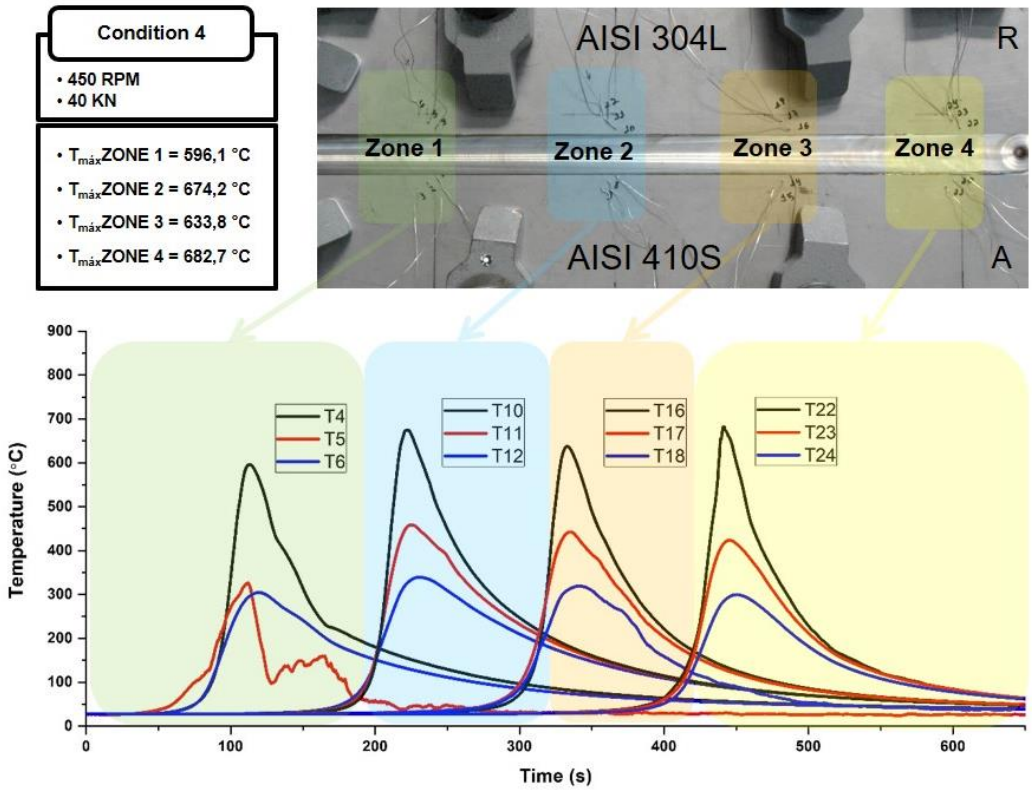

Source: The author.

Evaluating the equilibrium phase diagram for AISI 410S ferritic stainless steel in Figure 4.10 (a), it is possible to verify that in heating, from 808°C, the material starts to nuclear austenite, until at 881°C when the material becomes totally austenitic. The material remains utterly austenitic until reaching a temperature of 1062 °C, above which the austenite reverts to ferrite, completing this transformation at 1293 °C. Thus, there are two temperature ranges in which AISI 410S steel consists of two phases corresponding to ferrite and austenite: 808°C to 881°C and between 1062°C to 1293°C. Therefore, the AISI 410S steel, when submitted to the FSW process, is submitted to the first temperature interval, giving rise to austenitic grains nucleated in the ferrite grain boundaries, which when cooled will give rise to martensite. According to SONG et al. (2012), in FSW welding of ferritic stainless steels, since the chemical composition does not wholly stabilize the ferrite, any region exposed to temperatures around 800°C, can be subjected to cooling rates between 8.5°C/s to 2.2°C/s, providing the martensitic transformation.

Through the TTT (Transformation–Time–Temperature) diagram for AISI 410S ferritic stainless steel, shown in Fig. 4.10 (b), it is possible to verify that the precipitation

of $M_{23}C_6$ carbides is much easier in processes that submit these steels to fast cooling rates compared to AISI 304L steels. Thus, analyzing the ferrite/martensite interface on the advancing side after the chemical attack, it is possible to verify cavities which correspond to ditches due to probable precipitation of chromium carbides, probably $Cr_{23}C_6$. Precipitation occurred along with the grain boundaries of previous austenite at high temperatures. Although the alloy understudy has a low carbon concentration, reducing carbon contents below 0.03% does not prevent sensitization since the precipitation of chromium carbides can occur quickly when these steels are within the temperature range for precipitation, as verified by VAN NIEKERK, DU TOIT and ERWEE, (2012).

Figure 4.10 - (a) Equilibrium phase diagram for AISI 410S ferritic stainless steel simulated using the Thermo-Calc® software. NPM – molar fraction of the phases. (b) T.T.T (Transformation–Time–Temperature) diagram for AISI 410S ferritic stainless steel simulated using the JmatPro® software.

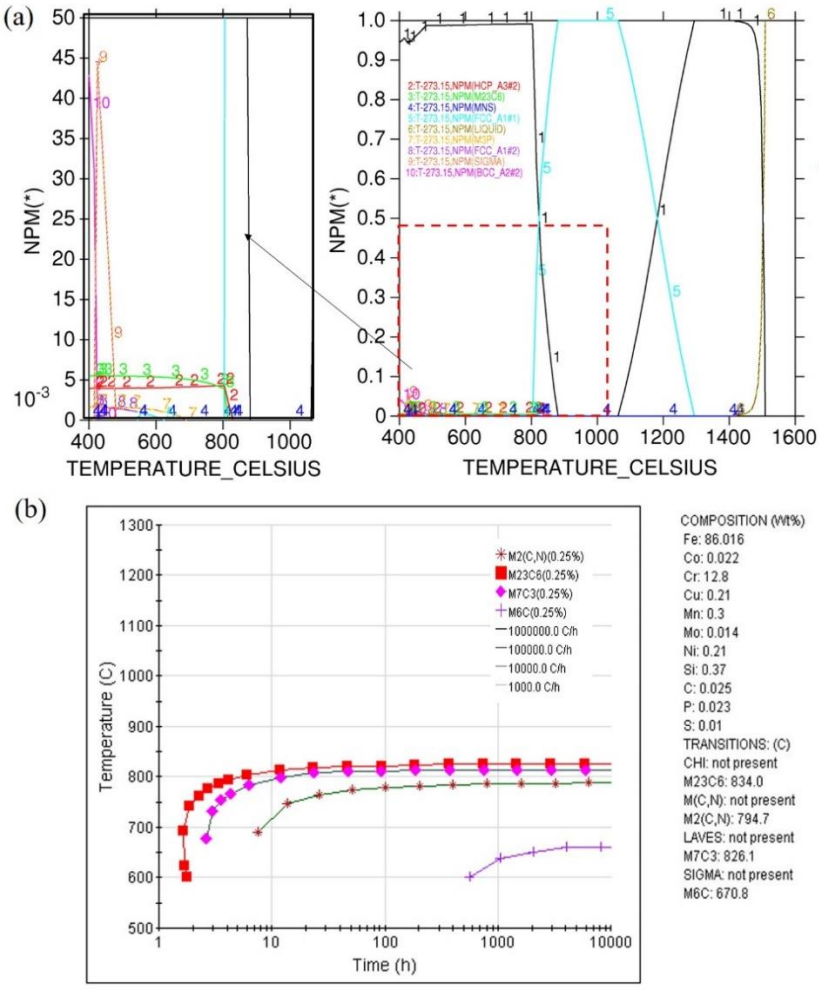

Source: The author.

In the thermomechanically affected zone (TMAZ), for the four conditions evaluated, AISI 410S ferritic stainless steel is plastically deformed by the intense deformation induced by tool rotation, showing deformed and elongated ferritic grains, following the direction of rotation of the tool and surrounded by martensite as shown in Fig. 4.11 (b) and Fig. 4.11(c). As the axial force increases from 25 kN to 30 kN, 35 kN and 40 kN, a refinement in ferritic grain size is noticeable in both the HAZ and the TMAZ of AISI 410S ferritic stainless steel, as shown in Fig. 4.8(b), Fig. 4.8(d) and the Fig. 4.11(b) and Fig. 4.11(c). When heated, the steel initially ferritic enters the austenitic field as shown in the equilibrium phase diagram of Figure 4.10 (a), nucleating austenite grains along ferritic grain boundaries. As the axial force increases, the heat input increases, providing a higher peak temperature, lower cooling rate and, therefore, longer residence time at high temperature. Thus, there are more favourable conditions for the growth of austenite grains, consuming the ferrite grains and providing its refining. During cooling, any transformation of the austenite, again for the ferrite is suppressed, providing the transformation of nucleated and grown austenitic grains into martensite.

Therefore, on the advancing side, the microstructural changes in the HAZ and TMAZ are similar to those observed by CAETANO et al. (2019) in similar welding of AISI 410S ferritic stainless steel, in which the presence of martensite was also observed surrounding the ferritic grains. CHOI et al. (2010) report that in dissimilar FSW welds for steels susceptible to martensitic transformation, this transformation will always be more critical when this steel is placed on the advancing side of the joint due to the higher temperatures in relation to the retreating side. However, in Chapter 02 the benefits of positioning the ferritic stainless steel on the advancing side were verified it was demonstrated, like the improvements in surface finish and elimination of voids in the stir zone that were achieved when the AISI 410S ferritic stainless steel was placed on the advancing side of the FSW butt joint.

Figure 4.11 – (a) Cross-section macrograph of the Condition 1 (b) TMAZ of AISI 410S steel, Condition 1, welded with an axial force of 25 kN (200x). (c) TMAZ of AISI 410S steel, Condition 4, welded with an axial force of 40 kN (200x). (d) Cross-section macrograph of Condition 4.

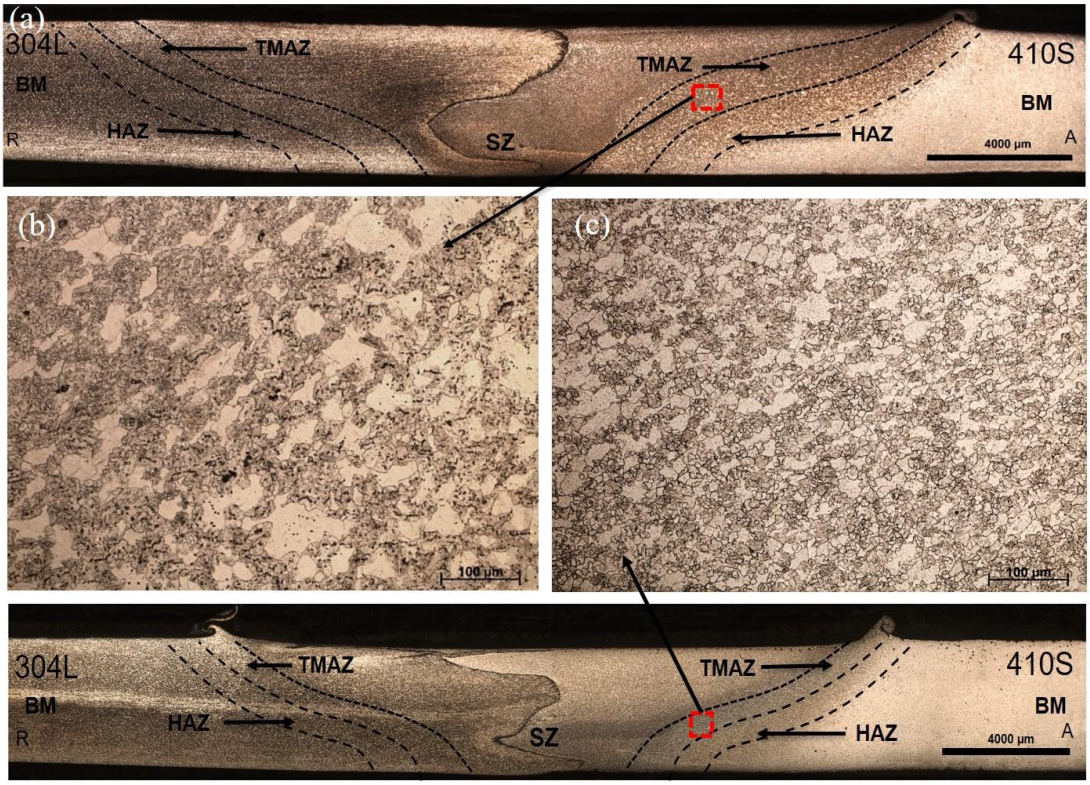

Source: The author.

4.4.2.3 Stir Zone - AISI 304L/410S

The central region of the weld corresponds to the stir zone. It has unique features because the weld zone material experiences severe thermomechanical excursions which drive recrystallization and recovery processes. In all conditions, an intense and superior grain refining compared to TMAZ can be observed to advancing and retreating side of SZ. HEIDARZADEH et al. (2021) noted that, dynamic recrystallization (DRX) is the dominant mode of microstructural evolution in the SZ and TMAZ. However, the homogeneity of the resulting microstructure is essentially independent of the DRX mechanism and dictated by the applied strain and temperatures reached resulting from the process parameters used, as the peak temperature and strain rate near surfaces of the pin and shoulder tend to decrease sharply toward the BM. Hence, a microstructure

recrystallized evolves in the SZ, while a partially recrystallized structure appears in the TMAZ.

In addition to the microstructural variations caused by the impact of different strain rates and temperature peaks reached between different zones, due to the characteristics of the process, in dissimilar FSW joints, the differences in properties of welded materials such as thermal conductivity, modulus of elasticity, flow stress and the stacking fault energy (SFE) strongly contribute to the consolidation of a microstructural heterogeneity in SZ. According to CAETANO (2016), the SFE of each welded material is an essential feature in the microstructural heterogeneity formation in the SZ, because it determines the metal's tendency to dynamically recover or recrystallize. Recrystallization is the generation of new grains, from the deformed metal, through the formation and migration of high-angle grain boundaries (HAGB), promoted by the energy stored in the material during deformation, in the form of dislocations, while recovery is the entire softening process occurred in the deformed metal without involving HAGB migration; the driving force for this transformation is the reduction of the energy accumulated during the deformation, through the rearrangement of the dislocations, which leads to the formation of low-angle grain boundaries (LAGB), as noted by PORTER; EASTERLING and SHERIF, (2009). According to HEIDARZADEH et al. (2021), recovery and recrystallization are competing processes since both are driven by the stored energy associated with the increased dislocation density. As highlighted by HEIDARZADEH et al. (2021), high-SFE metals commonly exhibit extensive cross-slip and dislocation climb; thus, the microstructural behaviour in such materials is often dominated by recovery, even at relatively high temperatures. In contrast, low-SFE materials typically experience almost no recovery. According to PADILHA (2000), materials with low stacking energy, such as austenitic stainless steels, produce a higher density of dislocations and higher accumulated deformation energy, favouring dynamic recrystallization and consequently the refining of grain and not the rearrangement of these dislocations leading to material softening as occurs in high-energy stacking materials.

In Fig. 4.12c, it is possible to observe the recrystallised and deformed fractions of the two steels in a central region of the stir zone. By locally analyzing of the morphology of these grains, it is possible to observe in Fig 4.12d, for the AISI 304L steel, recrystallised austenitic grains surrounded by deformed grains. According to CHATTERJEE, (2021) in ASS, the recrystallisation process promotes the release of stored energy, and the atoms

are oriented in such a way that strain-free crystals are developed; this fact induces the formation of refined austenitic grains together with larger grains, which are dispersed, partially recrystallised, with a high angle of disorientation and with a high degree of deformation. According to HUANG and LOGÉ (2016), the discontinuous recrystallisation DDRX found in ASSs generates along with the recrystallized grains a significant fraction of deformed austenitic grains with high dislocation density.

By analysing Fig 4.12e, for the AISI 410S steel, when the interface between the two steels approaches, there is an increase in recrystallised ferritic grains. However, these grains are more extensive and less refined than austenitic grains. According to PAN et al. (2021), in steels with a biphasic microstructure, as in low chromiun FSS, which will produce austenitic grains at high temperatures, there is competition between the recrystallisation of the ferritic grains and the austenitising process. This mechanism can impair the recristallisation and inhibits the refining of ferritic grains.. Thus, evaluating the fraction of grains that effectivelly experienced the reordering of their crystals, it has found some differences in recrystallized fraction between the AISI 304L and the AISI 410S steel plates. Although both steels have presented some fraction of recrystallised grains, the AISI 410S steel has shown a more significant fraction of recrystallised grains than the AISI 304L.

It is essential to highlight that the most significant fraction of deformed grains, painted in red in Fig. 4.12c and 4.12, were associated with the martensite grains. These grains result from multiples shears in the FCC lattice due to the thermal shrinkage, resulting in laths, sub-blocks, blocks and packet structures inside the grains of the previous austenite. This non-diffusional phase transformation produces a significant amount of crystal defects, such as dislocations and boundaries, which introduces a high distortion in the crystal lattice.

However, these grains of martensite have a peculiar feature in terms of crystallography, since their c/a ratio is relatively low, due to the low carbon content of the alloy, resulting in negligible tetragonality of the crystal. For this reason, their Kikuchi diffraction pattern is significantly similar to the BCC structure, making it difficult to differentiate both phases from the diffraction analysis correctly.

As the ferrite crystal lattice (BCC) has a significantly lower density of dislocations and boundaries, the Kikuchi pattern sharpness in the quality pattern is considerably better than the martensite structure (dark gray), making it possible to distinguish the martensite

grains from the ferrite (light gray), as shown in Fig 4.12. Therefore, will be adopted the quality pattern to distinguish the ferrite and martensite phases, and both will be indexed as BCC crystal lattice.

Examining the EBSD data, only a few recrystallised grains with small grain sizes were produced. This behaviour can be explained by the fact that the hard austenite phase before the martensitic transformation on cooling requires a more significant deformation degree for the occurrence of recrystallization, as it claims TANG et al. (2020). However, both sides of the dissimilar joint for Condition 4 are dynamically recrystallized (DRX). The recrystallization type can also explain the differences in recrystallization intensity in each material. Thus, the DRX type on the FSS AISI 410S side, with high SEF, is dominated by a continuous DRX mechanism (CDRX), and in the case of the ASS AISI 304L side with low SFE, the dominant mechanism is the discontinuous DRX (DDRX). According to HEIDARZADEH et al. (2021), the formation of LAGBs or dynamic recovery (DRV) can be considered the initial stage of CDRX, which includes the following steps. Due to the non-uniform nature of deformation in polycrystalline materials (the incompatibilities between grains), geometrically necessary dislocations (GNDs) are formed. By applying more deformation, dislocations rearrange to form geometrically necessary boundaries (GNBs), known as LAGBs. By increasing strain, dislocations slip and move to these GNBs and cause an increase in their misorientation angle up to 15°, which is the critical threshold of HAGBs. Thus, CDRX occurs by continuous formation and transformation of GNBs to HAGBs.

On the other hand, SAKAI et al. (2014) reports that DDRX occurs discontinuously, including distinct stages of nucleation and growth. Thus, the DDRX involves local grain boundary bulging, growth of the DRX nucleus driven by stored energy in the neighbouring deformed grains, and stagnant grain growth resulting from DRX grain impingement and a diminished driving force for growth because of work hardening of the growing recrystallized grains. In this mechanism, a network of subgrains readily develops near the grain boundaries leading eventually to boundary corrugations or serrations and the constitution of a refined microstructure, as shown in Fig. 4.13a and Fig. 4.13b. This greater intensity of grain refining provided by a DDRX recrystallization in an AISI 304 steel was also observed by JABRAEILI et al. (2021) in FSW welds dissimilar to ASS with an aluminium alloy.

Figure 4.12 – (a) Cross-section of the stir zone of condition 4, welded with an axial force of 40 kN. (b) Grain boundaries and predominant phases on each side of the joint. (c) Recrystallized and deformed fraction intensities in the interface region. (d) Recrystallized and deformed fraction to AISI 304L. (e) Recrystallized and deformed fraction to AISI 410S.

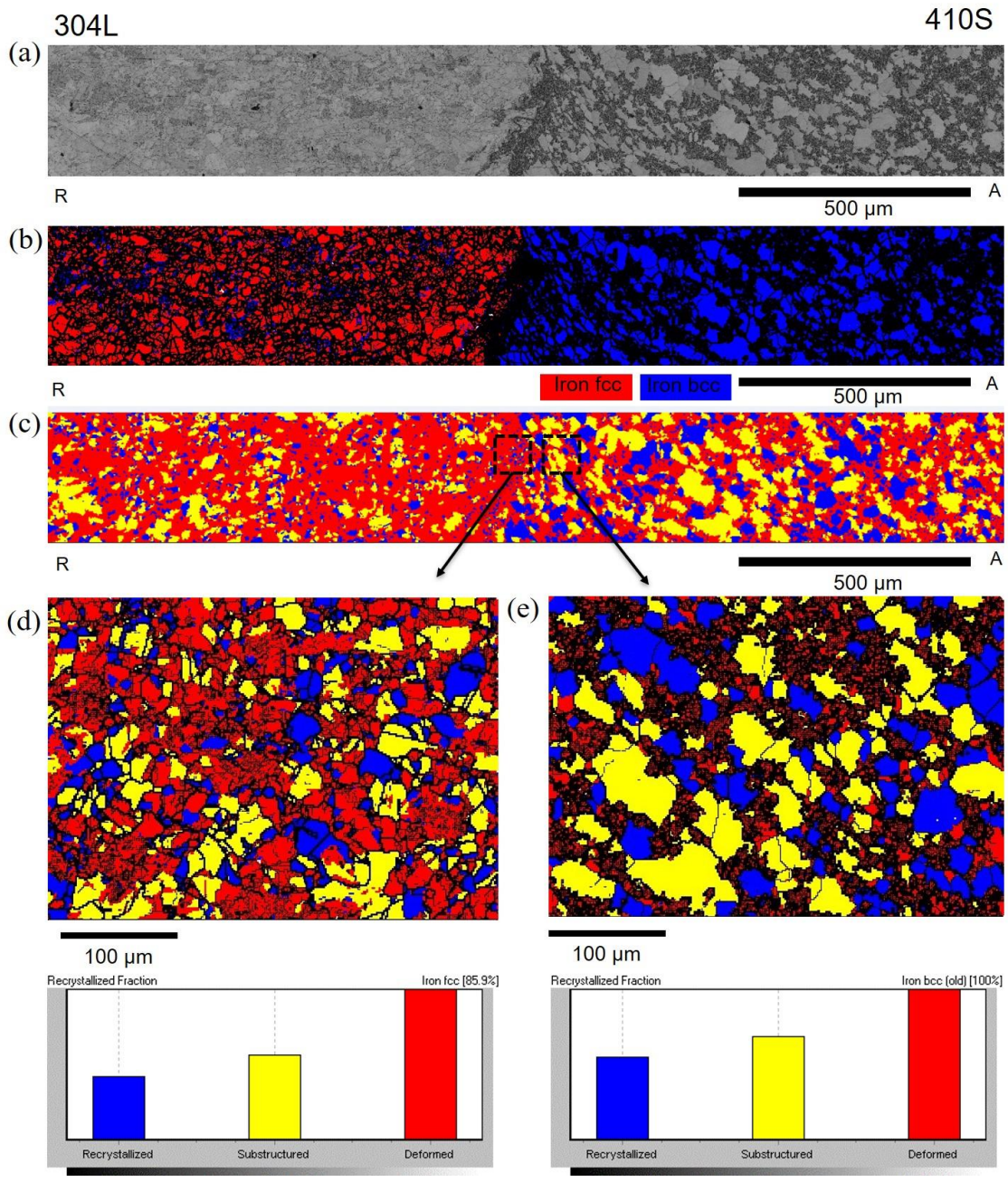

Source: The author.

Figure 4.13 - IPF map (a) and grain boundary map (b) of SZ in AISI 304L Austenitic stainless steel side showing the occurrence of DDRX mechanism. Arrows in (b) indicate the bulged grain boundaries and formation of DDRX grains.

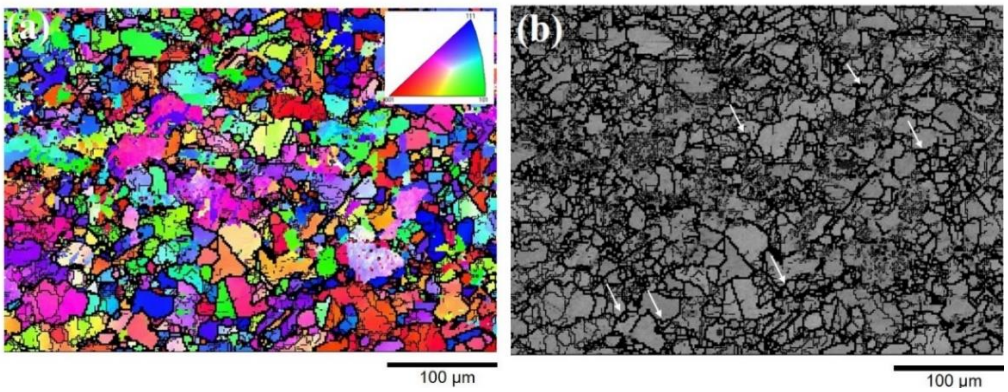

Source: The author.

This greater intensity of recrystallization and consequent generation of new grains by DDRX enables a greater intensity of grain refining, as can be seen in the grain size analysis for this same interface region between the two materials, performed in Figure 4.14 (a) and Figure 4.14 (b) to steel AISI 304L, and Figure 4.14 (c) and Figure 4.14 (d) to steel AISI 410S, where it is possible to verify a greater grain refining for AISI 304L steel. For AISI 410S steel, it is possible to visualize in the dual microstructure (ferrite/martensite) the presence of coarse ferrite grains in relation to extremely refined martensitic grains. This is because for AISI 410S steel there are two factors contributing to grain refinement. The first is the DRX effect that occurs at high temperature when part of the material is in the form of austenite. The second comes from the martensitic transformation that will “tear” the austenite grains into sub-units called packages, blocks and slats, as reported by SHIBATA et al. (2006), contributing even more to the refining. Therefore, for AISI 410S steel, grain refining does not occur uniformly. It is important to note that the region analyzed in the Fig. 4.14 corresponds to a region near the top of the joint, near the shoulder of the tool, region that reaches the highest temperatures and the lowest cooling rates, which further contributes to the non-uniformity of ferritic grain refinement.

For AISI 304L steel, this greater tendency towards DDRX recrystallization and consequent development of a sub-grain network positively impacts the mechanical properties. This microstructural uniformity of grain sizes brought about by DDRX recrystallization also increase the corrosion resistance of the joint, as reported by FU et

al. (2020) when analyzing the grain size and its uniformity on corrosion resistance of austenitic stainless steel, verified that the uniformity of grain refinement allows a better distribution of intermetallic compounds and stability of the passivation film. Another consequence of the differences between DDRX and CDRX can be seen in the lower intensity of deformation verified for ferritic grains of AISI 410S steel in the analysis of the degree of misorientation by Kernel Average Misorientation (KAM) performed in Fig. 4.14 (g) and Fig. 4.14 (f), which is correlated to the elastic deformation of the material. In AISI 410S steel occurred CDRX, as suggested by HEIDARZADEH et al. (2021) in this mechanism, the formation of LAGBs or dynamic recovery (DRV) can be considered as the initial stage of CDRX. The driving force for this transformation is the reduction of the energy accumulated during the deformation, through the rearrangement of the disagreements, resulting in a lower degree of deformed microstructure for the ferritic grains of steel AISI 410S. The martensitic grains of AISI 410S steel present a different behaviour, because, in the austenite/martensite transformation the martensite undergoes intense plastic deformation, generated by the high densities of dislocations, which strongly contribute to the distortion of the crystal lattice, for this reason, the martensitic grains appear in the Fig. 4.14 (g) and Fig. 4.14 (h) with a degree of misorientation superior to ferritic grains.

Figure 4.14 – (a) Grain size of steel AISI 304L of Condition 4 (b) Grain size of steel AISI 304L in interface zone of Condition 4 (c) Grain size of steel AISI 410S in interface zone (d) Grain size of steel AISI 410S of Condition 4 (e) Local misorientation of steel AISI 304L of Condition 4 (f) Local misorientation of steel AISI 304L in interface zone of Condition 4 (g) Local misorientation of steel AISI 410S in interface zone and (h) Local misorientation of steel AISI 410S of Condition 4.

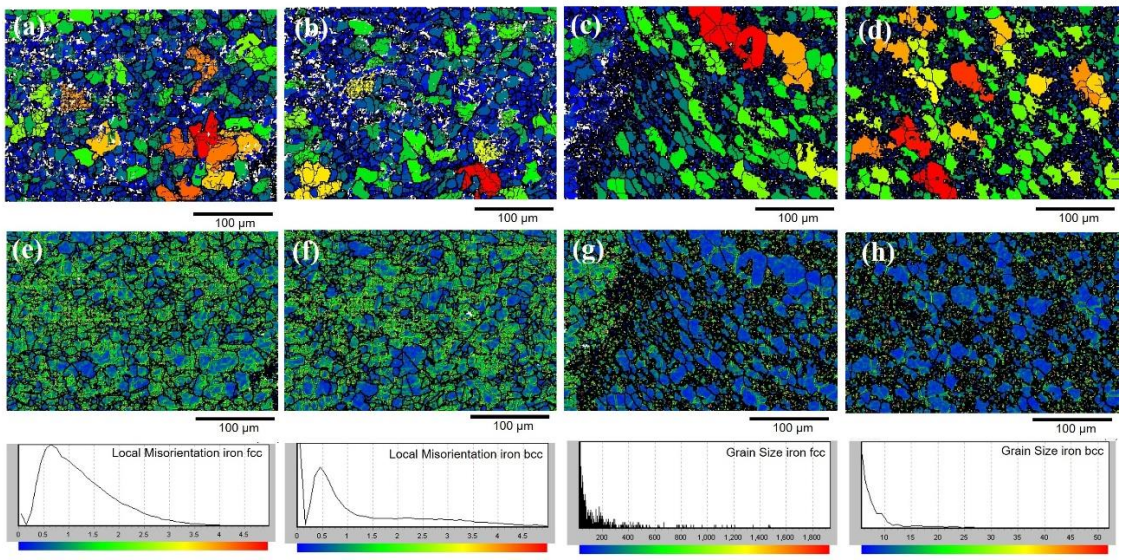

Source: The author.

Despite this greater uniformity, the grains in the stir zone are thicker at the top and more deformed and refined at the bottom, as can be seen for Condition 1 in Fig. 4.15 (a) and Fig. 4.15 (b) for austenitic stainless steel and in Fig. 4.15 (d) e Fig. 4.15 (e) for ferritic stainless steel. This happens because, as highlighted by MA, (2008), in the SZ, the peak temperature ranges from 0.9 to 0.75 Tm (melting temperature), decreasing away from the shoulder contact surface and in the transverse and longitudinal direction away from the pin surface, providing different cooling speeds, besides the differences between strain rate and intensity of dynamic recrystallization.

On the retreating side, although the AISI 304L steel has thick grains in the upper part of the stir zone compared to the lower part, these equiaxed austenitic grains are more refined compared to base metal structure grains, as noted by JAFARZADEGAN et al. (2013) welding by the FSW dissimilar process with the AISI 304 steel on the retreating side, there was a considerable grain refining in the SZ of the 304 steel. The average grain size for the 400 and 800 rpm welds was 3 and 8 µm, while the as-received material exhibits a microstructure of large equiaxed austenite grains approximately 15 µm in total

diameter. As previously reported, the austenite grains in the stir zone became dynamically recrystallized due to hot deformation during the FSW process. According to HUMPHREYS and HATHERLY (2012), the austenitic stainless steels have low stacking fault energy (SFE) thus it is suggested that the dynamic recrystallization DDRX occurs with nucleation and growth mechanism, and the evidence of DDRX remain intact in the 304L steel because there is not any phase transformation during FSW, contrary to the AISI 410S steel.

On the advancing side, AISI 410S steel also showed similar behaviour. However, in this region, the thick ferritic grains of the base metal were changed to a biphasic microstructure in the stir zone, with a very refined structure, consisting of ferrite and martensite, due to the austenitizing and fast cooling rates, and refined grains related to the severe plastic deformation. This is the same reason given by LAKSHMINARAYANAN and BALASUBRAMANIAN (2010), to the formation of the AISI 409M ferritic stainless steel stir zone, which has a chemical composition near to AISI 410S. With the use of high rotation speeds, the thick ferritic grains of the base metal also was modified to a biphasic microstructure in the stir zone. In the upper part of the stir zone, where the AISI 410S steel is positioned, is present larger ferritic grains, because in this region close to the shoulder of the tool, there are the highest peaks of temperature and deformation intensity contributing to lower cooling rates providing the growth of the ferritic grain.

Figure 4.15 – (a) Top SZ of AISI 304L steel, Condition 1, welded with an axial force of 25 kN (200x). (b) Bottom SZ of AISI 304L steel, Condition 1, welded with an axial force of 25 kN (200x). (c) Cross-section macrograph of the Condition 1 (d) Top SZ of AISI 410S steel, Condition 1, welded with an axial force of 25 kN (200x). (e) Bottom SZ of AISI 410S Steel, Condition 1, welded with an axial force of 25 kN (200x).

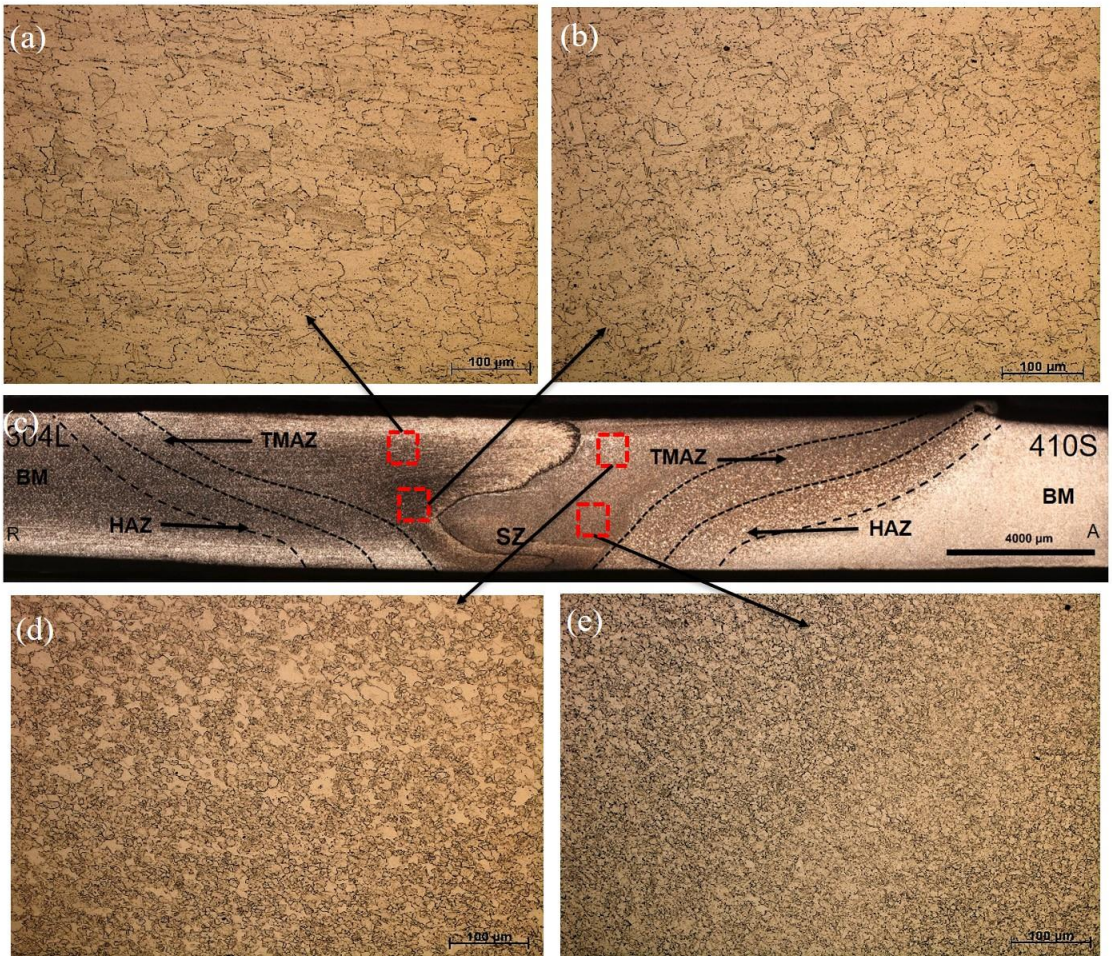

Source: The author.

As observed in the macrographic analysis of the different conditions welded by the FSW process, the stir zone of dissimilar welds presents a contact interface between the two materials. This profile was modified as the axial force application increased from 25 kN to 30 kN, 35 kN and 40 kN. Greater contact between the two steels in the stir zone, with the formation of larger inserts of AISI 304L austenitic stainless steel in AISI 410S ferritic stainless steel and of this in AISI 304L austenitic stainless steel AISI 304L, the greater the applied force, the greater the number of these insertions. In addition to the increased coupling of steels in the formation of the contact zone, with the increase in the number of inserts, it is possible to observe a structural modification in these inserts. For

both materials, the inserts are no longer rounded to present the most pointed shape with the formation of secondary inserts, enabling greater mixing between the two steels. For a more detailed analysis of the contact zone, scanning electron microscopy images show the formation of these secondary insertions, being more evident for condition 4, welded with an axial force of 40 kN as shown in Fig. 4.16 (b) and Fig. 4.16 (c).

Figure 4.16 – (a) Cross-section macrograph of the Condition 1 (b) Interface zone between AISI 410S and AISI 304L steels of Condition 4 (1000x). (b) Primary insertion and secondary insertions of Condition 4 (1000x).

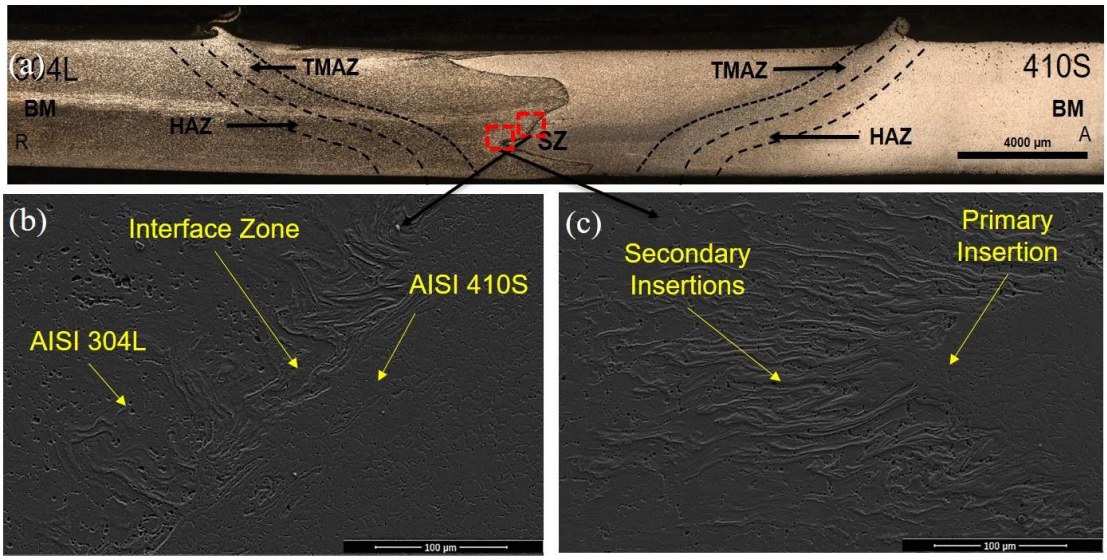

Source: The author.

EDS analysis of the contact zone detected the formation of intercalated regions of AISI 410S ferritic stainless steel and AISI 304L austenitic stainless steel, in a transition region between the two steels, as shown in Fig. 4.17. The wide variation in Cr and Ni contents in this region demonstrates the existence of this region intercalated by the two steels, for while AISI 304L steel has 18.5% chromium and 7.24% nickel, AISI 410S steel is composed of only 12.8% chromium and 0.21% nickel. However, there was no evidence of short-range diffusion between the steels at the AISI 304L/410S interface, due, among other factors, to the rapid cooling rates.

According to MURR (2010), during FSW process, interleaved blocks or segments may flow due to the solid-state flow promoted by the intense strain rate, as well as solid matter segments in the liquid matrix, forming thin intercalated strips within the stir zone.

This flux in thin strips also occurs in similar FSW welds. However, they are intensified in dissimilar FSW welds, as observed in the union of AISI 304L and AISI 410S steels.

Figure 4.17 – Analysis of the interface zone between the two steels performed by EDS (energy dispersive X-ray detector) showing the variation of chromium and nickel contents in an intercalated region composed of the two materials.

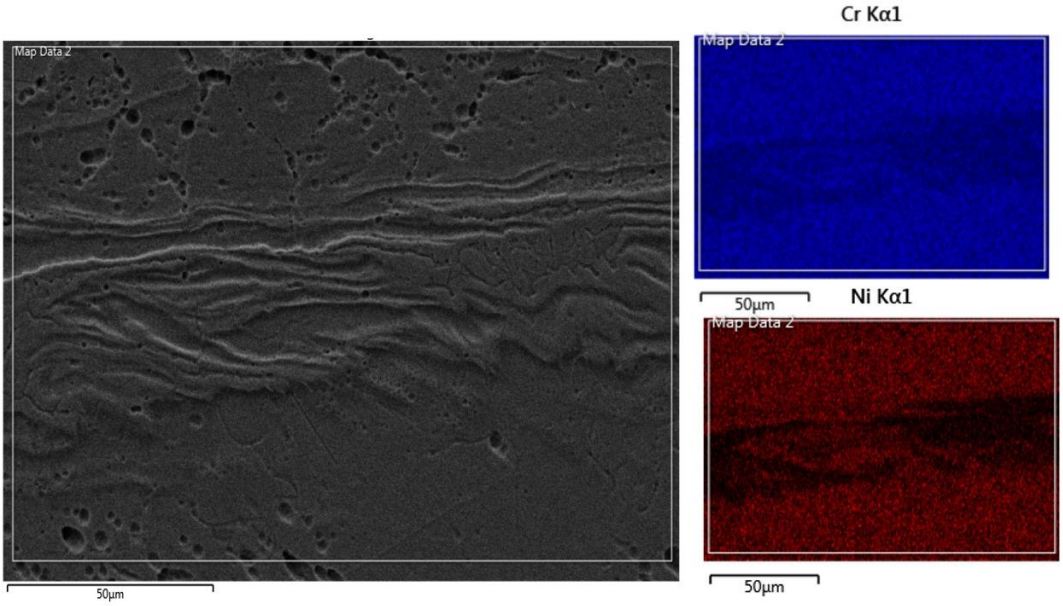

Source: The author.

Textural variations characterize friction stir welded joints through the thickness and across the width of the weld, but they can also occur along the length of the processed zone, as proposed by FONDA and KNIPLING, (2011). The SZ, TMAZ, and HAZ all have different thermomechanical histories and, hence, different textural features, as shown in Fig. 4.18. In all cases, the texture was weakly developed. In the FSS AISI 410S in the SZ and in the TMAZ close to the SZ, fine ferrite grains are located along the grain boundaries and in triple junctions of the martensite grains. Nearly equiaxed ferrite grains were observed in the TMAZ close to the HAZ. In addition, local textures develop within various regions of the SZ that derive from the final deformation state of each specific location. According to FIELD and NELSON, (2002) these are a function of tool design and weld parameters that alter flow in the SZ.

Thus, crystallographic textures vary dramatically from point to point within and near the zone produced by FSW. Because of this, local anisotropies exist that result in spatial variations in strength, hardness and corrosion susceptibility. An example is shown in Fig.

4.19c, Fig. 4.19d and Fig. 4.19e showing bands of distinct textures across the width of the FSW region to Condition 4, being these texture bands more evident for AISI 410S ferritic stainless steel located on the advancing side, as shown Fig. 4.19f. HEIDARZADEH et al. (2021) reports that these texture bands occurs because the shear direction of the last in time material to be processed in the plate is aligned with the tangent of the weld tool as it passes through the metal. This direction changes from point to point across the weld as the profile of the tool shoulder creates a semi-circle that follows behind the tool. As reported by EMAMI and SAEID, (2019) face-centered cubic (FCC)-structured materials with low stacking fault energy (SFE) like austenite are more susceptible than body-centered cubic (BCC)-structured materials like ferrite to the development of special high-angle boundaries known as coincidence site lattices (CSLs), that contributes to the greater misorientation of the austenitic microstructure, as noted in Condition 4.

Figure 4.18 - (a) EBSD IPF map across a cross-section of a friction stir weld in Condition 4 (a) SZ 410S (b) TMAZ 410S (c) HAZ 410S (d) SZ 304L (e) TMAZ 304L and (f) HAZ 304L.

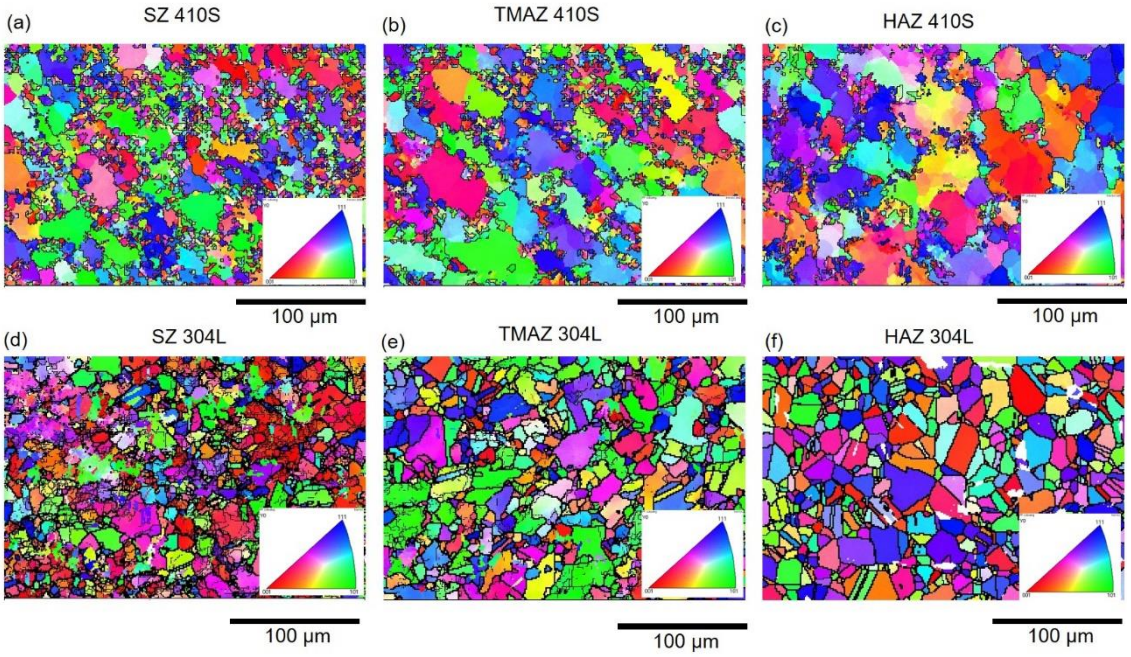

Source: The author.

Figure 4.19 – (a) Grain boundaries in the interface zone of Condition 4 (b) Predominant phases on each side of the joint (c) IPF map of interface zone in direction x (d) IPF map of interface zone in direction y (e) IPF map of interface zone in direction x and (f) IPF map across a cross-section of Condition 4.

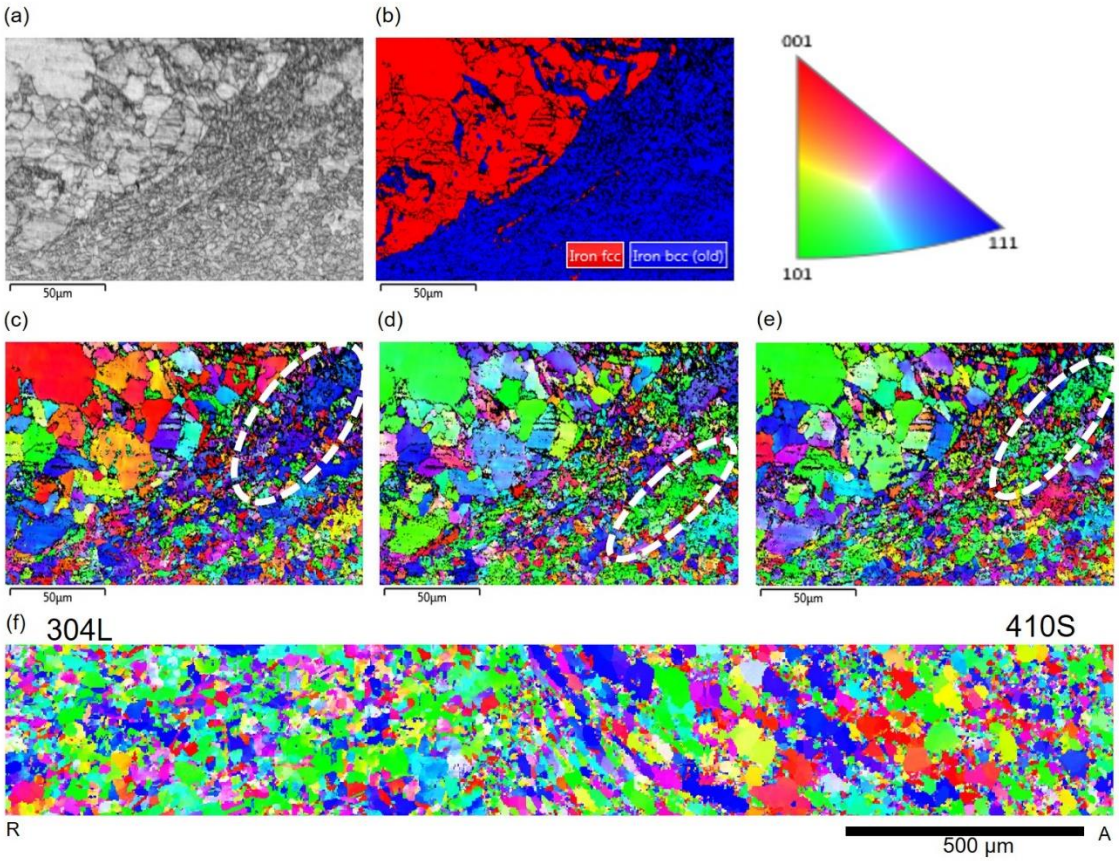

Source: The author.

Therefore, the microstructural analysis of the different dissimilar joints, composed of AISI 304L austenitic stainless steel and AISI 410S ferritic stainless steel produced by FSW process, shows that the microstructural profile of the joints is modified according to the application of axial force. On the retreating side, where is the AISI 304L austenitic stainless steel the applied axial force increases and consequently an increase in heat input, there is an increase in ferrite-δ intensity uniformly distributed in HAZ and TMAZ. On the advancing side of the dissimilar joint, where the AISI 410S ferritic stainless is positioned, in the HAZ and TMAZ as the axial force increases, provides higher peak temperature reached, lower cooling rate, and, therefore, lower cooling rate, longer is the residence time at high temperature. In the stir zone the larger contact zone between the two steels is observed for Condition 4, welded with an axial force of 40 kN, as in this condition the

sharp primary inserts and a large number of secondary inserts favour a greater interaction between the two steels and consequently a better consolidation of the joint. Thus, there are more favourable conditions for the growth of austenite grains that will be transformed into martensite during cooling, consuming the ferrite grains and providing its refining.

4.5 Conclusions

Based on the results of the microstructural analysis of the different zones formed in the FSW welding dissimilar, between the AISI 410S ferritic stainless steel located on the advancing side and the AISI 304L austenitic stainless steel on the retreating side, it was possible to conclude that:

1. It is possible to weld dissimilar FSW joints between the AISI 410S ferritic stainless steel located on the advancing side and the AISI 304L austenitic stainless steel on the retreating side, no grain growth on TMAZ and HAZ, intense grain refining in SZ and with significant interaction between the two steels and consequently a good consolidation of the joint.
2. As the axial force increases in conditions 2, 3 and 4, it is possible to observe a more significant coupling between the two steels in the stir zone; this increase in the application of axial force not only increases the number of steel insertions but also modifies the morphology of the contact zone between the two materials. It is possible to observe that these inserts, for both materials, are no longer rounded to present a more pointed shape with the formation of secondary inserts.
3. On the retreating side, where is the AISI 304L austenitic stainless steel as the applied axial force increases and consequently an increase in heat input, there are an increase in ferrite-δ intensity uniformly distributed in HAZ and TMAZ.
4. On the advancing side of the dissimilar joint, where the AISI 410S ferritic stainless is positioned, in the HAZ and TMAZ as the axial force increases, provides higher peak temperature reached, lower cooling rate, and, therefore, lower cooling rate, longer is the residence time at high temperature. Thus, there are more favourable conditions for the growth of austenite grains that will be transformed into martensite during cooling, consuming the ferrite grains and providing its refining.

5. In all conditions, an intense and higher grain refining compared to TMAZ can be observed to advancing and retreating side of SZ. However, despite this more significant grain refining, the grains in the stir zone are thicker at the top and more deformed and refined at the bottom.
6. In the stir zone, differences in intensity of recrystallized fraction are observed for AISI 304L and AISI 410S steels due to different dynamic recrystallization (DRX) mechanisms. The DRX type on the FSS AISI 410S side, with high SEF, is dominated by a continuous DRX mechanism (CDRX), and in the case of the ASS AISI 304L side with low SFE, the dominant mechanism is the discontinuous DRX (DDRX).
7. The SZ, TMAZ, and HAZ all have different thermomechanical histories and, hence, different textural features. The texture was weakly developed in all cases, but texture bands were more evident for AISI 410S ferritic stainless steel on the advancing side.

4.6 Acknowledgments

The authors are grateful for the support given by the following Institutions: Universidade Federal do Ceará, Laboratório de Pesquisa e Tecnologia em Soldagem (LPTS), in Brazil, and the Solid State Joining Processes, Helmholtz-Zentrum Geesthacht (HZG), in Germany and the Central Analítica-UFC/CT-INFRA/MCTI-SISANO/Pró-Equipamentos CAPES for the support. This study was financed in part by the Coordenação de Aperfeiçoamento de Pessoal de Nível Superior - Brasil (CAPES) - Finance Code 001, Brazilian funding agencies CNPq (Universal 472185/2011-0), and FUNCAP and CAPES (Project CI1-0050-00049.01.00/11 – International Cooperation).

4.7 References

AGUILAR, S.; TABARES, R.; SERNA, C. Microstructural Transformations of Dissimilar Austenite-Ferrite Stainless Steels Welded Joints. **Journal of Materials Physics and Chemistry**, [s.l.], v. 1, n. 4, p. 65–68, 14 nov. 2013.

AHN, B. W. et al. Microstructures and properties of friction stir welded 409L stainless steel using a Si3N4 tool. **Materials Science and Engineering: A**, [s.l.], v. 532, p. 476–479, 15 jan. 2012.

BARBINI, A.; CARSTENSEN, J.; DOS SANTOS, J. F. Influence of a non-rotating shoulder on heat generation, microstructure and mechanical properties of dissimilar AA2024/AA7050 FSW joints. **Journal of Materials Science & Technology**, 1 nov. 2017.

BARROS, I. F. DE. **Soldagem dissimilar do aço inoxidável ferrítico AISI 444 e do aço inoxidável austenítico AISI 316L por meio do processo TIG autógeno utilizando corrente pulsada**. 2013. Dissertação de Mestrado, Universidade Federal do Ceará, Fortaleza, 2013.

CAETANO, G. DE Q. et al. Influence of rotation speed and axial force on the friction stir welding of AISI 410S ferritic stainless steel. **Journal of Materials Processing Technology**, [s.l.], v. 262, p. 430–436, 1 dez. 2018.

CAETANO, G. DE Q. et al. Intergranular corrosion evaluation of friction stir welded AISI 410S ferritic stainless steel. **Journal of Materials Research and Technology**, fev. 2019.

CAETANO, G. Q. **Soldagem Similar de aços Inoxidaveis Ferríticos e Austenícios pelo Processo "Friction Stir Welding"**. Dissertação de Mestrado—Fortaleza: Universidade Federal do Ceará - UFC, 2016.

ÇAM, G. Friction stir welded structural materials: beyond Al-alloys. **International Materials Reviews**, [s.l.], v. 56, n. 1, p. 1–48, 1 jan. 2011.

ÇAM, G. et al. Applicability of Friction Stir Welding to steels. **Journal of Achievements in Materials and Manufacturing Engineering**, [s.l.], v. Vol. 80, n. nr 2, 2017.

CHATTERJEE, D. Effect of repeated warm rolling cold rolling and annealing on the microstructure and mechanical properties of AISI 301LN grade austenitic stainless steel. **Materials Today: Proceedings**, International Conference on Technological Advancements in Materials Science and Manufacturing. [s.l.], v. 46, p. 10604–10611, 1 jan. 2021

CHOI, D.-H. et al. Effect of fixed location variation in friction stir welding of steels with different carbon contents. **Science and Technology of Welding and Joining**, [s.l.], v. 15, n. 4, p. 299–304, 1 maio 2010.

CHUNG, Y. D. et al. Friction stir welding of high carbon steel with excellent toughness and ductility. **Scripta Materialia**, [s.l.], v. 63, n. 2, p. 223–226, 1 jul. 2010.

DEBROY, T.; BHADESHIA, H. Friction stir welding of dissimilar alloys–a perspective. **Science and Technology of Welding & Joining**, [s.l.]: [s.n.], 2013.

DOUDE, H. et al. Optimizing weld quality of a friction stir welded aluminum alloy. **Journal of Materials Processing Technology**, [s.l.], v. 222, p. 188–196, 2015.

DU, D. et al. Gradient characteristics and strength matching in friction stir welded joints of Fe–18Cr–16Mn–2Mo–0.85 N austenitic stainless steel. **Materials Science and Engineering: A**, [s.l.], v. 616, p. 246–251, 2014.

EMAMI, S. et al. Dissimilar friction stir welding of AISI 430 ferritic and AISI 304L austenitic stainless steels. **Archives of Civil and Mechanical Engineering**, [s.l.], v. 20, n. 4, p. 131, 18 out. 2020.

EMAMI, S.; SAEID, T. A comparative study on the microstructure development of friction stir welded 304 austenitic, 430 ferritic, and 2205 duplex stainless steels. **Materials Chemistry and Physics**, [s.l.], v. 237, p. 121833, 1 nov. 2019.

FIELD, D. P.; NELSON, T. W. Tool Geometry Dependence of Local Texture in Friction Stir Welds of 7050 Aluminum Plate. **Materials Science Forum**, [s.l.], v. 408–412, p. 1507–1512, 2002.

FONDA, R. W.; KNIPLING, K. E. Texture development in friction stir welds. **Science and Technology of Welding and Joining**, [s.l.], v. 16, n. 4, p. 288–294, 1 maio 2011.

FRATINI, L.; BUFFA, G. CDRX modelling in friction stir welding of aluminium alloys. **International Journal of Machine Tools and Manufacture**, [s.l.], v. 45, n. 10, p. 1188–1194, ago. 2005.

FU, X. et al. Effect of grain size and its uniformity on corrosion resistance of rolled 316L stainless steel by EBSD and TEM. **Materials Today Communications**, [s.l.], v. 25, p. 101429, 1 dez. 2020.

FUJII, H. et al. Friction stir welding of carbon steels. **Materials Science and Engineering: A**, [s.l.], v. 429, n. 1, p. 50–57, 15 ago. 2006.

GUO, G. et al. Effect of material position on microstructure and mechanical properties of friction stir welded dissimilar austenite–ferrite stainless steels joints. **Journal of Adhesion Science and Technology**, [s.l.], v. 35, n. 12, p. 1320–1336, 18 jun. 2021.

HAJIZADEH, M.; EMAMI, S.; SAEID, T. Influence of welding speed on microstructure formation in friction-stir-welded 304 austenitic stainless steels. **International Journal of Minerals, Metallurgy and Materials**, [s.l.], v. 27, n. 11, p. 1517–1524, 1 nov. 2020.

HAN, J. et al. Comparison of feasibility, microstructure and performance of hybrid laser arc, activated flux tungsten inert gas and friction stir welding for thick plate of innovative ultra-pure ferritic stainless steel. **Journal of Iron and Steel Research International**, [s.l.], v. 29, n. 4, p. 665–676, 1 abr. 2022.

HEIDARZADEH, A. et al. Friction stir welding/processing of metals and alloys: A comprehensive review on microstructural evolution. **Progress in Materials Science**, [s.l.], v. 117, p. 100752, 1 abr. 2021.

HUANG, K.; LOGÉ, R. E. A review of dynamic recrystallization phenomena in metallic materials. **Materials & Design**, [s.l.], v. 111, p. 548–574, 5 dez. 2016.

HUMPHREYS, F. J.; HATHERLY, M. **Recrystallization and Related Annealing Phenomena**. [s.l.] Elsevier, 2012.

JABRAEILI, R. et al. Effect of FSW process parameters on microstructure and mechanical properties of the dissimilar AA2024 Al alloy and 304 stainless steel joints. **Materials Science and Engineering: A**, [s.l.], v. 814, p. 140981, 13 maio 2021.

JAFARZADEGAN, M. et al. Microstructural characterization in dissimilar friction stir welding between 304 stainless steel and st37 steel. **Materials Characterization**, [s.l.], v. 74, p. 28–41, 1 dez. 2012.

JAFARZADEGAN, M. et al. Microstructure and Mechanical Properties of a Dissimilar Friction Stir Weld between Austenitic Stainless Steel and Low Carbon Steel. **Journal of Materials Science & Technology**, [s.l.], v. 29, n. 4, p. 367–372, 1 abr. 2013.

JOHNSON, P.; MURUGAN, N. Microstructure and mechanical properties of friction stir welded AISI321 stainless steel. **Journal of Materials Research and Technology**, [s.l.], v. 9, n. 3, p. 3967–3976, 1 maio 2020.

KADIAN, A. K.; BISWAS, P. The study of material flow behaviour in dissimilar material FSW of AA6061 and Cu-B370 alloys plates. **Journal of Manufacturing Processes**, [s.l.], v. 34, p. 96–105, 1 ago. 2018.

KASAI, H.; MORISADA, Y.; FUJII, H. Dissimilar FSW of immiscible materials: Steel/magnesium. **Materials Science and Engineering: A**, [s.l.], v. 624, p. 250–255, 29 jan. 2015.

KOKAWA, H. et al. Microstructures in Friction Stir Welded 304 Austenitic Stainless Steel. **Welding in the World**, [s.l.], v. 49, n. 3, p. 34–40, 1 mar. 2005.

LAKSHMINARAYANAN, A. K.; BALASUBRAMANIAN, V. An assessment of microstructure, hardness, tensile and impact strength of friction stir welded ferritic stainless steel joints. **Materials & Design**, [s.l.], v. 31, n. 10, p. 4592–4600, dez. 2010.

LIPPOLD, J. C.; KOTECKI, D. J. **Welding Metallurgy and Weldability of Stainless Steels**. 1 edition ed. Hoboken, NJ: Wiley-Interscience, 2005.

LIU, F. C. et al. A review of friction stir welding of steels: Tool, material flow, microstructure, and properties. **Journal of Materials Science & Technology**, [s.l.], v. 34, n. 1, p. 39–57, 1 jan. 2018.

MA, Z. Y. Friction stir processing technology: a review. **Metallurgical and Materials Transactions A**, [s.l.], v. 39, n. 3, p. 642–658, 2008.

MISHRA, R. S.; MA, Z. Y. Friction stir welding and processing. **Materials Science and Engineering: R: Reports**, [s.l.], v. 50, n. 1–2, p. 1–78, 31 ago. 2005.

MOHAN, D. G.; WU, C. A Review on Friction Stir Welding of Steels. **Chinese Journal of Mechanical Engineering**, [s.l.], v. 34, n. 1, p. 137, 14 dez. 2021.

MUKHERJEE, M.; PAL, T. K. Influence of Heat Input on Martensite Formation and Impact Property of Ferritic-Austenitic Dissimilar Weld Metals. **Journal of Materials Science & Technology**, [s.l.], v. 28, n. 4, p. 343–352, 1 abr. 2012.

MURR, L. E. A Review of FSW Research on Dissimilar Metal and Alloy Systems. **Journal of Materials Engineering and Performance**, [s.l.], v. 19, n. 8, p. 1071–1089, 1 nov. 2010.

PADILHA, A. F. **Materiais de engenharia: microestrutura e propriedades**. Edição Eletrônica ed. São Paulo: Hermus, 2000. v. V 1

PAN, H. et al. Understanding crystallographic orientation, microstructure and mechanical properties dependent interaction between recrystallization and phase transformation of a Fe–Al–Mn–Mo–C dual-phase steel. **Journal of Materials Research and Technology**, [s.l.], v. 15, p. 6190–6203, 1 nov. 2021.

PARK, S. H. C. et al. Rapid formation of the sigma phase in 304 stainless steel during friction stir welding. **Scripta Materialia**, [s.l.], v. 49, n. 12, p. 1175–1180, dez. 2003.

PORTER, D. A.; EASTERLING, K. E.; SHERIF, M. **Phase Transformations in Metals and Alloys,** Third Edition (Revised Reprint). [s.l.] CRC Press, 2009.

RAMIREZ, A. J. et al. **Effect of Tool Offset on Dissimilar Cu-AISI 316 Stainless Steel Friction Stir Welding**. The Twenty-first International Offshore and Polar Engineering Conference. **Anais**...International Society of Offshore and Polar Engineers, 2011. Disponível em: <https://www.onepetro.org/conference-paper/ISOPE-I-11-103>. Acesso em: 6 dez. 2016

SAKAI, T. et al. Dynamic and post-dynamic recrystallization under hot, cold and severe plastic deformation conditions. **Progress in Materials Science**, [s.l.], v. 60, p. 130–207, 1 mar. 2014.

SHIBATA, A. et al. Relation between martensite morphology and volume change accompanying fcc to bcc martensitic transformation in Fe–Ni–Co alloys. **Materials Science and Engineering: A**, Proceedings of the International Conference on Martensitic Transformations. [s.l.], v. 438–440, p. 241–245, 25 nov. 2006.

SILVA, C. C. et al. Austenitic and ferritic stainless steel dissimilar weld metal evaluation for the applications as-coating in the petroleum processing equipment. **Materials & Design**, [s.l.], v. 47, p. 1–8, 1 maio 2013.

SONG, C. et al. In Situ Observation of Phase Transformation and Structure Evolution of a 12 pct Cr Ferritic Stainless Steel. **Metallurgical and Materials Transactions B**, [s.l.], v. 43, n. 5, p. 1127–1137, 2012.

TANG, W. et al. Numerical and experimental investigation on friction stir welding of Ti- and Nb-modified 12 % Cr ferritic stainless steel. **Journal of Manufacturing Processes**, [s.l.], v. 59, p. 223–237, 1 nov. 2020.

THOMAS, W. M. et al. **Friction stir butt welding**. Cambridge, TWI, 1991.

THREADGILL, P. L. Terminology in friction stir welding. **Science and Technology of Welding and Joining**, [s.l.], v. 12, n. 4, p. 357–360, 1 maio 2007.

TONGNE, A. et al. Banded structures in friction stir welded Al alloys. **Journal of Materials Processing Technology**, [s.l.], v. 221, p. 269–278, 2015.

TSENG, C. C. et al. Fracture and the formation of sigma phase, M23C6, and austenite from delta-ferrite in an AlSl 304L stainless steel. **Metallurgical and Materials Transactions A**, [s.l.], v. 25, n. 6, p. 1147–1158, 1 jun. 1994.

VAN NIEKERK, C. J.; DU TOIT, M.; ERWEE, M. W. Sensitization Of Aisi 409 Ferritic Stainless Steel During Low Heat Input Arc Welding. **Welding in the World**, [s.l.], v. 56, n. 5–6, p. 54–64, maio 2012.

WANG, D. et al. Microstructural evolution and mechanical properties of friction stir welded joint of Fe–Cr–Mn–Mo–N austenite stainless steel. **Materials & Design**, [s.l.], v. 64, p. 355–359, 2014.

WANG, L. et al. Effect of δ-ferrite on the low-cycle fatigue behavior of the 0Cr17Ni10Mn5Mo2 steel. **Materialia**, [s.l.], v. 12, p. 100711, 1 ago. 2020.

XU, Y. et al. Effect of δ-ferrite on stress corrosion cracking of CF8A austenitic stainless steels in a simulated pressurised water reactor environment. **Journal of Materials Research and Technology**, [s.l.], v. 8, n. 6, p. 6420–6426, 1 nov. 2019.

ZHENG, H. et al. Effect of carbon content on microstructure and mechanical properties of hot-rolled low carbon 12Cr–Ni stainless steel. **Materials Science and Engineering: A**, [s.l.], v. 527, n. 27, p. 7407–7412, 25 out. 2010.

5 CHAPTER 5: Mechanical properties of dissimilar AISI 304L and AISI 410S stainless steel joints by the friction stir welding

5.1 Abstract

The mechanical properties of conditions welded by the FSW process, keeping the rotation speed at 450 rpm and increasing the axial force from 25 kN to 40 kN, between AISI 410S and 304L steels, were evaluated through bending, microhardness and uniaxial tensile tests. The bending results show an increase in the supported angle until the propagation of cracks in the root of the welds, as the axial force increases, with conditions 1 and 2 having the smallest angles due to the presence of flaws at the root of the joints. The microhardness maps for Conditions 3 and 4 showed little variation in microhardness values between BM, HAZ e TMAZ on the retreating side, however an increase of approximately 200 HV was observed between BM and SZ on the advancing side, due to the intense grain refining and the martensitic transformations occurred in the AISI 410S steel. The uniaxial tensile test showed yield strength and tensile strength limit values superior to that found in the base metal and stipulated by the ASTM A240 standard for AISI 410S steel. Thus, one can conclude that increasing the axial force to 40 kN, keeping the rotation speed constant at 450 rpm, in condition 4, enabled the constitution of a FSW joint dissimilar between AISI 304L and AISI 410S steel with high bending angle until crack propagation at the joint root, increase in microhardness values in HAZ, TMAZ and SZ and better results in the tensile test in relation to the base metal of the AISI 410S steel.

Keywords: Friction stir welding; Stainless Steels; Bending; Microhardness; The Uniaxial tensile Test.

5.2 Introduction

Among stainless steels, austenitic are the most used commercially due to their good combination of mechanical and corrosion resistance, while ferritics provide approximately the same corrosion resistance, but according to SMITH, W. F. (1993) have lower ductility, toughness and weldability when compared to austenitic stainless steels (ASS), especially due to lower plasticity and intergranular corrosion susceptibility. A great advantage of ferritic stainless steels (FSS) is the reduction or absence of nickel in

its composition, which considerably lowers the price of ferritic stainless steels compared to austenitic stainless steels as reported by SILVA et al. (2007) and LO et al. (2009). This aspect has attracted the attention of the steel industry, in order to develop new processing routes for these steels, aiming at improving the chemical composition, as noted by DU et al. (2010), SIQUEIRA et al. (2011) and COSTA et al. (2017), the refinement of grains by different recrystallization mechanisms, as proposed by RODRIGUES et al. (2017) and BRAGA et al. (2016), and the introduction of texture components that can improve the properties at the end of processing, according to SIQUEIRA et al. (2008), RODRIGUES et al. (2017a) and RODRIGUES et al. (2019).

Due to the lower cost and the improvements achieved in relation to its properties, these steels have become quite competitive in replacement of carbon steels and some austenitic stainless steels. RODRIGUES et al. (2019) highlights the application of FSS in kitchen utensils, automotive components, heaters, and equipment for the nitric acid processing. While CASHELL and BADDOO, (2014) highlight the use of FSS in vehicle chassis, railway wagons, conveyors, chutes, tanks and walkways in sectors such as road and rail transport, water distribution, power generation and mining. However, these steels have also been considered in other sectors such as the oil and gas industry, as reported by SILVA et al. (2007) and MACHADO et al. (2006).

One of the factors that make the application of ferritic stainless steels less effective in the industry is related to the metallurgical problems arising from the fusion welding of these steels. When subjected to thermal welding cycles, these materials undergo metallurgical changes that compromise their weldability, corrosion resistance and the mechanical response of the welds as verified by FOLKHARD, (1988) and by GREEF and TOIT, (2006). Ductility and toughness are properties especially affected, as they are directly related to grain size and the embrittlement of grain boundaries by deleterious phases in the heat-affected zone and fusion zone for fusion welding processes, as it shows SILVA et al. (2008).

SILVA et al. (2006) evaluated the changes in the HAZ of an AISI 410S ferritic stainless steel subjected to different heat inputs in SMAW fusion welding, and observed that in addition to the formation of martensite, there were zones with excessive growth of ferritic grains, which causes a decrease in hardness and compromises mechanical strength. Similar microstructural changes are reported for AISI 410S steel when welded

by other processes such as plasma and laser, as highlighted by KÖSE and TOPAL, (2019a) and (2019b).

Another problem verified was the precipitation of chromium nitrides (Cr_2N) and carbides ($Cr_{23}C_6$) finely dispersed in the HAZ. These nitrides (Cr_2N) precipitated so much intragranular in the ferrite grains that underwent growth, and intergranularly in grain and sub-grain ferrite-ferrite boundaries, or in a ferrite-martensite interface, may cause an embrittlement and intergranular corrosion effect. Finally, the precipitation of carbides $Cr_{23}C_6$ is also reported in these types of steel containing 12% Cr, causing the sensitization of grain boundaries and the consequent loss of corrosion resistance, as highlighted by VAN NIEKERK et al. (2012), and that can evolve into catastrophic failures, as highlighted by KHATTAK et al. (2020).

However, in recent decades the friction stir welding (FSW), a solid state welding process developed in The Welding Institute (TWI) by THOMAS et al. (1991) in Cambridge, England, revolutionized the joining of materials considered non-weldable or with low weldability. MISHRA e MA, (2005) report that this process uses a non-consumable tool that rotates and penetrates the joint, resulting in heating and plastic deformation of the materials to be joined, which can be heated to temperatures below those experienced in fusion welding. Since then, numerous advances have been made on this manufacturing process, enabling its expansion of materials that can be welded, the emergence of new process variants and their application in different sectors of the industry, as reported by NANDAN et al. (2008).

Among the advantages commonly attributed to the FSW process, stand out: good strength and ductility of the welds, minimal residual stress and distortion, absence of defects related to the melting of the material, smaller heat affected zone and microstructure with refined grains that increase the tensile resistance and fatigue life as proposed by BILGIN and MERAN, (2012), DEBROY and BHADESHIA, (2013) and SATHIYA et al. (2006). LIU et al. (2018) reports that compared to traditional fusion welding, FSW of steels exhibits great advantages due to the efficient control of the welding temperature and/or cooling rate, providing that unfavorable phase transformations that usually occur during traditional welding can be avoided and favorable phase fractions can be maintained in the welding zone, thus avoiding the property degradations commonly associated with fusion welding. However, for FSS it is not always possible to avoid frequent metallurgical changes such as the formation of

martensite during FSW welding, as reported by LAKSHMINARAYANAN and BALASUBRAMANIAN, (2011) and CAETANO et al. (2019).

However, it is possible to optimize the parameters to obtain some improvements, as reported by (CAETANO et al., 2019), whose proper choice of parameters in FSW welding of AISI 410S steel minimized the risk of sensitization caused by $Cr_{23}C_6$ carbides. In the same way, LAKSHMINARAYANAN and BALASUBRAMANIAN, (2010) evaluating the microstructure and mechanical properties of similar joints of AISI 409M ferritic stainless steel report that the coarse ferrite grains of the base material are changed to a very fine duplex structure of ferrite and martensite in the stir zone due to the rapid cooling rate and high plastic deformation caused by friction and material stir. This refinement contributes to great results in relation to hardness, tensile strength, and impact strength of welded joints.

Austenitic stainless steels, on the other hand, due to their good corrosion resistance, high mechanical strength at high temperature, good toughness even at low temperatures and better weldability, are widely used in industry. however, problems can occur in the welding of these steels due to some metallurgical changes such as segregation of impurities to the grain boundaries, excessive formation of δ-ferrite, precipitation of deleterious phases such as χ and σ, in addition to the sensitization caused by $M_{23}C_6$ carbides, as stand out SHANKAR et al. (2003), LIPPOLD and KOTECKI, (2005) and RODRIGUES et al. (2008).

Numerous situations in the industry can be optimized by partially replacing austenitic stainless steels with ferritic stainless steels, with each steel being applied in certain sections depending on the required properties. For this reason, dissimilar welding of steels is of great importance in the manufacture of components and equipment. The applications of the FSW process in similar welds of AISI 304 austenitic stainless steel have been reported in the literature since the 2000s, with studies carried out by KOKAWA et al. (2005), MERAN and CANYURT, (2011, 2013), MERAN, KOVAN and ALPTEKIN, (2007), PARK et al. (2003, 2004) and REYNOLDS et al. (2003). Although the process did not prevent the formation of deleterious phases at the advancing side of the stir zone, an important aspect for the mechanical properties success of the produced welds is the intense grain refining resulting from dynamic recrystallization, as observed by PARK et al. (2003).

In the dissimilar welding by the FSW process MURR, (2010) points out that the complex and intercalated flow, which is a characteristic for many dissimilar materials welds by FSW, causes fluctuations in microindentation hardness profiles, which strongly impact in the mechanical properties, depending on the advancing versus retreating side materials. EMAMI et al. (2020), welding ferritic and austenitic stainless steel by FSW, verified that despite the yield strength of the joint is comparable with that of the austenitic sample, the elongation percent of the welded sample significantly decreased. This fact is also noted by JAFARZADEGAN et al. (2013), that analyzing a dissimilar friction stir welding joint between a austenitic stainless steel and a low carbon steel, verified in the joint a decrease of around 50% in the elongation, in relation the steel with lower mechanical resistance, despite the high tensile strengths.

LIU et al. (2018) have considered that an progress has been achieved in friction stir welding (FSW) of steels in aspect of tool fabrication, microstructure control and properties evaluation in the past two decades, however advances in FSW welding dissimilar between ferritic and austenitic stainless steels are still incipient and more detailed information about the influence of process parameters on the mechanical properties of these joints becomes a topic of strong scientific and technological appeal. Thus, this work aims to evaluate the effect of FSW welding parameters on the mechanical properties of dissimilar joints between AISI 304L austenitic stainless steel and AISI 410S ferritic stainless steel, evaluating the performance of welded joints through bending, microhardness and uniaxial tensile tests.

5.3 Materials and Methods

The welds were made using 4-mm-thick plates of AISI 410S ferritic stainless steel and AISI 304L austenitic stainless. The materials' chemical composition was determined by optical emission spectroscopy (Shimadzu model PA7000 Japan) and is presented in Table 5.1.

Table 5.1 - Chemical composition of the base metals (% weight).

Material	Elements											
	C	Si	Mn	P	S	Cr	Ni	Mo	Cu	Co	N	Fe
410S	0.025	0.37	0.30	0.023	<0.010	12.8	0.21	0.01	0.21	0.02	0.033	Bal.
304L	0.026	0.32	1.21	0.029	<0.010	18.5	7.24	0.29	0.34	0.15	0.058	Bal.

Source: The author.

The FSW process joined the samples at Helmholtz-Zentrum Geesthacht (HZG) in Germany. All welds were made using the HZG Gantry System with a butt joint configuration, as shown in Fig. 5.1. An inert gas (Ar) injection system was used to protect the material during the process at temperatures above 535 °C; these stainless steels react with the atmosphere. Welds were performed in load control mode with an integrated system to record process data such as penetration depth, rotational speed, torque, tool forces, and tool position over time.

The welds were made with a tool of polycrystalline cubic boron nitride (PCBN). The tool had a conical diameter of 25 mm with a conical pin with a 9.2 mm diameter and a length of 3.7 mm. The pin had a conical surface with negative recesses, which were in the form of a spiral concerning the tool's axis of symmetry.

Figure 5.1 – Dissimilar butt joint configuration between AISI 410S and AISI 304L steels.

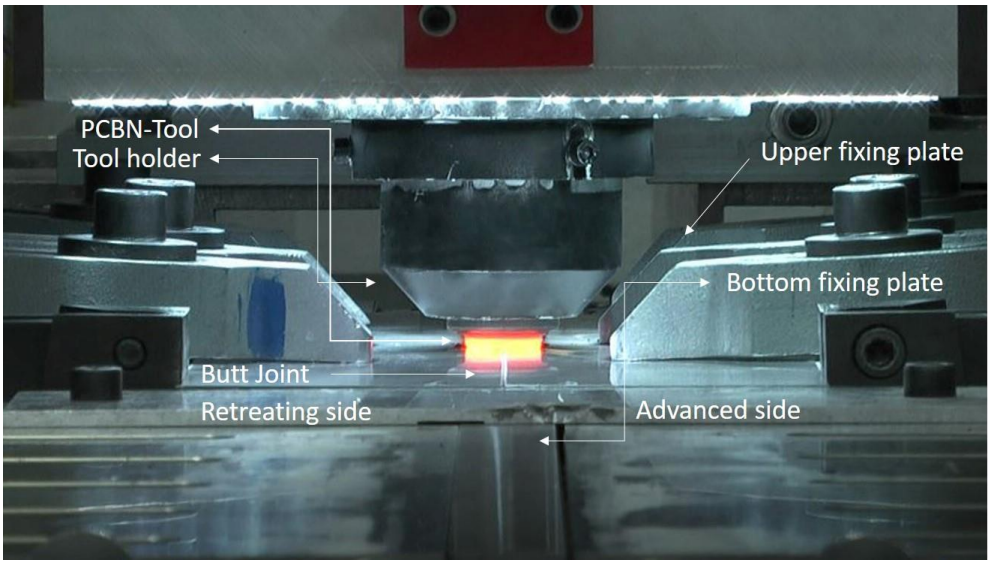

Source: CAETANO et al. (2019).

As shown in Chapter 02, preliminary tests were performed to evaluate the behavior of steels to the effects of different phenomena between the advancing side, where the direction of travel is the same as the direction of rotation of the tool, and the retreating side that has these opposite directions in the FSW welding. After performing the tests, the results of this study indicated that the condition that results in the best results for consolidation of a defect-free welded joint it is with AISI 304L austenitic stainless steel

placed on the retreating side and AISI 410S steel placed on the advancing side, as this gives a better surface finish and better joint consolidation.

After choosing the appropriate steel for the FSW joint's advancing and retreating side, four welding conditions were analyzed to evaluate the influence of process parameters on heat generation defect formation and mechanical properties. Under these conditions, the axial force was varied from 25 to 40 kN, maintaining the rotational speed at 450 rpm, the tool angle at 0º, and the welding speed at 1 mm/s, as shown in Table 5.2.

Table 5.2 – Welding Parameters for Dissimilar FSW Butt Welding of AISI 410S/304L Steels

Condition	Rotation Speed (rpm)	Axial Force (kN)	Advancing Side	Retreating Side
1	450	25	410S	304L
2	450	30	410S	304L
3	450	35	410S	304L
4	450	40	410S	304L

Source: The author.

Mechanical tests were performed in order to determine the mechanical properties and correlate them with the microstructural characteristics observed along the joints. For this, bending, Vickers microhardness and uniaxial tensile tests were performed, all analysed at room temperature. The bending test was performed as a qualitative test in order to analyse the ductility of the samples. This was the first step in evaluating the quality of the FSW weld and selecting the samples that will go to the next mechanical test. Basically, the expected answer for this test is that the sample bends more than 90º degrees, without root flaws propagating in the weld. The distance between supports was based on the standard ASTM E290-09.

Vickers microhardness maps were performed on the cross section of the welded joints according to the standard ASTM E384-99, for an evaluation of changes in the microhardness of the material resulting from the welding process. The distance between each indentation was 500 µm, by applying a charge of 0,1 kgf (HV 0,1) during 13 s. The microhardness lines were positioned to cover all regions of the weld. The microhardness meter Leco LM110AT was used in the measurements, which features a fully automatic system integrated to the software Comerstone AMH55 to obtain the data.

For the tensile tests, the specimens were produced with the dimensions established by the standard ASTM E8M-04 for tensile tests of metallic materials. The welded joint is

located exactly in the middle of the specimen. The specimens were properly fixed in a universal mechanical testing machine Zwick/Roell, integrated into the operating platform TestXpert to obtain the data. The tests were carried out with five repetitions for each welding condition and for the base material. Tests were performed at room temperature, with a constant speed of 1mm/min. The deformation was measured by MTS strain gauge of 50 mm.

5.4 Results and Discussions

5.4.1 Bending Test

The bending test was used to evaluate the quality of dissimilar welds produced between AISI 304L austenitic stainless steel and AISI 410S ferritic stainless steel, by the FSW process as a function of ductility, evidencing their ability to resist the cracks propagation in the root of the welds during the bending. For the Fig. 5.2 it is possible to verify that the combination of parameters used in Condition 1 and Condition 2, both welded at a rotation speed of 450 rpm and with a reduction in axial force to 25 kN and 35 kN, respectively, resulted in welds capable of withstanding the smallest bending angles. With Condition 2 supporting an angle of 40° and Condition 1 an angle of only 14° until crack propagation at the joint root.

Based on the defect analysis carried out in Chapter 2, it is evident that both in Condition 1 and in Condition 2 were found root flaws with the observation of a line, referring to the interface between the two butt joint plates and a lack of cohesion between the two steels forming a recess in the joint root, being associated with insufficient penetration of the tool, as reported by EDWARDS and RAMULU, (2015).

Another aggravating factor found for Condition 1 welded with an axial force of 25 kN was the presence of small voids in the stir zone in a region close to the weld root. This defect, as noted by TONGNE et al., (2015), is attributed to less interaction between tool and material, due to low axial force and consequent reduction in friction force and heat to achieve a plasticizing state, suitable for material flow during the FSW process. DOUDE et al. (2015), shows that these voids in the agitation zone in regions close to the weld root indicate the use of parameters with values below the recommended ideal set for consolidation of a defect-free FSW joint and this is due to the use of low rotational speed and low axial force.

Figure 5.2 – Samples of dissimilar joints of AISI 410S/304L steels, produced by the FSW process, submitted to bending test.

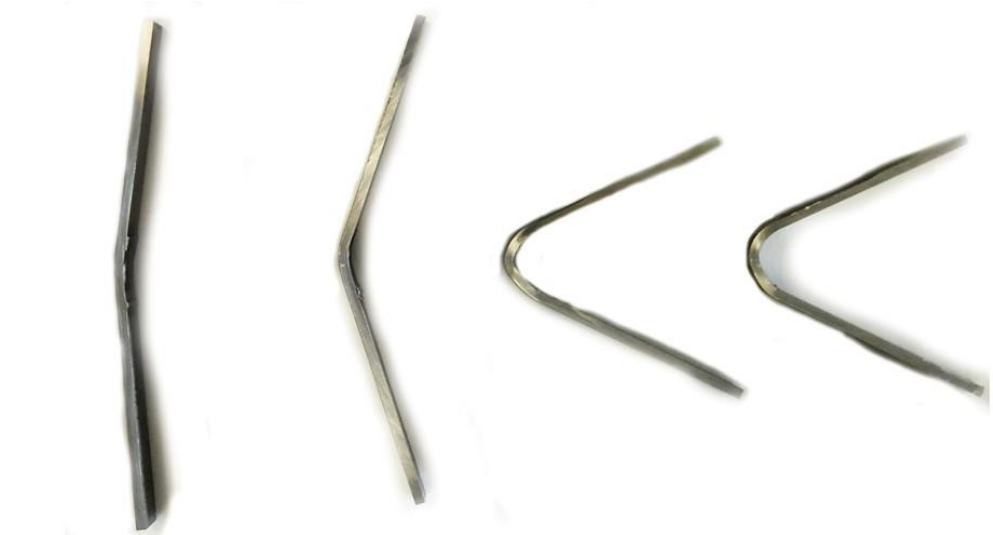

Condition 1		Condition 2		Condition 3		Condition 4	
450 RPM 25 kN	14°	450 RPM 30 kN	40°	450 RPM 35 kN	128°	450 RPM 40 kN	134°

Source: The author.

Therefore, the combination of rotation speed at 450 rpm, welding speed at 1 mm/s and axial force of 30 kN for Condition 2 and 25 kN for Condition 1 constituted an inadequate combination of parameters, with low quality of the FSW dissimilar joint between the AISI 410S and AISI 304L steels, with the presence of root flaws of both joints and voids near the root for Condition 1, being detrimental to the properties of the weld, as detected already in the bending test.

Condition 3 and Condition 4, welded with axial force of 35 kN and 40 kN, respectively, withstood bending angles of 128° and 134° until crack propagation at the root of the joints, these values, higher than the 90° established as a minimum, and much higher than the values measured for the previous conditions. Thus, greater bending angles were evidenced as the axial force increases, as noted in Chapter 2, the increase in axial force contributes for the material flow to reach a more adequate state of plasticization, due to the higher heat intensity obtained, providing the absence of defects such as root flaws and voids and also a greater contact between the two steels in the stir zone with the increase in the number of inserts, thus allowing greater bending angles until the propagation of cracks at the root of the welds.

5.4.2 Microhardness

Based on the result of the bending tests, which was the first indication of the mechanical evaluation, of the dissimilar FSW welds produced between AISI 304L austenitic stainless steel and AISI 410S ferritic stainless steel. Conditions 3 and 4 were selected, which presented a better relationship between surface finish, absence of defects and bending angle and, therefore, capable of being submitted to microhardness tests.

The microhardness maps shown in Fig. 5.3 indicate for both conditions a base metal zone on the retreating side composed of AISI 304L steel with an average microhardness of 190 ± 12 HV and on the advancing side a base metal zone composed of AISI 410S steel with an average microhardness of 140 ± 15 HV.

Figure 5.3 – Microhardness maps of dissimilar joints of AISI 410S/304L steels, produced by the FSW process. (a) Condition 3 (b) Condition 4.

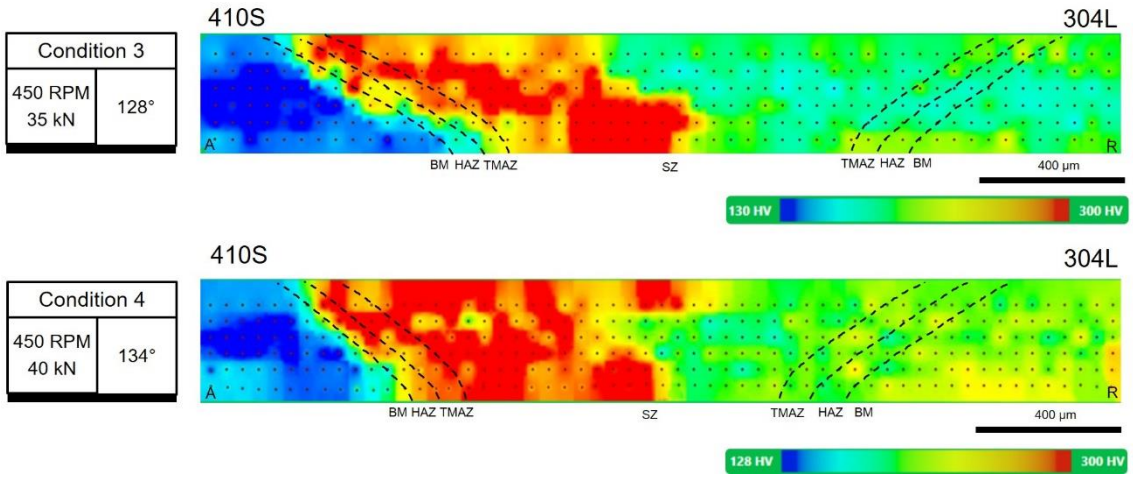

Source: The author.

Between base metal (BM), heat affected zone (HAZ) and thermomechanically affected zone (TMAZ) on the retreating side, where the AISI 304L steel is positioned, few changes in microhardness values are observed for both Condition 3 and Condition 4. The microstructural analysis, carried out in Chapter 04, shows that the TMAZ of AISI 304L steel has austenitic grains affected by both the heat rate and the deformation induced by the tool rotation and friction during the FSW process, ceasing to be equiaxial with faceted grain contours, to present a microstructure with serrated and deformed austenitic grains following the direction of rotation of the tool, as presented for Condition 4 in the

Fig. 5.4. However, these microstructural transformations in retreating side was irrelevant in changing the microhardness values. KOKAWA et al. (2005) observed in similar FSW welds of AISI 304 steel that the TMAZ of the advancing side showed the maximum hardness, which was attributed to the slightly finer grain structure having a relatively higher density of sub-boundaries and dislocations, however, it is not possible to carry out this analysis in conditions 3 and 4, as the AISI 410S steel is positioned on the advancing side.

Figure 5.4 - (a) Cross-section macrograph of the Condition 4, welded with an axial force of 40 kN. (b) BM of AISI 304L steel, Condition 4, (500x). (c) TMAZ of AISI 304L steel, Condition 4, (500x).

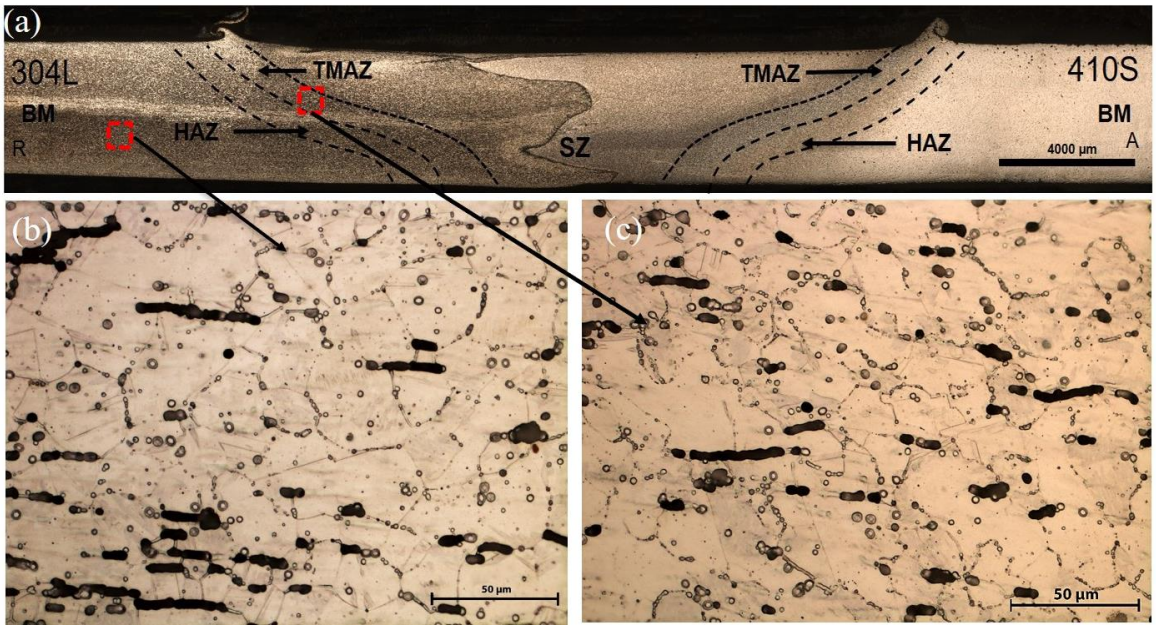

Source: The author.

Between Condition 3 and Condition 4, it is possible to observe regions with higher microhardness in the HAZ, TMAZ, and SZ on the retreating side of Condition 4 compared with Condition 3, because, as shown JAFARZADEGAN et al. (2013) in dissimilar FSW welding of steels, positioning AISI 304 steel on the retreating side, the increase in recrystallization driven by the increase in axial force provides greater grain refinement and, consequently, higher microhardness values.

In HAZ, TMAZ and SZ on the advancing side, which comprises AISI 410S steel, it is possible to observe regions with microhardness values greater than 340 HV. This considerable increase in microhardness values on the advancing side occurs due to the

considerable grain refining resulting from the dynamic recrystallisation seen in TMAZ and SZ and also due to the martensitic transformations that occurred in HAZ, TMAZ and SZ. As detailed in Chapter 04, in FSW welding of ferritic stainless steels whose chemical composition is not able to completely stabilize the ferrite, any region exposed to temperatures between 400 and 800 °C, where partial transformation of ferrite into austenite occurs, whose nucleation occurs along the grain boundaries of the ferrite, the austenite formed on heating transforms into martensite on subsequent cooling entre 8.5º C/s a 2.2º C/s, giving rise to the biphasic microstructure as also noted by SONG et al. (2012) and observed in the HAZ, TMAZ and SZ of the AISI 410S steel, as shown by Fig 5.

As reported in Chapter 04, for the four conditions evaluated, the TMAZ of advancing side composed of AISI 410S ferritic stainless steel, has ferritic grains deformed by the intense deformation induced by tool rotation, elongated following the direction of tool rotation and surrounded by martensite, as presented in Fig.5.5b and Fig. 55d. As the axial force increases from 25 kN to 30 kN, 35 kN and 40 kN, an increase in the amount of martensite surrounding the ferritic grains in both HAZ, TMAZ and SZ of AISI 410S steel is noticeable, occurring as a result of changes in thermal cycles and in the intensity of plastic deformation with increased of axial force. This fact is proven by the microhardness map for the TMAZ on the advancing side between conditions 3 and 4, since Condition 4, presents higher microhardness values, both in the region of contact with the tool shoulder and in the region closest to the weld root, with Condition 3, presenting high microhardness values concentrated in the central region of the weld.

Second FRATINI and BUFFA, (2005) and THREADGILL, (2007), in the stir zone (SZ), corresponding to the central region of the FSW welds, the grain and sub-grain boundaries favor the formation of new and fine equiaxed grains, due to recrystallization caused by the combined action of the tool's shoulder and pin, generating frictional heat and plastic deformation simultaneously. In Condition 3 and Condition 4 the combined action of grain refining and martensitic transformations in the stir zone are evidenced in the microhardness maps, as it is in this region where the highest microhardness peaks are found, with the highest values observed for Condition 4, welded with the highest axial force and presenting microhardness peaks of 362 HV in a region closer to the weld surface, as it shows LIU et al. (2010) this surface region of the stir zone is subject to higher temperatures and more intense deformations imposed by the action of the tool

shoulder. In the case of FSS, this temperature increase in the stir zone determines a greater potential for austenitization and consequent intensity of martensitic transformation in cooling, contributing to the increase in microhardness values.

Figure 5.5 – (a) Cross-section macrograph of the Condition 3 (b) TMAZ of AISI 410S steel, Condition 3, welded with an axial force of 35 kN (200x). (c) HAZ of AISI 410S steel, Condition 1, welded with an axial force of 35 kN (200x). (d)TMAZ of AISI 410S steel, Condition 4, welded with an axial force of 40 kN (200x). (e) HAZ of AISI 410S steel, Condition 4, welded with an axial force of 40 kN (200x). (f) Cross-section macrograph of the Condition 4.

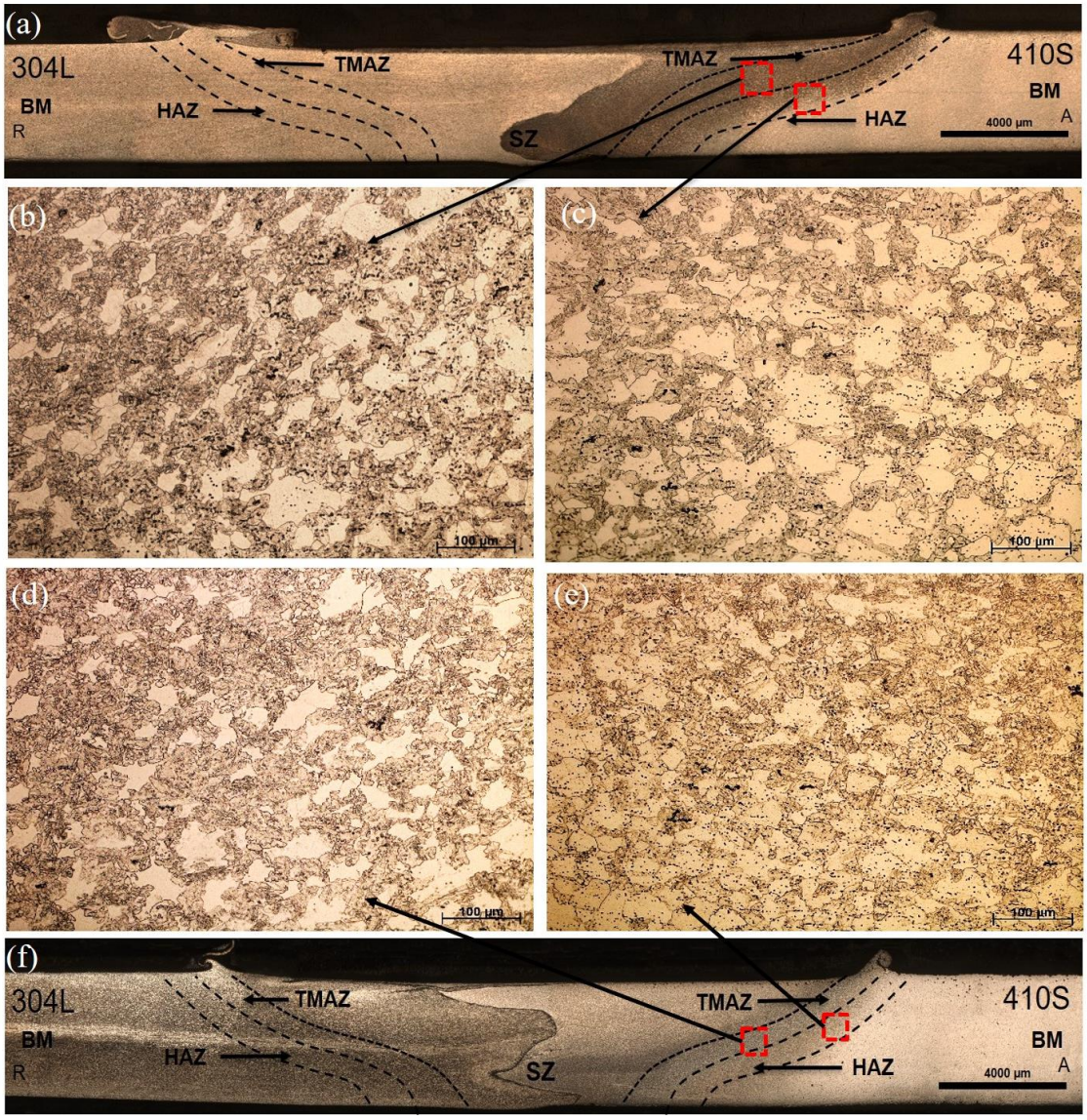

Source: The author.

5.4.3 Tensile Test

Conditions 3 and 4 were also submitted to the uniaxial tensile test, with the load applied transversely to the weld direction and, consequently, the rolling direction. The Fig. 4 presents the engineering stress versus strain curves for each of the conditions evaluated, as well as for the base metal. Yield strength, tensile strength limit and elongation values are presented in Table 5.3, in addition to the values established in the ASTM A240 standard for these steels. As you can see in the Table 5.3, both conditions had a yield strength higher than that found in the ASTM A240 standard, however a little lower than the base metal of AISI 304L and AISI 410S steels. The tensile strength values for Condition 3 and Condition 4 are higher than ASTM A240 and base metal for AISI 410S steel, however lower than that observed for the base metal of AISI 304L steel. The tensile strength observed for condition 4 is greater than that found by REYNOLDS et al. (2003) in similar FSW welds of AISI 304L, using parameters close to the one used in condition 4, and the elevated strength of the weld metals relative to the base metal was consistent with the observation of refined grains in the weld nuggets.

In relation to the yield strength, tensile strength and elongation, the Condition 4, welded with greater axial force, showed the best results. This fact can be correlated with the microstructural analysis performed in Chapter 4, which shows that the greater potential for martensitic transformation, with the greater intensity of plastic deformation and consequent intensity of recrystallization of Condition 4 contributed to greater grain refining and cohesion between the steels in the stir zone. Condition 4 presents yield strength and tensile strength values higher than those stipulated by ASTM A240 and the base metal of AISI 410S steel and an elongation very close to 22%, indicated by the standard for flat rolled AISI 410S steel, considering the standard deviation.

The lowest mechanical performance, as shown in Fig. 5.5 was observed for the elongation achieved by the specimens, with values for conditions 3 and 4 below both the standard and the base metal of AISI 304L and 410S steels. In all specimens, the fracture occurred in the base metal of AISI 410S steel, because AISI 304L steel has a high degree of hardening, due to its FCC structure, significantly increasing its strength before breaking, a fact not presented in AISI 410S steel. The low elongation in relation to the base metal of austenitic stainless steel in dissimilar joints was also observed by WANG et al. (2019), that positioning AISI 304 steel on the retreating side of a dissimilar FSW joint, observed the elongation in 17%, which shows a decrease of around 50% in relation

the base metal of the low carbon steel positioned on the advancing side, however without compromising of the yield strength and tensile strength as observed for Condition 4. In similar FSW welds AHN et al. (2012) noted for the AISI 409L ferritic stainless steel an elongation of approximately 17% which is half elongation of the base metal, KIM et al. (2017) evaluating joint properties of 430M2 ferritic stainless steel welded by FSW find a notably decreased elongation of 19.6% compared to the base metal. These facts prove that both in similar and dissimilar FSW welds of these steels the microstructural changes responsible for the increase in yield strength and tensile strength are not able to ensure satisfactory elongations.

Table 5.3 - Mechanical properties obtained from tensile tests for dissimilar joints of AISI 410S/304L steels, produced by the FSW process.

Condition	Yield Strength (MPa)	Tensile strength (MPa)	Elogation (%)
3	298.1 ± 1.0	431,4 ± 0.8	13,2 ± 1.7
4	307.2 ± 1.7	441,5 ± 15.3	18,9 ± 5.1
304L BM	320.6 ± 1.2	722,8 ± 4.2	58,0 ± 1.2
410S BM	312 ± 1.1	429 ± 1.5	44,37 ± 0.4
304L ASTM A240	170	485	40
410S ASTM A240	205	415	22

Source: The author.

Figure 5.6 - Engineering tensile stress-strain diagram comparing the curve for FSW Condition 3 and Condition 4 with AISI 304L e 410S base metal.

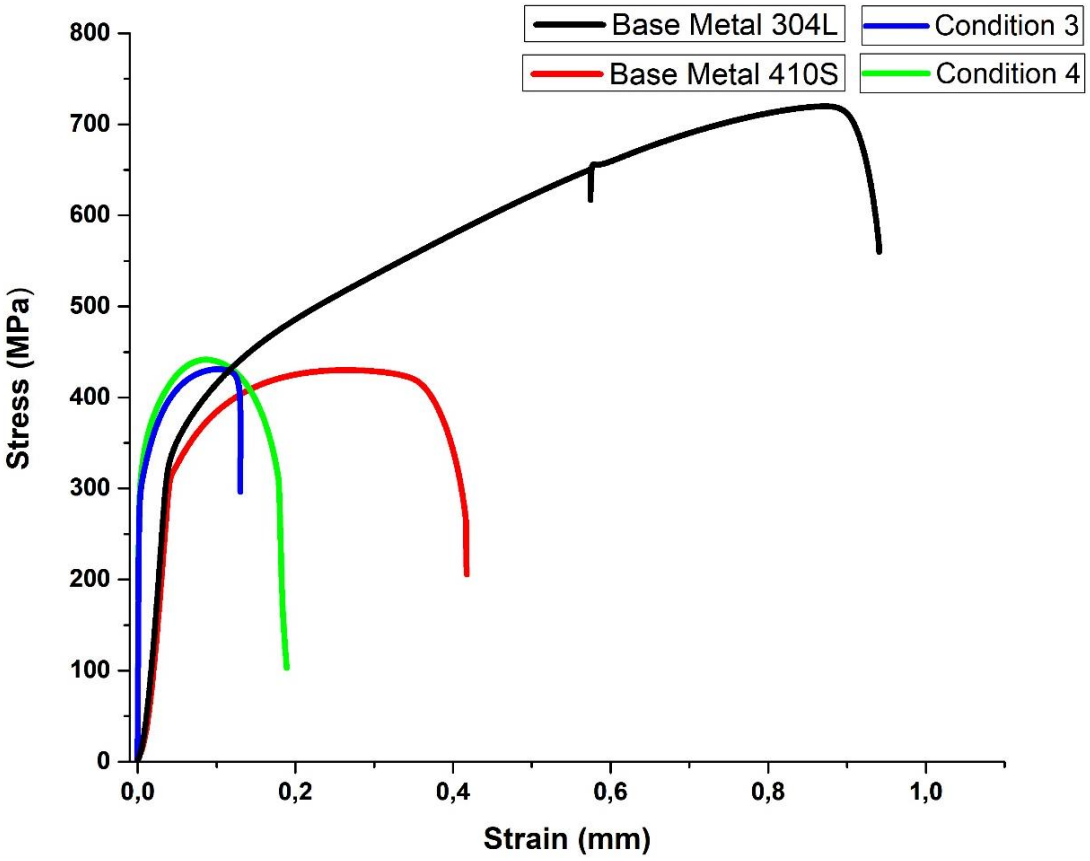

Source: The author.

Therefore, the analysis of the different weld conditions shows that it is possible to produce dissimilar joints of AISI 410S ferritic stainless steel and AISI 304L austenitic stainless steel by the FSW process with satisfactory mechanical properties compared to those found in the base metal for AISI 410S ferritic stainless steel. The increase of the axial force to 40 kN, keeping the rotation speed constant at 450 rpm, in condition 4, not only allowed greater bending angles until the propagation of cracks at the root of the joints, as an increase in microhardness values in the stir zone and a better yield strength and tensile strength limit compared to AISI 410S steel, in addition to a percentage elongation very close to the value recommended by the standard.

5.5 Conclusions

Based on the experimental results of the evaluation of the mechanical properties of dissimilar joints between AISI 410S ferritic stainless steel and AISI 304L austenitic stainless steel, produced by the FSW process, it was possible to conclude that:

1. By increasing the axial force to 35 kN and 40 kN and keeping the rotation speed at 450 rpm, it is possible to produce a dissimilar FSW joint between AISI 410S ferritic stainless steel and AISI 304L austenitic stainless steel with high bending angle, high values of microhardness and good tensile strength properties
2. Larger bending angles were evidenced as the axial force increased from 25 kN to 40 kN, with the smallest angles found for Condition 1 and Condition 2, due to root flaws in the joints.
3. The TMAZ and SZ on the advancing side, where the AISI 410S steel is located, has regions with microhardness values greater than 340 HV and greater than those found on the retreating side, due to the excessive amount of martensite and refined ferritic grains in both regions, due to the intense dynamic recrystallization and the cooling rates achieved.
4. The combined action of grain refining and martensitic transformations in the SZ are evidenced in the microhardness maps, as it is in this region where the highest microhardness peaks are found.
5. The highest microhardness values were observed for Condition 4, welded with the highest axial force and showing microhardness peaks of 362 HV in a region closer to the weld surface and the contact interface between the material and the tool shoulder.
6. The uniaxial tensile test of Condition 4 presents yield strength and tensile strength limit values higher than those stipulated by ASTM A240 to the base metal of AISI 410S steel and an elongation very close to 22%, indicated by the standard, considering the deviation achieved.

5.6 Acknowledgments

The authors are grateful for the support given by the following Institutions: Universidade Federal do Ceará, Laboratório de Pesquisa e Tecnologia em Soldagem (LPTS), in Brazil, and the Solid State Joining Processes, Helmholtz-Zentrum Geesthacht (HZG), in Germany. This study was financed in part by the Coordenação de Aperfeiçoamento de Pessoal de Nível Superior - Brasil (CAPES) - Finance Code 001, Brazilian funding agencies CNPq (Universal 472185/2011-0), and FUNCAP and CAPES (Project CI1-0050-00049.01.00/11 – International Cooperation).

5.7 References

AGUIAR LIMA RODRIGUES, C. et al. Mechanical and metallurgical evaluation of ANSI/AWS A5.4-06 E309 weld metals. **Soldagem & inspeção**, [s.l.], v. 13, p. 32–45, 1 jan. 2008.

AHN, B. W. et al. Microstructures and properties of friction stir welded 409L stainless steel using a Si 3 N 4 tool. **Materials Science and Engineering: A**, [s.l.], v. 532, p. 476–479, 2012.

BILGIN, M. B.; MERAN, C. The effect of tool rotational and traverse speed on friction stir weldability of AISI 430 ferritic stainless steels. **Materials & Design**, [s.l.], v. 33, p. 376–383, jan. 2012.

CAETANO, G. DE Q. et al. Intergranular corrosion evaluation of friction stir welded AISI 410S ferritic stainless steel. **Journal of Materials Research and Technology**, fev. 2019.

CASHELL, K.; BADDOO, N. **Ferritic stainless steels in structural applications**. [s.l.]: [s.n.], 2014.

COSTA, R. J. G. et al. Comparative Study of Microstructure, Texture, and Formability Between 11CrTi and 11CrTi+Nb ASTM 409 Ferritic Stainless Steel. **Materials Research**, [s.l.], v. 20, p. 1593–1599, 31 ago. 2017.

DEBROY, T.; BHADESHIA, H. Friction stir welding of dissimilar alloys–a perspective. **Science and Technology of Welding & Joining**, [s.l.]: [s.n.], 2013.

DOUDE, H. et al. Optimizing weld quality of a friction stir welded aluminum alloy. **Journal of Materials Processing Technology**, [s.l.], v. 222, p. 188–196, 2015.

DU, W. et al. Microstructure, Texture, and Formability of Nb+Ti Stabilized High Purity Ferritic Stainless Steel. **Journal of Iron and Steel Research International**, [s.l.], v. 17, n. 6, p. 47–52, 1 jun. 2010.

EDWARDS, P. D.; RAMULU, M. Material flow during friction stir welding of Ti-6Al-4V. **Journal of Materials Processing Technology**, [s.l.], v. 218, p. 107–115, 2015.

EMAMI, S. et al. Dissimilar friction stir welding of AISI 430 ferritic and AISI 304L austenitic stainless steels. **Archives of Civil and Mechanical Engineering**, [s.l.], v. 20, n. 4, p. 131, 18 out. 2020.

FOLKHARD, E. **Welding Metallurgy of Stainless Steels, Texto original**. Wien: Springer-Verlag, 1988.

FRATINI, L.; BUFFA, G. CDRX modelling in friction stir welding of aluminium alloys. **International Journal of Machine Tools and Manufacture**, [s.l.], v. 45, n. 10, p. 1188–1194, ago. 2005.

GREEF, M.; TOIT, M. Sensitisation of Two 11–12 % Chromium Type EN 1.4003 Ferritic Stainless Steels During Continuous Cooling after Welding. 2006.

JAFARZADEGAN, M. et al. Microstructure and Mechanical Properties of a Dissimilar Friction Stir Weld between Austenitic Stainless Steel and Low Carbon Steel. **Journal of Materials Science & Technology**, [s.l.], v. 29, n. 4, p. 367–372, 1 abr. 2013.

KHATTAK, M. A. et al. Failure investigation of welded 430 stainless steel plates for conveyor belts. **Engineering Failure Analysis**, [s.l.], v. 116, p. 104754, 1 out. 2020.

KIM, K. H. et al. Joint properties of ultra thin 430M2 ferritic stainless steel sheets by friction stir welding using pinless tool. **Journal of Materials Processing Technology**, [s.l.], v. 243, p. 381–386, 1 maio 2017.

KOKAWA, H. et al. Microstructures in Friction Stir Welded 304 Austenitic Stainless Steel. **Welding in the World**, [s.l.], v. 49, n. 3, p. 34–40, 1 mar. 2005.

KÖSE, C.; TOPAL, C. Effect of post weld heat treatment and heat input on the microstructure and mechanical properties of plasma arc welded AISI 410S ferritic stainless steel. **Materials Research Express**, [s.l.], v. 6, n. 6, p. 066517, mar. 2019a.

KÖSE, C.; TOPAL, C. Laser welding of AISI 410S ferritic stainless steel. **Materials Research Express**, [s.l.], v. 6, n. 8, p. 0865g4, jun. 2019b.

LAKSHMINARAYANAN, A.; BALASUBRAMANIAN, V. **Comparison of Electron Beam and Friction Stir Weldments of Modified 12 wt% Ferritic Stainless Steel**. [s.l.]: [s.n.], 2011.

LAKSHMINARAYANAN, A. K.; BALASUBRAMANIAN, V. An assessment of microstructure, hardness, tensile and impact strength of friction stir welded ferritic stainless steel joints. **Materials & Design**, [s.l.], v. 31, n. 10, p. 4592–4600, dez. 2010.

LIPPOLD, J. C.; KOTECKI, D. J. **Welding Metallurgy and Weldability of Stainless Steels**. 1 edition ed. Hoboken, NJ: Wiley-Interscience, 2005.

LIU, F. C. et al. A review of friction stir welding of steels: Tool, material flow, microstructure, and properties. **Journal of Materials Science & Technology**, [s.l.], v. 34, n. 1, p. 39–57, 1 jan. 2018.

LIU, H. J.; ZHOU, L.; LIU, Q. W. Microstructural characteristics and mechanical properties of friction stir welded joints of Ti–6Al–4V titanium alloy. **Materials & Design**, [s.l.], v. 31, n. 3, p. 1650–1655, 2010.

LO, K. H.; SHEK, C. H.; LAI, J. K. L. Recent developments in stainless steels. **Materials Science and Engineering: R: Reports**, [s.l.], v. 65, n. 4, p. 39–104, 29 maio 2009.

MACHADO, J. P. S. E. et al. Effect of temperature on the level of corrosion caused by heavy petroleum on AISI 304 and AISI 444 stainless steel. **Materials Research**, [s.l.], v. 9, n. 2, p. 137–142, 2006.

MERAN, C.; CANYURT, O. E. The effects of tool rotation speed and traverse speed on friction stir welding of AISI 304 austenitic stainless steel. **International Journal of Materials Research**, [s.l.], v. 102, n. 4, p. 420–428, 1 abr. 2011.

MERAN, C.; CANYURT, O. E. Joint strength of friction stir welded AISI 304 austenitic stainless steels. **International Journal of Materials Research**, [s.l.], v. 104, n. 12, p. 1197–1204, 12 dez. 2013.

MERAN, C.; KOVAN, V.; ALPTEKIN, A. Friction stir welding of AISI 304 austenitic stainless steel. **Materialwissenschaft und Werkstofftechnik**, [s.l.], v. 38, n. 10, p. 829–835, 2007.

MISHRA, R. S.; MA, Z. Y. Friction stir welding and processing. **Materials Science and Engineering: R: Reports**, [s.l.], v. 50, n. 1–2, p. 1–78, 31 ago. 2005.

MURR, L. E. A Review of FSW Research on Dissimilar Metal and Alloy Systems. **Journal of Materials Engineering and Performance**, [s.l.], v. 19, n. 8, p. 1071–1089, 1 nov. 2010.

NANDAN, R.; DEBROY, T.; BHADESHIA, H. K. D. H. Recent advances in friction-stir welding – Process, weldment structure and properties. **Progress in Materials Science**, [s.l.], v. 53, n. 6, p. 980–1023, ago. 2008.

PARK, S. H. C. et al. Rapid formation of the sigma phase in 304 stainless steel during friction stir welding. **Scripta Materialia**, [s.l.], v. 49, n. 12, p. 1175–1180, dez. 2003.

PARK, S. H. C. et al. Corrosion resistance of friction stir welded 304 stainless steel. **Scripta Materialia**, [s.l.], v. 51, n. 2, p. 101–105, 1 jul. 2004.

REYNOLDS, A. P. et al. Structure, properties, and residual stress of 304L stainless steel friction stir welds. **Scripta Materialia**, [s.l.], v. 48, n. 9, p. 1289–1294, maio 2003.

RODRIGUES, D. G. et al. Effects of Annealing Conditions on Recrystallization, Texture, and Average Normal Anisotropy Coefficient of a Niobium-Stabilized Ferritic Stainless Steel. **steel research international**, [s.l.], v. 88, n. 12, p. 1700214, 2017a.

RODRIGUES, D. G. et al. Evaluation of Intermediate Annealing on Nb-Stabilized Ferritic Stainless Steel. **Materials Research**, [s.l.], v. 20, p. 298–303, 7 ago. 2017b.

RODRIGUES, D. G. et al. The effect of grain size and initial texture on microstructure, texture, and formability of Nb stabilized ferritic stainless steel manufactured by two-step cold rolling. **Journal of Materials Research and Technology**, [s.l.], v. 8, n. 5, p. 4151–4162, 1 set. 2019.

SATHIYA, P.; ARAVINDAN, S.; HAQ, A. N. Effect of friction welding parameters on mechanical and metallurgical properties of ferritic stainless steel. **The International Journal of Advanced Manufacturing Technology**, [s.l.], v. 31, n. 11–12, p. 1076–1082, 21 jan. 2006.

SHANKAR, V. et al. Solidification cracking in austenitic stainless steel welds. **Sadhana**, [s.l.], v. 28, n. 3, p. 359–382, 1 jun. 2003.

SILVA, C. C. et al. Alterações Microestruturais na ZAC do aço inoxidável ferrítico 410S-Efeitos sobre a resistência à corrosão. **Soldagem & Inspeção**, [s.l.], v. 11, 2006.

SILVA, C. C. et al. High-temperature hydrogen sulfide corrosion on the heat-affected zone of the AISI 444 stainless steel caused by Venezuelan heavy petroleum. **Journal of Petroleum Science and Engineering**, [s.l.], v. 59, n. 3–4, p. 219–225, nov. 2007.

SILVA, C. C. et al. Microstructural characterization of the HAZ in AISI 444 ferritic stainless steel welds. **Materials Characterization**, [s.l.], v. 59, n. 5, p. 528–533, maio 2008.

SIQUEIRA, R. P. et al. Composition and orientation effects on the final recrystallization texture of coarse-grained Nb-containing AISI 430 ferritic stainless steels. **Materials Science and Engineering: A**, [s.l.], v. 528, n. 9, p. 3513–3519, 15 abr. 2011.

SIQUEIRA, R. P.; SANDIM, H. R. Z.; OLIVEIRA, T. R. Texture evolution in Nb-containing ferritic stainless steels during secondary recrystallization. **Materials Science and Engineering: A**, [s.l.], v. 497, n. 1, p. 216–223, 15 dez. 2008.

SMITH, W. F. **Structure and Properties of Engineering Alloys**. n. 2, [s.l.], McGraw-Hill (New York), 1993.

SONG, C. et al. In Situ Observation of Phase Transformation and Structure Evolution of a 12 pct Cr Ferritic Stainless Steel. **Metallurgical and Materials Transactions B**, [s.l.], v. 43, n. 5, p. 1127–1137, 2012.

THOMAS, W. M. et al. **Friction stir butt welding**, Cambridge, TWI, 1991.

THREADGILL, P. L. Terminology in friction stir welding. **Science and Technology of Welding and Joining**, [s.l.], v. 12, n. 4, p. 357–360, 1 maio 2007.

TONGNE, A. et al. Banded structures in friction stir welded Al alloys. **Journal of Materials Processing Technology**, [s.l.], v. 221, p. 269–278, 2015.

VAN NIEKERK, C. J.; DU TOIT, M.; ERWEE, M. W. Sensitization Of Aisi 409 Ferritic Stainless Steel During Low Heat Input Arc Welding. **Welding in the World**, [s.l.], v. 56, n. 5–6, p. 54–64, maio 2012.

VIEIRA BRAGA, F. et al. Recrystallization of niobium stabilized ferritic stainless steel during hot rolling simulation by torsion tests. **Journal of Materials Research and Technology**, [s.l.], v. 5, n. 1, p. 92–99, 1 jan. 2016.

WANG, H. et al. Microstructure and mechanical properties of dissimilar friction stir welded type 304 austenitic stainless steel to Q235 low carbon steel. **Materials Characterization**, [s.l.], v. 155, p. 109803, 1 set. 2019.

6 CHAPTER 6: Assessment of corrosion resistance of dissimilar AISI 304L and AISI 410S stainless steel joints by the friction stir welding

6.1 Abstract

The intergranular corrosion resistance of conditions welded by the FSW process, keeping the rotation speed at 450 rpm and increasing the axial force from 25 kN to 40 kN, between AISI 410S and AISI 304L steels, was evaluated through the DL-EPR technique and salt spray test. The DL-EPR tests showed that the welding thermal cycle may promote microstructural changes capable of making some areas of the weld susceptible to corrosion. Thus, the increase in heat input with the increment in the axial force application and the higher temperatures reached on the advancing side of the joints becomes a region critical to high values of Ir/Ia and sensitization. In conditions 3 and 4, after being submitted to 1000 h in the salt spray test, it is possible to observe cavities in the grain boundaries in regions close to the contact zone between the material and the tool shoulder. These cavities correspond to ditches due to probable precipitation of chromium carbides. While in Condition 4, macroscopic pits are observed in TMAZ on the advancing side, macroscopic pits are not observed in Condition 3, which was 1000h tested in salt spray camera presented a lower corrosion rate than the base metal of AISI 410S steel. Thus, it is possible to weld AISI 410S ferritic stainless steel and AISI 304L austenitic stainless steel in a dissimilar FSW joint with low Ir/Ia levels and with corrosion rates in the salt spray test lower than the base metal.

Keywords: Friction stir welding; Stainless steel; DL-EPR; Salt spray

6.2 Introduction

Austenitic stainless steels (ASSs) are probably the most common and widely used of all stainless steels. They are frequently used in automotive industries, nuclear power plants and high-temperature components, such as heat exchangers, chemical reactors, among others. Their use is mainly due to their excellent mechanical properties and corrosion resistance, as reported by KHATAK and RAJ, (2002). On the other hand, ferritic stainless steels (FSSs), despite their lower ductility, toughness and weldability

when compared to austenitic stainless steels, can be used in a wide variety of applications where pitting and stress corrosion resistance is more important than mechanical strength as noted by LIPPOLD e KOTECKI, (2005). Thus, LAKSHMINARAYANAN and BALASUBRAMANIAN, (2013a) highlight that FSS is usually used in a mildly corrosive atmosphere for chemical processing equipment, furnace parts, heat exchangers, oil burner parts, petroleum refining equipment, protection tubes, recuperates, storage vessels, electrical appliances, solar water heaters, and household appliances.

The lower application of ferritic stainless steel in the industry is related to the metallurgical problems arising from the fusion welding of these steels. When subjected to the thermal welding cycles of traditional processes, these materials undergo metallurgical changes, which compromise their weldability and the corrosion resistance of the joints. SILVA et al. (2006) evaluated the changes in the HAZ of an AISI 410S ferritic stainless steel subjected to different energy levels in a fusion welding process and observed that in addition to the martensite transformation, there was a precipitation of chromium nitrides and finely dispersed carbides in the HAZ, which cause embrittlement and intergranular corrosion.

However, in recent decades considerable progress has been made in the welding of stainless steels by the friction stir welding (FSW) process, mainly in aspects related to microstructural control and consequently in the corrosion resistance properties of these welded joints. Compared to traditional fusion welding, FSW welding has unique advantages. According to MISHRA e MA, (2005) this process uses a non-consumable tool that rotates and penetrates the joint, resulting in heating and plastic deformation of the materials to be joined, which can be heated to temperatures below those experienced in fusion welding. LIU et al., (2018) report that the FSW process applied to steels exhibits excellent advantages, as the combination of low temperatures and intense plastic deformation results in dynamic recrystallisation and grain refinement. In addition to avoiding unfavourable phase transformations that can impair the corrosion resistance.

PARK et al. (2004) studied the application of the FSW process on the similar welds of AISI 304 austenitic stainless steel and verified that the selection of welding parameters capable of increasing the cooling rate, avoids the delta ferrite (δ) formed at high temperatures to decompose in sigma phase (σ), thus the refined stir zone presented a resistance to intergranular corrosion superior to the base metal. This behaviour is observed because the sigma phase particles, when formed along the grain boundaries of

this region, contain a high content of Cr and, therefore, locally reduce the Cr available for the formation of the protective oxide layer. RODRÍGUEZ et al. (2010), evaluating the different degrees of sensitization through the DL-EPR test of similar FSW joints of austenitic stainless steel 304, has proved that the intergranular corrosion resistance of the stir zone is superior to the base metal, and this can be attributed to the microstructural defects of the metal base, as high density of dislocations and twin boundaries, which act as a diffusion path for the chromium atoms towards the grain boundaries, this fact is not observed after the high deformation rates to which the stir zone is subjected.

Evaluating ferritic stainless steels, KIM et al. (2017) have proved that 430M2 ferritic stainless steel FSW joints significantly decreased sigma phase precipitation compared to arc welding processes. In another study, LAKSHMINARAYANAN and BALASUBRAMANIAN (2012) realized a reduction in susceptibility to intergranular corrosion of AISI 409M steel when welded by the FSW process, as the fast cooling rates achieved prevent the diffusion of chromium. In addition, the authors reported a reduction of the HAZ extension, which is a region that favours the carbides precipitation.

Different industrial segments use dissimilar welding joints of different metals to bring together different properties, minimize costs, and maximize the performance of equipment and machinery with different welding processes. SILVA et al. (2013) pointed out be promising to join different stainless steels in dissimilar joints in the petroleum distillation towers in the gas and petroleum industries through fusion welding processes. MUKHERJEE and PAL, (2012) claim that the dissimilar joints between ferritic and austenitic stainless steels are efficient for prolonging metals' service life due to improved toughness, mechanical strength, and corrosion resistance.

According to MURR (2010), when the FSW process is applied to the weld of dissimilar joints, the asymmetry between the retreating and advancing sides is intensified because there will have different behaviours concerning thermal conductivity and plastic deformation in HAZ, TMAZ and SZ, due to differences in the physical and chemical properties of the materials involved, which support the asymmetry of heat generation and material flow. LIU et al. (2018) and WANG et al. (2019) report that in the dissimilar welding of steels by FSW, correct adjustment of process parameters leads to proper heat input and flow pattern for material coalescence and joint integrity. Therefore, studies have shown a significant effect of joint configuration and process parameters on material flow and defect formation. However, studies are still developing on the analysis of the impact

of these parameters on the formation of precipitates and phase transformations that may impact the corrosion resistance of the FSW joints produced. Thus, a detailed analysis of these aspects in FSW welding dissimilar between ferritic and austenitic stainless steels is still required. More detailed information on the influence of process parameters on the corrosion resistance of these joints has become a important scientific subject with a strong technological appeal. Thus, this work aims to evaluate the intergranular corrosion resistance of FSW dissimilar joints between the AISI 304L austenitic stainless steel and the AISI 410S ferritic stainless steel. The study is addressed to evaluate the corrosion resistance of welded joints through a non-destructive and quantitative technique called the double loop electrochemical potentiokinetic reactivation (DL-EPR) technique to determine the degree of sensitization of stainless steel and accelerated laboratory test provides a controlled corrosive in salt spray environment.

6.3 Materials and Methods

The welds were made using 4-mm-thick plates of AISI 410S ferritic stainless steel and AISI 304L austenitic stainless. The materials' chemical composition was determined by optical emission spectroscopy (Shimadzu model PA7000 Japan) and is presented in Table 6.1.

Table 6.1 - Chemical composition of the base metals (% weight).

Material	Elements											
	C	Si	Mn	P	S	Cr	Ni	Mo	Cu	Co	N	Fe
410S	0.025	0.37	0.30	0.023	<0.010	12.8	0.21	0.01	0.21	0.02	0.033	Bal.
304L	0.026	0.32	1.21	0.029	<0.010	18.5	7.24	0.29	0.34	0.15	0.058	Bal

Source: The author.

The FSW process joined the samples at Helmholtz-Zentrum Geesthacht (HZG) in Germany. All welds were made using the HZG Gantry System with a butt joint configuration, as shown in Fig. 6.1. An inert gas (Ar) injection system was used to protect the material during the process at temperatures above 535 °C; these stainless steels react with the atmosphere. Welds were performed in load control mode with an integrated system to record process data such as penetration depth, rotational speed, torque, tool forces, and tool position over time.

The welds were made with a tool of polycrystalline cubic boron nitride (PCBN). The tool had a conical diameter of 25 mm, a conical pin with a 9.2 mm diameter and a length

of 3.7 mm. The pin had a conical surface with negative recesses, which were in the form of a spiral concerning the tool's axis of symmetry.

Figure 6.1 – Dissimilar butt joint configuration between AISI 410S and AISI 304L steels.

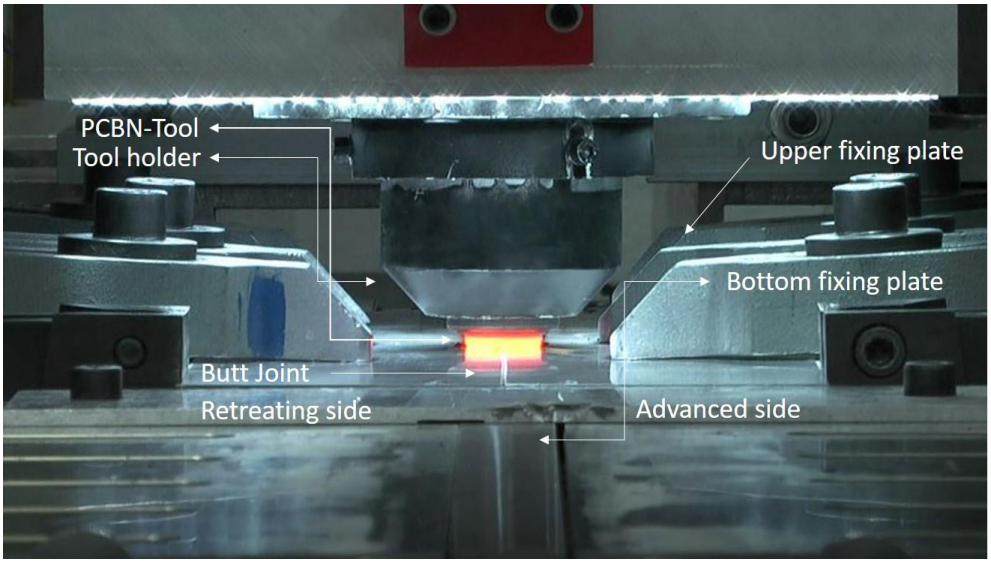

Source: CAETANO et al. (2019).

As shown in Chapter 03, preliminary tests were performed to evaluate the behavior of steels to the effects of different flow direction between the advancing and retreating side in the FSW process. After performing the tests, the results of this study indicated that the condition that results in the best results for consolidation of a defect-free welded joint is with AISI 304L austenitic stainless steel placed on the retreating side and AISI 410S steel placed on the advancing side, as this gives a better surface finish and better joint consolidation.

After choosing the appropriate steel for the FSW joint's advancing and retreating side, four welding conditions were analyzed to evaluate the influence of process parameters on heat generation, defect formation and mechanical properties. Under these conditions, the axial force was varied from 25 to 40 kN, maintaining the rotational speed at 450 rpm, the tool angle at 0º, and the welding speed at 1 mm/s, as shown in Table 6.2.

Table 6.2 – Welding Parameters for Dissimilar FSW Butt Welding of AISI 410S/304L Steels

Condition	Rotation Speed (rpm)	Axial Force (kN)	Advancing Side	Retreating Side
1	450	25	410S	304L
2	450	30	410S	304L
3	450	35	410S	304L
4	450	40	410S	304L

Source: The author.

The coefficient of friction of the material, the pressure exerted by the tool, the rotational speed, and the geometry of the tool used in welding are the inputs needed to determine that heat input and are calculated according to the equation formulated by DEQING et al., (2004). These parameters were related to the heat input generated during FSW welding. Equation 1 shows the equivalent heat input total required for the joint consolidation among the different ways to calculate the heat generated during the FSW process.

$$E_t = \pi \,.\, \mu \,.\, Ps \,.\, Vr \,.\, \frac{D^2 + D\,.d + d^2}{45\,.(D+d)} \quad (1)$$

Where E_t is the equivalent total heat input (kJ/mm), μ is the coefficient of friction of the material, Ps is the pressure exerted by the tool on the material (Pa), Vr is the speed of rotation (rad/s), D is the shoulder diameter and d is the pin diameter (m). Another way to calculate the heat input to the FSW process is by using Equation 2 to determine the equivalent heat input per unit length per second, proposed by LIENERT et al. (2002):

$$E_l = \eta \,.\, \frac{T\,.Vr}{Vs} \quad (2)$$

Where E_l is the heat input per unit length (kJ/mm), η is the efficiency of the FSW process for steels, T the Torque (Nm), Vr the rotational speed (rad/s), and Vs the welding speed. (mm/s).

To analyse the temperature achieved during the FSW process, were used 24 thermocouples divided into four different zones separated by 110 mm, with three thermocouples positioned on the advancing side and three positioned on the retreating side in each zone. To help understand the metallurgical transformations resulting from the different temperatures reached during the process, the equilibrium phase diagram was

simulated using the Thermo-Calc® software, and TTT (Transformation–Time–Temperature) diagram for AISI 410S ferritic stainless steel was simulated using the JmatPro® software. The welds were initially cut with a diamond abrasive disc on a Struers Discotom-6 cutter for microscopic analysis. Sandpapers with a grain size between 120 and 2500 mesh were used for sanding. The polishing step was carried out on a universal polishing machine (Buehler Phoenix 4000) with 3μ, 1μ and 1/4μ diamond pastes and a 150 rpm rotation speed. As the joints are composed of AISI 316L and AISI 444 steels, the combination of 10% oxalic acid and 10% chromic acid reagents was efficient in creating contrasts in the phases and microconstituents present in the sample, enabling a complete analysis of its microstructure. Optical microscopy (OM) analysis was used using a Carl Zeiss optical microscope integrated with the AxioVision SE64 software to assess the disposition and characteristics of the different zones. However, for a more detailed investigation of possible precipitates and the constitution of the interfaces between the AISI 316L/444 steels, analyzes were carried out by scanning electron microscopy with an FEG Quanta 450.

The double loop electrochemical potentiokinetic reactivation (DL-EPR) tests of the welds produced by FSW were performed at room temperature, about 30 °C, using a portable electrochemical cell. This cell is formed by a platinum counter electrode and a reference electrode consisting of a silver wire immersed in KCl. . According to the analyzed steel, two working solutions were used using a solution containing 0,5 mol/l H2SO4 + 1000 mg/l KSCN to steel AISI 304L and a solution containing 0.1 mol/l H2SO4 + 0.4 mol/l Na2SO4 + 1000 mg/l KSCN to steel AISI 410S. The cell was placed in contact with the sample surface using a flexible nozzle adhering to the material, and the area of contact was approximately 0.8 mm2. A total of 24 different points were used for the analysis. This allowed all the different FSW welding zones were analysed, from the advancing side of steel AISI 304L to the retreating side of steel AISI 410S, as shown in Fig. 6.2. The current versus the potential curve was acquired with the Palm SensPc software loaded with the parameters after stabilizing the potentiostat and using a constant scan speed of 3 mV/s.

Figure 6.2 - The 24 different points for DL-EPR analysis

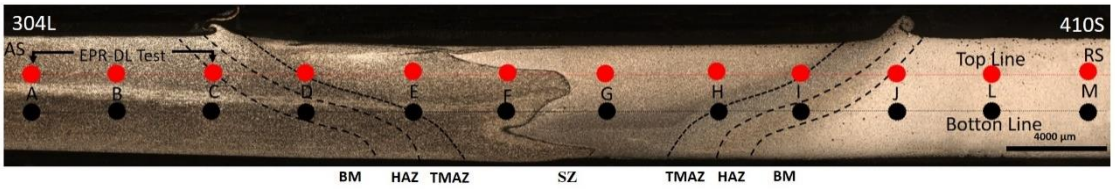

Source: The author.

The conditions with the highest reactivation peaks in the EPR-DL graphs and consequently with the highest values of Ir/Ia, were evaluated using the salt spray test. To perform the salt spray test two samples of each condition from the welded joints and two samples of each base metal were first removed, which were cut into approximate dimensions of 17 cm long by 7 cm wide and 4 cm thick, and then all sides of each sample were sanded to a 1200 mesh size sandpaper. The specimens were previously cut to dimensions that would allow the evaluation of all regions of the weld, from the base metal of the 410S steel on the advancing side to the base metal of the AISI 304L steel on the retreating side of the joint.

Since the salt spray test detects surface flaws and suboptimal surface states very sensitively, this uniformity of finish of all faces of all samples becomes extremely important. Smoother finishes tend to show better test behaviour, but roughness is not the only influencing factor. More important is a coherent surface without micro-cracks and micro-crevices. One advantage of the salt spray test is that it tests the corrosion resistance of the base material and shows the influence of surface preparation on the resistance of stainless steel to atmospheric corrosion. After surface preparation, the samples were inserted into a cyclic accelerated corrosion chamber QFOG model CCT, according to the Standard Practice for Operating Salt Spray ASTM B117. According to the test specification, the salt fog must fall vertically. With flat samples standing inclined, according to the standard, the test medium does not stagnate on the surface but drains off rapidly and is continuously replenished. Therefore, it is recommended to test only plane samples rather than constructional elements with complex geometries. So, the samples were exposed to a continuous salt spray whose composition corresponds to 5% by mass of sodium chloride at 35°C per 1000h. At each 100-hour cycle, the material degradation was monitored through macrographs and mass loss analysis. The corrosion rate was determined by Eq. (3), following ASTM G1 – 03, (2010).

$$\mathbf{r} = \frac{\mathbf{8{,}76 \times 10^{4} \times W}}{\mathbf{A \times D \times t}} \quad (3)$$

Where r is corrosion rate in (mm/year), w is the weight loss in g; A is the surface area of the specimen in cm^2; D is the density of the material in g/cm^3; and t is the corrosion time in h.

6.4 Results and Discussions

6.4.1 Heat input and Temperature Analysis

The process parameters directly affect the heat input, which strongly influences the heating and cooling rates of the thermal cycle and, consequently, the resulting microstructure. However, the heat input calculated based on the process parameters corresponds to equivalent heat input and not precisely to the heat input produced during the process since there are losses that are not considered, being the main ones by conduction and convection in the weld region. The rotational speed is the main parameter related to the friction force at the interface between the base metals and the tool. It is directly linked to heat generation during the welding process, as reported by BILGIN e MERAN, (2012) and LAKSHMINARAYANAN and BALASUBRAMANIAN, (2013). Frictional coupling of the tool surface with the base metal governs the heating mechanism and tool rotation, thereby allowing the stirring and mixing of the material around the pin. Thus, the higher the rotational speed, the higher the process temperature, and this is due to increased friction heating as proposed by COLEGROVE et al. (2007), SHIRI et al. (2013), and UDAY et al. (2010).

The strong influence of the rotational speed on heat generation was observed among similar welds of AISI 410S ferritic stainless steel produced by FSW, as pointed out by CAETANO et al. (2019), which observed that the reduction in rotational speed from 800 to 450 rpm generates a drop-in equivalent heat input total and equivalent heat input per unit length around 0.4 kJ/mm, keeping the axial force around 20 kN. This difference in heat input was enough for the welded sample with the highest rotation speed to present susceptible to intergranular corrosion, showing the presence of precipitations of Cr carbides, while in the sample welded with the lowest rotation speed, no evidence of microstructural changes detrimental to corrosion resistance.

For the results of equivalent heat input per unit length and total heat input calculated for FSW dissimilar welding conditions between ferritic and austenitic stainless steels, shown in Fig. 6.3, it is possible to observe that when the constant rotational speed is maintained at 450 rpm, and the axial force is changed from 25 kN to 40 kN, it can be inferred that the 5 kN force increase between conditions 1, 2, 3 and 4, also produced a significant amount of heat in the process. Considering the differences between total heat input between conditions 1 and 4, it is possible to observe that the value increases from 0.64 kJ to 1.02 kJ, corresponding to a 37% increase in total heat input, increasing only 15 kN in applied force. Therefore, this increase in axial force will help raise the temperature and increase the material's softening degree. However, the axial force has less influence on the heat generation than other parameters such as the rotation speed, as previously discussed in Chapter 3 and presented by CAETANO et al. (2018).

Figure 6.3 - Equivalent heat input per unit length and total heat input calculated for the different conditions of AISI 410S/304L steels dissimilar welding performed by the FSW process.

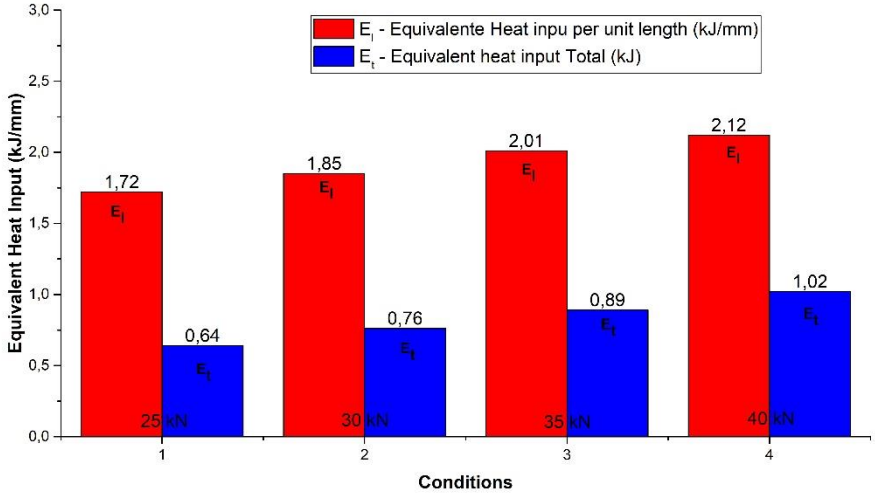

Source: The author.

The temperature analysis produced using 24 thermocouples divided into 4 different zones of condition 4, welded with the highest axial force, proved the thermal asymmetry between the advancing and retreating sides of the dissimilar FSW joints AISI 304L/410S. By Fig. 6.4 it can be seen that, on average, the temperatures on the advancing side are 60° higher than those observed on the retreating side, despite a measurement error in zone 3,

due to the contact of the flash produced during the process with the thermocouple number 13, show a peak temperature of 813°C for the retreating side. DARVAZI and IRANMANESH (2014) have already proved this thermal asymmetry, showing that in the cross-section of the FSW process, along transverse direction and perpendicular to the weld line, the temperature distribution is toward advancing side and the maximum temperature distribution is in the back half of shoulder region and toward advancing side. In dissimilar FSW joints, in addition to the characteristics of the FSW process, the difference in properties of the welded materials also contributes to this asymmetry in the temperatures reached and in the heat distribution.

Several studies have shown there is a more significant heat generation on the advancing side of the FSW welds, as reported by NANDAN, DEBROY and BHADESHIA, (2008). SANTOS, IDAGAWA and RAMIREZ, (2014) also have shown that the heat intensity produced in the upper part of the FSW weld is high, mainly due to the greater contact of the material with the tool shoulder, promoting a more significant heat generation. Thus, the effects of higher heat input in the upper region of the advancing side become this region susceptible to relevant microstructural changes that may affect properties, including corrosion resistance.

Figure 6.4 - Thermal analysis for the four different zones showing to the temperature peaks of Condition 4, welded with a rotation speed of 450 rpm and an axial force of 40 kN .

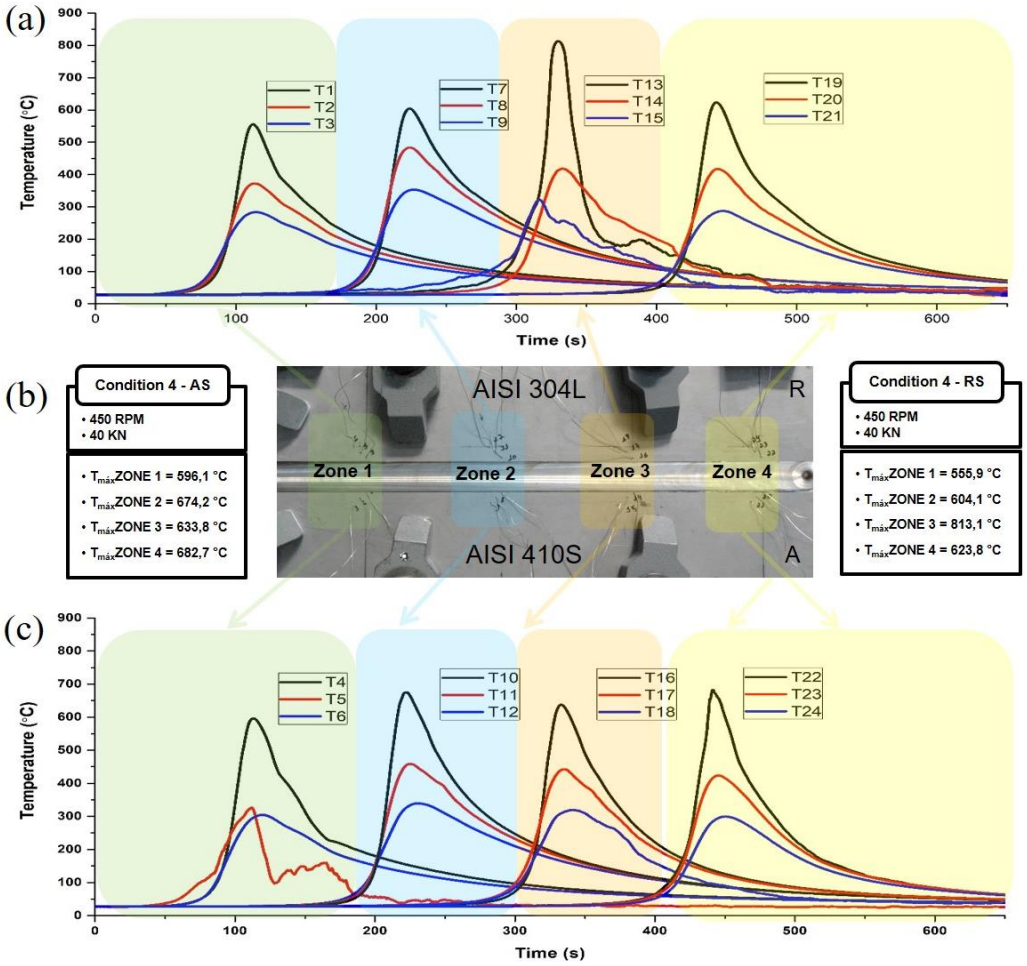

Source: The author.

In the modelling and simulation of austenitic and ferritic stainless steel joints by the FSW process SILVA, (2021) reports that from conditions with a rotation speed of 450 rpm and axial force of 35 kN, keeping the welding speed at 1 mm/s, some tests reached temperatures above 85% of the melting point. The results verified that the heat generated by the increased rotation, axial force and low welding speed contribute to a temperature very close to the melting point in a zone close to the contact surface between the tool shoulder and the steel. Thus, it is proved that the temperatures reached in SZ, TMAZ and HAZ of AISI 410S steel are sufficiently high for the martensitic transformation and precipitation of chromium carbides.

6.4.2 EPR-DL Test

Sensitization is a phenomenon that occurs when stainless steel is exposed to a high temperature for an extended period. The chromium carbide precipitation is dominated by $Cr_{23}C_6$ and is strongly dependent on the carbon and chromium content of the alloy used. As reported by DOERR et al., (2017), this carbide, when precipitating, sequesters the chromium in its vicinity. This reduction or impoverishment renders the surrounding region incapable of keeping the passive chromium film stable to remain immune to corrosive attack. So, in some regions, the material presents less than 12% chrome and is susceptible to intergranular corrosion, as noted by PARVATHAVARTHINI et al. (2009). The research to determine the degree of sensitization of stainless steel led to the development of a simple, non-destructive and quantitative technique called the double-loop electrochemical potentiokinetic reactivation test (DL-EPR). In this test, the polarization curve in the anodic direction, called the activation loop, promotes the formation of a passive layer in the material, as presented by MAJIDI and STREICHER, (1986). This curve is compared with the reactivation loop, which evaluates the integrity formed when applying the reverse potential. According to RAHIMI, ENGELBERG and MARROW (2011), the presence and intensity of the reactivation peak in the reverse polarization and the relationship between the reactivation current (Ir) and the activation current (Ia) are a direct response to the susceptibility of the material to intergranular corrosion. The DL-EPR test has been consolidated over the years as a simple and efficient technique to analyse the susceptibility of stainless steels to intergranular corrosion after they have been subjected to different types of processing, such as heat treatments and welding processes, as can be seen in studies of TAJI, MOAYED and MIRJALILI (2015) and KIM et al. (2009).

Through the analysis of current versus voltage graphs obtained by the technique (DL-EPR), it is possible to observe that reactivation peaks are found on the advancing side from Condition 1, welded with an axial force 25 kN, as can be seen in Fig. 6.5b. This behaviour has been proven by CAETANO et al. (2019), analysing similar FSW joints of AISI 410S steel, it was observed that from conditions subjected to an axial force of 20 kN and a rotation speed of 450 rpm, low intensities of reactivation peaks are present on the advancing side of the weld joint. Stainless steels have different levels of sensitization, which are represented in the EPR-DL test by different intensities of reactivation peaks. Thus, low reactivation peaks, as observed in Condition 1 and Condition 2, represent early

stages of this sensitization process, with likely low intensities of carbide precipitation and grains not fully surrounded by these precipitates, as observed by ABIGAIL RODRÍGUEZ et al. (2010) and LAKSHMINARAYANAN and BALASUBRAMANIAN, (2012b), for both ferritic and austenitic stainless steels.

With the increase of the axial force from 35 kN in Condition 3 to 40 kN in Condition 4, as shown in Fig. 6.5f and Fig. 6.5h, there is a considerable increase in the peak of reactivation in the voltage versus current graph in the region where the AISI 410S steel is positioned, caused by the contribution of the increase in heat input and the consequent decrease in cooling rates in the material sensitization process. Analysing the relation between the reactivation and activation peaks (Ir/Ia) for the different conditions welded in Fig. 6.5a, Fig. 6.5c, Fig. 6.5e and Fig. 6.5g, it is possible to observe low Ir/Ia values for the retreating side, where the AISI 304L steel is positioned, even with the increased application of axial force. This concentration of reactivation peaks on the advance side is due to the differences in intergranular corrosion resistance of the welded alloys, this resistance being higher for AISI 304L steel with higher Cr, Mo and Ni contents. In addition to the differences in metallurgical transformations occurred in welded steels. As highlighted in Chapter 04, the main microstructural changes observed in the advancing side in the FSW 304L/410S joints were the martensitic transformations presented in the SZ, TMAZ and HAZ, of the steel AISI 410S. This behaviour is due to the low chromium content of the alloy, causing instability of the ferrite. During the heating, ferrite will partially transform to austenite at a temperature above 870 °C. According to DU TOIT; VAN ROOYEN and SMITH, (2007), at this temperature, most carbides can be dissolved, and the carbon migrates to the austenite, where it is absorbed and maintained in solid solution in the interstitial sites of the FCC lattice, due to the higher carbon solubility of the austenite. When the cooling rate is fast enough, the austenite will transform into untempered martensite supersaturated with carbon in solid solution, avoiding the Cr-rich carbide precipitation. Thus, despite this critical phase transformation occurring for both the conditions evaluated, the martensite formation along the SZ, TMAZ and HAZ, as a general rule, was not directly associated with the corrosion results since regions with a high volumetric fraction of martensite were not sensitive to DL-EPR.

Thus, it is believed that the susceptibility to intergranular corrosion is, in fact, directly associated with the microstructural changes caused by the thermal cycle, especially with the precipitation of Cr-rich compounds formed along grain boundaries, which depends

on the selected welding parameters. As shown in Fig. 6.3, when the axial force is increased from 25 kN to 35 kN, the total equivalent heat input increases from 0.64 kJ/mm to 0.94 kJ/mm in Condition 3 and only from this condition that the Ir/Ia ratios exceed values of 0.1, with peaks close to 0.18 only in Condition 4. However, these peaks are lower than that observed by CAETANO et al. (2019) in the stir zone of similar FSW joints of AISI 410S steel, sensitized by the presence of Cr-rich carbide precipitation and with regions presenting a concentration of 21% of Cr. These conditions were welded with an axial force of 22 kN, a rotation speed of 800 rpm and the highest Ir/Ia ratios exceeding 0.2, which demonstrates the significant impact of increasing the rotation speed on the heat input and the joints subjected at temperatures and time sufficient for the development of the sensitisation process.

Figure 6.5 – (a) Ir/Ia ratio for Condition 1 (b) Current versus voltage graphs to point I in the top line of Condition 1 (c) Ir/Ia ratio for Condition 2 (d) Current versus voltage graphs to point I in the top line of Condition 2. (e) Ir/Ia ratio for Condition 3 (f) Current versus voltage graphs to point I in the top line of Condition 3. (g) Ir/Ia ratio for Condition 4 (h) and Current versus voltage graphs to point I in the top line of Condition 4.

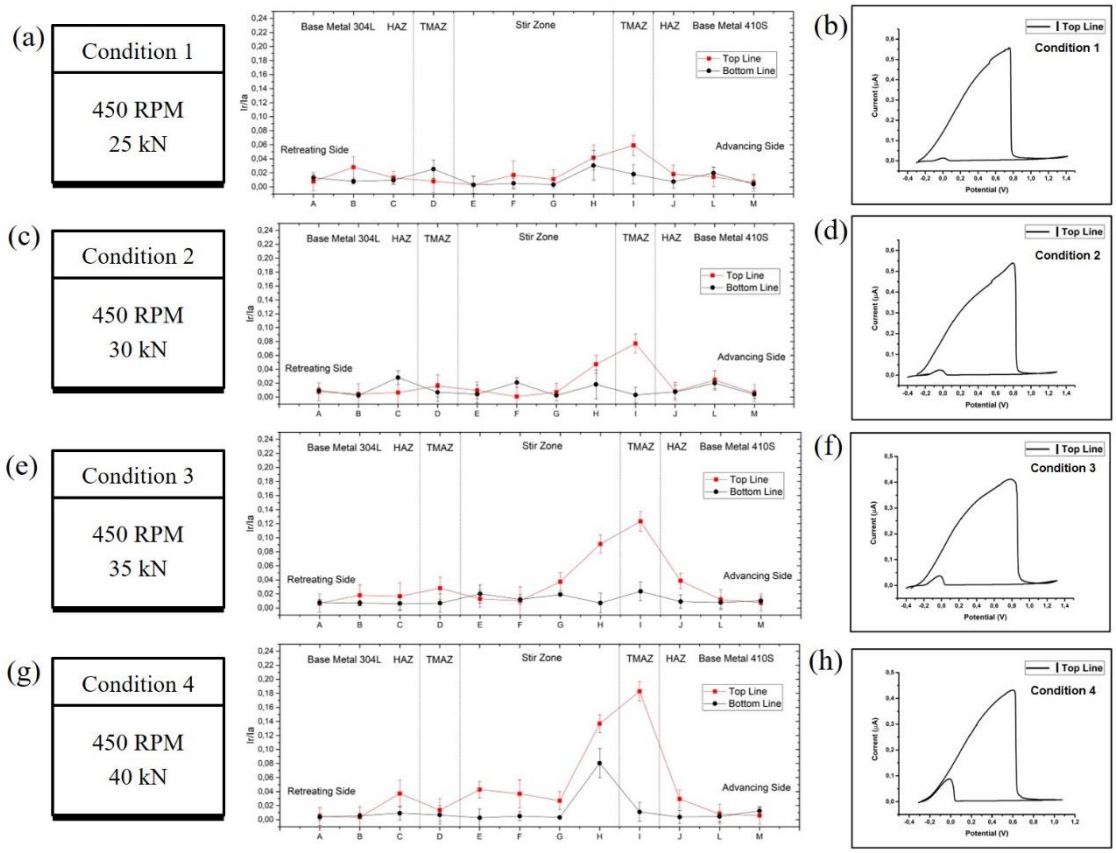

Source: The author.

Normally chromium carbide precipitation in stainless steels requires some time to occur due to nucleation and growth kinetics. However, the effect of plastic deformation and recrystallization may have some influence on the kinectic, accelerating the precipitation phenomena, especially on the advancing side, where this phenomenon occurs with greater intensity. PARK et al. (2004), has reported this effect on the sigma phase precipitation on the advancing side of FSW welds of austenitic stainless steels. VASCONCELOS and SILVA, (2011) using the DL-EPR test evaluated the modifications caused by the autogenous TIG welding process with AISI 410S ferritic stainless steel. The DL-EPR tests showed that all weld regions were susceptible to intergranular corrosion due to the presence of fine Cr_2N precipitates dispersed in the ferritic matrix.

These authors determined that the presence of reactivation peaks in all current versus voltage graphs along the cross-section of the weld, for all different levels of energy tested, had higher Ir/Ia values than those found in the most susceptible regions to corrosion of the FSW welds evaluated in this study. (2012) studied the susceptibility to intergranular corrosion of AISI 409M ferritic stainless steel, immersed in a solution of copper sulfate and sulfuric acid. The results of the analysis showed that, although this material presents better resistance to intergranular corrosion when welded by the FSW process in comparison to the TIG process, the use of a rotational speed of 400 rpm and an axial force of 22 kN still shows sensitization in regions subjected to higher temperatures, similar to the one observed in this work.

Thus, the DL-EPR tests, performed for the different weld conditions, showed whether the welding thermal cycle may promote microstructural changes capable of making some areas of the weld susceptible to corrosion. The test also showed that the difference in the heat input caused by increased axial force applied in the dissimilar welds 304L/410S produced by FSW caused different levels of susceptibility to intergranular corrosion on the advancing side, where is positioned the AISI 410S steel.

6.4.3 Salt Spray Test

The salt spray test is the oldest “corrosion test” and the most widely used to evaluate the behaviour of a material when exposed to prolonged periods in an environment containing chlorides. This accelerated laboratory test provided a controlled corrosive environment and was used to produce relative corrosion-resistance information for Conditions 3 and 4 exposed in a test chamber. The salt spray test ASTM B117 atomises a salt solution into uniform droplets on specimens suspended in the vertical. The salt solution is a solution of 5% (in weight) of NaCl (more than seawater, which is only 1.8% to max 3%). The exposure zone of the salt spray chamber was maintained at 35°C. The salt spray is completely different from other tests applied to stainless steels, like those performed by LAYCOCK and NEWMAN, (1998), such as critical pitting potential or critical pitting temperature measurements in NaCl and $FeCl_3$ solution, respectively. In these tests, corrosivity is progressively increased by shifting continuously or stepwise one test parameter, such as the potential or the temperature, until critical conditions are reached, and corrosion initiates. The critical value of the variable test parameter where corrosion initiates then serves to measure the corrosion resistance of the material tested.

Therefore, critical pitting potentials or temperatures of different materials can be determined, serve as a quantitative measure of corrosion resistance, and be compared. With the salt spray test, it is not possible to measure corrosion resistance in such a quantitative manner. Thus, the salt spray test serves as a ranking test for stainless steel samples under conditions of accelerated atmospheric corrosion, such as tests performed on austenitic stainless steels (ASS) by LI et al. (2013) and CHIANG et al. (2012) to assess the mechanical degradation of these materials in salt-spray environment.

At each cycle of 100h, samples were taken to assess the mass loss. Corrosion at the cut edges of the sample often makes the carrying out a salt spray test and its evaluation more difficult if corrosion products emerging at the upper and lateral edges spread out over the sample surface, masking large area fractions after longer testing times. The appearance of the sample is then governed by the corrosion behaviour of the cut edges, while the corrosion behaviour of the rolled surfaces can no longer be adequately evaluated. During the test, if corrosion products emerging at the upper and lateral edges spread out over the sample surface, masking large area fractions after longer testing times. The appearance of the sample is then governed by the corrosion behaviour of the cut edges, while the corrosion behaviour of the welding surfaces can no longer be adequately evaluated. To avoid this problem, every 100h, the corrosion products were duly removed by immersing the samples in a 10% HNO_3 solution.

Macroscopically evaluating the upper and lower surfaces of the samples from conditions 3 and 4, after being submitted to 1000h in the salt spray test, presented in Fig. 6.5b, Fig. 6.5c, Fig. 6.5e and Fig. 6.5f, it is possible to observe that for all conditions the base metal of the AISI 410S steel presents a considerable formation of macroscopic pits, this surface degradation being more intense in regions close to HAZ for condition 4, welded with greater heat input; however, this fact was not observed for the AISI 304L steel base metal. Chromium and molybdenum are the most important alloying elements of stainless steel in corrosion resistance. The higher the content of these two metals, the more aggressive must the conditions be to initiate pitting and crevice corrosion. Molybdenum is more effective than chromium, which is expressed by the socalled PRE-value:

$$PRE = \%Cr + 3.3 \times \%Mo$$

As highlighted by AHMAD, (2006), the Pitting Resistance Equivalent (PRE) value is the resistance of stainless steel against pitting and crevice corrosion that can be expected based on its alloy composition. Besides the alloying elements chromium and molybdenum, nickel is beneficial for salt spray test behaviour. In contrast to chromium and molybdenum, nickel does not increase resistance to pitting and crevice corrosion initiation, but it very effectively slows down the corrosion process once it has started. Thus nickel-austenitic grades often show better salt spray test results, with much less rusting than low-nickel ferritic grades with similar PRE-values. This difference in nickel contents between AISI 304L and AISI 410S steels justifies the differences in pitting corrosion resistance between the two analysed steels, with the AISI 410S steel having the lowest nickel content and the lowest PRE value presenting the lowest resistance.

In a macroscopic analysis of the cross-section of samples submitted to the salt spray test in the Fig. 6.5a and Fig. 6.5d it is possible to observe that the SZ of the two conditions, both for the advancing side and for the retreating side, presented a corrosion resistance superior to the MB of the AISI 410S steel, without the formation of macroscopic pits. However, in the TMAZ of Condition 4 one pit was formed with an average diameter of 0.14 mm and located at 0.66 mm from the upper edge and 8.83 mm from the interface between the two materials. The formation of this pit proves that the increase in axial force to 40 kN in Condition 4 was sufficient to subject the material in the welded region to a temperature range that allows for metallurgical transformations that degrade the corrosion resistance of the joint.

Figure 6.1 – (a) Cross-sectional macrograph of Condition 3 subjected to 1000h to the salt spray test (b) Upper surface of Condition 3 subjected to 1000h to the salt spray test (c) Lower surface of Condition 3 subjected to 1000h to the salt spray test (d) Cross-sectional macrograph of Condition 4 subjected to 1000h to the salt spray test (e) Upper surface of Condition 4 subjected to 1000h to the salt spray test and (f) Lower surface of Condition 4 subjected to 1000h to the salt spray test.

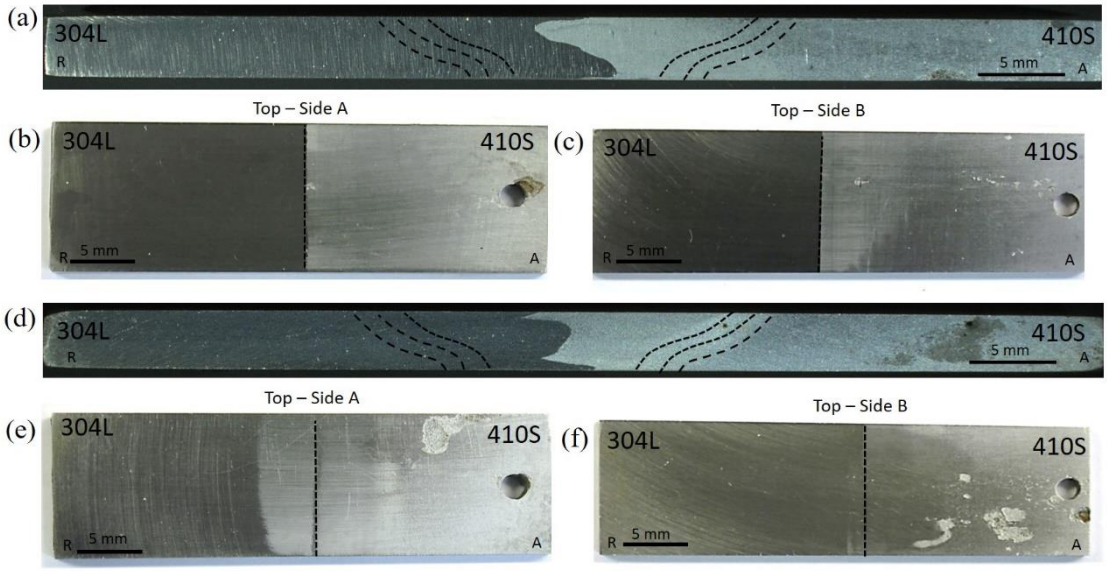

Source: The author.

Microscopically evaluating the cross-section of Condition 4, it is possible to observe, in the sample submitted to 1000h in the salt spray test, cavities in the grain boundaries in the stir zone of the AISI 410S steel in regions close to the contact zone between the material and the tool shoulder, as shown in Fig. 6.6b. These cavities at the ferrite/martensite interface of the upper stir zone of AISI 410S steel, shown in Fig. 6.7b, correspond to ditches due to probable precipitation of chromium carbides $Cr_{23}C_6$. Precipitation occurred, at first, in the grain boundaries of the previous austenite at high temperature, as also observed by CAETANO et al. (2019) welding by FSW similar joints of AISI 410S steel. Although the alloy under study has a low carbon concentration, reducing carbon contents below 0.03% does not prevent sensitization since the precipitation of chromium carbides can occur quickly when these steels are within the temperature range for precipitation. These temperatures are higher in this interface region between the tool shoulder and the material. In the lower stir zone, these cavities in the grain boundaries are not observed, as shown in Figure 6.7c, because as the distance between the shoulder interface region of the tool and material occurs, the temperature

decreases, which in the case of the lower stir zone, due to the parameters used, did not reach enough temperature peaks to sensitize the material.

Figure 6.6 – (a) Cross-sectional micrograph of Condition 4 (b) Grain boundaries of the upper part of the stir zone of AISI 410S (c) (d) Cross-sectional macrograph of Condition 4 submitted to 100h in the Salt Spray test (e) Pites formation in TMAZ and (f) Pites formation in HAZ.

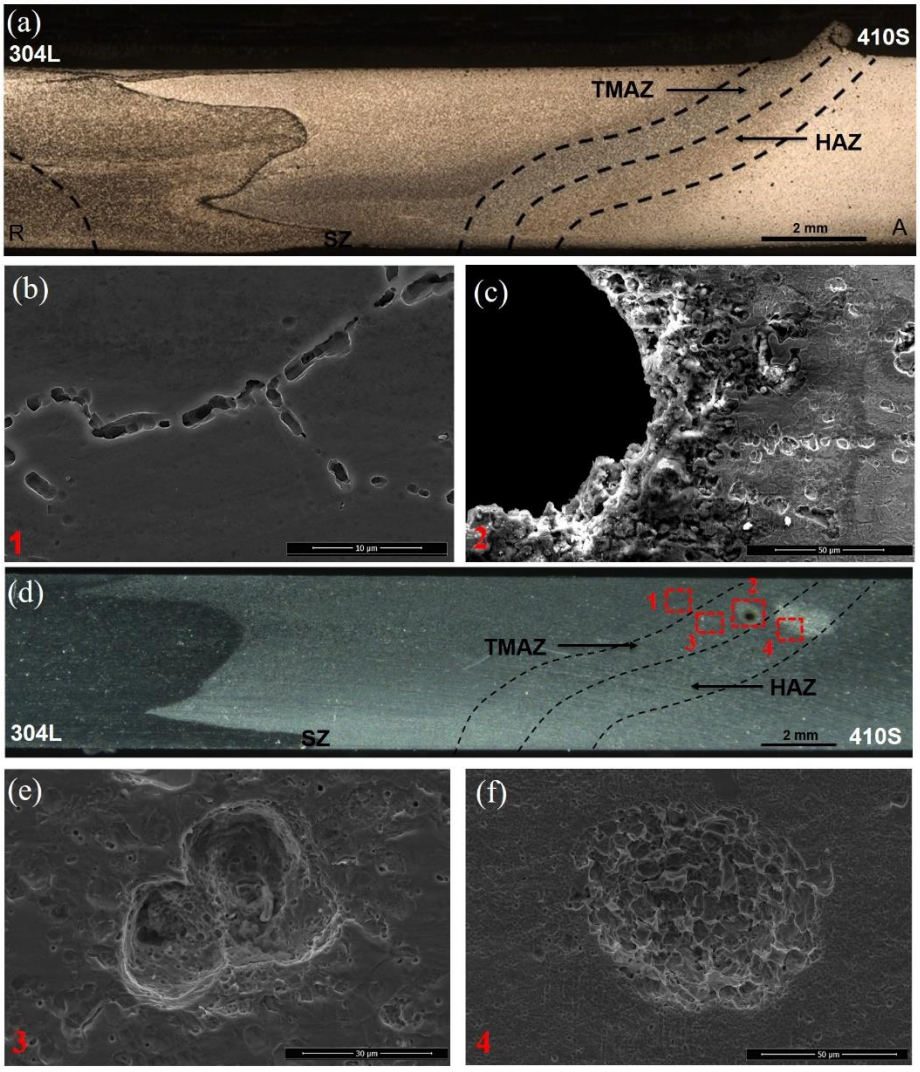

Source: The author.

As it approaches TMAZ and HAZ, it is possible to visualize macroscopic and microscopic pits concentrated in the upper part of the sample. These pits are deeper and have smaller diameters at TMAZ, as shown in Fig. 6.6c and Fig. 6.6e and shallow in the HAZ, as shown in Fig. 6.6f. The ferritic stainless steels (FSS) are prone to corrosion in

the salt spray test, with no general thinning, but forms of localized attack are typically observed. The prevalent types are pitting and crevice corrosion. With these corrosion forms, the attack usually is confined to tiny surface areas, while the surrounding surface shows no thinning and exhibits the original surface topography, more or less covered with rusty corrosion products. The corrosion morphology is characterized by pits with a small diameter compared to their depth. However, one can have regions with a high concentration of pits leading to the union of different cavities, as shown in Fig. 6.6e, contributing to more significant surface degradation.

According to ZHOU and ENGELBERG, (2021), in FSS the pitting corrosion follows three general stages: (i) pit nucleation, (ii) metastable pit growth, followed by (iii) stable pit growth. Pit nucleation sites are influenced by metallurgical variables, such as the presence of inclusion (e.g. MnS) and second phase particles (e.g. carbides), as the possible responses for the cavities in the grain boundaries shown in the Fig. 6.6b. The Cl^- concentration and temperature also play an essential role in the metastable pit growth. Segundo MOLLAPOUR and POURSAEIDI, (2021) the pitting corrosion requires the presence of chloride, an aqueous environment, and a standard temperature and pressure, and the presence of stress in the specimens accelerates the pitting corrosion growth. This fact may have contributed to the more remarkable growth of pits formed in TMAZ compared with HAZ due to the higher temperatures and stress reached in the TMAZ. In this test and many actual applications, chloride salts are the most relevant corrosive species for stainless steel and pitting, and crevice corrosion is the corrosion form encountered.

Figure 6.7 – (A) Cross-sectional micrograph of Condition 4 and (b) Scanning electron microscopy images in SE mode of the upper stir zone on the advancing side; (c) Scanning electron microscopy images in SE mode of the lower stir zone of the advancing side.

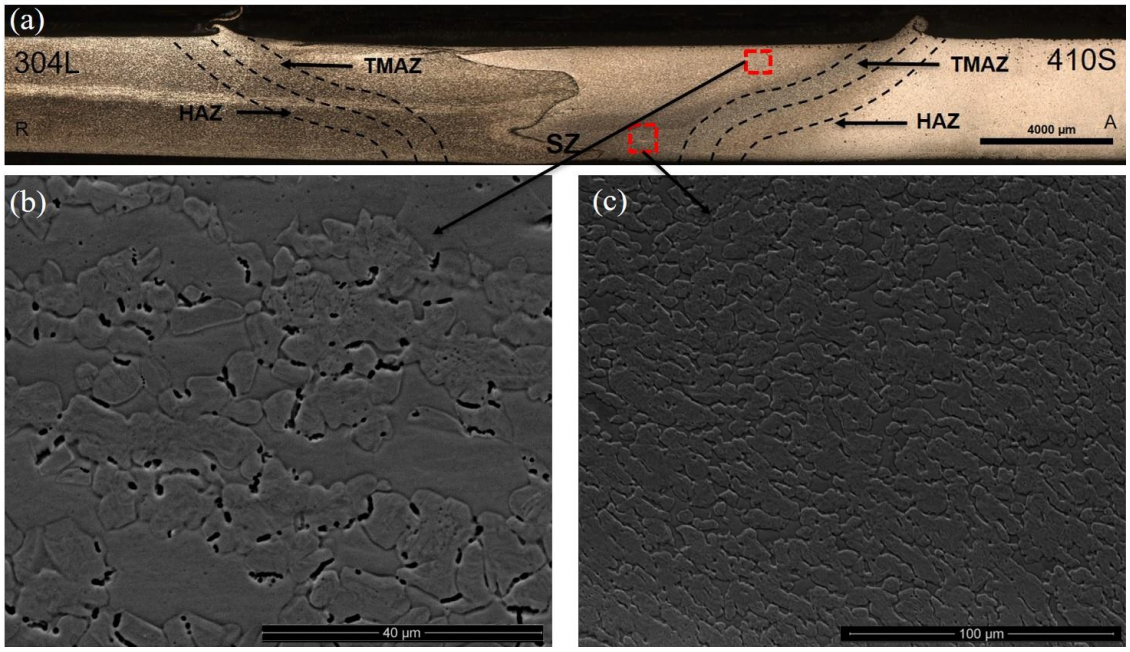

Source: The author.

Evaluating the equilibrium phase diagram for AISI 410S ferritic stainless steel in Fig. 6.8 (a), it is possible to verify that in heating, from 808 °C, the material starts to nucleate austenite, until at 881 °C, the material becomes completely austenite. The material remains completely austenitic until reaching a temperature of 1062 °C, above which the austenite reverts back to ferrite, completing this transformation at 1293 °C. Thus, there are two temperature ranges in which AISI 410S steel consists of two phases corresponding to ferrite and austenite: 808 °C to 881 °C and between 1062 °C to 1293 °C. Therefore, the AISI 410S steel, when submitted to the FSW process, is submitted to the first temperature interval, giving rise to austenitic grains nucleated in the ferrite grain boundaries, which, when cooled, will give rise to martensite. According to SONG et al. (2012), in FSW welding of ferritic stainless steels, since the chemical composition does not entirely stabilize the ferrite, any region exposed to temperatures around 800°C, can be subjected to cooling rates between 8.5°C/s to 2.2°C/s, providing the martensitic transformation.

Through the TTT (Transformation–Time–Temperature) diagram for AISI 410S ferritic stainless steel, shown in Fig. 6.8 (b), it is possible to verify that the precipitation of $M_{23}C_6$ carbides is much easier in processes that submit these steels to fast cooling rates compared to AISI 304L steels. Thus, by analysing the ferrite/martensite interface on the advancing side, after the chemical attack, it is possible to verify cavities, which correspond to ditches due to probable precipitation of chromium carbides $Cr_{23}C_6$. Precipitation occurred in the grain boundaries of previous austenite at high temperatures. Although the alloy understudy has a low carbon concentration, reducing carbon contents below 0.03% does not prevent sensitization, since the precipitation of chromium carbides can occur quickly when these steels are within the temperature range for precipitation, as verified by VAN NIEKERK, DU TOIT and ERWEE, (2012).

Figure 6.8 - (a) Equilibrium phase diagram for AISI 410S ferritic stainless steel simulated using the Thermo-Calc® software. NPM – molar fraction of the phases. (b) T.T.T (Transformation–Time–Temperature) diagram for AISI 410S ferritic stainless steel simulated using the JmatPro® software.

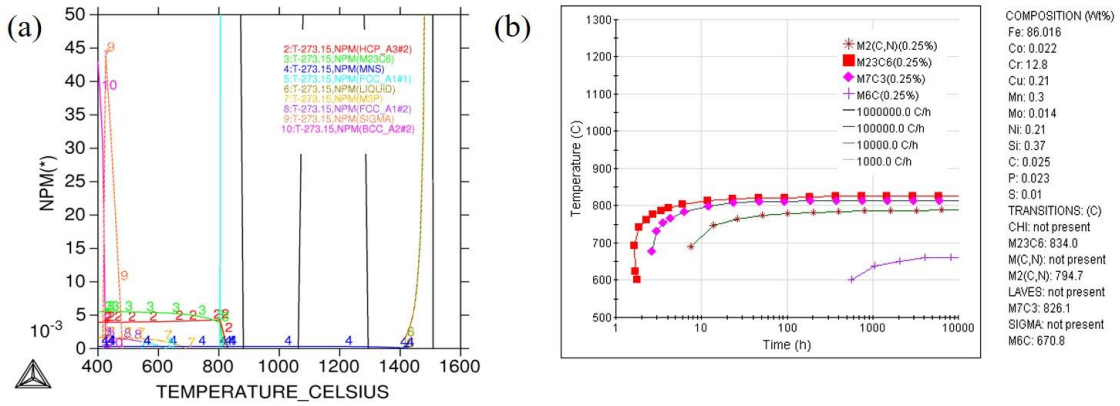

Source: The author.

The mass loss of steel in this salt spray test depends on the area of steel exposed, the temperature, time of exposure, salt solution makeup and purity, pH, spray conditions, and the metallurgy of the steel. Therefore, the ASTM B117 – 16 and ASTM G1 – 03 standards were used to determine the average mass loss of the samples submitted to the test, the standard deviations (Sr) and the corrosion rates (r) at each 100h interval. Through the analysis of Table 6.3 for Condition 3, welded at a rotation speed of 450 rpm and axial force of 35 kN, it is possible to observe that up to 600 h of test the average mass loss

remains below 0.0201 g. However, after 700 h of testing, there is an increase in this value every 100 h, achieving an average mass loss of 0.0412 g after 1000 h of testing. Regarding the corrosion rate, the highest values were observed at 100 h and 200 h of test, achieving an average corrosion rate of 0.02 mm/year. For test times greater than 300 h, the corrosion rate remained at an average of 0.015 mm/year until completing the 1000 h testing.

Table 6.3 – Correlation between Salt Spray Test Duration, Average Mass Loss, Standard Deviations, Coefficient of Variation and Corrosion Rate to Condition 3.

Test Duration, h	Average Mass Loss, g	Rate Corrosion, mm/year
100	$0.0048 \pm 1.2\ 10^{-3}$	$0.0211 \pm 12.5\ 10^{-3}$
200	$0.0093 \pm 1.7\ 10^{-3}$	$0.0200 \pm 10.7\ 10^{-3}$
300	$0.0100 \pm 1.6\ 10^{-3}$	$0.0144 \pm 7.4\ 10^{-3}$
400	$0.0149 \pm 2.7\ 10^{-3}$	$0.0150 \pm 2.9\ 10^{-3}$
500	$0.0200 \pm 8.3\ 10^{-3}$	$0.0154 \pm 0.8\ 10^{-3}$
600	$0.0200 \pm 8.2\ 10^{-3}$	$0.0128 \pm 0.6\ 10^{-3}$
700	$0.0291 \pm 7.4\ 10^{-3}$	$0.0165 \pm 2.0\ 10^{-3}$
800	$0.0344 \pm 6.8\ 10^{-3}$	$0.0173 \pm 3.1\ 10^{-3}$
900	$0.0384 \pm 7.5\ 10^{-3}$	$0.0171 \pm 3.1\ 10^{-3}$
1000	$0.0412 \pm 8.6\ 10^{-3}$	$0.0165 \pm 2.7\ 10^{-3}$

Source: The author.

By analysing Table 6.4 to Condition 4, welded with a rotation speed of 450 rpm and an axial force of 40 kN, it is possible to observe that although Condition 4 showed the presence of pits in the ZTMA and HAZ in the macroscopic analysis, the average mass loss after 1000h of testing was lower than that observed in condition 3. However, when considering the high standard deviation observed after 700h of testing for samples of condition 4, it is observed that some samples reached a mass loss of up to 0.05 g after 1000h of exposure to salt spray and, therefore, more significant than Condition 3. Similar to what was observed for condition 3, in terms of corrosion rate, condition 4 also showed the highest rates between 100h and 200h of testing. According to KOVALEV et al. (2019) this initial increase in corrosion rate in the salt spray test occurs due to the absence or

little formation of corrosion products in the initial stages, intensifying the contact of the corrosive medium with the surface of the material. Considering the standard deviations for the corrosion rates of conditions 3 and 4, it is observed that both conditions presented a similar behaviour during the entire exposure time to the salt spray test.

Table 6.4 – Correlation between Salt Spray Test Duration, Average Mass Loss, Standard Deviations, Coefficient of Variation and Corrosion Rate to Condition 4.

Test Duration, h	Average Mass Loss, g	Rate Corrosion, mm/year
100	$0.0046 \pm 2.2\ 10^{-3}$	$0.0187 \pm 9.1\ 10^{-3}$
200	$0.0083 \pm 2.0\ 10^{-3}$	$0.0166 \pm 3.7\ 10^{-3}$
300	$0.0111 \pm 2.6\ 10^{-3}$	$0.0148 \pm 3.3\ 10^{-3}$
400	$0.0114 \pm 2.2\ 10^{-3}$	$0.0114 \pm 2.0\ 10^{-3}$
500	$0.0133 \pm 3.1\ 10^{-3}$	$0.0106 \pm 2.4\ 10^{-3}$
600	$0.0159 \pm 5.3\ 10^{-3}$	$0.0106 \pm 3.3\ 10^{-3}$
700	$0.0213 \pm 10.7\ 10^{-3}$	$0.0122 \pm 5.9\ 10^{-3}$
800	$0.0279 \pm 15.8\ 10^{-3}$	$0.0139 \pm 7.7\ 10^{-3}$
900	$0.0306 \pm 17.0\ 10^{-3}$	$0.0136 \pm 7.4\ 10^{-3}$
1000	$0.0325 \pm 20.1\ 10^{-3}$	$0.0129 \pm 7.8\ 10^{-3}$

Source: The author.

Correlating the corrosion rate of Conditions 3 and 4 with the base metal of AISI 410S and AISI 304L steel over the duration of the test through Fig. 6.9, it is possible to verify that for Condition 3 and Condition 4, the corrosion rates remained lower than that observed for the base metal of AISI 410S steel throughout the test. The rates for weld conditions averaged between 0.01 and 0.02 throughout the test. In addition to the higher rates, the corrosion rate intensifies after 600 hours of testing for the base metal of AISI 410S steel, starting to show corrosion rate values greater than 0.04 mm/year. This fact demonstrates the superiority of the corrosion resistance of the welded joints concerning the base metal of AISI 410S steel.

Despite the average values of the corrosion rates of Condition 3 being higher than Condition 4, considering their respective standard deviations, the conditions remain very

similar throughout the test. With Condition 4 reaching absolute values greater than Condition 3. This similarity of corrosion rates between welded conditions, occurs due to the low variation of heat input between them, allowing similar thermal welding cycles between the conditions. However, as shown in the macroscopic analysis, only in condition 4 the weld region was compromised. During the entire test, the corrosion rate of the AISI 304L steel base metal remained practically unchanged at around 0.001, which proves the high pitting corrosion resistance of austenitic stainless (ASS) steels. As observed by CHUAIPHAN and SRIJAROENPRAMONG, (2020), when welding different ASS, it was verified that this pitting corrosion resistance is greater the higher the content of elements such as Cr, Mo and Ni. Due to its very high chloride level, the salt spray test often induces corrosion in stainless steels resistant to the much lower chloride impact of current applications.

Figure 6.9 – Corrosion rate in relation to the salt spray test duration time for Condition 3, Condition 4 and base metals AISI 410S and AISI 304L.

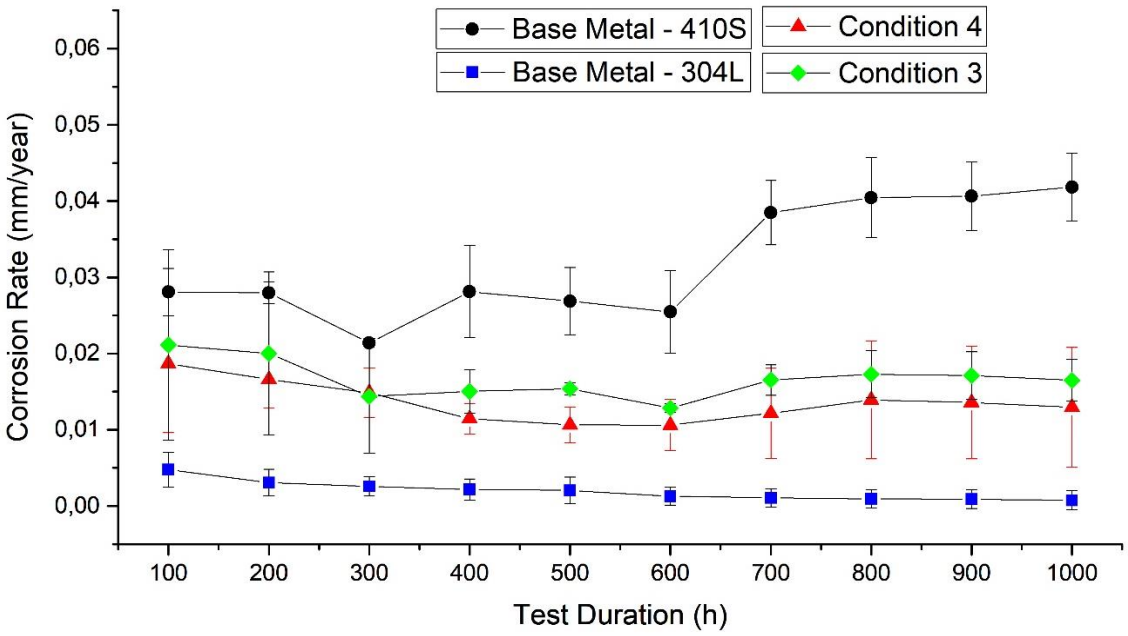

Source: The author.

6.5 Conclusions

Based on the experimental results of the evaluation of the corrosion resistance of dissimilar joints between ferritic stainless steel AISI 410S and austenitic stainless steel AISI 304L, produced by the FSW process, using the EPRP-DL technique and salt spray test, it was possible to conclude that:

1. It is possible to weld AISI 410S ferritic stainless steel and AISI 304L austenitic stainless steel in a dissimilar joint by the FSW process with low sensitization levels and corrosion rates in the salt spray test lower than the base metal of AISI 410S steel.
2. The heat input and temperature analysis prove the increase in heat input with the increased application of axial force. The thermal asymmetry between the advancing and retreating sides of dissimilar FSW joints AISI 304L/410S was verified, showing average temperatures on the advancing side are 60° higher than observed on the retreating side, which becomes a region critical to the occurrence of precipitates.
3. The DL-EPR tests, performed for the different weld conditions, showed whether the welding thermal cycle may promote microstructural changes, as carbide precipitation capable of making some areas of the weld susceptible to corrosion.
4. The low reactivation peaks observed on the advancing side of Condition 1 and Condition 2 represent the early stages of the AISI 410S steel sensitization process, with probable low carbide precipitation intensities and grains not entirely surrounded by these precipitates.
5. With the increase of the axial force to 35 kN in Condition 3 and to 40 kN in Condition 4, there is a considerable increase in the reactivation peak at points located between SZ and TMAZ of AISI 410S steel, a fact caused by the contribution of the increase in heat input and the consequent decrease in cooling rates in the material's sensitization process.
6. Macroscopically evaluating the upper and lower surfaces of the samples from conditions 3 and 4, after being submitted to 1000h in the salt spray test, it is possible to observe that for all conditions, the base metal of the AISI 410S steel

presents a considerable formation of macroscopic pits, with this surface degradation being more intense in regions close to HAZ for condition 4, welded with higher heat input.

7. Microscopically evaluating the cross-section of Condition 4, it is possible to observe, in the sample submitted to 1000h in the salt spray test, cavities in the grain boundaries in the stir zone of the AISI 410S steel in regions close to the contact zone between the material and the tool shoulder, corresponding to ditches due to probable precipitation of chromium carbides, probably $Cr_{23}C_6$.
8. Correlating the corrosion rate of conditions 3 and 4 with the base metal of AISI 410S and AISI 304L steel, it is possible to verify that welded conditions showed corrosion rates lower than the base metal of AISI 410S steel. Proving the superiority of corrosion resistance of welded joints concerning the ferritic stainless steel base metal.

6.6 Acknowledgments

The authors are grateful for the support given by the following Institutions: Universidade Federal do Ceará, Laboratório de Pesquisa e Tecnologia em Soldagem (LPTS) and The Analytical Center, in Brazil, and the Solid State Joining Processes, Helmholtz-Zentrum Geesthacht (HZG), in Germany. This study was financed in part by the Coordenação de Aperfeiçoamento de Pessoal de Nível Superior - Brasil (CAPES) - Finance Code 001, Brazilian funding agencies CNPq (Universal 472185/2011-0), and FUNCAP and CAPES (Project CI1-0050-00049.01.00/11 – International Cooperation).

6.7 References

ABIGAIL RODRÍGUEZ, N. et al. Analysis of sensitization phenomenon in friction stir welded 304 stainless steel. **Frontiers of Materials Science in China**, [s.l.], v. 4, n. 4, p. 415–419, 1 dez. 2010.

AHMAD, Z. CHAPTER 9 - SELECTION OF MATERIALS FOR CORROSIVE ENVIRONMENT. Em: AHMAD, Z. (Ed.). **Principles of Corrosion Engineering and Corrosion Control**. Oxford: Butterworth-Heinemann, 2006. p. 479–549.

ASTM G1 – 03. **Standard practice for preparing, cleaning, and evaluating corrosion test specimens.** ASM International, , 2010.

BILGIN, M. B.; MERAN, C. The effect of tool rotational and traverse speed on friction stir weldability of AISI 430 ferritic stainless steels. **Materials & Design**, [s.l.], v. 33, p. 376–383, jan. 2012.

CAETANO, G. DE Q. et al. Influence of rotation speed and axial force on the friction stir welding of AISI 410S ferritic stainless steel. **Journal of Materials Processing Technology**, [s.l.], v. 262, p. 430–436, 1 dez. 2018.

CAETANO, G. DE Q. et al. Intergranular corrosion evaluation of friction stir welded AISI 410S ferritic stainless steel. **Journal of Materials Research and Technology**, fev. 2019.

CHIANG, M. F. et al. Mechanical degradation of cold-worked 304 stainless steel in salt spray environments. **Journal of Nuclear Materials**, [s.l.], v. 422, n. 1, p. 58–68, 1 mar. 2012.

CHUAIPHAN, W.; SRIJAROENPRAMONG, L. Evaluation of microstructure, mechanical properties and pitting corrosion in dissimilar of alternative low cost stainless steel grade 204Cu and 304 by GTA welding joint. **Journal of Materials Research and Technology**, [s.l.], v. 9, n. 3, p. 5174–5183, 1 maio 2020.

COLEGROVE, P. A.; SHERCLIFF, H. R.; ZETTLER, R. Model for predicting heat generation and temperature in friction stir welding from the material properties. **Science and Technology of Welding and Joining**, [s.l.], v. 12, n. 4, p. 284–297, 1 maio 2007.

DOERR, C. et al. Evaluation of sensitization in stainless steel 304 and 304L using nonlinear Rayleigh waves. **NDT & E International**, [s.l.], v. 88, p. 17–23, 1 jun. 2017.

DU TOIT, M.; VAN ROOYEN, G. T.; SMITH, D. Heat-Affected Zone Sensitization and Stress Corrosion Cracking in 12% Chromium Type 1.4003 Ferritic Stainless Steel. **CORROSION**, [s.l.], v. 63, n. 5, p. 395–404, 1 maio 2007.

KHATAK, H. S.; RAJ, B. **Corrosion of Austenitic Stainless Steels: Mechanism, Mitigation and Monitoring**. [s.l.] Woodhead Publishing, 2002.

KIM, J. K. et al. Intergranular corrosion of Ti-stabilized 11wt% Cr ferritic stainless steel for automotive exhaust systems. **Corrosion science**, [s.l.], v. 51, n. 11, p. 2716–2723, 2009.

KIM, K. H. et al. Joint properties of ultra thin 430M2 ferritic stainless steel sheets by friction stir welding using pinless tool. **Journal of Materials Processing Technology**, [s.l.], v. 243, p. 381–386, 1 maio 2017.

KOVALEV, M. et al. Predicting the durability of zinc coatings based on laboratory and field tests. **E3S Web of Conferences**, [s.l.], v. 121, p. 01008, 1 jan. 2019.

LAKSHMINARAYANAN, A. K.; BALASUBRAMANIAN, V. Assessment of sensitization resistance of AISI 409M grade ferritic stainless steel joints using Modified Strauss test. **Materials & Design**, [s.l.], v. 39, p. 175–185, 2012a.

LAKSHMINARAYANAN, A. K.; BALASUBRAMANIAN, V. Sensitization resistance of friction stir welded AISI 409 M grade ferritic stainless steel joints. **The International Journal of Advanced Manufacturing Technology**, [s.l.], v. 59, n. 9, p. 961–967, 1 abr. 2012b.

LAKSHMINARAYANAN, A. K.; BALASUBRAMANIAN, V. Use of DL-EPR Test to Assess Sensitization Resistance of AISI 409M Grade Ferritic Stainless Steel Joints. **Journal of materials engineering and performance**, [s.l.], v. 22, n. 8, p. 2293–2303, 2013a.

LAKSHMINARAYANAN, A. K.; BALASUBRAMANIAN, V. Process Parameters Optimisation for Friction Stir Welding of AISI 409M Grade Ferritic Stainless Steel. **Experimental Techniques**, [s.l.], v. 37, n. 5, p. 59–73, 2013b.

LAYCOCK, N. J.; NEWMAN, R. C. Temperature dependence of pitting potentials for austenitic stainless steels above their critical pitting temperature. **Corrosion Science**, [s.l.], v. 40, n. 6, p. 887–902, 1 jun. 1998.

LI, W. J. et al. The effects of rolling and sensitization treatments on the stress corrosion cracking of 304L stainless steel in salt-spray environment. **Corrosion Science**, [s.l.], v. 68, p. 25–33, 1 mar. 2013.

LIENERT, T. J.; STELLWAG JR, W.; LEHMAN, L. Comparison of heat inputs: friction stir welding vs. arc welding. **American Welding Society**, p. 1–3, 2002.

LIPPOLD, J. C.; KOTECKI, D. J. **Welding Metallurgy and Weldability of Stainless Steels**. 1 edition ed. Hoboken, NJ: Wiley-Interscience, 2005.

LIU, F. C. et al. A review of friction stir welding of steels: Tool, material flow, microstructure, and properties. **Journal of Materials Science & Technology**, [s.l.], v. 34, n. 1, p. 39–57, 1 jan. 2018.

MAJIDI, A. P.; STREICHER, M. A. Four Nondestructive Electrochemical Tests for Detecting Sensitization in Type 304 and 304L Stainless Steels. **Nuclear Technology**, [s.l.], v. 75, n. 3, p. 356–369, 1 dez. 1986.

MISHRA, R. S.; MA, Z. Y. Friction stir welding and processing. **Materials Science and Engineering: R: Reports**, [s.l.], v. 50, n. 1–2, p. 1–78, 31 ago. 2005.

MOLLAPOUR, Y.; POURSAEIDI, E. Experimental and numerical analysis of Pitting Corrosion in CUSTOM 450 Stainless Steel. **Engineering Failure Analysis**, [s.l.], v. 128, p. 105589, 1 out. 2021.

MUKHERJEE, M.; PAL, T. K. Influence of Heat Input on Martensite Formation and Impact Property of Ferritic-Austenitic Dissimilar Weld Metals. **Journal of Materials Science & Technology**, [s.l.], v. 28, n. 4, p. 343–352, 1 abr. 2012.

MURR, L. E. A Review of FSW Research on Dissimilar Metal and Alloy Systems. **Journal of Materials Engineering and Performance**, [s.l.], v. 19, n. 8, p. 1071–1089, 1 nov. 2010.

NANDAN, R.; DEBROY, T.; BHADESHIA, H. K. D. H. Recent advances in friction-stir welding – Process, weldment structure and properties. **Progress in Materials Science**, [s.l.], v. 53, n. 6, p. 980–1023, ago. 2008.

PARK, S. H. C. et al. Corrosion resistance of friction stir welded 304 stainless steel. **Scripta Materialia**, [s.l.], v. 51, n. 2, p. 101–105, 1 jul. 2004.

PARVATHAVARTHINI, N. et al. Sensitization control in AISI 316L (N) austenitic stainless steel: defining the role of the nature of grain boundary. **Corrosion Science**, [s.l.], v. 51, n. 9, p. 2144–2150, 2009.

RAHIMI, S.; ENGELBERG, D. L.; MARROW, T. J. A new approach for DL-EPR testing of thermo-mechanically processed austenitic stainless steel. **Corrosion Science**, [s.l.], v. 53, n. 12, p. 4213–4222, 2011.

SANTOS, T. F. A.; IDAGAWA, H. S.; RAMIREZ, A. J. Thermal history in UNS S32205 duplex stainless steel friction stir welds. **Science and Technology of Welding and Joining**, [s.l.], v. 19, n. 2, p. 150–156, 1 fev. 2014.

SHIRI, S. G. et al. Diffusion in FSW Joints by Inserting the Metallic Foils. **Journal of Materials Science & Technology**, [s.l.], v. 29, n. 11, p. 1091–1095, 1 nov. 2013.

SILVA, C. C. et al. Alterações Microestruturais na ZAC do aço inoxidável ferrítico 410S-Efeitos sobre a resistência à corrosão. **Soldagem & Inspeção**, [s.l.], v. 11, 2006.

SILVA, C. C. et al. Austenitic and ferritic stainless steel dissimilar weld metal evaluation for the applications as-coating in the petroleum processing equipment. **Materials & Design**, [s.l.], v. 47, p. 1–8, 1 maio 2013.

SILVA, Y. C. DA. **Modeling and simulating of stainless steel joints by the Friction stir welding**. [s.l.]: [s.n.], 2021.

SONG, C. et al. In Situ Observation of Phase Transformation and Structure Evolution of a 12 pct Cr Ferritic Stainless Steel. **Metallurgical and Materials Transactions B**, [s.l.], v. 43, n. 5, p. 1127–1137, 2012.

TAJI, I.; MOAYED, M. H.; MIRJALILI, M. Correlation between sensitisation and pitting corrosion of AISI 403 martensitic stainless steel. **Corrosion Science**, [s.l.], v. 92, p. 301–308, 2015.

UDAY, M. B. et al. Advances in friction welding process: a review. **Science and Technology of Welding & Joining**, [s.l.], v. 15, n. 7, p. 534–558, 2010.

VAN NIEKERK, C. J.; DU TOIT, M.; ERWEE, M. W. Sensitization Of Aisi 409 Ferritic Stainless Steel During Low Heat Input Arc Welding. **Welding in the World**, [s.l.], v. 56, n. 5–6, p. 54–64, maio 2012.

VASCONCELOS, P. M. A.; SILVA, C. C. **Soldagem Autógena do Aço Inoxidável Ferrítico AISI 410S**. Fortaleza: Universidade Federal do Ceará - UFC, 2011.

WANG, H. et al. Microstructure and mechanical properties of dissimilar friction stir welded type 304 austenitic stainless steel to Q235 low carbon steel. **Materials Characterization**, [s.l.], v. 155, p. 109803, 1 set. 2019.

ZHOU, Y.; ENGELBERG, D. L. Time-lapse observation of pitting corrosion in ferritic stainless steel under bipolar electrochemistry control. **Journal of Electroanalytical Chemistry**, [s.l.], v. 899, p. 115599, 15 out. 2021.

7 CHAPTER 7: Assessment of joint configuration and welding parameters for AISI 316L and AISI 444 dissimilar welding by friction stir welding

7.1 Abstract

The welding parameters of the FSW process for dissimilar welding of AISI 444 and 316L steels were varied to provide a combination of acceptable surface finish, absence of voids, and total tool penetration. Three types of joint configurations were used, the first type was the butt-joint, the other two types were overlapped joints. The main welding parameters evaluated were the axial force ranging from 25 to 50 kN and the rotation speed varying between 350 and 450 rpm. The welding speed kept constant at 1.0 mm/s. The results show that a butt joint with ferritic stainless steel AISI 444 positioned on the advancing side and with an overlap joint with austenitic stainless steel AISI 316L at the top of the joint is possible to consolidate a stirred zone with absence voids at the interface 316L/444 and free from indentations or remaining lines that characterize the formation of root flaws. Thus, it is possible to produce dissimilar joints between AISI 444 and AISI 316L steels by the FSW process with a good surface finish and without defects in the stir zone.

Keywords: Friction stir welding; Stainless Steel; Axial Force; Rotation Speed; Defects.

7.2 Introduction

Stainless steels are Fe-based alloys, which have chromium content ranging from 11 to 30% and may contain Mo, Nb, and Ti additions, among others. Among stainless steels, austenitic is the most used commercially due to its high mechanical and corrosion resistance. They have a predominantly austenitic microstructure at room temperature, with a crystalline structure face-centered cubic (FCC). However, ferritic stainless steels are characterized by an essentially ferritic microstructure with a body-centered cubic structure (BCC). SMITH, W. F. (1993) observed that ferritic stainless steels supply approximately the same corrosion resistance but have lower ductility, toughness, and weldability when equated to austenitic stainless steels. However, LIPPOLD and KOTECKI, (2005) have shown that ferritic stainless steels can be used in various applications where resistance to pitting and/or stress corrosion cracking is more critical

than mechanical strength. Another significant advantage of ferritic stainless steels is the reduction or absence of nickel in its composition, as nickel is one of the most expensive alloying elements and considerably increases the price of austenitic stainless steels over ferritic stainless steels as reported by SILVA et al. (2007).

The lower application of ferritic stainless steels in the industry is related to the metallurgical problems arising from fusion welding processes. When subjected to the thermal welding cycles, these materials go through metallurgical changes, that can cause the in the weld the formation of some secondary phases and the precipitation of chromium nitrides and finely dispersed carbides in the HAZ, which impair their weldability and the mechanical and/or corrosion response of the welds. As noted by WEI et al. (2020) studying the anti-corrosion behavior of different ferritic stainless steels at elevated temperature and verified that the precipitation of laves phase in the vicinity of oxide film can affect the diffusion of reactive elements, growth mechanism and failure mechanism of oxide film compromising the corrosion resistance of these materials. The toughness is significantly affected as it is directly related to grain growth in the heat-affected zone and melting zone for autogenous welds, as shown by SILVA et al. (2008). Some studies have been addressed to improve the mechanical properties by modifying the metal transfer mode, as pointed out by MUKHERJEE et al. (2015), which investigated the effect of the current pulse mode compared to spray mode of metal transfer to enhance the microhardness and toughness of welded joints.

Austenitic stainless steels also confront some problems due to the appearance of undesirable metallurgical transformations when submitted to the thermal welding cycle, such as the sensitization, solidification crack and fase formation as delta ferrite and sigma phase. BARLA et al. (2021) analyzing the stress induced sensitization on heat affected zone (HAZ) in multipass weld of 304LN austenitic stainless steel and demonstrates the critical requirement of the control of residual stress in the arc weld of the steel because increase in magnitude of stress, irrespective of its compressive and tensile nature, enhances sensitization of HAZ. KADOI et al. (2020) investigating the effect of secondary phase formation such as MC carbide during the fusion welding on solidification cracking susceptibility of austenitic stainless steels, it is considered that the susceptibility dependent on the type, morphology, amount of secundary phases, as well as the start temperature during solidification corresponding to the composition of alloying elements and carbon.

In recent decades, Friction Stir Welding (FSW), a solid-state welding process developed by WAYNE et al. (1991), in The Welding Institute (TWI) in Cambridge, England, has revolutionized the joining of materials considered non-weldable or difficult to weld. MISHRA and MA, (2005) reported that this process uses a non-consumable tool that rotates and penetrates the joint, resulting in heating and plastic deformation of the materials to be joined and are heated to temperatures below those experienced in fusion welding.

Advantages commonly attributed to the FSW process include good weld strength and ductility, minimal residual stress and distortion, absence of melt-related defects, and fine-grained microstructure that increase resistance to traction and fatigue life as proposed by BILGIN and MERAN, (2012), DEBROY and BHADESHIA, (2013) e SATHIYA et al. (2006). The applications of the FSW process in similar welds of austenitic stainless steel show that, although the process did not prevent the formation of deleterious phases in the HAZ, an essential aspect for the success of the welds produced was the intense grain refining resulting from the dynamic recrystallization, as observed by PARK et al., (2003) and HAJIAN et al. (2015). However, ÇAM, (2011) mentions that in the application of the FSW process in ferritic stainless steels, there is some difficulty in recrystallization and grain refining, although studies show promising applications from the point of view of mechanical properties, what can be achieved with the correct setting of the FSW parameters like the welding speed that has the greatest inuence on tensile strength and impact toughness, followed by rotational speed and tool shoulder diameter, as observed by LAKSHMINARAYANAN and BALASUBRAMANIAN, (2011).

However, combining these aspects in dissimilar FSW welding between ferritic and austenitic stainless steel is still incipient. More detailed information about the influence of process parameters and the phenomena involved in producing faultless and good-quality welds becomes a scientific hot spot with technological appeal.

In the FSW process, rotational speed and axial force are the two main parameters directly related to heat generation, as shown by CAETANO et al. (2019) and MISHRA and MA, (2005). A proper combination of welding speed, axial force, and rotational speed is critical in achieving a balanced welding parameter set. Correct adjustment of these parameters allows the joining of metals, especially those with lower weldability when traditional fusion processes are applied, as noted by SILVA et al. (2008). For ferritic stainless steels, low heat input and high welding speed are recommended to minimize

ferritic grain growth and form a refined microstructure. CAETANO et al. (2018) and BILGIN and MERAN (2012) showed that such characteristics could very well be achieved using the FSW process. Thus, this work aims to determine the effect of different FSW welding parameters, such as rotation speed, axial force, torque, thickness, and joint configuration, in the production of dissimilar welds between austenitic stainless steel AISI 316L and ferritic stainless steel AISI 444, evaluating aspects such as the effects of these parameters on the plasticization process and consequently on the formation of defects.

7.3 Materials and Methods

The welds were made with plates of AISI 444 ferritic stainless steel, with 2 mm of thicknesses and AISI 316L austenitic stainless steel, presenting thicknesses of 4 mm or 3 mm, depending on the joint configuration used. The chemical composition analysis of the base metal was carried out by optical emission spectroscopy (Shimadzu model PA7000 Japan) and is presented in Table 7.1.

Table 7.1 - Chemical composition of the base metals (% weight).

Material	Elements											
	C	Si	Mn	P	S	Cr	Ni	Mo	Cu	Co	N	Fe
316L	0.026	0.56	0.84	0.029	<0.010	17.1	9.97	1.96	0.32	0.20	0.056	Bal.
444	0.017	0.53	0.16	0.47	<0.010	17.8	0.24	1.75	0.57	----	----	Bal

Source: The author.

The samples were joined by the FSW process at the Helmholtz-Zentrum Geesthacht (HZG) in Germany. All welds were made using the HZG Gantry System, and an inert gas (Ar) injection system was used to protect the material during the process at temperatures above 535 °C; these stainless steels react with the atmosphere. The welds were carried out in the load control mode with an integrated system to record the process data, such as depth of penetration, rotation speed, torque, forces applied to the tool and position of the tool over time. The welds were made with a tool of polycrystalline cubic boron nitride (PCBN). The tool had a conical diameter of 25 mm with a conical pin with a 9.2 mm diameter, and a length of 3.7 mm. The pin had a conical surface with opposing recesses, which were in the form of a spiral concerning the tool's axis of symmetry.

Three different joint configurations were welded. The first was a butt joint with 4 mm of thickness, with AISI 316L steel on the retreating side and AISI 444 steel on the advancing side as shown in Figure 7.1a. According to the tests carried out in the previous study performed by Caetano et al. 2021, the alloys' disposition was chosen where the benefits of positioning austenitic stainless steel on the retreating side and ferritic stainless steel on the advancing side were verified. The other two configurations are overlapping joints, one with the AISI 316L steel at the top and 5 mm of thickness in the stir zone and the other with the AISI 444 steel at the top and 6 mm of thickness in the stir zone, all showing an overlapping region of 70 mm in length, as shown in Figure 7.1b and Figure 7.1c.

Figure 7.1 – Three different weld joint configurations (a) Butt joint with AISI 316L steel on the retreating side (b) Overlap joint with the AISI 316L steel at the top and and (c) Overlap joint with the AISI 444 steel at the top.

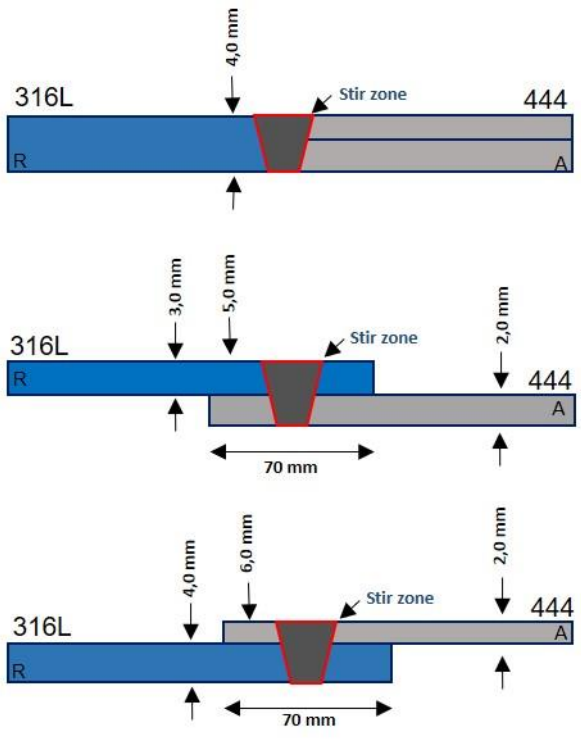

Source: The author.

To define the welding parameters, CAETANO et al. (2018) found the best set of parameters in similar FSW welding of AISI 444 ferritic stainless steel and AISI 316L austenitic stainless steel. Thus, in the butt joint, the rotation speed varied between 350 to

450 rpm and the axial force from 25 to 30 kN, as shown in Table 7.2. For the overlapped joints with the AISI 444 ferritic stainless steel on the AISI 316 steel plate, the rotation speed was kept at 450 rpm, and the axial force was varied between 20 and 30 kN. When the AISI 316L austenitic stainless steel was placed on the AISI 444 steel, the rotation speed was also varied from 350 to 450 rpm, but due to the higher strength and hardening of the AISI 316L steel, the axial force was increased to 45 and 50 kN, as shown by Table 7.4 and Table 7.3. For all 9 welded conditions, the welding speed was kept constant at 1.0 mm/s and the tool angle at 0º.

Table 7.2 – Welding Parameters for Dissimilar FSW Butt Welding of AISI 316L/444 Steels

Condition	Rotation Speed (rpm)	Axial Force (kN)	Advancing Side	Retreating Side
1	350	30	444	316L
2	450	25	444	316L
3	450	30	444	316L

Source: The author.

Table 7.3 - Welding Parameters for Dissimilar FSW Overlap Welding of AISI 316L/444 Steels

Condition	Rotation Speed (rpm)	Axial Force (kN)	Advancing Side	Retreating Side
4	350	50	444	316L
5	450	45	444	316L
6	450	50	444	316L

Source: The author.

Table 7.4 - Welding Parameters for Dissimilar FSW Overlap Welding of AISI 444/316L Steels

Condition	Rotation Speed (rpm)	Axial Force (kN)	Advancing Side	Retreating Side
7	450	20	444	316L
8	450	25	444	316L
9	450	30	444	316L

Source: The author.

These parameters were related to the heat input generated during FSW welding. Equation 1 shows the equivalent heat input total required for the joint consolidation among the different ways to calculate the heat generated during the FSW process. The coefficient of friction of the material, the pressure exerted by the tool, the rotational speed,

and the geometry of the tool used in welding are the inputs needed to determine that heat input and are calculated according to the equation formulated by DEQING et al., (2004):

$$E_t = \pi \,.\, \mu \,.\, Ps \,.\, Vr \,.\, \frac{D^2 + D\,.d + d^2}{45\,.(D+d)} \quad (1)$$

Where E_t is the equivalent total heat input (kJ/mm), μ is the coefficient of friction of the material, P_s is the pressure exerted by the tool on the material (Pa), Vr is the speed of rotation (rad/s), D is the shoulder diameter and d is the pin diameter (m). Another way to calculate the heat input to the FSW process is by using Equation 2 to determine the equivalent heat input per unit length per second, proposed by LIENERT et al., (2002):

$$E_l = \eta \,.\, \frac{T\,.Vr}{Vs} \quad (2)$$

Where El is the heat input per unit length (kJ/mm), η is the efficiency of the FSW process for steels, T the Torque (Nm), V_r the rotational speed (rad/s), and V_s the welding speed (mm/s).

7.4 Results and Discussions

7.4.1 Heat Generation

The process parameters directly affect the heat input, which strongly influences the heating and cooling rates of the thermal cycle and, consequently, the resulting microstructure. However, the heat input calculated based on the process parameters corresponds to equivalent heat input and not precisely to the heat input produced during the process since there are losses that are not considered, being the main ones by conduction and convection in the weld region

The main parameter related to the friction force at the interface between the base metals and the tool is the rotational speed. It is directly linked to heat generation during the welding process, as reported by BILGIN and MERAN, (2012) and LAKSHMINARAYANAN and BALASUBRAMANIAN, (2013). Frictional coupling of the tool surface with the base metal governs the heating mechanism and tool rotation, allowing the stirring and mixing of the material around the pin. Thus, the higher the rotational speed, the higher the process temperature, and this is due to increased friction

heating as proposed by COLEGROVE et al., (2007), MISHRA and MA, (2005) and UDAY et al. (2010).

The strong influence of the rotational speed on heat generation was observed among similar welds of AISI 410S ferritic stainless steel produced by FSW, as pointed out by CAETANO et al. (2018), which observed that the reduction in rotational speed from 800 to 450 rpm generates a drop-in equivalent heat input total and equivalent heat input per unit length around 0.4 kJ/mm, keeping the axial force constant. Observing Figure 7.2, in the dissimilar FSW welding between ferritic stainless steel AISI 444 and austenitic AISI 316L, it is possible to observe the influence of both the rotation speed and the axial force in the heat generation. Thus, between the condition 8 and 9 where the rotation speed is kept constant at 450 rpm and the axial force is increased from 25 to 30 kN, a variation of the equivalent heat input per unit length of around 0.13 kJ/mm are obtained. In the conditions 1 and 3, where the axial force was kept constant at 30 kN and in the condicions 4 and 6, where the axial force was kept constant at 50 kN, the increase in rotation speed from 350 to 450 rpm varied the equivalent heat input per unit length in around 0.29 kJ/mm, which demonstrates for the welded conditions the more significant influence of the rotation speed in the heat generation concerning the axial force.

Figure 7.2 – Equivalent heat input per unit length and total heat input calculated for the different conditions of AISI 316L/444 steels dissimilar welding performed by the FSW process.

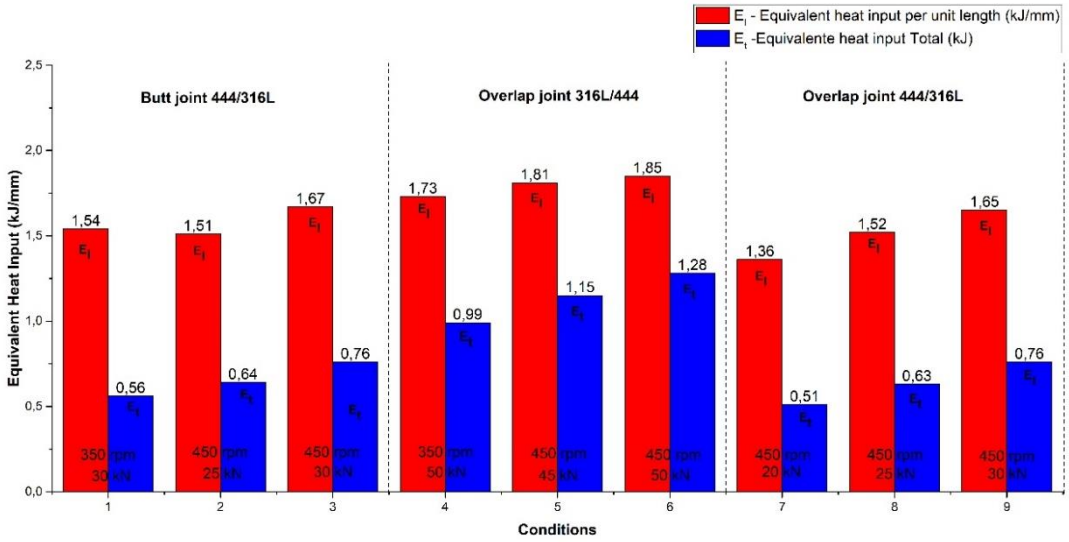

Source: The author.

7.4.2 Axial Force

By analyzing the graphics presented in Figure 7.3 , which presents the behavior of the axial force over the welding time, it is possible to observe that no significant oscillation in the axial force application was observed after start the steady regimen, independent of the joint configuration and rotation speed. The nine axial force curves over time initially exhibited similar behavior. It can be observed that during the initial stage of the process, a pressure gradient emerged along with the penetration channel development. This initial variation in axial force occurs due to increasing tool contact area between the tool and the joint surface as the tool progressively penetrates the steel and, consequently, the variation of the area where the force is being applied. The increase in axial force counterbalances the increase in pressure.

After the tool reaches the desired penetration depth, the pressure gradient decreases until it reaches a stable state. New abrupt changes in the axial force versus time curve, after reaching equilibrium, characterize a non-uniform application of force, compromising the material flow and resulting in defects. This information is essential to assure weld quality to the joint since it is directly related to the metal flow and the forging process. According to KIM et al. (2006), the instability in the axial force application

results in a lack of forging necessary to ensure the consolidation of the welded joint and, consequently, leads to the formation of volumetric defects.

Figure 7.3 - Axial force variation during the AISI 316L/444 steels dissimilar welding by the FSW process

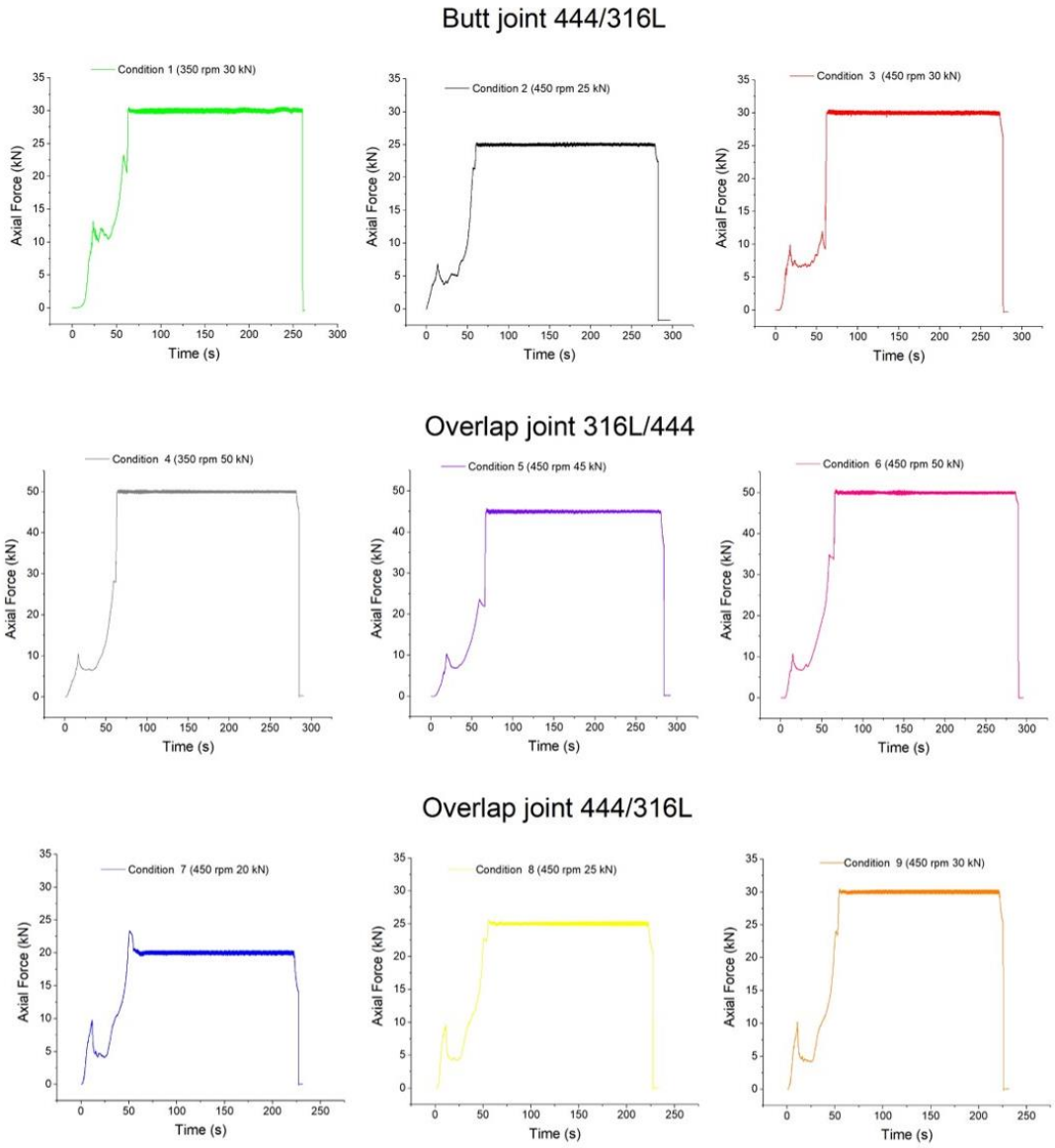

Source: The author.

KIM et al. (2006) claimed that there is a proper rotation and forward speed for each applied axial force that results in defect-free welds. It is possible to observe through the analysis of the axial force over the welding time that significant interference was not observed after stabilization, resulting in an adequate material flow, as observed by CAETANO et al., (2018) in similar welding of AISI 410S steel plates.

7.4.3 Torque

An analysis of the parameters applied for the 316L/444 stainless steels dissimilar welding by the FSW process shows that, for the nine welded conditions evaluated, the values and stability of the torque exerted by the tool varied according to changes in axial force, rotation speed, and joint configuration. Analyzing the torque between conditions 1, 2, and 3, welded in butt joint configuration, through Figure 7.4 a, it is possible to observe that the greater the axial force applied, the greater the torque values, because the more significant the force, the greater the pressure of the tool on the material and the greater torque is required to rotate the tool. Under these same conditions, welded in the butt joint configuration, the rotation speed also causes changes in torque, this value being higher the lower the rotation speed, this fact occurs due to the decrease in the heat input, generating a lesser degree of plasticity of the metal, being necessary a greater torque for the consolidation of the rotation tool. Thus, both the rotation speed and the axial force applied are determining factors in the evolution of torque during the FSW process.

As reported by LEITAO et al. (2012), which analyzed different aluminum alloys, varying the axial force between 7 and 20 kN and the rotation speed between 300 and 100 rpm, the strong influence of these parameters of the plastic behavior of the material and in determining significant changes in the torque values during the welding. In their tests, the author highlights the rotation speed of the tool among the main factors in determining the torque values due to its strong influence on the generation and distribution of frictional heat and the material flow.

In the analysis of the torque application between the conditions welded in overlap joints configurations, shown in Figure 7.4 b and Figure 7.4 c, despite the increase in the thickness of the stir zone, the influence of axial force and rotation speed was similar to that observed in the conditions welded in butt joints. However, the change in the positioning of the AISI 316L austenitic stainless steel, which has less elasticity modulus and yield strength limit and higher ultimate tensile strength compared to AISI 444 ferritic stainless steel, from the bottom in conditions 7, 8, and 9 to the top in conditions 4, 5 and 6 generated greater instability in the torque application over the welding time, the fact that may be related to greater difficulty in establishing an adequate degree of plasticization and material flow.

BUCHIBABU et al. (2017), evaluated the effect of the plate thickness and the mechanical resistance on the torque application, in different FSW welds of aluminum

alloys. Their results proved that if parameters such as axial force, rotation speed, and welding speed were kept constant, the increase of the thickness as well as the mechanical resistance of material, the welds generates higher torques, as these factors contribute to a greater transverse force and resulting in maximum shear stress.

Figure 7.4 - Torque variation during the AISI 444/316L steels dissimilar welding by the FSW process for the different joint configurations (a) Butt joint 316L/4444 (b) Overlap joint 316L/444 and (c) Overlap joint 444/316L.

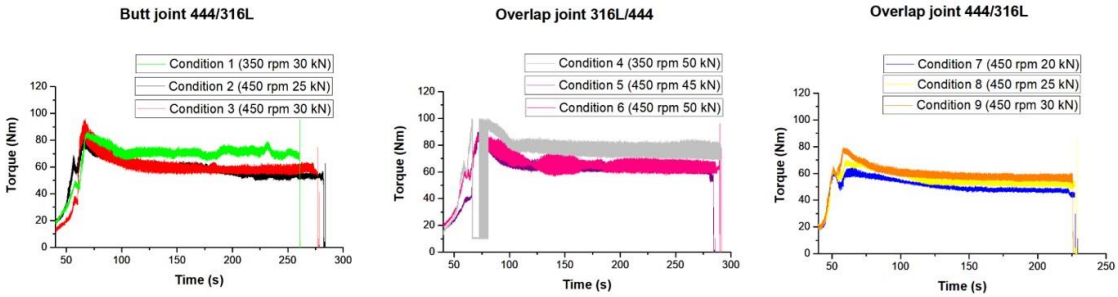

Source: The author.

7.4.4 Surface Finishing

An analysis of the surface of the AISI 444 / 316L dissimilar weld joints performed in this study shown that for conditions welded on butt joints as well as welded on overlap joints produced flashes. The flash produced is related both to variations in rotation speed and axial force and the instability of their application. Figure 7.5 a shows that between conditions 1, 2, and 3, welded in the butt joint configuration, that despite the absence of surface grooves along the stir zone, larger flash productions were observed as the axial force decreased and the rotation speed increased, as observed for Condition 2 welded with a decrease in axial force to 25 kN and an increase in rotation speed to 450 rpm.

Among the conditions welded in the overlap joint, due to changes in the positioning of the AISI 316L austenitic stainless steel plate between the top and bottom joint positions, the amount of flash production both increased as the axial force increased, as noted in Figure 7.5 c, between conditions 7, 8 and 9, with steel AISI 316L at the bottom of the joint, as the flash production decreased as the axial force decreased, as noted in Figure 7.5 b, between conditions 4, 5 and 6.

TRUEBA et al. (2015) noted that the increase in axial force causes an increase in heat input. In turn, higher welding temperatures in the FSW process cause a decrease in viscosity and the displacement of a greater amount of material by the tool pin, the difficulty of containing the metal displaced by the tool shoulder being the source of the most significant flash production. In another study, SILVA et al. (2020) performed a numerical investigation for the AISI 304L stainless steel to predict two essential defects commonly found in the FSW welds: the flashes and the wormholes. Their results have shown that the flashes were directly connected to the axial forces. The authors also proposed a coefficient called parameter Y, which depends on the minimum viscosity, the axial force, and the deformation rate. It has been pointed out that when the parameter Y increases, the tendency of flash forming is also increased.

However, at low axial forces, the flash production may be associated with instability in the application of FSW process parameters during welding, which can cause irregularities in the stir zone, generating an inadequate material flow, with losses of plasticized material. Between conditions 1, 2, 3 and 4, 5 and 6, which presented larger flash production with a reduction in axial force, although it is not possible to observe significant instabilities in the application of axial force in Figure 7.3, these conditions are those that present more significant variations in the application of torque over the welding time, as can be seen in Figure 7.4 a and Figure 7.4 b. These distinct origins in flash production were also observed in the analysis of defects in FSW welds carried out by THREADGILL (2007), which found that the flash production can occur both due to the high heat input as well as instabilities in the application of parameters such as axial force and torque.

Figure 7.5 - The surface finish of dissimilar welding of AISI 316L/444 steels by FSW process in a function of rotational speed and axial force applied for the different joint configurations (a) Butt joint 316L/44 (b) Overlap joint 316L/444 and (c) Overlap joint 444/316L.

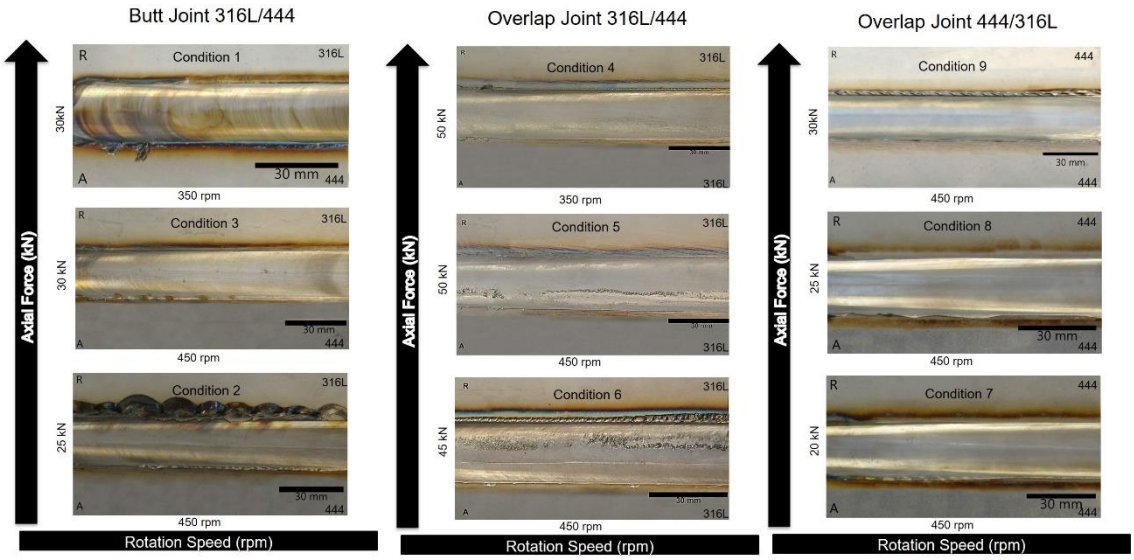

Source: The author.

Between the overlapping joints, the change in the positioning of AISI 316L austenitic stainless steel, with less elasticity modulus and yield strength limit and greater mechanical resistance, compared to AISI 444 ferritic stainless steel, for the top of the joint, generated the formation of significant superficial grooves, as can be seen in the conditions 5 and 6 at Figure 7.5 b. According to SAEID et al. (2008), these grooves in FSW welds of stainless steels are formed due to the use of high welding speeds combined with low heat input. However, they can also be associated with a greater mechanical response of the material in contact with the tool shoulder. Thus, the establishment of an elastoplastic state adequate to the material flow, generating greater friction of this material flow with the tool shoulder. Despite the formation of these irregular grooves, no superficial cavities in any of the nine welded conditions were observed.

Thus, in terms of surface finish, among the conditions welded in butt joint configuration stands out the Condition 3, welded with an axial force of 30 kN and a rotation speed of 450 rpm, and between the conditions welded in overlap joints to Condition 4, welded with an axial force of 50 kN and a rotation speed of 350 rpm, both with no excessive flash production, grooves, and surface cavities.

7.4.5 Defect Analysis

7.4.5.1 Butt Joints 444/316L

The analysis of the cross-section of AISI 444/316L stainless steel dissimilar joints, welded by the FSW process in the butt joint configuration, is shown in Figure 7.6. The joint consolidation without the presence of internal voids is verified only for Condition 1 as noted in Figure 7.6a, welded with a rotation speed of 350 rpm and an axial force of 30 kN. This result indicates that the material flow has reached an appropriate state of plasticization due to the heat intensity obtained by combining the parameters used. However, for conditions 2 and 3, welded with an axial force of 25 kN and 30 kN and rotation speed of 450 rpm, the presence of small voids in the stir zone in a region closer to the weld root and in the interface between AISI 316L and AISI 444 steel plates was observed. These voids were more significant for the welded condition with the lowest axial force.

According EMAMI et al. (2020), these voids in FSW butt joints and dissimilar between stainless steels are formed due to the establishment of a chaotic flow of plasticized material in the stir zone. They tend to be directed and more prominent on the advancing side compared to the retreating side, as can be seen in Figure 7.6b and Figure 7.6c because in this advanced region, the material flow is being directed opposite to the tool displacement, creating in this region a flow similar to a vortex that can lead, depending on the parameters used, to the formation of voids.

Figure 7.6 – Cross-section macrograph of the butt joint with AISI 316L austenitic stainless steel on the retreating side and AISI 444 ferritic stainless steel on the advancing side. (a) Condition 1 without defects (b) Condition 2 with root flaws and voids and (c) Condition 3 with root flaws and voids.

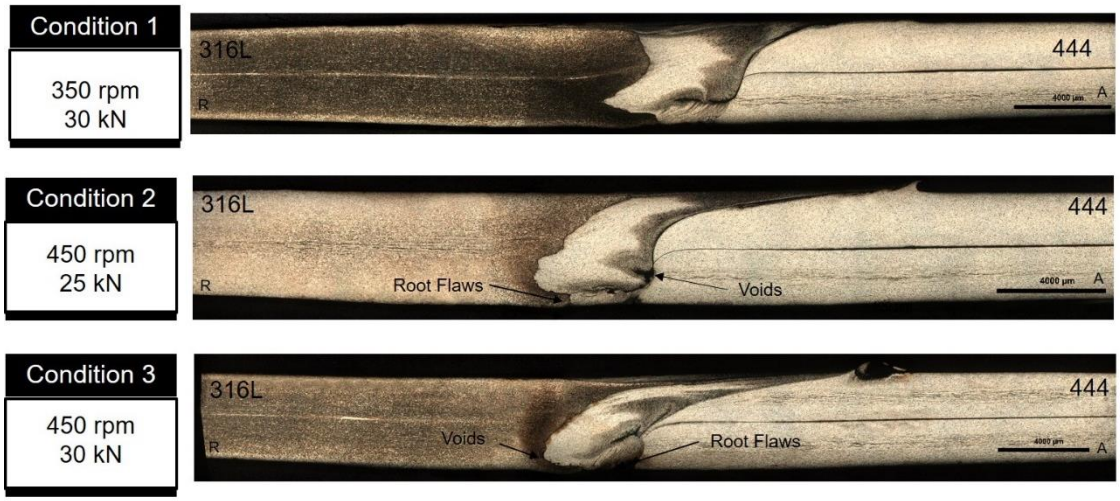

Source: The author.

The largest voids found in Condition 2 were ascribed to a lower interaction between the tool and the material due to the low axial force, and consequent reduction of the frictional force, and the decrease of the heat required to reach an elastoplastic state suitable for the material flow during the FSW process, similar behavior was observed by TONGNE et al., (2015). According to DOUDE et al. (2015), these voids in the stir zone in regions close to the weld root, as noted in Conditions 2 and 3, indicate a combination of parameters with values outside the recommended ideal set for proper material flow and setting of a defect-free FSW joint.

In Condition 2 and Condition 3, root flaws were found in the joins. In Condition 2, welded with an axial force of 25 kN, a root flaws was found with the observation of a line as can be seen in the Figure 7.7 (b). This line is referring to the interface of the plates and the lack of complete mixing between the steels in butt joint. Such defect is associated with insufficient penetration of the tool, as reported by EDWARDS and RAMULU (2015). KUMAR and KAILAS (2013), studying the material flow in dissimilar joints welded by the FSW process. These authors also observed the formation of this remaining line, finding its attenuation with the displacement of the tool to the advancing side concerning the center of the butt joint, with this the plastic deformation is intensified.

However, the study also shows that the presence of the remaining line did not change the mechanical strength properties of the material. In the present study, it was observed that when the axial force increases to 30 kN and the rotation speed was kept at 450 rpm (Condition 3), an excess of penetration occurs, resulting in the presence of grooves from the removal of the joint from the backplate, as can be seen in Figure 7.7 (c), also corresponding a root flaws of the joint.

Figure 7.7 – (a) Cross-section macrograph of the Condition 2 (b) Root flaws due to lack of penetration in Condition 2. (50x) (c) Root flaws due to excess penetration in Condition 3 (50x) and (d) Cross-section macrograph of the Condition 3.

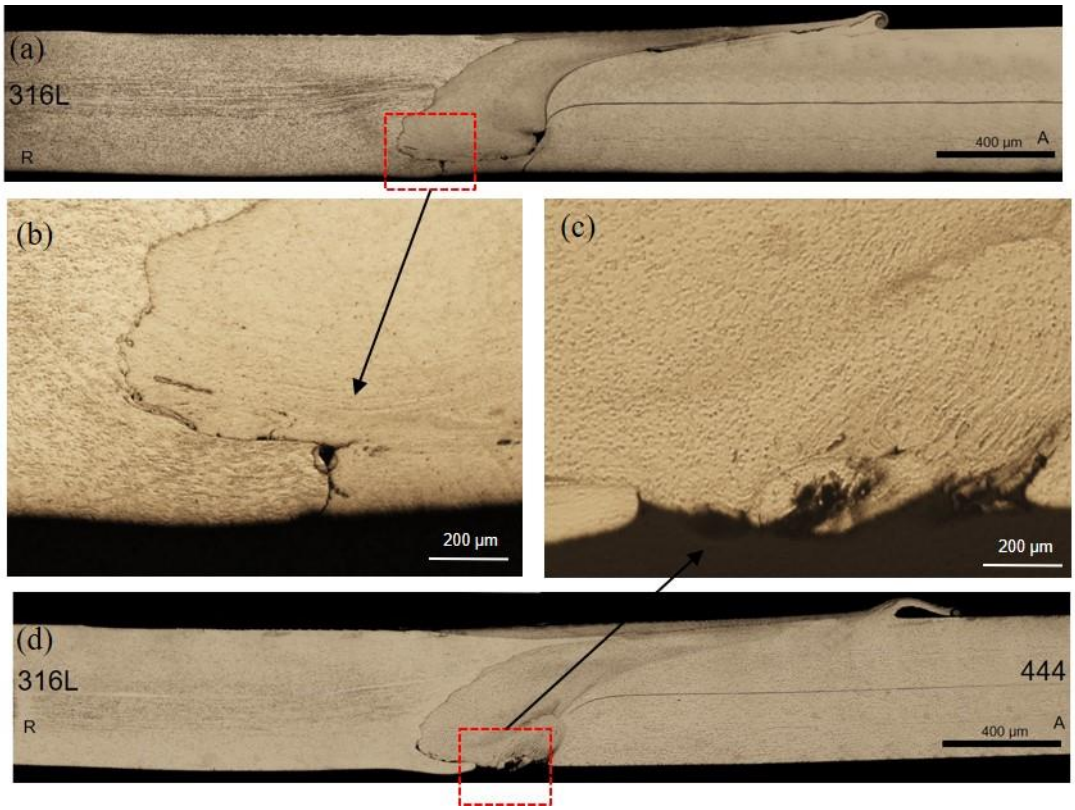

Source: The author.

CAETANO et al. (2018) observed different morphologies of root faults investigating FSW welds. According to the authors, this type of defect occurs under different mechanisms. It can be formed by both excessive or insufficient axial force application. When excessive axial force is applied, the tool pin tends to pass close to the backplate caused by the excessive penetration. The second mechanism results from a lesser interaction between the tool and the material and, consequently, reduce the friction force and the heat generation necessary to achieve an adequate state of plasticization of the

material flow, such as the failure observed in Condition 2 (Figure 7.7 a). An inadequate plasticization hinders the material's movement around the tool and the consolidation of the stir zone during the FSW process.

SHULTZ et al. (2010), reported that in FSW butt weld joints, the formation of root failures due to both excess or lack of penetration, and has demonstrated there is an optimum balance between axial force and tool angle, in which the production of FSW joints without root failures should be achieved, due to the greater immersion of the pin in the joint. This statement is in agreement with other few studies found in literature as reported by PIETRAS and WĘGLOWSKI. (2014) and TABATABAEIPOUR et al. (2016).

Although a correct balance between tool angle and axial force is a way to consolidate FSW butt joints without root defects, it can also be achieved by the correct balance between axial force and rotational speed without the need to vary the tool angle, as shown in Condition 1. In this case, reducing the rotation speed to 350 rpm together with the axial force at 30 kN was sufficient to consolidate an FSW joint with no root failure and no internal voids.

7.4.5.2 Overlap Joints 316L/444

Through surface and cross-section analysis of FSW welds produced by changing the austenitic stainless steel AISI 316L to the upper part of the overlap joint and decreasing the stir zone thickness to 5 mm, on conditions 4, 5, and 6 it is possible to verify great results in relation the consolidation of the FSW joint as shown in Figure 7.8. Among the different configurations of welded joints, in these overlap joints, the highest axial forces were used due to the positioning of the steel with greater mechanical resistance in the upper part of the joint, seeking a good relation between tool penetration and the degree of material plasticization. As the axial force increases from 45 kN to 50 kN and the rotation speed decreases, there is a decrease in surface grooves, improving the surface finish and the reduction of voids at the 316L/444 interface, making it possible to weld AISI 316L and AISI 444 steels in overlap joints, with AISI 316L steel on top, with no defects in the stir zone.

As observed by GEYER et al. (2021) during friction stir lap joint welding, hooks are systematically formed at the interface of dissimilar plates. Various hooks dimensions and shapes are observed in overlap joints according to the welding parameters. Contrary to butt joints, lap joints are very sensitive to material flow which leads to the formation of hooks on the stir zone as observed in the Figure 7.8. BATISTÃO et al. (2020), welding dissimilar joints between aluminum and steel using the FSW process in overlap configuration, observed smaller hooks of the material positioned at the bottom of the joint. Thus, it was observed at the top of the joint, as the rotation speed decreases, enabling better joint consolidation and a reduction in defects such as voids and tunnel defects in Condition 5 and voids in condition 6, as shown in Figure 7.9 (b) and Figure 7.9 (c). This decrease in the steel hook occurs due to the decrease in heat input caused by the decrease in the rotation speed and, consequently, the amount of AISI 444 steel positioned in the lower part of the joint being directed to the upper part, reducing and eliminating defects, as noted by XIONG et al. (2012) also in dissimilar FSW joints in overlap configuration.

Among other factors, the positioning of AISI 316L steel on the top of the joint configuration, which has higher flow stress and lower storage capacity for plastic deformation at high temperatures compared to AISI 444 steel, may have favored the excellent results, as the highest temperatures and tensions occur in the upper part of the joint, favoring this material a higher plasticity state concerning the conditions in which AISI 316L steel is placed in the lower part of the joint. This joint configuration provides a more significant amount of plasticized material towards the 316L/444 interface, consolidating in Condition 4 a stir zone without voids both in the central region and in the region closest to the weld root, as shown in Figure 7.8 (a).

Figure 7.8 - Cross-section macrograph of overlap joint with AISI 316L austenitic stainless steel on top. (a) Condition 4 without defects (b) Condition 5 with voids in the stir zone and (c) Condition 6 without defects.

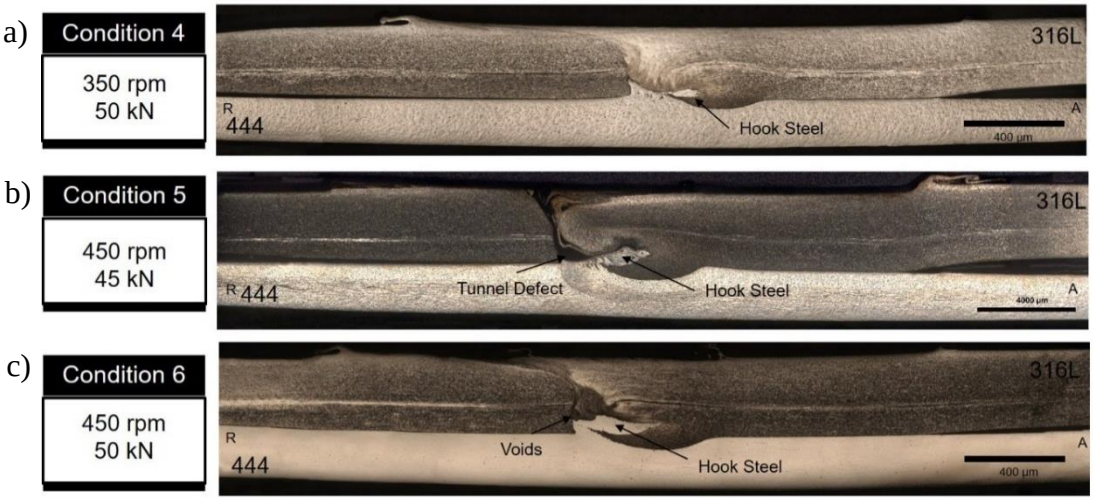

Source: The author.

Figure 7.9 – (a) Cross-section macrograph of the Condition 5 (b) Tunnel defect on the stir zone of Condition 5 (100x). (c) Voids on the stir zone of Condition 6 (200x) and (d) Cross-section macrograph of the Condition 6.

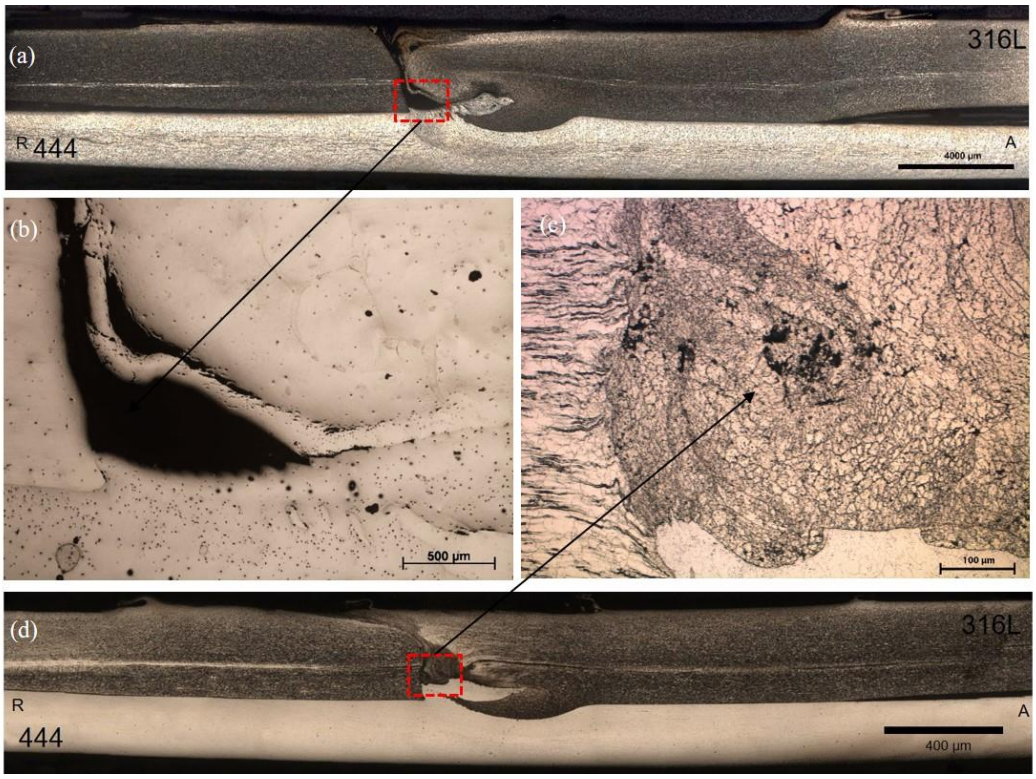

Source: The author.

7.4.5.3 Overlap Joints 444/316L

The macrographs evaluation along the cross-section of FSW samples in overlap joint configuration, with AISI 444 ferritic stainless steel on the top of the joint, proves the increase of flash production as the axial force increases. Additionally, more significant formation of these flashes on the retreating side compared with the advancing side, as shown in Figure 7.10 . According to BOGAARD et al. (1993) and MANDAL et al. (2009), ferritic stainless steel has higher thermal diffusivity and lower flow stress compared to austenitic stainless steels at high temperature. Thus, in the overlap joint, with AISI 444 steel at the top, as the axial force increases and the temperature rises, a greater flow of AISI 444 steel in the elastoplastic state is reached on the advancing side and directed to the retreating side, in this situation the tool shoulder is insufficient to restrain the large volume of plasticized material. Among the welded conditions tested in this study, the conditions 7 to 9 were selected for a comparison, considering different intensities of flash production as function of the axial force variation between the overlapping joints, as shown in Figure 7.11 (b) for Condition 7, welded with an axial force of 20 kN and in the Figure 7.11 (d) for condition 9, welded with an axial force of 30 kN.

The presence of voids in the 444/316L interface region, for the overlap joint with AISI 444 ferritic stainless steel at the top decreases considerably as the axial force increases, however even for condition 9, welded with the highest axial force, voids at the 444/316L interface are still observed, as shown in Figure 7.11 (e). This lack of filling or tunnel defect consists of internal regions of the welded joint without material, forming voids along the length of the weld. The presence of these voids in all conditions welded with this configuration reflects, in addition to the parameters used, the insufficiency of the welding tool to adequately consolidate a stirred zone of 6 mm thick.

In addition, the positioning of AISI 316L austenitic stainless steel in the bottom of the joint and, therefore, being distanced from the region of contact with the tool shoulder and of more significant heat input and intensity of plastic deformation in FSW joints contributing to the formation of an inadequate material flow in the stir zone, with the formation of voids in the interface region between the welded materials. According to SATYANARAYANA et al. (2005), austenitic stainless steel has a high flow stress compared to ferritic stainless steels, requiring greater intensities of plastic deformation to establish an adequate material flow. FARGAS et al. (2008) shown that the austenitic

phase is less soft and plastic at high temperature, which allows it to accommodate three to five times less deformation than the ferritic phase.

According to MISHRA and MA, (2005), these voids are caused by the lack of heat produced by an inadequate combination of parameters, such as low rotation speeds and low axial forces, which generate less friction and less plastic deformation. KUMAR and KAILAS (2008) state that, in addition to low heating, the lack of pressure on the tool's shoulder on the material also affects the flow, preventing it from filling the entire weld region.

Figure 7.10 - Cross-section macrograph of overlap joint with AISI 444 ferritic stainless steel on top. (a) Condition 7 with the lowest flash production and voids (b) Condition 8 with flash production and voids and (c) Condition 9 with the highest flash production and voids.

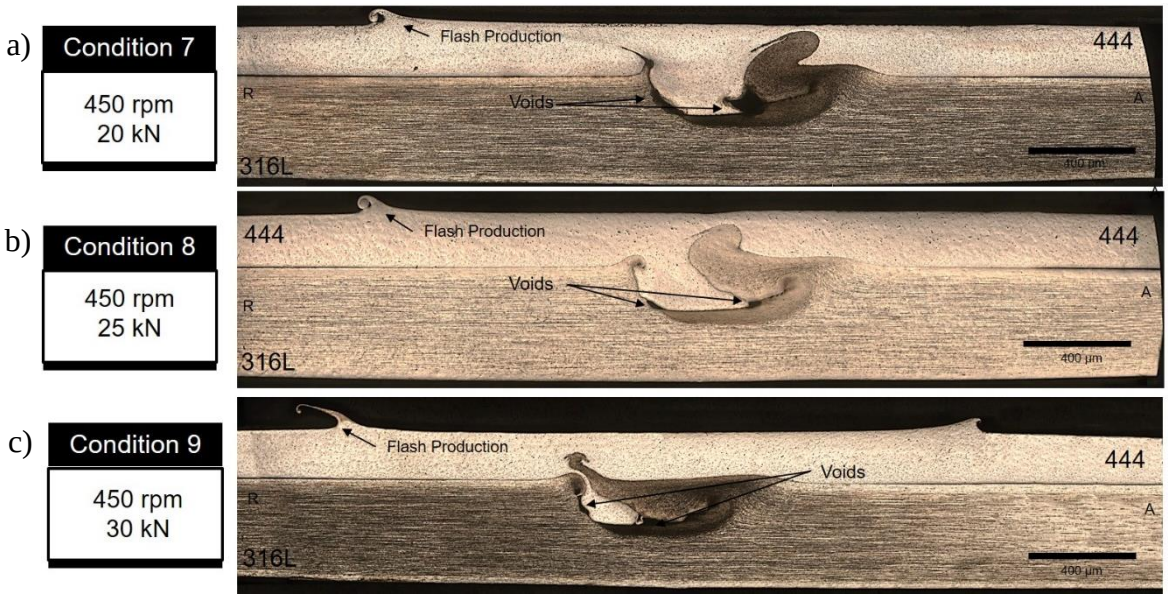

Source: The author.

Figure 7.11 – (a) Cross-section macrograph of the Condition 7 (b) Small flash production on the retreating side of Condition 7 (100x) (c) Voids at the 316L/444 interface of the overlap joint in the stir zone of Condition 7 (100x) (d) Larger flash production on the retreating side of Condition 9 (50x) (e) Voids at the 316L/444 interface in the center of the stir zone in Condition 9 (100x) and (f) Cross-section macrograph of the Condition 9.

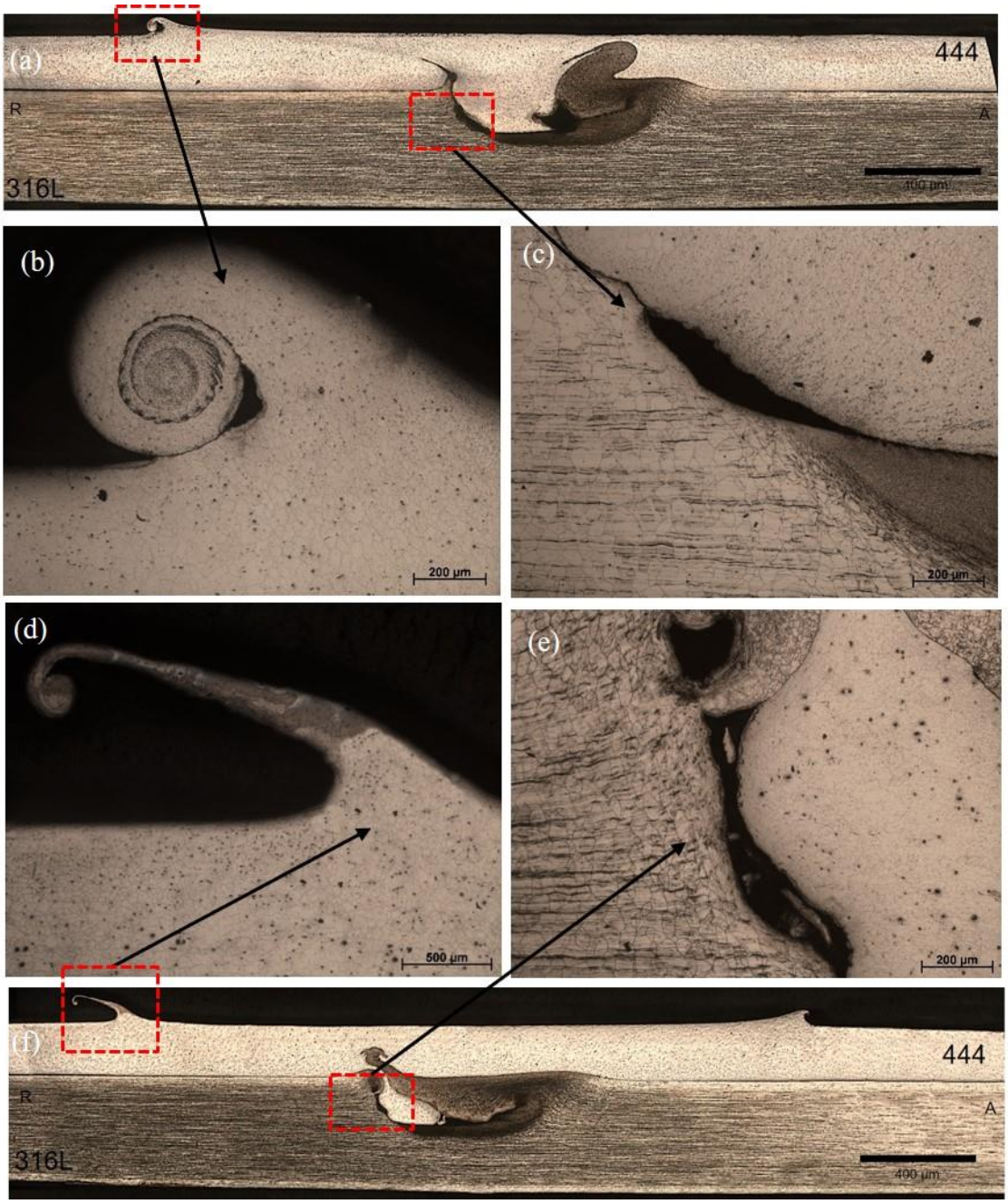

Source: The author.

Therefore, the analysis of different joint configurations and combinations of parameters show that it is possible to produce dissimilar joints between AISI 444 ferritic stainless steel and AISI 316L austenitic stainless steel by the FSW process, with good surface finish and no defects in the stir zone. This achievement is possible thanks to use of the right choice of parameters that ensure an adequate heat intensity to plasticize the material flow for each joint configuration. In this study, a well-consolidated weld with good quality was achieved for the dissimilar butt joint, with AISI 444 ferritic stainless steel placed on the advancing side and AISI 316L austenitic stainless steel placed on the retreating side. For this joint configuration, the best welding parameter combination found was an axial force of 30 kN with a rotation speed of 350 rpm and keeping the welding speed at 1mm/s, as shown in Condition 1. Regarding the lap-joint configuration, the best result was achieved when theAISI 316L austenitic stainless steel was placed over the AISI 444 ferritic stainless steel. An increase of the axial force to 50 kN and keeping the rotation speed at 350 rpm and the welding speed at 1 mm/s was successfully applied, as observed in Condition 4. In both conditions, consolidation of a stir zone with the absence of voids at the 316L/444 interface and free of recesses or remaining lines that characterize the formation of root flaws was observed.

7.5 Conclusions

Based on the experimental results of the FSW process parameters and their implications in the formation of defects for the dissimilar welding between the AISI 444 ferritic stainless steel and the AISI 316L austenitic stainless steel, it was possible to conclude that:

1. Among the different configurations of dissimilar joints between AISI 444 ferritic stainless steel and AISI 316L austenitic stainless steel welded by the FSW process, conditions with good surface finish and no defects in the stir zone was observed in the butt joint configuration welds, with AISI 444 ferritic stainless steel placed on the advancing side and AISI 316L austenitic stainless steel placed on the retreating side.

2. Among the conditions welded by the FSW process in overlaplap joint configuration, only the conditions with AISI 316L austenitic stainless steel on top of the joint, reached a well-consolidated weld with good quality.
3. With the proper combination of welding parameters, it is possible to successfully weld a dissimilar joint between AISI 444 ferritic stainless steel and AISI 316L austenitic stainless steel, producing a joint with no voids at the 316L/444 interface and free of recesses or remaining lines that characterize the formation of root flaws.
4. Through the analysis of the axial force over the welding time, it is possible to observe that in all welded conditions, there is the absence of significant interferences in the application of force that lead to lack of forging and good consolidation of the joint and formation of voids.
5. In the overlap joints, the change in the positioning of the AISI 316L austenitic stainless steel from the bottom in conditions 7, 8, and 9 to the top in conditions 4, 5, and 6 generated greater instability in the torque application over the welding time, a fact that may be related to greater difficulty in establishing an adequate degree of plasticization and material flow of the Steel AISI 316L.
6. The production of dissimilar joints between stainless steel AISI 444/316L welded by the FSW process without root flaws can be obtained through a correct balance between the axial force and rotation speed, allowing a greater immersion of the pin in the welded joint.
7. It is possible to produce good dissimilar welds of AISI 444 ferritic stainless steel and AISI 316L austenitic stainless steel by the FSW process through a butt joint with AISI 316L austenitic stainless steel on the retreating side, with an axial force of 30 kN and speed of 350 rpm rotation.
8. Dissimilar FSW joints of AISI 444 ferritic stainless steel and AISI 316L austenitic stainless steel are also satisfactorily consolidated through an overlap joint with AISI 316L austenitic stainless steel on top, increasing the axial force to 50 kN and maintaining the rotation speed at 350 rpm.

7.6 Acknowledgments

The authors are grateful for the support given by the following Institutions: Universidade Federal do Ceará, Laboratório de Pesquisa e Tecnologia em Soldagem (LPTS), in Brazil, and the Solid State Joining Processes, Helmholtz-Zentrum Geesthacht (HZG), in Germany. This study was financed in part by the Coordenação de Aperfeiçoamento de Pessoal de Nível Superior - Brasil (CAPES) - Finance Code 001, Brazilian funding agencies CNPq (Universal 472185/2011-0), and FUNCAP and CAPES (Project CI1-0050-00049.01.00/11 – International Cooperation).

7.7 References

BARLA, N. A. et al. Simulated stress induced sensitization of HAZ in multipass weld of 304LN austenitic stainless steel. **Journal of Manufacturing Processes**, [s.l.], v. 62, p. 784–796, 1 fev. 2021.

BATISTÃO, B. F. et al. Characterization of dissimilar friction stir welded lap joints of AA5083 and GL D36 steel. **Journal of Materials Research and Technology**, [s.l.], v. 9, n. 6, p. 15132–15142, 1 nov. 2020.

BILGIN, M. B.; MERAN, C. The effect of tool rotational and traverse speed on friction stir weldability of AISI 430 ferritic stainless steels. **Materials & Design**, [s.l.], v. 33, p. 376–383, jan. 2012.

BOGAARD, R. H. et al. Thermophysical properties of stainless steels. **Thermochimica Acta**, [s.l.], v. 218, p. 373–393, 3 maio 1993.

BUCHIBABU, V.; REDDY, G. M.; DE, A. Probing torque, traverse force and tool durability in friction stir welding of aluminum alloys. **Journal of Materials Processing Technology**, [s.l.], v. 241, p. 86–92, 2017.

CAETANO, G. DE Q. et al. Influence of rotation speed and axial force on the friction stir welding of AISI 410S ferritic stainless steel. **Journal of Materials Processing Technology**, [s.l.], v. 262, p. 430–436, 1 dez. 2018.

CAETANO, G. DE Q. et al. Intergranular corrosion evaluation of friction stir welded AISI 410S ferritic stainless steel. **Journal of Materials Research and Technology**, fev. 2019.

ÇAM, G. Friction stir welded structural materials: beyond Al-alloys. **International Materials Reviews**, [s.l.], v. 56, n. 1, p. 1–48, 1 jan. 2011.

CHUAIPHAN, W.; SRIJAROENPRAMONG, L. Microstructure, mechanical properties and pitting corrosion of TIG weld joints alternative low-cost austenitic stainless steel grade 216. **Journal of Advanced Joining Processes**, [s.l.], v. 2, p. 100027, 1 jul. 2020.

COLEGROVE, P. A.; SHERCLIFF, H. R.; ZETTLER, R. Model for predicting heat generation and temperature in friction stir welding from the material properties. **Science and Technology of Welding and Joining**, [s.l.], v. 12, n. 4, p. 284–297, 1 maio 2007.

DA SILVA, Y. C. et al. Numerical investigation of the influence of FSW parameters on the heat and mass transfer of austenitic stainless steels. **Welding in the World**, [s.l.], v. 64, n. 12, p. 2019–2032, 1 dez. 2020.

DEBROY, T.; BHADESHIA, H. Friction stir welding of dissimilar alloys–a perspective. **Science and Technology of Welding & Joining**, [s.l.]: [s.n.], 2013.

DEQING, W.; SHUHUA, L.; ZHAOXIA, C. Study of friction stir welding of aluminum. **Journal of materials science**, [s.l.], v. 39, n. 5, p. 1689–1693, 2004.

DOUDE, H. et al. Optimizing weld quality of a friction stir welded aluminum alloy. **Journal of Materials Processing Technology**, [s.l.], v. 222, p. 188–196, 2015.

EDWARDS, P. D.; RAMULU, M. Material flow during friction stir welding of Ti-6Al-4V. **Journal of Materials Processing Technology**, [s.l.], v. 218, p. 107–115, 2015.

EMAMI, S. et al. Dissimilar friction stir welding of AISI 430 ferritic and AISI 304L austenitic stainless steels. **Archives of Civil and Mechanical Engineering**, [s.l.], v. 20, n. 4, p. 131, 18 out. 2020.

GEYER, M. et al. Investigations on the material flow and the role of the resulting hooks on the mechanical behaviour of dissimilar friction stir welded Al2024-T3 to Ti-6Al-4V

overlap joints. **Journal of Materials Processing Technology**, [s.l.], v. 292, p. 117057, 1 jun. 2021.

HAJIAN, M. et al. Microstructure and mechanical properties of friction stir processed AISI 316L stainless steel. **Materials & Design**, [s.l.], v. 67, p. 82–94, 15 fev. 2015.

KADOI, K. et al. Effect of MC carbide formation on weld solidification cracking susceptibility of austenitic stainless steel. **Journal of Alloys and Compounds**, [s.l.], v. 828, p. 154423, 5 jul. 2020.

KIM, Y. G. et al. Three defect types in friction stir welding of aluminum die casting alloy. **Materials Science and Engineering: A**, [s.l.], v. 415, n. 1, p. 250–254, 2006.

KUMAR, K.; KAILAS, S. V. The role of friction stir welding tool on material flow and weld formation. **Materials Science and Engineering: A**, [s.l.], v. 485, n. 1, p. 367–374, 2008.

KUMAR, K.; KAILAS, S. V. Positional dependence of material flow in friction stir welding: analysis of joint line remnant and its relevance to dissimilar metal welding. **Science and Technology of Welding & Joining**, 2013.

LAKSHMINARAYANAN, A. K.; BALASUBRAMANIAN, V. Understanding the parameters controlling friction stir welding of AISI 409M ferritic stainless steel. **Metals and Materials International**, [s.l.], v. 17, n. 6, p. 969–981, 1 dez. 2011.

LAKSHMINARAYANAN, A. K.; BALASUBRAMANIAN, V. Process Parameters Optimisation for Friction Stir Welding of AISI 409M Grade Ferritic Stainless Steel. **Experimental Techniques**, [s.l.], v. 37, n. 5, p. 59–73, 2013.

LEITAO, C.; LOURO, R.; RODRIGUES, D. M. Using torque sensitivity analysis in accessing Friction Stir Welding/Processing conditions. **Journal of Materials Processing Technology**, [s.l.], v. 212, n. 10, p. 2051–2057, 2012.

LIENERT, T. J.; STELLWAG JR, W.; LEHMAN, L. Comparison of heat inputs: friction stir welding vs. arc welding. **American Welding Society**, p. 1–3, 2002.

LIPPOLD, J. C.; KOTECKI, D. J. **Welding Metallurgy and Weldability of Stainless Steels**. 1 edition ed. Hoboken, NJ: Wiley-Interscience, 2005.

MANDAL, S. et al. Constitutive equations to predict high temperature flow stress in a Ti-modified austenitic stainless steel. **Materials Science and Engineering: A**, [s.l.], v. 500, n. 1, p. 114–121, 25 jan. 2009.

MISHRA, R. S.; MA, Z. Y. Friction stir welding and processing. **Materials Science and Engineering: R: Reports**, [s.l.], v. 50, n. 1–2, p. 1–78, 31 ago. 2005.

MUKHERJEE, M. et al. Enhancement of Microstructural and Mechanical Properties by Pulse Mode of Metal Transfer in Welded Modified Ferritic Stainless Steel. **ISIJ International**, [s.l.], v. 55, n. 7, p. 1439–1447, 2015.

PARK, S. H. C. et al. Rapid formation of the sigma phase in 304 stainless steel during friction stir welding. **Scripta Materialia**, [s.l.], v. 49, n. 12, p. 1175–1180, dez. 2003.

PIETRAS, A.; WĘGLOWSKI, M. S. Imperfections in FSW joints and NDT methods of their detection. **Biuletyn Instytutu Spawalnictwa w Gliwicach**, [s.l.], v. Vol. 58, No. 2, 2014.

SAEID, T. et al. Effect of friction stir welding speed on the microstructure and mechanical properties of a duplex stainless steel. **Materials Science and Engineering: A**, [s.l.], v. 496, n. 1, p. 262–268, 25 nov. 2008.

SATHIYA, P.; ARAVINDAN, S.; HAQ, A. N. Effect of friction welding parameters on mechanical and metallurgical properties of ferritic stainless steel. **The International Journal of Advanced Manufacturing Technology**, [s.l.], v. 31, n. 11–12, p. 1076–1082, 21 jan. 2006.

SATYANARAYANA, V. V.; MADHUSUDHAN REDDY, G.; MOHANDAS, T. Dissimilar metal friction welding of austenitic–ferritic stainless steels. **Journal of Materials Processing Technology**, [s.l.], v. 160, n. 2, p. 128–137, 20 mar. 2005.

SHULTZ, E. F. et al. Effect of compliance and travel angle on friction stir welding with gaps. **Journal of Manufacturing Science and Engineering**, [s.l.], v. 132, n. 4, p. 041010, 2010.

SILVA, C. C. et al. Alterações Microestruturais na ZAC do aço inoxidável ferrítico 410S-Efeitos sobre a resistência à corrosão. **Soldagem & Inspeção**, [s.l.], v. 11, 2006.

SILVA, C. C. et al. High-temperature hydrogen sulfide corrosion on the heat-affected zone of the AISI 444 stainless steel caused by Venezuelan heavy petroleum. **Journal of Petroleum Science and Engineering**, [s.l.], v. 59, n. 3–4, p. 219–225, nov. 2007.

SILVA, C. C. et al. Microstructural characterization of the HAZ in AISI 444 ferritic stainless steel welds. **Materials Characterization**, [s.l.], v. 59, n. 5, p. 528–533, maio 2008.

SMITH, W. F. **Structure and Properties of Engineering Alloys**. n. 2, [s.l.], McGraw-Hill (New York), 1993.

TABATABAEIPOUR, M. et al. Non-destructive ultrasonic examination of root defects in friction stir welded butt-joints. **NDT & E International**, [s.l.], v. 80, p. 23–34, 1 jun. 2016.

THREADGILL, P. L. Terminology in friction stir welding. **Science and Technology of Welding and Joining**, v. 12, n. 4, p. 357–360, 1 maio 2007.

TONGNE, A. et al. Banded structures in friction stir welded Al alloys. **Journal of Materials Processing Technology**, [s.l.], v. 221, p. 269–278, 2015.

UDAY, M. B. et al. Advances in friction welding process: a review. **Science and Technology of Welding & Joining**, [s.l.], v. 15, n. 7, p. 534–558, 2010.

WAYNE M, THOMAS WM, NORRIS IM, NICHOLAS ED, NEEDHAM; JC, MURCH MG, TEMPLE-SMITH P, DAWES CJ. **Friction stir welding process developments and variant techniques**, Cambridge, TWI, 1991.

WEI, L. et al. Precipitation Behavior of Laves Phase in the Vicinity of Oxide Film of Ferritic Stainless Steel: Selective Oxidation-Induced Precipitation. **Oxidation of Metals**, [s.l.], v. 93, n. 1, p. 195–213, 1 fev. 2020.

XIONG, J. T. et al. High strength lap joint of aluminium and stainless steels fabricated by friction stir welding with cutting pin. **Science and Technology of Welding and Joining**, [s.l.], v. 17, n. 3, p. 196–201, 1 abr. 2012.

8 CHAPTER 8: Microstructure evolution of dissimilar AISI 316L and AISI 444 stainless steel joints by the friction stir welding

8.1 Abstract

The present study investigated the main microstructural characteristics of dissimilar welding between AISI 316L and AISI 444 stainless steel. In the welds, 25 to 50 kN axial forces were applied, varying the rotation speed between 350 and 450 rpm and keeping the welding speed constant at 1 mm/s. Three types of joint configurations were used; the first type was the butt-joint, and the other two types were overlapped joints. Under all conditions, relevant microstructural changes were not observed between BM and HAZ. In the TMAZ and SZ of the butt joint, the increase in the axial force and the rotational speed shows austenitic and ferritic grains that are poorly refined at the top and more deformed grains with intense refining at the bottom. In the overlap joints, the positioning of AISI 316L steel, with low-SFE and easier recrystallisation at the top of the joint, provided a more negligible difference in deformed and recrystallised grains between the upper and lower ZTMA and SZ, where AISI 444 steel is positioned. In none of the welded conditions is it possible to observe areas of excessive grain growth and formation of undesirable phases such as Chi, Sigma and Laves. Despite these phases being predicted in the phase diagram of these steels in the temperature range reached in these dissimilar FSW welds. Therefore, it is possible to produce dissimilar joints between AISI 444 and AISI 316L steels by the FSW process with excellent grain refinement, absence of defects and undesirable phases and high cohesion between the two materials.

Keywords: Friction stir welding; Stainless Steel; Microstructure

8.2 Introduction

Welding is one of the most used manufacturing processes because products with complex shapes and designs can be effectively joined, repaired and coated. However, obtaining a successful joint is influenced mainly by the type of welding process, as well as the correct choice of input parameters and their impact on the microstructural evolution

of welded materials. As noted by LO; SHEK and LAI (2009), most stainless steels, when subjected to welding thermal cycles of fusion welds, these materials go through metallurgical changes, which compromise their weldability and the mechanical and/or corrosion response of welds.

In ferritic stainless steels (FSS), SILVA et al. (2008) observed that the toughness of AISI 444 steel is significantly affected in autogenous fusion welds, as it is directly related to grain growth in the heat-affected zone and melting zone. In these welds, the precipitation of CrN, Cr_7C_3, $Cr_{23}C_6$, sigma, chi, and Fe_2Nb Laves phase could have also decreased the corrosion resistance. Austenitic stainless steels (ASS) also confront some problems due to undesirable metallurgical transformations when submitted to the thermal welding cycle, such as the sensitisation, solidification crack and phase formation as delta ferrite and sigma phase. KUMAR; SINGH and SINGH UPPAL (2022), studying the influence of the GTAW process on metallurgical behaviour of AISI 316L stainless steel, showed that despite the technique being efficient in increasing microhardness and positive implications for other surface properties, the formation of interdendritic carbides along the δ–γ interface is inevitable.

These microstructural problems related to fusion and solidification can be avoided by using solid-state welding processes, such as the Friction Stir Welding (FSW) process developed by The Welding Institute (TWI) by THOMAS et al. (1991) in Cambridge, England. FSW is a solid-state welding process that uses a non-consumable tool, which rotates and penetrates the joint, resulting in heating and plastic deformation of the materials to be joined. MISHRA and MA (2005) claim that there are significant differences in the microstructure of the joints welded by the FSW process compared to conventional processes. As noted by DEBROY and BHADESHIA (2013) and ÇAM et al. (2017), during the FSW process, the temperature and the plastic deformation generated, mainly by the friction between the tool and the material, resulting in significant microstructural evolution in certain aspects, including grain size, grain boundaries, dissolution and hardening of precipitates, dissolution and redistribution of dispersoids, as well as the modification of the crystallographic texture.

Even in similar FSW joints, it is possible to observe an asymmetrical arrangement of the different zones formed because we have the welding side where the displacement direction is the same tool rotation direction called the “advancing side” and the side where the directions are opposite, called the “retreating side”. Thus, FSW welds present

asymmetries in temperature distribution and strain intensity transversely and longitudinally. According to THREADGILL, (2007), the cross-section of FSW welded joints is divided into four main regions: the base metal (BM), which is the region not affected by heat and which does not suffer deformation rate induced by tool rotation; the heat-affected zone (HAZ), being the region affected by the thermal cycle during welding, but without residual plastic deformation in the microstructure; the thermomechanically affected zone (TMAZ), in which the material was plastically deformed by the tool, and the resulting heat flow exerted some influence on the material; and the zone that extends to the centre corresponding to the shoulder width of the tool which is called the stir zone (SZ). According to FRATINI and BUFFA (2005), the arrangement of these zones along the cross-section of FSW joints varies depending on the maximum temperature reached, the degree of deformation, and the stacking fault energy (SFE) of each material to be welded, as this determines the metal's tendency to dynamically recover or recrystallise. The FSW procedure frequently gives fine dynamically recrystallised (DRX) grains in the stir zone (SZ) and outstanding mechanical properties.

With the critical advance in creating welding tools for joining high-temperature melting point materials, various FSW examinations have been devoted to joining different steels, as shown by FUJII et al. (2006) and CHUNG et al. (2010) specifically, for the stainless steels as presented in the studies of BILGIN and MERAN, (2012) and CAETANO et al. (2018). The applications of the FSW process in ASS welds appear in an attempt to solve problems like solidification cracking, weld decay and knife-line attack in the weld region, and these problems are recurrent in the welded region, which experiences high thermal cycles during the fusion welding processes. In FSW of ASS, although the formation of deleterious phases is expected in the stir zone, as proved by KOKAWA et al., (2005) and PARK et al., (2003), an essential aspect for the success of the welds produced is the intense grain refining resulting from dynamic recrystallization, as observed by WANG et al., (2014). The peak temperature primarily influences the microstructural properties at the weld SZ during FSW. According to JOHNSON and MURUGAN (2020), apart from peak temperature, two different mechanisms, namely the pace of heat generation and the rate of material deformation, also govern microstructure evolution. An increase in heat generation results in grain coarsening, whereas the increase in deformation rate results reduction in grain size due to recrystallisation contribution. Despite the lower temperatures experienced in FSW welds of ASS, some researchers,

such as KOKAWA et al. (2005) and PARK et al. (2003), have reported the precipitation of the sigma phase during FSW of ASS AISI 304. The authors speculate that the sigma phase precipitation was due to the emergence of δ-ferrite at higher welding temperatures experiencing severe strain in the material during frictional stirring, which subsequently led to the decomposition of delta ferrite to the sigma phase during the thermal cooling cycle.

Among the ASS, KOCABEKIR et al. (2008) highlight that although ASS AISI 316 was initially developed for use in paper mills and food processing industries, its modified form called AISI 316L, which has a lower carbon content of 0.03% and molybdenum about 2–3% (percentage by weight) made it possible for wide application in most marine and offshore sectors such as heat exchangers, boat fittings, food processing equipment, chemical transportation containers and laboratory equipment. According to TRIGWELL and SELVADURAY, (2005), carbon reduction provided greater resistance to sensitisation, while the presence of molybdenum offers greater resistance to pitting corrosion in environments containing chlorides. SHASHI KUMAR; MURUGAN and RAMACHANDRAN, (2019), applying the FSW process in the production of similar joints of austenitic stainless steel 316L proved that with the correct adjustment of the process parameters, it is possible to reduce secondary phases and produce an intensely refined stir zone with a positive influence on the mechanical performance.

Ferritic stainless steels, which are widely used in many manufacturing processes in the chemical and petrochemical industries, stands out the AISI 444, a ferritic type stainless steel containing 18% Cr, 2% Mo and Ti and/or Nb as stabilising elements. This steel, as noted by TAVARES et al. (2008), due to the Cr and Mo contents, it has greater resistance to pitting corrosion than other ferritic grades, as the Ti and/or Nb stabilising elements help to form fine carbides that prevent sensitisation. HAN et al. (2014) evaluating the microstructure of similar joints of a ferritic stainless steel 18Cr-2Mo, with a chemical composition similar to AISI 444 steel, proved that the FSW process is capable of producing a stirred zone with refined equiaxed ferritic grains enabling a high hardness in the stir zone and a good impact resistance of the welded joints. Caetano et al. (2021) analysing the AISI 444 ferritic stainless steel similar weld produced by the FSW process, successfully achieved outstanding data in terms of FSW processing, realising joints without defects, with excellent resistance to intergranular corrosion, without significant

chromium carbides and embrittlement phases capable of compromising the excellent results of resistance to intergranular corrosion in the SZ, HAZ and TMAZ.

Among the factors that aroused interest in evaluating the microstructural behavior of steels AISI 316L e AISI 444 in dissimilar FSW joints. It is noteworthy the fact that different industrial segments use dissimilar welding joints of different metals to bring together different properties, minimize costs, and maximize the performance of equipment and machinery with different welding processes. SILVA et al. (2013) point out to be promising to join different stainless steels in dissimilar joints in the petroleum distillation towers in the gas and petroleum industries through fusion welding processes. Some industrial applications need the joining of ASSs to FSSs. As observed by EMAMI et al. (2020), such a combination of dissimilar materials is commonly found in high-temperature applications such as energy conversion systems. For example, central power stations include boiler sections made from FSSs operating at low temperatures. The section is usually connected with another section made from ASSs, which operates at higher temperatures. Therefore, the transition occurs through a dissimilar weld between these two materials. MUKHERJEE and PAL (2012) claim that the dissimilar joints between ferritic and austenitic stainless steels are efficient for prolonging metals' service life due to improved toughness, mechanical strength, and corrosion resistance.

In this regard, some fusion and solid-state welding techniques were used to produce dissimilar joints of Austenitic/Ferritic (A/F) stainless steels. AGUILAR; TABARES and SERNA, (2013) studied the metallurgical transformations that occurred during the SMAW welding of AISI 316L austenitic stainless steel with AISI 430 ferritic stainless steel. They evaluated the influence of heat input and usage of two different electrodes on the microstructural evolution of the heat-affected and the fusion zone; in the results, the heat-affected zone of the ferritic side showed grain coarsening. BARROS (2013) welded AISI 316L and AISI 444 in dissimilar joints by TIG welding autogenous (without filler metal) with pulsed current, although the use of pulse frequency is effective in reducing the grain size in the HAZ and the molten zone of the welded samples, this refining was not efficient in ensuring good tenacity of the produced joints. According to KOU (2003), grain growth in ferritic stainless steels, which can occur both in the molten zone and in the HAZ when subjected to arc welding, is mainly responsible for compromising the mechanical performance with a decrease in hardness, ductility and tenacity.

According to MURR (2010), when the FSW process is applied to the weld of dissimilar joints, the asymmetry between the retreating and advancing sides is intensified because we have in HAZ, TMAZ, and SZ different behaviours concerning thermal conductivity and plastic deformation due to differences in the physical and chemical properties of the materials involved, which support in the asymmetry of heat generation and material flow. Despite significant progress on issues related to the application of the FSW process in dissimilar joints of aluminium alloys and other light alloys, in studies like BARBINI et al. (2017) and KADIAN and BISWAS (2018) and these alloys with steels as shown RAMIREZ et al. (2011) and KASAI et al. (2015), the understanding of flow and microstructural evolution in dissimilar FSW joints involving the wide variety of existing stainless steels are still developing. Thus, this work aims to evaluate the effect of different FSW welding parameters in the microstructural evolution of dissimilar joints between AISI 316L austenitic stainless steel and AISI 444 ferritic stainless steel.

8.3 Materials and Methods

The welds were carried out with plates of AISI 444 ferritic stainless steel, 2 mm thick and AISI 316L austenitic stainless steel, with thicknesses of 4 mm or 3 mm, depending on the joint configuration used. The chemical composition of the materials was determined by optical emission spectroscopy (Shimadzu model PA7000 Japan) and is presented in Table 8.1.

Table 8.1 - Chemical composition of the base metals (% weight).

Material	Elements											
	C	Si	Mn	P	S	Cr	Ni	Mo	Cu	Co	N	Fe
316L	0.026	0.56	0.84	0.029	<0.010	17.1	9.97	1.96	0.32	0.20	0.056	Bal.
444	0.017	0.53	0.16	0.47	<0.010	17.8	0.24	1.75	0.57	----	----	Bal

Source: The author.

The samples were joined by the FSW process in the Helmholtz-Zentrum Geesthacht (HZG), Germany. All welds, evaluated for mechanical properties, were made using the HZG Gantry System. An inert gas (Ar) injection system was used to protect the material during the process at temperatures above 535 °C; these stainless steels react with the atmosphere. The welds were carried out in the load control mode with an integrated system to record the process data, such as depth of penetration, rotation speed, torque,

forces applied to the tool and position of the tool over time. The welds were made with a tool of polycrystalline cubic boron nitride (PCBN). The tool had a conical diameter of 25 mm, a conical pin of 9.2 mm diameter, and a length of 3.7 mm. The pin had a conical surface with opposing recesses, which were in the form of a spiral concerning the tool's axis of symmetry. Three different joint configurations were welded. The first was a butt joint with 4 mm of thickness, with AISI 316L steel on the retreating side and AISI 444 steel on the advancing side, as shown in Figure 8.1a. The other two configurations are overlapping joints, one with the AISI 316L steel at the top and 5 mm of thickness in the stir zone and the other with the AISI 444 steel at the top and 6 mm of thickness in the stir zone, all showing an overlapping region of 70 mm in length, as shown Figure 8.1b and Figure 8.1c.

Figure 8.1 – Different configurations of welded joints (a) Butt joint with AISI 316L steel on the retreating side (b) Overlap joint with AISI 316L steel on the top (c) Overlap joint with AISI 444 steel on the top.

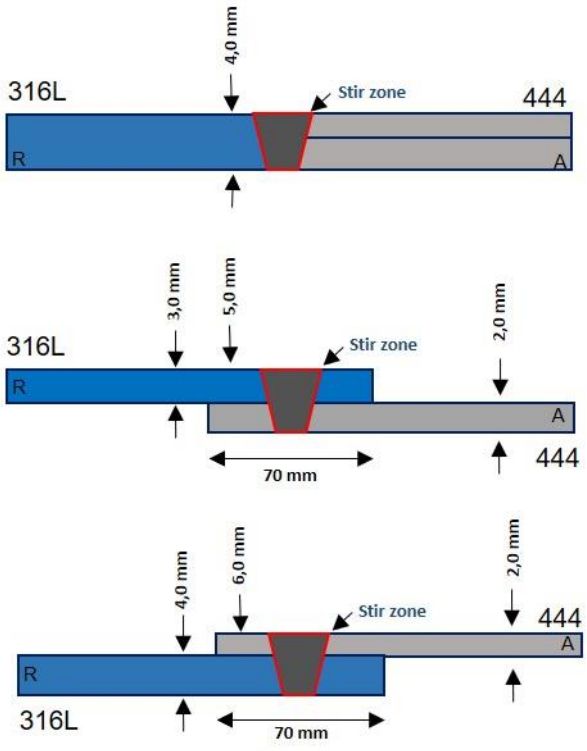

Source: The author.

To define the welding parameters, CAETANO et al. (2018) found the best set of parameters in similar FSW welding of AISI 444 ferritic stainless steel and AISI 316L

austenitic stainless steel. Thus, in the butt joint, the rotation speed varied between 350 to 450 rpm and the axial force from 25 to 30 kN, as shown in Table 8.2. For the overlapped joints with the AISI 444 ferritic stainless steel on the AISI 316 steel plate, the rotation speed was kept at 450 rpm, and the axial force was varied between 20 and 30 kN. When the AISI 316L austenitic stainless steel was placed on the AISI 444 steel, the rotation speed also varied from 350 to 450 rpm, but due to the higher strength and hardening of the AISI 316L steel, the axial force was increased to 45 and 50 kN, as shown by Table 8.3 and Table 8.4. For all nine welded conditions, the welding speed was kept constant at 1.0 mm/s and the tool angle at 0º.

Table 8.2 – Welding Parameters for Dissimilar FSW Butt Welding of AISI 444/316L Steels

Condition	Rotation Speed (rpm)	Axial Force (kN)	Advancing Side	Retreating Side
1	350	30	444	316L
2	450	25	444	316L
3	450	30	444	316L

Source: The author.

Table 8.3 - Welding Parameters for Dissimilar FSW Overlap Welding of AISI 316L/444 Steels

Condition	Rotation Speed (rpm)	Axial Force (kN)	Advancing Side	Retreating Side
4	350	50	444	316L
5	450	45	444	316L
6	450	50	444	316L

Source: The author.

Table 8.4 - Welding Parameters for Dissimilar FSW Overlap Welding of AISI 444/316L Steels

Condition	Rotation Speed (rpm)	Axial Force (kN)	Advancing Side	Retreating Side
7	450	20	444	316L
8	450	25	444	316L
9	450	30	444	316L

Source: The author.

The welds were initially cut with a diamond abrasive disc on a Struers Discotom-6 cutter for macroscopic and microscopic analysis. Sandpapers with a grain size between 120 and 2500 mesh were used for grinding. The polishing step was performed in a Struers universal polishing machine with 3μ, 1μ and 1/4μ diamond pastes and a rotation speed of

150 rpm. As the joints are composed of AISI 316L and AISI 444 steels, a combination of reagents was necessary. After several tests, 10% oxalic acid and 10% chromic acid reagents were chosen for the adequate production of contrasts between the phases and microconstituents present in the sample, enabling a complete analysis of its microstructure. Optical microscopy (OM) analysis was performed using a Carl Zeiss optical microscope integrated with the AxioVision SE64 software to assess the layout and characteristics of the different zones. However, for a more detailed investigation of the possible precipitates and the constitution of the interfaces between the AISI 304L/410S steels, analyses were performed by scanning electron microscopy (SEM) in an FEI Quanta 250 microscope with an Oxford Nordlys EDS system coupled. Finally, further thermodynamic simulations were carried out to enrich the metallurgical discussion. All simulations were performed using ThermoCalc® software.

8.4 Results and Discussions

8.4.1 Macrostructural Analysis

8.4.1.1 Butt joints 316L/444

Macrostructural analysis of the cross section of dissimilar welds, produced by the FSW process, with AISI 316L stainless steel on the retreating side and AISI 444 ferritic stainless steel on the advancing side, forming a butt joint with a 4 mm thick in the stir zone, it is possible to visualise defects such as flash, voids and root flaws, as shown in Figure 8.2. However, the parameters used in Condition 1, welded with a rotational speed of 350 rpm and an axial force of 30 kN, can consolidate the joint without the presence of these defects. In Condition 1, the material flow reached an adequate state of plasticisation due to the effective heat intensity obtained by the combination of the parameters used. In welded conditions with a rotation speed of 450 rpm, the flash production is more prominent as the axial force increases from 25 kN to 30 kN and, consequently, the heat input. According to TRUEBA et al. (2015), higher welding temperatures in FSW cause an increase in viscosity and displacement of a more significant amount of material around the tool pin; the difficulty of containing the metal displaced by the tool shoulder is the origin of the greater flash production.

Regarding the penetration of the tool and the formation of root defects, both in Condition 2 and Condition 3, flaws were found in the joint root. In Condition 2, welded

with 25 kN axial force, root flaws were found with the observation of a line. This line refers to the plate interface and the lack of complete mixing between the steels in the butt joint. Such defect is associated with insufficient tool penetration, as reported by EDWARDS and RAMULU (2015). KUMAR and KAILAS (2013) studied the material flow in dissimilar joints welded by the FSW process. These authors also observed the formation of this remaining line, finding its attenuation with the displacement of the tool to the advancing side concerning the centre of the butt joint; with this the plastic deformation is intensified. However, the study also shows that the presence of the remaining line did not change the mechanical strength properties of the material. In the present study, it was observed that when the axial force increases to 30 kN and the rotation speed is kept at 450 rpm in Condition 3, an excess of penetration occurs, resulting in the presence of grooves from the removal of the joint from the backplate, also corresponding a root flaw of the joint.

CAETANO et al. (2018) observed different morphologies of root faults investigating FSW welds. According to the authors, this type of defect occurs under different mechanisms. It can be formed by both excessive or insufficient axial force application. When excessive axial force is applied, the tool pin tends to pass close to the backplate caused by the excessive penetration. The second mechanism results from a lesser interaction between the tool and the material and, consequently, reduce the friction force and the heat generation necessary to achieve an adequate state of plasticisation of the material flow, such as the failure observed in Condition 2. An inadequate plasticisation hinders the material's movement around the tool and the consolidation of the stir zone during the FSW process.

In FSW butt weld joints, the formation of root failures due to both excess or lack of penetration demonstrated there is an optimum balance between axial force and tool angle, in which the production of FSW joints without root failures should be achieved due to the greater immersion of the pin in the joint. This statement agrees with other studies found in the literature as reported by SHULTZ et al. (2010) and PIETRAS and WĘGLOWSKI. (2014). Although a correct balance between tool angle and axial force is a way to consolidate FSW butt joints without root defects, it can also be achieved by the correct balance between axial force and rotational speed without the need to vary the tool angle, as shown in Condition 1. In this case, reducing the rotation speed to 350 rpm with the

axial force at 30 kN was sufficient to consolidate an FSW joint with no root failure and internal voids.

Small voids are observed in the stir zone in conditions 2 and 3, welded with an axial force of 25 kN and 30 kN and a rotation speed of 450 rpm. These voids are located in a region closer to the weld root and at the interface between AISI 316L and AISI 444 steels. The voids are larger for the welded condition with the lowest axial force. According to DOUDE et al. (2015), the voids in the stir zone in regions close to the weld root, as observed in Conditions 2 and 3, indicate the use of parameters that determine a suboptimal heat input for consolidating a defect-free FSW joint. This behaviour, as observed by TONGNE et al. (2015), was attributed to less interaction between tool and material because the low axial force reduces the friction force and insufficient heat to achieve a suitable plasticising state for material flow during the FSW process.

At the contact interface between the two steels, it is possible to observe inserts of AISI 444 FSS towards AISI 316L ASS and vice versa. As observed in Chapter 04, the greater the application of axial force, the greater the increase in the length of these inserts occurs. Therefore, the temperature and the plasticization state of the steels in the stir zone are increased. The parameters used in condition 1, welded with a rotational speed of 350 rpm and an axial force of 30 kN, guaranteed an adequate plasticisation state not only to prevent the formation of voids and flash production presented in conditions 2 and 3, but how it made it possible to increase the number of insertions between the steels. In condition 1, three inserts of ASS AISI 316L towards FSS AISI 444 are visible, and two inserts of AISI 444 FSS towards AISI 316L ASS. In addition to the increase in the amount of inserts, they have a more pointed shape compared to the inserts seen in conditions 2 and 3.

Figure 8.2 - Transverse macrographs of the different dissimilar welding conditions of AISI 444/316L stainless steels by the FSW process in butt joint configuration. (a) Condition 1 (b) Condition 2 and (c) Condition 3.

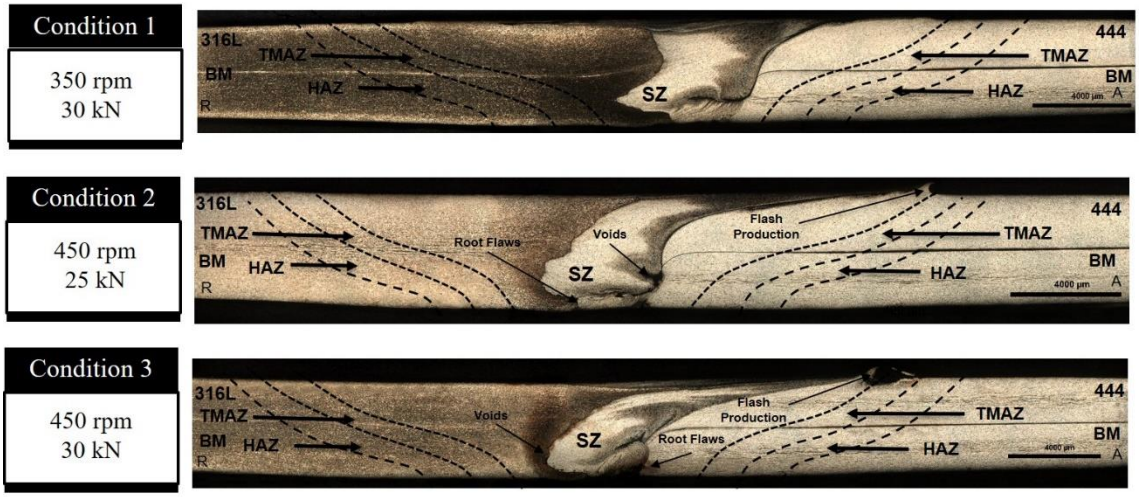

Source: The author.

8.4.1.2 Overlap joints 316L/444

In order to consolidate a greater penetration of the tool in the AISI 316L/444 overlap joint, the AISI 316L steel plate, located in the upper part, was machined from 4 to 3 mm, consolidating a stirred zone with a 5 mm thick overlap zone. Through the analysis of the cross section of the dissimilar FSW welds of the overlap joint, with the positioning of AISI 444 FSS on the bottom, it is possible to verify excellent results concerning the consolidation of the FSW joint, as shown in Figure 8.3. As the axial force increases from 45 kN to 50 kN, there is a decrease in voids at the 316L/444 interface, being possible to weld AISI 316L and AISI 444 steels in an overlap joint, with AISI 316L steel at the top, with no voids in the stir zone and high cohesion between the materials.

According to DEBROY and BHADESHIA (2013), the main difference between similar and dissimilar FSW welds is the discontinuity in physical and chemical properties found on the interface between the two materials, as well as the morphology of this contact influenced by the adopted welding parameters and, consequently, of the flow of these materials in the stir zone. BOGAARD et al. (1993) and MANDAL et al. (2009), FSSs has higher thermal diffusivity and lower flow stress compared to ASSs at high temperature. So, the less elasticity modulus and yield strength limit and greater

mechanical resistance of steel AISI 316L about steel AISI 444 may have favoured the excellent results of this joint configuration. The AISI 316L steel placed in the upper part, where the highest temperatures and stresses occur, may have favoured a greater plasticity state concerning its positioning in the lower part of the joint. Thus, a more significant amount of plasticised material towards the 316L/444 interface is formed, allowing the consolidation of a void-free stir zone both in the central region and in the region closest to the weld root, as occurs for Condition 4.

In the contact zone between the two steels, it is possible to observe that as the axial force increases from 45 kN to 50 kN, keeping the rotation speed constant at 450 rpm, it favours an increase in temperature, a greater plasticisation of the material and the annulment of the tunnel defect. Keeping the axial force at 50 kN and decreasing the rotation speed to 350 rpm in Condition 4, there is a decrease in the central inserts, that in FSW, overlap joints are called hooks. With the reduction of central hooks steels in Condition 4, the complete nullification of the existing voids in the interface region of Conditions 5 and 6 occurs. As pointed out by GEYER et al. (2021), hooks are systematically formed at the interface of dissimilar plates during friction stir lap joint welding. Various hooks dimensions and shapes are observed in overlap joints according to the welding parameters; thus lap joints are susceptible to material flow leading to the formation of hooks on the stir zone. BATISTÃO et al. (2020), welding dissimilar joints between aluminium and steel using the FSW process in overlap configuration, found smaller hooks of the material positioned at the bottom of the joint at the top as the rotation speed decreases, enabling better joint consolidation and a reduction in defects such as voids and tunnel defects. This decrease in the steel hook occurs due to the decrease in heat input caused by the decrease in the rotation speed and, consequently, the amount of AISI 444 steel positioned in the lower part of the joint being directed to the upper part, reducing and eliminating defects, as noted by XIONG et al. (2012) also in dissimilar FSW joints in overlap configuration.

Figure 8.3 - Transverse macrographs of the different dissimilar welding conditions of AISI 316L/444 stainless steels by the FSW process in overlap joint configuration with austenitic stainless steel AISI 316L on top. (a) Condition 4 (b) Condition 5 and (c) Condition 6.

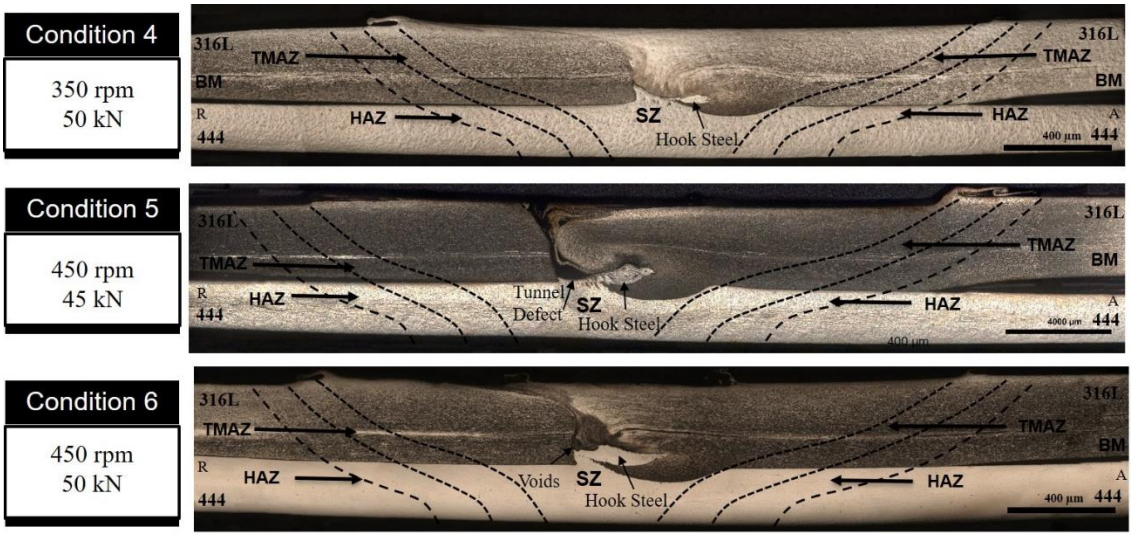

Source: The author.

8.4.1.3 Overlap joints 444/316L

Macrographic evaluation along the cross section of dissimilar FSW welds in overlap joint, with AISI 444 ferritic stainless steel on top, forming a 6 mm thick stir zone, also reaffirmed the increase in flash production as the axial force increases. These flash productions are more prominent on the retreating side compared to the advancing side, as can be seen in the analysis of the cross section of Condition 9, welded with the axial force of 30 kN, presented in Figure 8.4.

The presence of voids in the lap joint's 444/316L interface region decreases considerably as the axial force increases. However, even for condition 9, welded with the highest axial force, voids at the 444/316L interface are still observed. These voids or lack of fill consist of internal regions of the weld joint without material, forming voids along the length of the weld. According to MISHRA e MA, (2005), this is caused by the low heat input produced by an inadequate selection of process parameters, such as low rotational speeds and low axial forces. KUMAR and KAILAS (2008) stated that, in addition to low heating, the lack of pressure on the material's shoulder also affects the flux, preventing it from filling the entire weld region.

In the stir zone, in the region of contact between the two steels, only two large hooks steels are observed. One from the AISI 444 FSS towards the bottom of the joint and the other from the AISI 316L ASS towards the top. As the axial force increases from 20 kN to 30 kN, the amount of AISI 444 steel material at the bottom of the joint decreases, because to AISI 316L steel hook at the top is directed with greater intensity from the advancing side to the retreating side. In this way, with the increase of the axial force, there is an intensification of the compaction and a decrease in the hook of the steel AISI 444; however still insufficient to reduce the voids existing in the contact between the two materials, as noted by BATISTÃO et al. (2020).

Figure 8.4 - Transverse macrographs of the different dissimilar welding conditions of AISI 444/316L stainless steels by the FSW process in overlap joint configuration with ferritic stainless steel AISI 444 on top. (a) Condition 7 (b) Condition 8 and (c) Condition 9.

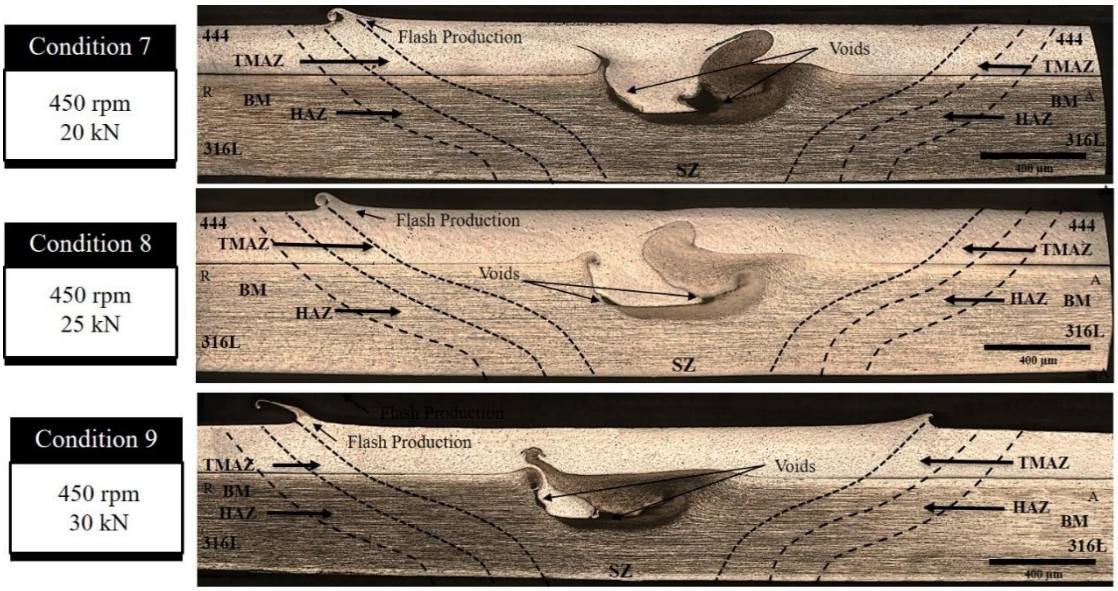

Source: The author.

8.4.2 Microstructural Analysis

8.4.2.1 Butt Joints 316L/444

In the microstructural characterization of 316L/444 butt joint, it was observed on the advancing side of the dissimilar FSW joint, where the direction of displacement is the same as the direction of rotation of the tool, the base metal (BM), the heat affected zone

(HAZ) and the thermomechanically affected zone (TMAZ) of the AISI 444 ferritic stainless steel. For all conditions evaluated, in the BM, as it is not affected by the heat rate or deformation induced by the tool rotation during the FSW process, no metallurgical changes were observed, in addition to those resulting from the sheet manufacturing process. Between BM and HAZ, within the range of parameters used between conditions 1, 2 and 3, no relevant microstructural changes were observed, only the presence of ferritic grains slightly larger than those found in the MB, as shown by Figure 8.5(c). This fact was also observed on the setback side for ASS AISI 316L, because in the HAZ of the AISI 316L steel, only a few equiaxed austenitic grains slightly larger than those found in the BM are observed. Therefore, it is challenging to determine the limit between the BM and HAZ regions for both steels. DU et al. (2014) noted that for austenitic stainless steel, there are many similarities between BM and HAZ, except for the apparent reduction in deformation twins density and slightly larger grains as shown in Figure 8.5(e).

Nonetheless, in TMAZ, ferritic grains on the advancing side and austenitic grains on the retreating side are heavily deformed following the direction of tool rotation, as shown in Figure 8.5 (b) and Figure 8.5 (d), with the greater intensity of deformation and recrystallization of the grains, the greater the axial force applied. In the TMAZ, due to the grains of this region being affected by both the heat and strain rate induced by the rotation and tool friction during the FSW process, austenitic grains no longer are presented equiaxed with grain boundaries faceted. However, they present a microstructure with serrated and deformed austenitic grains following the direction of material flow around the tool. SHASHI KUMAR; MURUGAN and RAMACHANDRAN, (2019), identifying the optimal FSW process parameters of friction stir welded AISI 316L butt joints, also observed similar behaviour on the TMAZ and attributed it to the effects of plastic deformation and dynamic recrystallisation to which the material was submitted.

Figure 8.5 – (a) Cross-section macrograph of the Condition 1 (b) ZTMA of AISI 444 steel, Condition 1, welded with a rotation speed of 350 rpm (200x). (c) HAZ of AISI 444 steel, Condition 1, welded with a rotation speed of 350 rpm (200x). (d) ZTMA of AISI 316l steel, Condition 3, welded with a rotation speed of 450 rpm (200x). (e) HAZ of AISI 316l steel, Condition 3, welded with a rotation speed of 450 rpm (f) Cross-section macrograph of Condition 3.

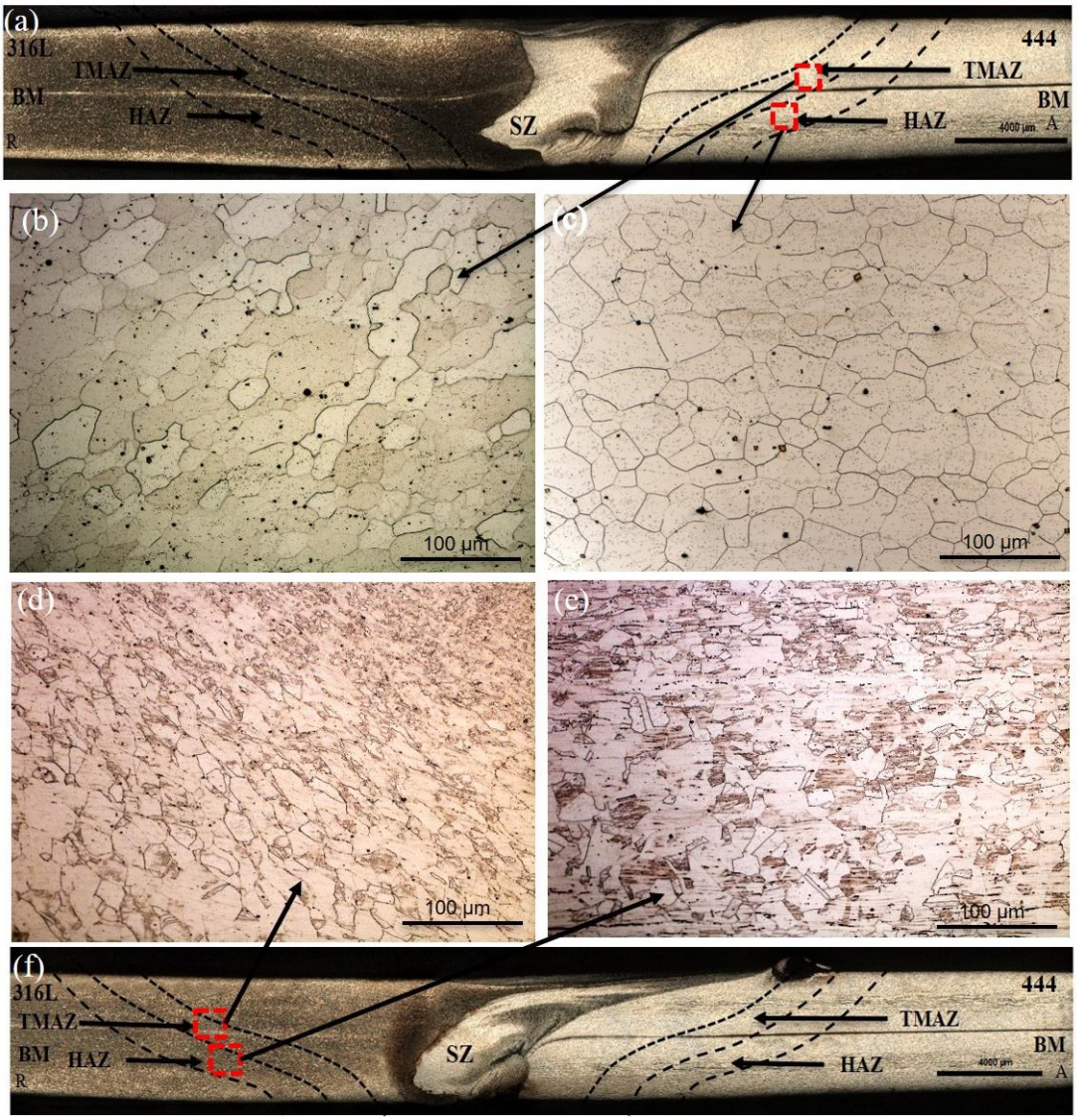

Source: The author.

All conditions butt joint welded, with FSS AISI 444 on the advancing side and ASS AISI 316L on the retreating side, presented SZ with deformed and refined grains. However, this grain refining in the stir zone is not homogeneous because the greater the axial force and the rotation speed and the consequent increase in the heat input, austenitic and ferritic grains are presented poorly refined in the upper part, as presented in Figure

8.6 (a) e Figure 8.6 (d) and more deformed grains with intense refining in the lower region, as shown in Figure 8.6 (b) e Figure 8.6 (e). HEIDARZADEH et al. (2021) noted that dynamic recrystallisation (DRX) is the dominant mode of microstructural evolution in the SZ and TMAZ. However, the homogeneity of the resulting microstructure is essentially independent of the DRX mechanism. The applied strain dictates the microstructural homogeneity and the temperatures reached as a result of the process parameters used. The peak temperature and strain rate near the pin and shoulder surfaces tend to decrease sharply toward the BM and joint root.

According to THREADGILL (2007), the intense refining in the stir zone, mainly in regions closer to the shoulder and the tool pin, occurs due to the combined action of the shoulder with the tool pin, acting as sources of friction and plastic deformation, favouring the boundaries of the original grains and subgrains to form new and refined equiaxed grains. The grain refinement is one essential aspect observed in the FSW of the dissimilar and similar joints between steels. It was proposed that the grain refinement in FSW is different from the other severe plastic deformation processes, such as equal channel angular pressing (ECAP), and high-pressure torsion (HPT), as noted by NENE et al. (2017). According to VALIEV and LANGDON (2006), the fine grain structure obtained from FSW is mainly related to the dynamic recrystallisation caused by the severe hot plastic deformation and the limited grain growth in the subsequent cooling process. However, applying parameters that determine high heat inputs can provide considerable differences between the cooling rates between the upper and lower regions of the stir zone, providing different intensities of grain refining. As noted by SHASHI KUMAR; MURUGAN, and RAMACHANDRAN (2019), grain refining in FSW welds of AISI 316L ASS in butt joint configuration, is dependent on the rotation speed used and its impact on heat generation. The lack of grain refining in the stir zone can occur both at low and high rotation speeds; according to the authors the rotation speed is suitable for intense refining of AISI 316L steel, varying between 400 and 600 rpm. However, in dissimilar joints, intense grain refining is observed with the positioning of AISI 316L steel on the retreating side of the butt joint, even in Condition 1, welded with a rotation speed of 350 rpm.

Figure 8.6 – (a) Top SZ of AISI 444 steel, Condition 1, welded with an axial force of 30 kN (200x). (b) Bottom SZ of AISI 444 steel, Condition 1, welded with an axial force of 30 kN (200x). (c) Cross-section macrograph of the Condition 1 (d) Top SZ of AISI 316L steel, Condition 1, welded with an axial force of 30 kN (200x). (e) Bottom SZ of AISI 316L Steel, Condition 1, welded with an axial force of 30 kN (200x).

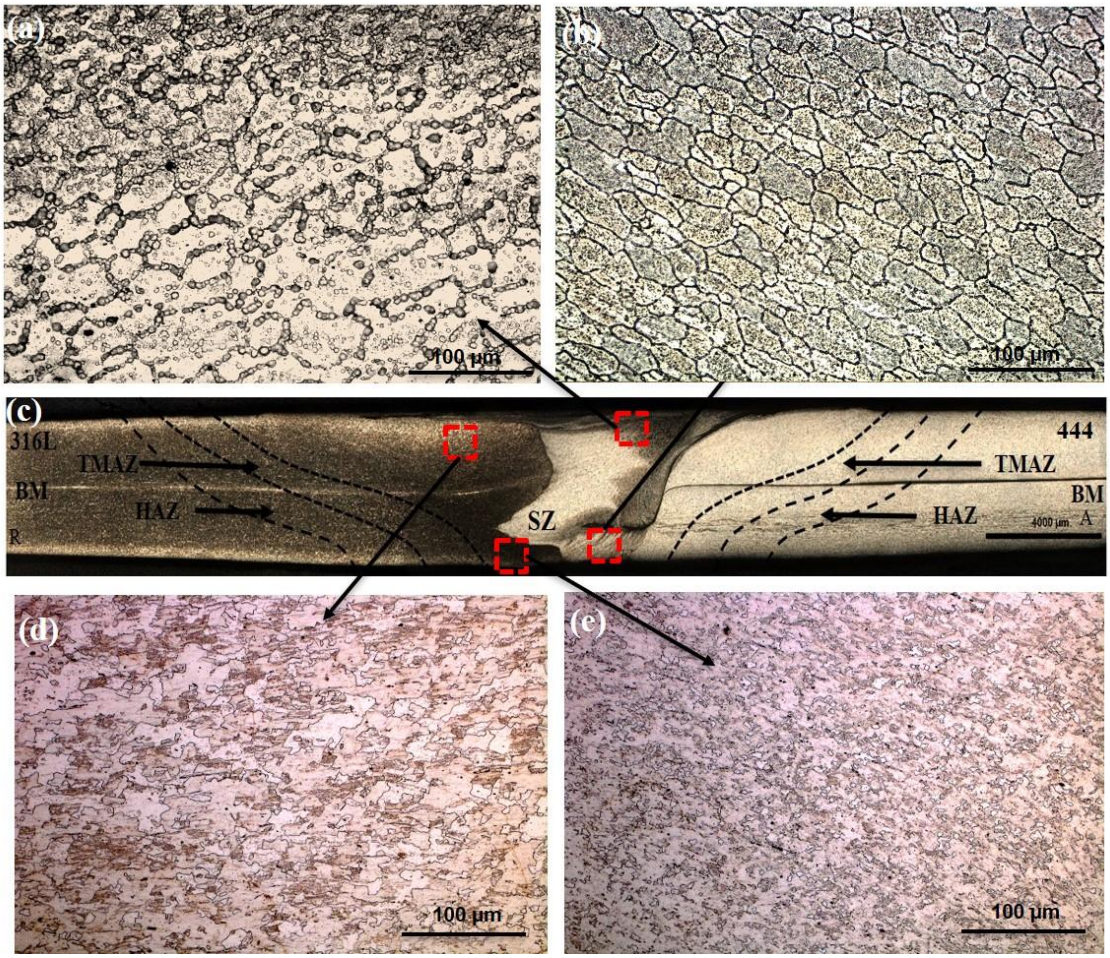

Source: The author.

Evaluating the upper region of the stir zone by scanning electron microscopy, it is possible to observe the presence of intense corrosion in the grain boundaries of the ferrite on the advancing side, where the AISI 444 steel is positioned, shown by Figure 8.7b and Figure 8.7c. This fact is possibly due to this region's precipitation of carbides and nitrides. Depending on the parameters used, this upper region of the advance side, becomes prone to the presence of such precipitates. As reported by NANDAN; DEBROY and BHADESHIA, (2008) there is a more significant generation of heat on the advancing side of the FSW welds. The heat intensity produced in the upper part of the FSW weld is high,

mainly due to the more excellent contact and the friction of the material with the tool shoulder, promoting a more significant generation of heat. Thus, the advancing side becomes a region critical to the occurrence of precipitates, as it is subjected to the effects of higher heat input. KIM et al. (2009) reported the possibility of the intergranular corrosion mechanism of Ti-stabilized ferritic stainless steels when subjected to temperatures of around 600 °C. These authors observed fine precipitates of Ti, Cr and C nucleates intergranular, which favoured the formation of regions with low Cr contents, compromising the resistance to intergranular corrosion of the material. However, these fine precipitates were only clearly detected with the use of transmission electron microscopy (TEM).

Figure 8.7 – (a) Cross-section macrograph of the Condition 1 (b) Micrographs obtained by Scanning Electron Microscopy of Top SZ of AISI 444 steel, Condition 1 (1000x). (c) Micrographs obtained by Scanning Electron Microscopy of Top SZ of AISI 444 steel, Condition 1 (5000x).

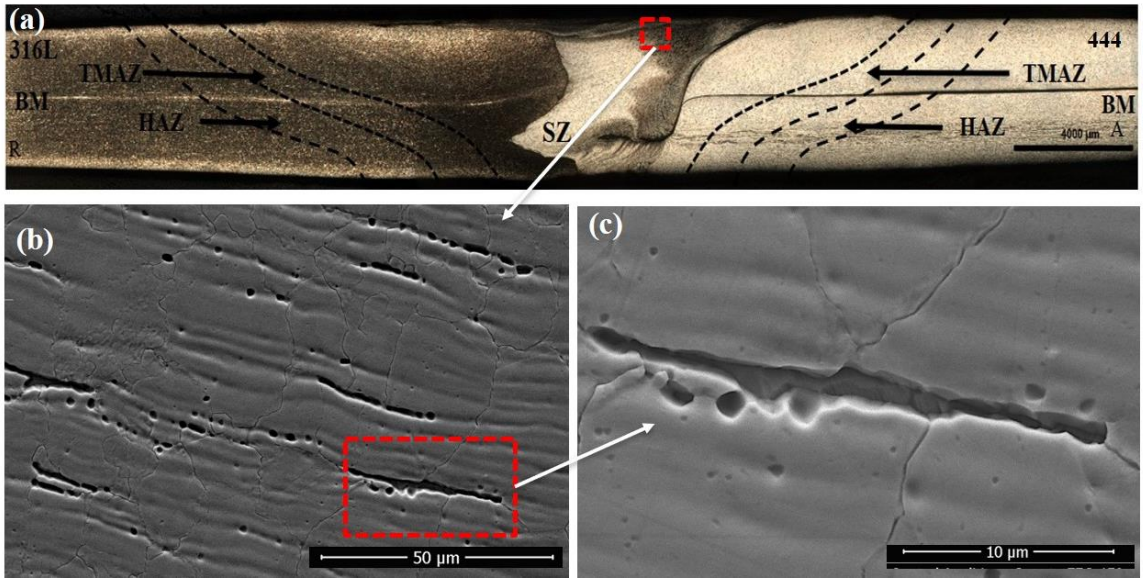

Source: The author.

Evaluating the equilibrium phase diagrams of AIS 316L and AISI 444 steels, performed using ThermoCalc® software, it is possible to verify the possible phase transformations that occurred in the TMAZ and SZ in the temperature range reached in the FSW welds. In this diagram, the horizontal axis corresponds to temperature, and the vertical axis denotes the molar fraction of the formed phases. Although the phase transformations resulting from the heating and cooling cycles in welding occur outside

equilibrium conditions, this can result in changes in the effective temperatures at which these transformations occur and may even partially or entirely suppress some phase transformations. Still, this diagram is handy, helping to understand the likely structure changes based on an approach considering thermodynamic equilibrium conditions. In the analysis of the phase diagram of the AISI 316L steel, presented in Figure 8.8, it is possible to observe that in the temperature range from 400° C to 800° C, the σ phase formation zone is expressive. However, under all conditions, both in the ZTMA and in the ZM of AISI 316L steel, the σ phase was not observed. According to KHERROUBA et al. (2021), entre the detrimental secondary phases in ASS 316 steels, the σ phase is the most undesirable because causes brittle fracture, hot cracking, creep failure and intergranular corrosion. SHASHI KUMAR; MURUGAN and RAMACHANDRAN (2019) also did not observe σ phase formation in similar FSW joints of AISI 316L steel, the formation of σ phase is diffusion controlled, and the diffusion of chromium and molybdenum governs its growth, however, the rapid deformation and cooling rates experienced during FSW welding can make this diffusional process difficult.

Figure 8.8 - Equilibrium phase diagram for AISI 316L Austenitic stainless steel simulated using the Thermo-Calc® software. BPW – molar fraction phases. (a) 0 – 10 molar fraction phases (b) 0 -100 molar fraction phases.

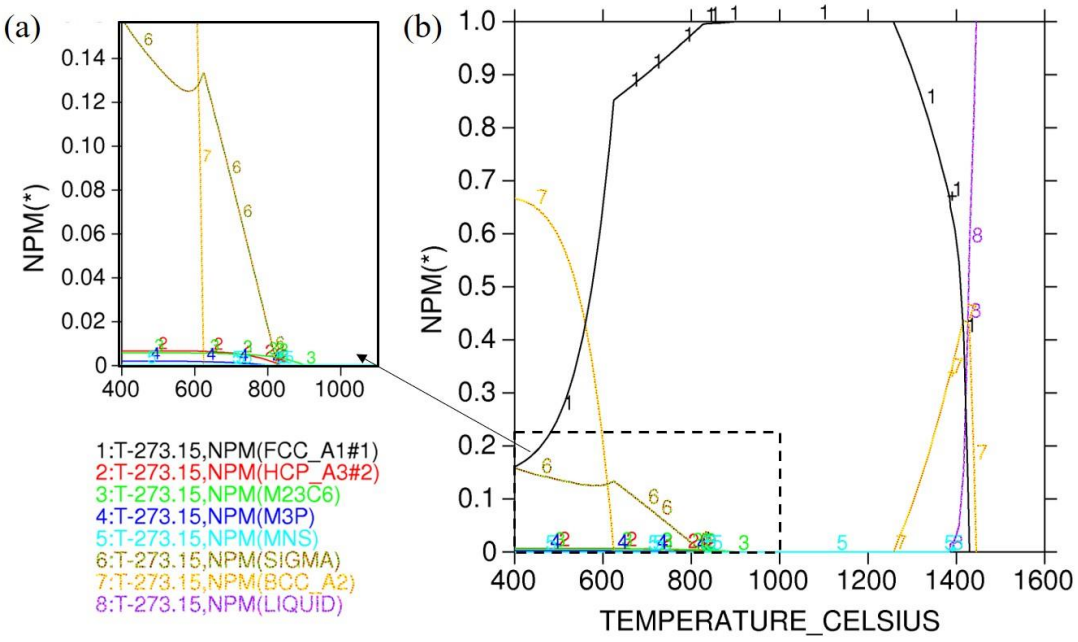

Source: The author.

In contrast to FSW welds produced with FSS AISI 410S by CAETANO et al. (2019), in the FSW welds of the AISI 444 steel, there was no formation of martensite in the TMAZ and SZ, even with the positioning of the AISI 444 steel on the advancing side, where the highest temperatures are observed. This lack of martensitic transformation occurs due to the chemical composition of AISI 444 steel, with higher levels of Cr and Mo, which stabilise the ferrite even at high temperature. Evaluating the equilibrium phase diagram for AISI 444 ferritic stainless steel in Figure 8.9 it is possible to verify that in the temperature range reached in FSW welds, between 500°C and 700°C, the austenitic transformation is inexpressive. Therefore, there is no formation of austenitic grains nucleated at the ferritic grain boundaries. If austenite is formed on heating, it transforms into martensite on subsequent cooling, giving rise to the biphasic microstructure, as observed in the HAZ of the AISI 410S steel by CAETANO et al. (2019). According to SONG et al. (2012), in FSW welding of ferritic stainless steels, provided that the chemical composition does not wholly stabilise the ferrite, any region exposed to temperatures around 800ºC can undergo cooling rates between 8.5º C/s and 2.2º C/s, providing the martensitic transformation. Although the phase diagram of AISI 444 steel shows the formation of Chi, Sigma and Laves phases in the temperature range from 450 °C to 850 °C. In the HAZ, TMAZ and SZ of any of the weld conditions these phases were observed.

Figure 8.9 - Equilibrium phase diagram for AISI 444 ferritic stainless steel simulated using the Thermo-Calc® software. BPW – weight fraction phases. (a) 0 – 10 weight fraction phases (b) 0 -100 weight fraction phases.

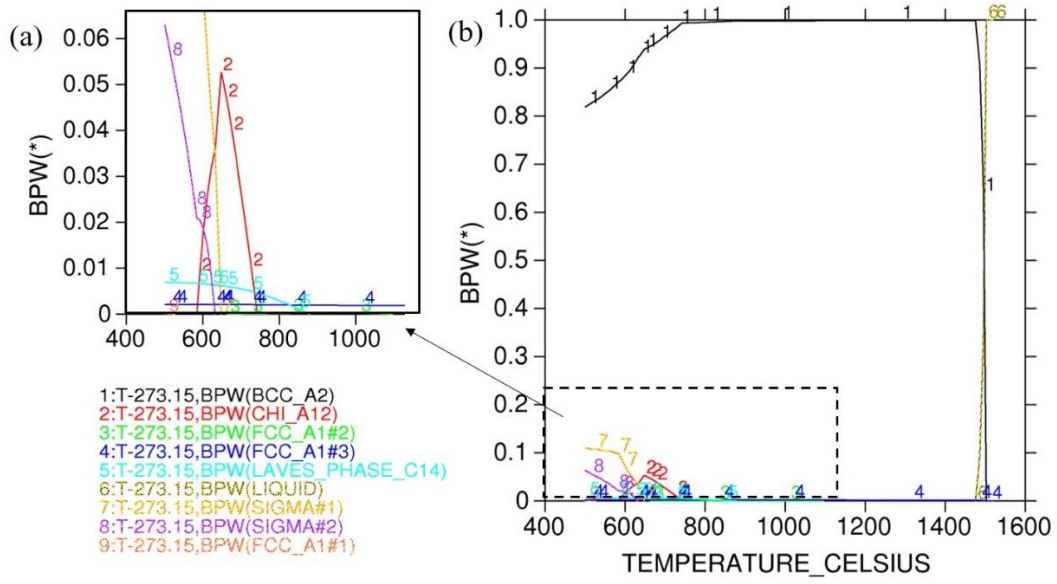

Source: The author.

As shown in the macrostructural analysis, in the contact zone between the two steels, it is possible to observe insertions of the FSS AISI 444 towards the ASS AISI 316L and vice versa. The increase in the length of these inserts is greater the application of axial force. Microstructurally, in this region of contact between AISI 316L and AISI 444 steels, it is possible to observe highly deformed austenitic and ferritic grains, especially as it approaches the 316L/444 interface. While in Condition 2, welded with the lowest axial force of 25 kN, there is the presence of more rounded inserts and short secondary inserts, as shown in Figure 8.10 (b). In conditions 1 and 3, welded with increasing axial force to 30 kN, greater cohesion is observed between the steels at the 316L/444 interface, with sharper insertions and greater secondary insertions, as shown in Figure 8.10(c). This fact is similar to that observed by YU et al. (2019), analysing the influence of FSW welding parameters on the evolution of the interface of dissimilar joints, which observed that the increase in heat generated by the increase in axial force promotes the formation of a greater mixed zone at the interface between the two materials. According to DEBROY and BHADESHIA (2013), the main difference between similar and dissimilar FSW welds is the discontinuity in physical and chemical properties found on the interface between the two materials, as well as the morphology of this contact influenced by the adopted welding parameters as axial force and, consequently, of the flow of these materials in the stir zone.

Figure 8.10 – (a) Cross-section macrograph of Condition 1. (b) Interface zone between AISI 444 and AISI 316L steels of Condition 1, welded with an axial force of 30 kN (500x). (c) Interface zone between AISI 444 and AISI 316L steels of Condition 2, welded with an axial force of 25 kN (d) Cross-section macrograph of Condition 2.

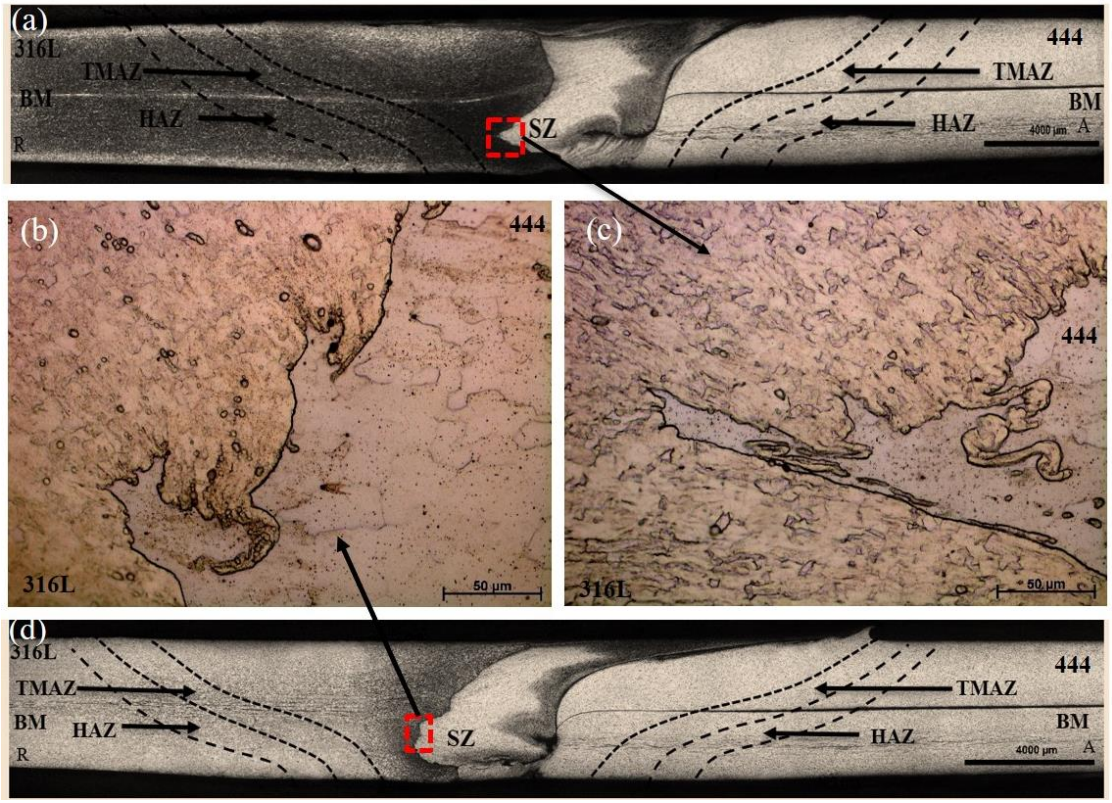

Source: The author.

8.4.2.2 Overlap Joints 316L/444

Changing the butt joint configuration between conditions 1, 2 and 3 to the lap joint, in conditions 4, 5 and 6. The main difference observed is that in the overlap joint, both for the retreating side and for the advancing side, there is the formation of two HAZ and two TMAZ, due to the presence of the two steels on both sides of the joint, as shown in Figure 8.11 (c). Similar to the butt joint, significant microstructural changes are not observed between the BM and the HAZ for both FSS AISI 444, located on the lower part, and for ASS AISI 316L, located on the upper part of the joint. However, in the overlap joints, the TMAZ of the AISI 316L steel, located in the upper part, presents more deformed and recrystallised grains than the TMAZ of the AISI 444 steel, located in the lower part of the joint, as shown in Figure 8.11 (a) and Figure 8.11 (b). In the stir zone,

differences in the intensities of the formation of recrystallised grains can also be observed. Intense refining and recrystallisation of the austenitic grains is observed in the upper stir zone near the surface and the centre, as shown in Figure 8.11 (d). While the ferritic grains in the central region show attenuated recrystallisation as they approach the root of the joint, even in this region close to the root, the ferritic grains are still thermomechanically affected and refined, as shown in Figure 8.11 (e).

According to CAETANO (2016), the microstructural characteristics of the different regions of an FSW welded joint is determined by the degree of deformation and the maximum temperature reached resulting from the process parameters. However, another critical element in forming these regions is the stacking fault energy (SFE) of each welded material, as this determines the metal's tendency to recover or recrystallise dynamically. As observed by ÇAM (2011) and PARK et al. (2003), austenitic stainless steels are more easily recrystallised and refined by the FSW process compared to ferritic stainless steels because of the stack failure energy (SFE) differences between ferritic and austenitic structures. As highlighted by HEIDARZADEH et al. (2021), high-SFE metals commonly exhibit extensive cross-slip and dislocation climb. Thus, the microstructural behavior in such materials is often dominated by recovery, even at relatively high temperatures. In contrast, low-SFE materials typically experience almost no recovery. According to PADILHA (2000), materials with low stacking energy, such as austenitic stainless steels, produce a higher density of disagreements and higher accumulated deformation energy, favouring dynamic recrystallization and consequently the refining of grain and not the rearrangement of these disagreements leading to material softening as occurs in high-energy stacking materials. Thus, in addition to the low-SFE and greater ease of recrystallisation of the AISI 316L ASS, its positioning at the top of the joint, where the highest temperatures and strain rates are experienced, provided a more significant difference in deformed and recrystallised grains between the upper and lower TMAZ and SZ.

However, the greater penetration of the tool in conditions 4, 5 and 6, achieved due to the decrease in the thickness of the AISI 316L steel sheet from 4 to 3 mm, and the greater axial forces applied contributed to intense recrystallisation of the FSS, even in regions closer to the joint root. This increase in recrystallisation of the FSS AISI 444, positioned at the bottom of the lap joint, is mainly observed for Condition 4 and Condition 6, welded with the highest axial forces. Thus, the positioning of AISI 316L ASS, 3 mm thick, in the

upper part of the joint, together with the increase in axial force from 45 kN to 50 kN, provided greater cohesion between the steels, greater tool penetration and intensification of recrystallisation for both AISI 316L and AISI 444 steel.

Figure 8.11 - (a) Top ZTMA of Condition 4, where the AISI 316L steel is positioned (200x) (b) Bottom ZTMA of Condition 4, where the AISI 444 steel is positioned (200x) (c) Cross-section macrograph of the Condition 4 (d) Top SZ of Condition 4, where the AISI 316L steel is positioned (200x) (e) Bottom SZ of Condition 4, where the AISI 444 steel is positioned (200x).

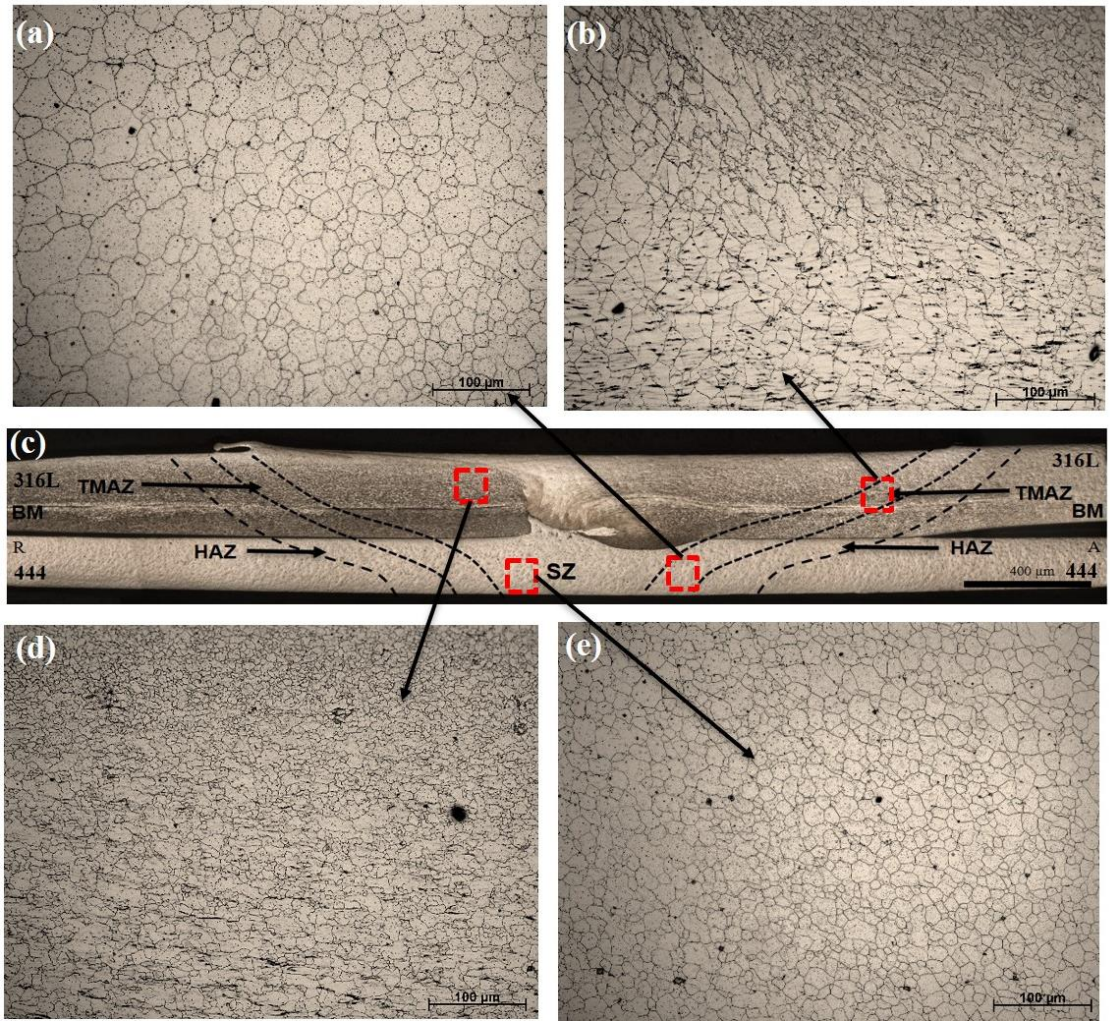

Source: The author.

Similar to what occurs with the inserts presented in the region of contact between the two steels in conditions 1, 2 and 3. In overlap joints 4, 5 and 6, the microstructure of the hooks steel of FSS AISI 444 towards the top of the joint and that of the ASS AISI 316L towards the bottom of the joint also present recrystallised and intensely deformed

grains, this deformation being intensified as it moves away from the center of the hook to the region of contact between the two materials. Between conditions 4, 5 and 6, as the axial force increases from 45 kN to 50 kN, the size of hooks steels is reduced. Still, the presence and increase in the number of secondary hooks steels occur in the intersection regions between the two materials as shown in Figure 8.12 (b) Figure 8.12 (c), enabling greater cohesion between the ASS AISI 316L sheet located at the top and the FSS AISI 444 located at the bottom. YU et al. (2019), evaluating the influence of welding parameters on interface evolution and mechanical properties of FSW Al/Ti lap joints, noted that under conditions with a high heat input, the excessively plasticised Al and Ti alloys were extruded by the pin tool, resulting in the formation of larger hooks helping to cohesive materials. When the heat input increased, the diffusive interface transformed into a mixed interface, accompanied by the formation of Ti fragments and hooks, owing to the sufficient plasticisation of the Ti alloy.

Figure 8.12 – (a) Cross-section macrograph of Condition 5. (b) Interface zone between AISI 444 and AISI 316L steels of Condition 5, welded with an axial force of 45 kN (500x) (c) Interface zone between AISI 444 and AISI 316L steels of Condition 6, welded with an axial force of 50 kN (500x) (d) Cross-section macrograph of the Condition 6.

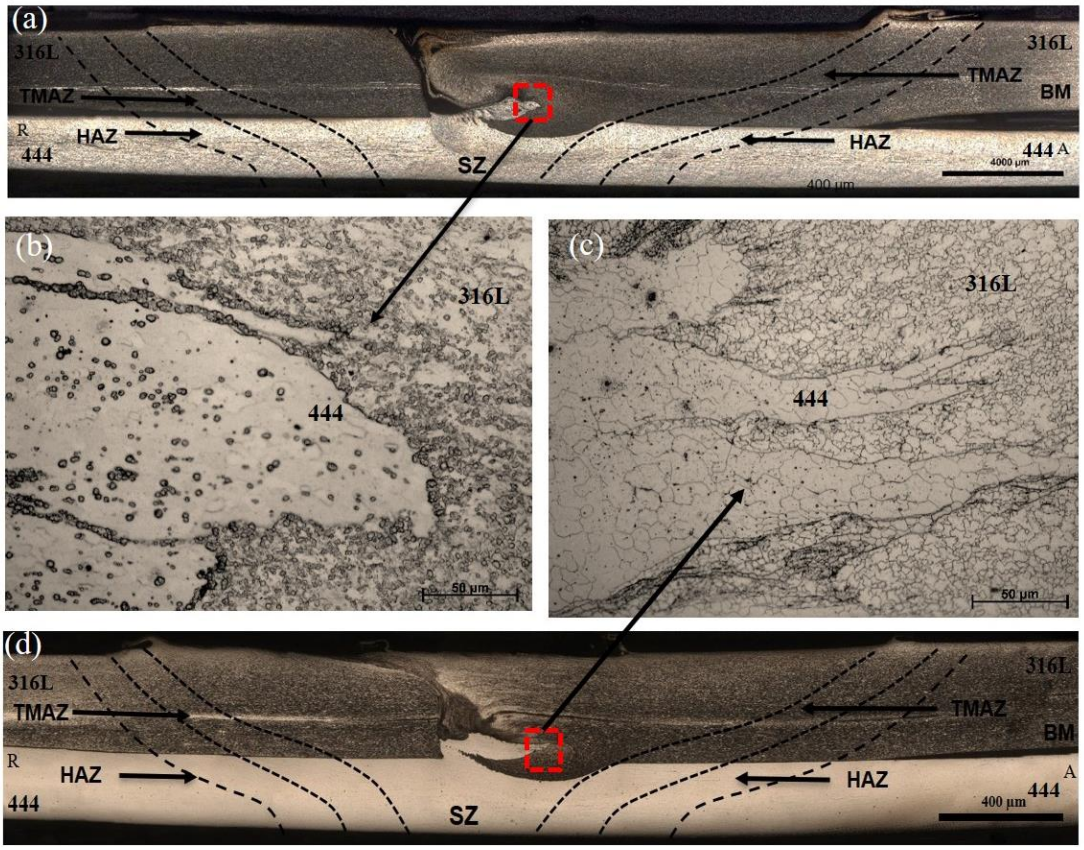

Source: The author.

EDS analysis of the contact zone of the overlap joints with AISI 316L steel at the top detected the formation of intercalated regions of FSS AISI 444 inside the ASS AISI 316L hook, being intensified in Condition 6, welded with the highest axial force and the highest rotational speed. The significant variation of Ni contents in this region demonstrates the existence of this region interspersed by these two steels, as shown by Figure 8.13 (b) and Figure 8.13 (c). This contrasting behaviour is possible because while AISI 316L steel has 9.97% nickel, AISI 444 steel is composed of only 0.24% nickel. In Chapter 4, these interspersed regions between the two materials were also observed in the contact interface between AISI 304L and AISI 410S steels welded in a butt joint. However, these intercalated regions were observed in the contact zone between two insertions due to the appearance of thin secondary insertions.

According to MURR (2010), during the FSW process, interleaved blocks or segments may flow due to solid-state flow conditions promoted by intense dynamic recrystallisation segments of solid matter in the liquid matrix, forming thin strips interspersed within the stir zone. This flux in thin strips that also occurs in similar FSW welds is intensified in dissimilar FSW welds due to the different properties of the materials welded at high temperatures, as observed in the dissimilar welding of AISI 316L and AISI 444 steels.

Figure 8.13 - (a) Cross-section macrograph of the Condition 6 (b) Hook steel of AISI 316L in interface zone between AISI 444 and AISI 316L steels of Condition 6 (c) Analysis of the Hook steel of AISI 316L in Condition 6 performed by EDS (energy dispersive x-ray detector) showing the variation of nickel contents.

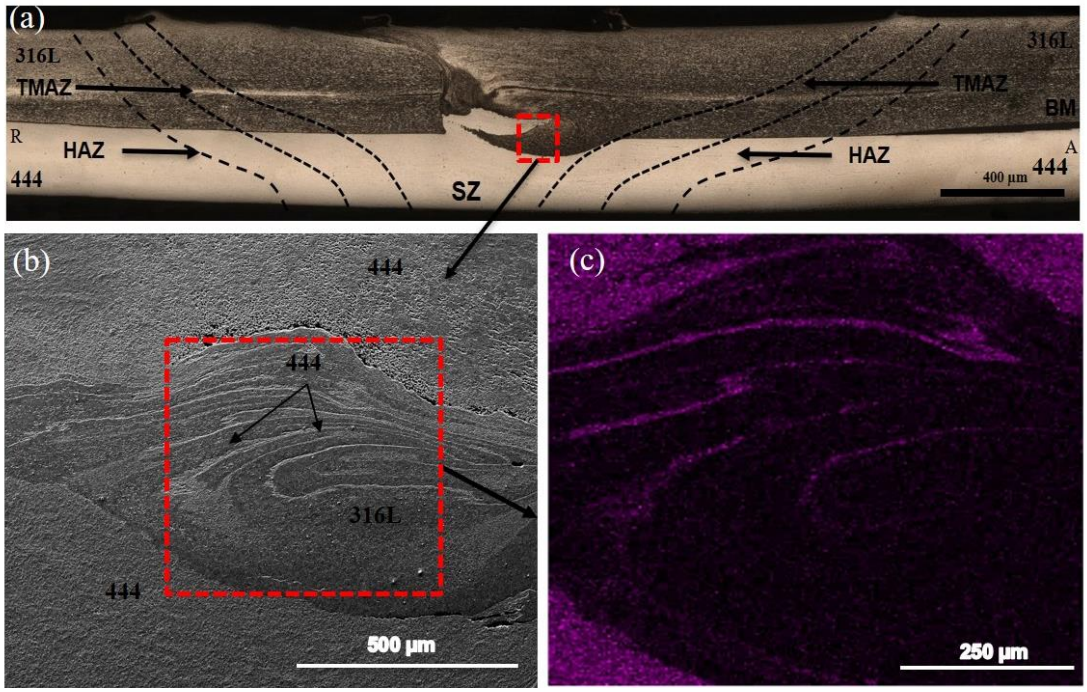

Source: The author.

8.4.2.3 Overlap Joints 444/316L

Changing the positioning of FSS AISI 444, with 2 mm thick, to the top of the lap joint, conditions 7, 8 and 9 were welded. In these welds, the thickness of the ASS AISI 316L plate was maintained at 4 mm, similar to that found in butt joints, so these joints are 6 mm thick in the overlap area. As observed in the other joints, significant microstructural changes are not observed between the BM and the HAZ, both for the FSS AISI 444,

located at the top, and for the ASS AISI 316L, located at the bottom, as shown by Figure 8.14 (b) and Figure 8.14 (e). The TMAZ of these conditions present intensely refined and recrystallised austenitic and ferritic grains, as shown in Figure 8.14 (a) and Figure 8.14 (d). However, this recrystallisation and deformation for AISI 316L steel decreases from the interface region between the two materials to the joint root. Thus, in regions close to the root, the austenitic grains present morphological characteristics similar to those in the HAZ and BM. GENG et al. (2022), evaluating the microstructural of dissimilar Al/steel friction stir lap welds, observed that the recrystallisation of the steel positioned at the bottom of the joint is intensified by increasing the axial force but decreases significantly as it approaches the underside of the joint, which can be observed by the expressive decrease of the microhardness in this region.

Figure 8.14 – (a) Top HAZ of Condition 7, where the AISI 444 steel is positioned (200x) (b) Top TMAZ of Condition 7, where the AISI 444 steel is positioned (200x) (c) Cross-section macrograph of the Condition 7 (d) Bottom ZTMA of Condition 4, where the AISI 316L steel is positioned (200x) (d) Bottom ZTMA of Condition 4, where the AISI 316L steel is positioned (200x).

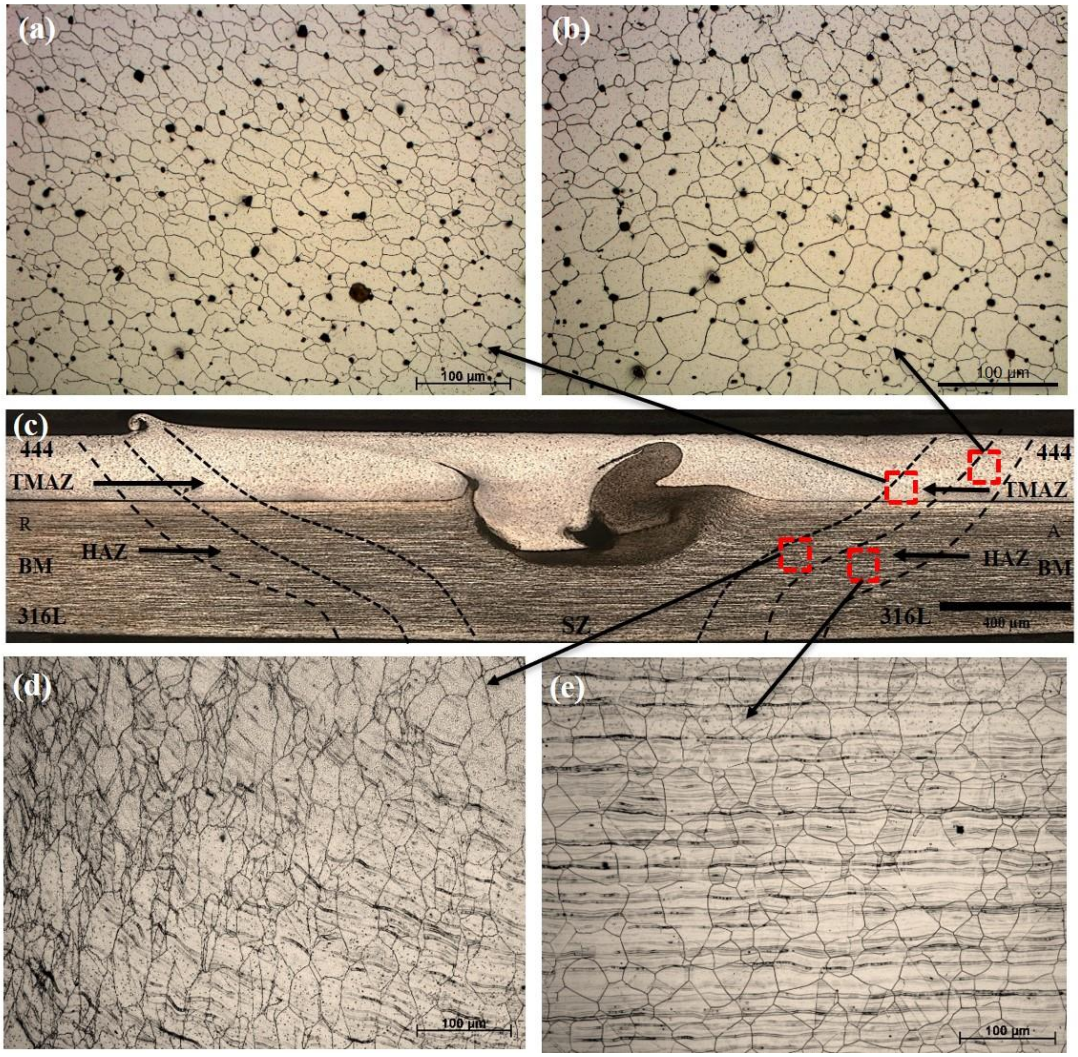

Source: The author.

In the stir zone of the overlap joints of conditions 7, 8 and 9, it is possible to observe for the AISI 444 steel, positioned at the top, a highly recrystallized layer of ferritic grains, as shown in Figure 8.15 (a). Below this region and more to the center is the formation of more deformed ferritic grains following the direction of rotation of the tool, as shown in Figure 8.15 (b). However, for austenitic stainless steel, only in the region situated more to the centre of the joint more refined and recrystallised austenitic grains are found, as shown by Figure 8.15 (d). In the lower region of the joint, in a region close

to the material interface with the backing plate, due to the lack of complete penetration of the tool, an austenitic microstructure similar to that found in the HAZ and the BM can be found, as can be seen in Figure 8.15 (e). ZHENG et al. (2017), evaluated the effect of plunge depth on microstructure and mechanical properties of FSW lap joint, and reported that the plunging depth of the pin has a vital influence on joint strength, being decisive for the adequate intensity of plastic deformation and recrystallisation of the material located in the lower part of the overlap joint.

Figure 8.15 – (a) Top SZ of Condition 9, where the AISI 444 steel is positioned (200x) (b) Central SZ of Condition 9, where the AISI 444 steel is positioned (200x) (c) Cross-section macrograph of the Condition 9 (d) Central SZ of Condition 9, where the AISI 316L steel is positioned (200x) (e) Bottom SZ of Condition 9, where the AISI 316L steel is positioned (200x).

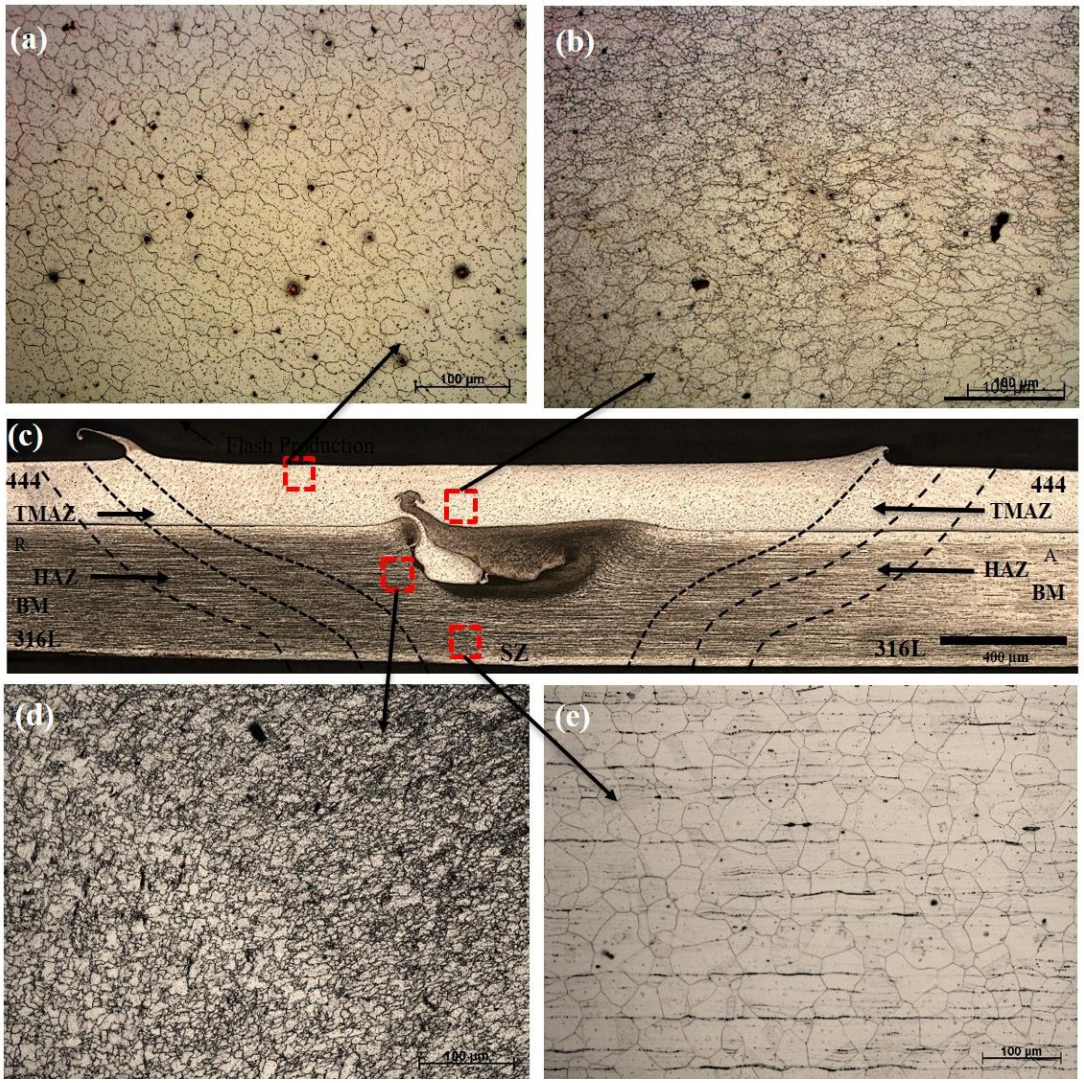

Source: The author.

In the stir zone, the microstructure of the interface region between AISI 316L and AISI 444 steels is strongly modified by increasing axial force. Between conditions 7, 8 and 9, as the axial force increases from 20 kN to 30 kN, the AISI 316L steel hook in the upper part of the joint is directed with greater intensity from the advancing side to the retreating side. With the increase in axial force, this movement of the AISI 316L steel hook compacts the recess of the AISI 444 steel, as can be seen in Figure 8.16 (a) and Figure 8.16 (d). The increase in heat input provided by the increase in axial force also modifies the morphology of hooks steels because it increases the size of secondary hooks, forming regions composed of layers interspersed between ferritic and austenitic stainless steel.

The formation of these intercalated layers occurs due to the different properties of the two materials at high temperatures during the establishment of the elastoplastic state. According to HUMPHREYS and HATHERLY (2012), materials with high stacking failure energy (SFE), such as FSS, deform by sliding of complete dislocations because such materials are mostly free from stacking faults. SHASHI KUMAR; MURUGAN and RAMACHANDRAN (2019), highlight that for low SFE materials like AISI 316L steel, deformation occurs by twinning and creates partial displacements that cannot slip through stacking faults, even under high tension. These SFE differences provide different intensities of dynamic recrystallisation and differences in the elastoplastic state between materials in a dissimilar FSW joint. Thus, in FSW of low SFE materials such as AISI 316L steel, higher strain rates are required than in FSW welds of AISI 444 steel to reach the same plasticisation state. Therefore, only with the increase of the axial force, there is the advancement of the secondary hooks of the AISI 316L steel over the AISI 444 steel. The increase in these secondary hooks can be seen in the differences between Condition 7, welded with an axial force of 20 kN, presented in Figure 8.16 (b), and Condition 9, welded with 30 kN axial force and shown in Figure 8.16 (c). In this interface region, the presence of intermetallic compounds was not observed. Despite being common in FSW welding of dissimilar materials with a wide variety of chemical compositions, such as those found by ABDOLLAH-ZADEH et al. (2008) in the FSW joint in aluminum and copper overlap joints and by CAMPO et al. (2014) in titanium and stainless steel lap joints.

Figure 8.16 - (a) Cross-section macrograph of Condition 7. (b) Interface zone between AISI 444 and AISI 316L steels of Condition 7, welded with an axial force of 20 kN (500x) (c) Interface zone between AISI 444 and AISI 316L steels of Condition 9, welded with an axial force of 30 kN (500x) (d) Cross-section macrograph of the Condition 9.

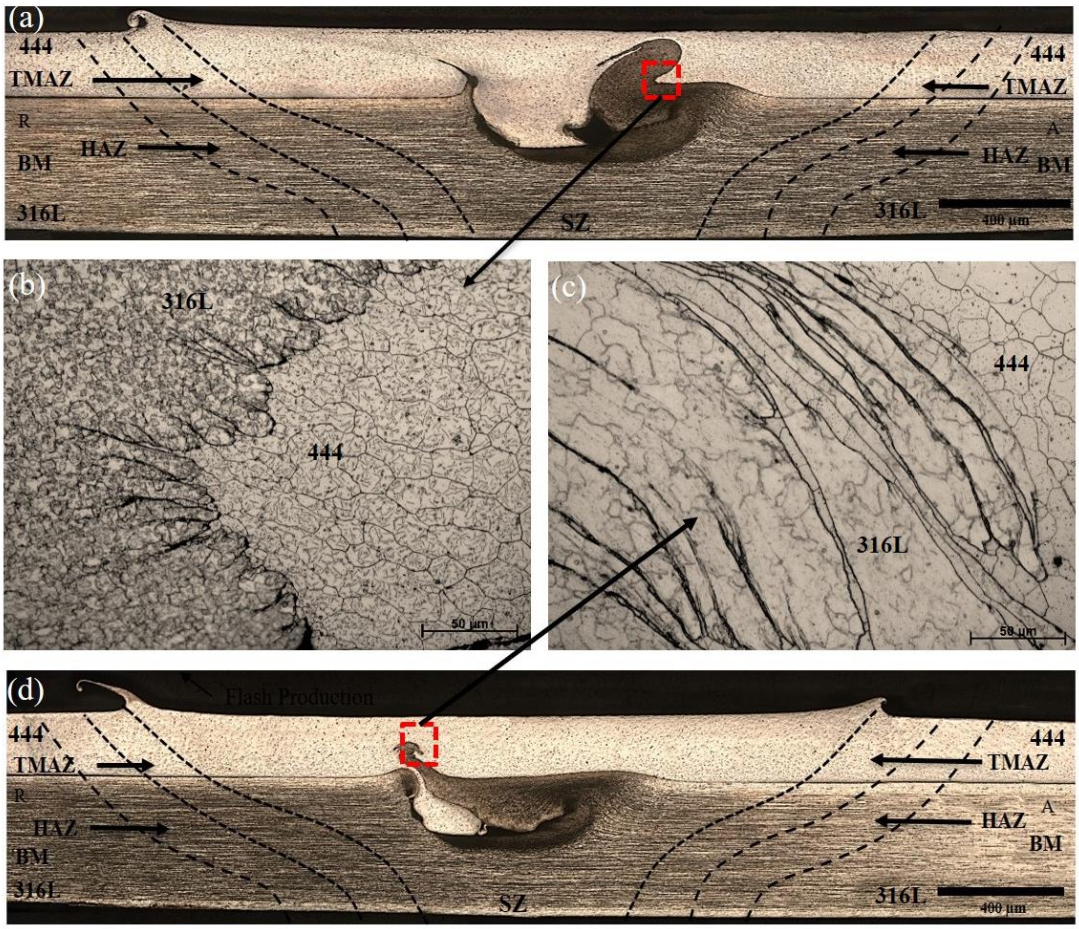

Source: The author.

Therefore, the microstructural analysis of the different weld conditions shows that it is possible to produce dissimilar FSW joints with AISI 316L and AISI 444 steels, both in butt and lap joint configurations. No harmful microstructural changes in HAZ and TMAZ, such as intense grain growth and undesirable phase formation. In addition to the consolidation of a refined ZM with high cohesion between the two materials. These characteristics can be obtained either through a butt joint with AISI 316L austenitic stainless steel on the retreating side, with an axial force of 30 kN and a rotational speed of 350 rpm, in Condition 1, as through an overlap joint with AISI 316L austenitic stainless

steel on top, increasing the axial force to 50 kN and keeping the rotation speed at 350 rpm, as observed in Condition 4.

8.5 Conclusions

Based on the results of the microstructural evaluation of the dissimilar welding between ferritic stainless steel AISI 444 and austenitic stainless steel AISI 316L, resulting from the use of different welding parameters such as axial force, rotational speed and joint configurations, it was possible to conclude that:

1. With the proper combination of welding parameters, it is possible to successfully weld a dissimilar joint between ferritic stainless steel AISI 444 and austenitic stainless steel AISI 316L, producing a joint without harmful microstructural changes in the HAZ, with intense grain refining in the TMAZ and a refined stir zone with high cohesion between the two materials.
2. In the butt joint, the parameters used in condition 1, welded with a rotation speed of 350 rpm and an axial force of 30 kN, ensured an adequate plasticization state not only to cancel out the formation of voids and flash production as it made it possible to increase the number of inserts between the steels, ensuring greater cohesion between them.
3. In the overlap joint, with the positioning of the ferritic stainless steel AISI 444 at the bottom, it is possible to verify excellent results about the consolidation of the FSW joint because as the axial force increases from 45 kN to 50 kN and the rotation speed decreases to 350 rpm, there is a reduction in voids at the 316L/444 interface, making it possible to weld AISI 316L and AISI 444 steels in an overlap joint with no voids in the stir zone.
4. With the positioning of AISI 444 ferritic stainless steel in the upper position of the lap joint, as the axial force increases from 20 kN to 30 kN, the amount of AISI 444 steel material at the bottom decreases and the AISI 316L steel hook at the top is directed with greater intensity from the advancing side to the retreating side, compacting the AISI 444 steel hook, however, still insufficient to nullify the voids existing in the contact zone between the two materials.

5. Under all conditions, both on the retreating and advance sides, relevant microstructural changes were not observed in the HAZ, making it difficult to limit the BM to the HAZ.
6. In the thermomechanically affected zone of lap joints, for both ferritic and austenitic stainless steel, deformed and recrystallised grains are found, this recrystallisation being intensified in conditions 4, 5 and 6, with AISI 316L steel in the upper part of the overlap joint and with the use of high axial forces.
7. In the stir zone, there is an intense recrystallisation and grain refining, this refining being observed in greater intensity in regions closer to the surface of the joints and in the regions of contact between the two materials.
8. The contact interface between the two steels is strongly modified by increasing the axial force. In butt joints, the increase in axial force causes the appearance of tipped inserts. In the overlap joints, with AISI 316L steel at the bottom, the reduction of central hooks steels and the complete nullification of the existing voids in the interface region occurs. In overlap joints, with AISI 316L steel at the top, it causes the appearance of hooks composed of regions interleaved between the two steels.

8.6 Acknowledgments

The authors are grateful for the support given by the following Institutions: Universidade Federal do Ceará, Laboratório de Pesquisa e Tecnologia em Soldagem (LPTS) and The Analytical Center, in Brazil, and the Solid State Joining Processes, Helmholtz-Zentrum Geesthacht (HZG), in Germany. This study was financed in part by the Coordenação de Aperfeiçoamento de Pessoal de Nível Superior - Brasil (CAPES) - Finance Code 001, Brazilian funding agencies CNPq (Universal 472185/2011-0), and FUNCAP and CAPES (Project CI1-0050-00049.01.00/11 – International Cooperation).

8.7 References

ABDOLLAH-ZADEH, A.; SAEID, T.; SAZGARI, B. Microstructural and mechanical properties of friction stir welded aluminum/copper lap joints. **Journal of Alloys and Compounds**, [s.l.], v. 460, n. 1, p. 535–538, 28 jul. 2008.

AGUILAR, S.; TABARES, R.; SERNA, C. Microstructural Transformations of Dissimilar Austenite-Ferrite Stainless Steels Welded Joints. **Journal of Materials Physics and Chemistry**, [s.l.], v. 1, n. 4, p. 65–68, 14 nov. 2013.

BARBINI, A.; CARSTENSEN, J.; DOS SANTOS, J. F. Influence of a non-rotating shoulder on heat generation, microstructure and mechanical properties of dissimilar AA2024/AA7050 FSW joints. **Journal of Materials Science & Technology**, [s.l.], 1 nov. 2017.

BARROS, I. F. DE. **Soldagem dissimilar do aço inoxidável ferrítico AISI 444 e do aço inoxidável austenítico AISI 316L por meio do processo TIG autógeno utilizando corrente pulsada**. 2013. Dissertação de Mestrado, Universidade Federal do Ceará, Fortaleza, 2013.

BATISTÃO, B. F. et al. Characterization of dissimilar friction stir welded lap joints of AA5083 and GL D36 steel. **Journal of Materials Research and Technology**, [s.l.], v. 9, n. 6, p. 15132–15142, 1 nov. 2020.

BILGIN, M. B.; MERAN, C. The effect of tool rotational and traverse speed on friction stir weldability of AISI 430 ferritic stainless steels. **Materials & Design**, [s.l.], v. 33, p. 376–383, jan. 2012.

BOGAARD, R. H. et al. Thermophysical properties of stainless steels. **Thermochimica Acta**, [s.l.], v. 218, p. 373–393, 3 maio 1993.

CAETANO, G. DE Q. et al. Influence of rotation speed and axial force on the friction stir welding of AISI 410S ferritic stainless steel. **Journal of Materials Processing Technology**, [s.l.], v. 262, p. 430–436, 1 dez. 2018.

CAETANO, G. DE Q. et al. Intergranular corrosion evaluation of friction stir welded AISI 410S ferritic stainless steel. **Journal of Materials Research and Technology**, [s.l.], fev. 2019.

CAETANO, G. Q. **Soldagem Similar de aços Inoxidaveis Ferríticos e Austenícios pelo Processo "Friction Stir Welding"**. Dissertação de Mestrado—Fortaleza: Universidade Federal do Ceará - UFC, 2016.

ÇAM, G. Friction stir welded structural materials: beyond Al-alloys. **International Materials Reviews**, [s.l.], v. 56, n. 1, p. 1–48, 1 jan. 2011.

ÇAM, G. et al. Applicability of Friction Stir Welding to steels. **Journal of Achievements in Materials and Manufacturing Engineering**, [s.l.], v. 80, n. 2, 2017.

CAMPO, K. N. et al. Microstructure and interface characterization of dissimilar friction stir welded lap joints between Ti–6Al–4V and AISI 304. **Materials & Design (1980-2015)**, [s.l.], v. 56, p. 139–145, 1 abr. 2014.

CHUNG, Y. D. et al. Friction stir welding of high carbon steel with excellent toughness and ductility. **Scripta Materialia**, [s.l.], v. 63, n. 2, p. 223–226, 1 jul. 2010.

DEBROY, T.; BHADESHIA, H. Friction stir welding of dissimilar alloys–a perspective. **Science and Technology of Welding & Joining**, [s.l.]: [s.n.], 2013.

DOUDE, H. et al. Optimizing weld quality of a friction stir welded aluminum alloy. **Journal of Materials Processing Technology**, [s.l.], v. 222, p. 188–196, 2015.

DU, D. et al. Gradient characteristics and strength matching in friction stir welded joints of Fe–18Cr–16Mn–2Mo–0.85 N austenitic stainless steel. **Materials Science and Engineering: A**, [s.l.], v. 616, p. 246–251, 2014.

EDWARDS, P. D.; RAMULU, M. Material flow during friction stir welding of Ti-6Al-4V. **Journal of Materials Processing Technology**, [s.l.], v. 218, p. 107–115, 2015.

EMAMI, S. et al. Dissimilar friction stir welding of AISI 430 ferritic and AISI 304L austenitic stainless steels. **Archives of Civil and Mechanical Engineering**, [s.l.], v. 20, n. 4, p. 131, 18 out. 2020.

FRATINI, L.; BUFFA, G. CDRX modelling in friction stir welding of aluminium alloys. **International Journal of Machine Tools and Manufacture**, [s.l.], v. 45, n. 10, p. 1188–1194, ago. 2005.

FUJII, H. et al. Friction stir welding of carbon steels. **Materials Science and Engineering: A**, [s.l.], v. 429, n. 1, p. 50–57, 15 ago. 2006.

GENG, P. et al. Prediction of residual stresses within dissimilar Al/steel friction stir lap welds using an Eulerian-based modeling approach. **Journal of Manufacturing Processes**, [s.l.], v. 79, p. 340–355, 1 jul. 2022.

HAN, J. et al. Microstructure and mechanical properties of friction stir welded 18Cr–2Mo ferritic stainless steel thick plate. **Materials & Design**, [s.l.], v. 63, p. 238–246, 1 nov. 2014.

HEIDARZADEH, A. et al. Friction stir welding/processing of metals and alloys: A comprehensive review on microstructural evolution. **Progress in Materials Science**, [s.l.], v. 117, p. 100752, 1 abr. 2021.

HUMPHREYS, F. J.; HATHERLY, M. **Recrystallization and Related Annealing Phenomena**. [s.l.] Elsevier, 2012.

JOHNSON, P.; MURUGAN, N. Microstructure and mechanical properties of friction stir welded AISI321 stainless steel. **Journal of Materials Research and Technology**, [s.l.], v. 9, n. 3, p. 3967–3976, 1 maio 2020.

KADIAN, A. K.; BISWAS, P. The study of material flow behaviour in dissimilar material FSW of AA6061 and Cu-B370 alloys plates. **Journal of Manufacturing Processes**, [s.l.], v. 34, p. 96–105, 1 ago. 2018.

KASAI, H.; MORISADA, Y.; FUJII, H. Dissimilar FSW of immiscible materials: Steel/magnesium. **Materials Science and Engineering: A**, [s.l.], v. 624, p. 250–255, 29 jan. 2015.

KHERROUBA, N. et al. Experimental study and simulation of the σ phase precipitation in the stabilized 316Ti austenitic stainless steel. **Materials Chemistry and Physics**, [s.l.], v. 266, p. 124574, 1 jul. 2021.

KIM, J. K. et al. Intergranular corrosion of Ti-stabilized 11wt% Cr ferritic stainless steel for automotive exhaust systems. **Corrosion science**, [s.l.], v. 51, n. 11, p. 2716–2723, 2009.

KOCABEKIR, B. et al. An effect of heat input, weld atmosphere and weld cooling conditions on the resistance spot weldability of 316L austenitic stainless steel. **Journal of Materials Processing Technology**, [s.l.], v. 195, n. 1, p. 327–335, 1 jan. 2008.

KOKAWA, H. et al. Microstructures in Friction Stir Welded 304 Austenitic Stainless Steel. **Welding in the World**, [s.l.], v. 49, n. 3, p. 34–40, 1 mar. 2005.

KUMAR, K.; KAILAS, S. V. The role of friction stir welding tool on material flow and weld formation. **Materials Science and Engineering: A**, [s.l.], v. 485, n. 1, p. 367–374, 2008.

KUMAR, K.; KAILAS, S. V. Positional dependence of material flow in friction stir welding: analysis of joint line remnant and its relevance to dissimilar metal welding. **Science and Technology of Welding & Joining**, [s.l.], 2013.

KUMAR, M.; SINGH, J.; SINGH UPPAL, A. Improvement in corrosion resistance of AISI 316L stainless steel weld cladding using GTA remelting technique. **Materials Today: Proceedings**, [s.l.], 2 jun. 2022.

LO, K. H.; SHEK, C. H.; LAI, J. K. L. Recent developments in stainless steels. **Materials Science and Engineering: R: Reports**, [s.l.], v. 65, n. 4, p. 39–104, 29 maio 2009.

MANDAL, S. et al. Constitutive equations to predict high temperature flow stress in a Ti-modified austenitic stainless steel. **Materials Science and Engineering: A**, [s.l.], v. 500, n. 1, p. 114–121, 25 jan. 2009.

MISHRA, R. S.; MA, Z. Y. Friction stir welding and processing. **Materials Science and Engineering: R: Reports**, [s.l.], v. 50, n. 1–2, p. 1–78, 31 ago. 2005.

MUKHERJEE, M.; PAL, T. K. Influence of Heat Input on Martensite Formation and Impact Property of Ferritic-Austenitic Dissimilar Weld Metals. **Journal of Materials Science & Technology**, [s.l.], v. 28, n. 4, p. 343–352, 1 abr. 2012.

MURR, L. E. A Review of FSW Research on Dissimilar Metal and Alloy Systems. **Journal of Materials Engineering and Performance**, [s.l.], v. 19, n. 8, p. 1071–1089, 1 nov. 2010.

NANDAN, R.; DEBROY, T.; BHADESHIA, H. K. D. H. Recent advances in friction-stir welding – Process, weldment structure and properties. **Progress in Materials Science**, [s.l.], v. 53, n. 6, p. 980–1023, 1 ago. 2008.

NENE, S. S. et al. Enhanced strength and ductility in a friction stir processing engineered dual phase high entropy alloy. **Scientific Reports**, [s.l.], v. 7, n. 1, p. 16167, 23 nov. 2017.

PADILHA, A. F. **Materiais de engenharia: microestrutura e propriedades**. Edição Eletrônica ed. São Paulo: Hermus, [s.l.], v. 1, 2000.

PARK, S. H. C. et al. Rapid formation of the sigma phase in 304 stainless steel during friction stir welding. **Scripta Materialia**, [s.l.], v. 49, n. 12, p. 1175–1180, dez. 2003a.

PARK, S. H. C. et al. Rapid formation of the sigma phase in 304 stainless steel during friction stir welding. **Scripta Materialia**, [s.l.], v. 49, n. 12, p. 1175–1180, dez. 2003b.

PIETRAS, A.; WĘGLOWSKI, M. S. Imperfections in FSW joints and NDT methods of their detection. **Biuletyn Instytutu Spawalnictwa w Gliwicach**, [s.l.], v. Vol. 58, No. 2, 2014.

RAMIREZ, A. J. et al. Effect of Tool Offset on Dissimilar Cu-AISI 316 Stainless Steel Friction Stir Welding. *In*: The Twenty-first International Offshore and Polar Engineering Conference, 2011, [s.l.]. **Anais**...International Society of Offshore and Polar Engineers, 2011. Disponível em: <https://www.onepetro.org/conference-paper/ISOPE-I-11-103>. Acesso em: 6 dez. 2016

SHASHI KUMAR, S.; MURUGAN, N.; RAMACHANDRAN, K. K. Identifying the optimal FSW process parameters for maximizing the tensile strength of friction stir welded AISI 316L butt joints. **Measurement**, [s.l.], v. 137, p. 257–271, 1 abr. 2019.

SHULTZ, E. F. et al. Effect of compliance and travel angle on friction stir welding with gaps. **Journal of Manufacturing Science and Engineering**, [s.l.],v. 132, n. 4, p. 041010, 2010.

SILVA, C. C. et al. Microstructural characterization of the HAZ in AISI 444 ferritic stainless steel welds. **Materials Characterization**, [s.l.], v. 59, n. 5, p. 528–533, 1 maio 2008.

SILVA, C. C. et al. Austenitic and ferritic stainless steel dissimilar weld metal evaluation for the applications as-coating in the petroleum processing equipment. **Materials & Design**, [s.l.], v. 47, p. 1–8, 1 maio 2013.

TAVARES, S. S. M. et al. Microstructural, magnetic and mechanical property changes in an AISI 444 stainless steel aged in the 560 °C to 800 °C range. **Materials Characterization**, [s.l.], v. 59, n. 2, p. 112–116, 1 fev. 2008.

THOMAS, W. M. et al. **Friction stir butt welding**. Cambridge, TWI, 1991.

THREADGILL, P. L. Terminology in friction stir welding. **Science and Technology of Welding and Joining**, [s.l.], v. 12, n. 4, p. 357–360, 1 maio 2007.

TONGNE, A. et al. Banded structures in friction stir welded Al alloys. **Journal of Materials Processing Technology**, [s.l.], v. 221, p. 269–278, 2015.

TRIGWELL, S.; SELVADURAY, G. Effects of welding on the passive oxide film of electropolished 316L stainless steel. **Journal of Materials Processing Technology**, [s.l.], v. 166, n. 1, p. 30–43, 15 jul. 2005.

TRUEBA, L. et al. Effect of tool shoulder features on defects and tensile properties of friction stir welded aluminum 6061-T6. **Journal of Materials Processing Technology**, [s.l.], v. 219, p. 271–277, 2015.

VALIEV, R. Z.; LANGDON, T. G. Principles of equal-channel angular pressing as a processing tool for grain refinement. **Progress in Materials Science**, [s.l.], v. 51, n. 7, p. 881–981, 1 set. 2006.

WANG, D. et al. Microstructural evolution and mechanical properties of friction stir welded joint of Fe–Cr–Mn–Mo–N austenite stainless steel. **Materials & Design**, [s.l.], v. 64, p. 355–359, 2014.

XIONG, J. T. et al. High strength lap joint of aluminium and stainless steels fabricated by friction stir welding with cutting pin. **Science and Technology of Welding and Joining**, [s.l.], v. 17, n. 3, p. 196–201, 1 abr. 2012.

YU, M. et al. Influence of welding parameters on interface evolution and mechanical properties of FSW Al/Ti lap joints. **Journal of Materials Science & Technology**, [s.l.], v. 35, n. 8, p. 1543–1554, 1 ago. 2019.

ZHENG, Q. et al. Effect of plunge depth on microstructure and mechanical properties of FSW lap joint between aluminum alloy and nickel-base alloy. **Journal of Alloys and Compounds**, [s.l.], v. 695, p. 952–961, 25 fev. 2017.

9 CHAPTER 9: Effect of fsw process parameters on mechanical properties of dissimilar welded joints of AISI 316L and AISI 444 stainless steel joints

9.1 Abstract

The mechanical properties of the conditions welded by the FSW process, between AISI 444 and 316L steels in butt and overlap joints, were evaluated through bending, microhardness, uniaxial tensile and shear tests. In the bending results, the best-welded condition was an overlap joint supported a greater bending angle concerning the conditions in the butt joint due to a better consolidation of the joint root. The most remarkable changes in microhardness values occurred between BM, HAZ, TMAZ and SZ of AISI 316L steel due to the greater ease of this steel, compared to AISI 444 steel, in recrystallizing and refining the grain. In the uniaxial tensile and shear test, Condition 4 was the condition that best managed to combine good results in yield strength, tensile strength and elongation. Thus, we can conclude that decreasing the rotation speed to 350 rpm maintaining axial force at 50 kN, in Condition 4 welded in an overlap joint, allowed the constitution of a dissimilar FSW joint between AISI 316L and AISI 444 steels with greater bending angle until crack propagation at the joint root and better results in the yield and tensile strength compared to Condition 1, welded in butt joint and the base metal of AISI 444 steel.

Keywords: Friction stir welding; Stainless Steels; Bending; Microhardness; Uniaxial Tensile Test; Shear Test.

9.2 Introduction

AISI 316L austenitic stainless steel is the low carbon version of AISI 316 steel, seeking the attenuation of carbide precipitation. Compared to other austenitic steels, AISI 316L steel stands out due to its excellent mechanical properties at low and high temperatures and with higher corrosion resistance, as noted by SAMANTA et al. (2006). AISI 444 ferritic stainless steel has the highest corrosion resistance among ferritic stainless steels, which can be compared to AISI 316L steel, as shown by BELLEZZE et al. (2008). Ferritic stainless steels (FSS) typically have lower ductility, toughness and weldability compared

to austenitic stainless steels (ASS), as reported by SMITH, W. F. (1993). The structure of body-centred cubic (BCC) crystallography in FSS, limits the number of available slip systems and causes high ductile to brittle transition temperature (DBTT) above room temperature, this being a challenge for the application of AISI 444 steel in the industry, as reported by PATON, (1998).

A significant advantage of ferritic stainless steels is the reduction or absence of nickel in their composition, which considerably lowers the price of ferritic stainless steels compared to austenitic stainless steels as reported by SILVA et al. (2007) and LO; SHEK and LAI. (2009). This aspect has attracted the attention of the steel industry in order to develop new processing routes for these steels, aiming at improving the chemical composition, seeking better formability and plastic strain ratio and recrystallization mechanisms, as proposed by DU et al. (2010), SIQUEIRA et al. (2011) and COSTA et al. (2017), the refinement of grains by different recrystallization mechanisms, using intermediate annealing in rolling process as used by RODRIGUES et al. (2017) and investigating the effect of finishing hot rolling temperature as proposed by and VIEIRA BRAGA et al. (2016). Thus, with the advancement of these improvements, it is also necessary to evolve in terms of manufacturing processes, as in the case of welding, to ensure that these improvements are ensured.

Due to the lower cost and the improvements achieved in its properties; these steels have become quite competitive in replacing carbon steels and austenitic stainless steels. RODRIGUES et al. (2019) highlight the application of FSS in kitchen utensils, automotive components, heaters and equipment for nitric acid processing. At the same time, CASHELL and BADDOO, (2014) highlight the use of FSS in vehicle chassis, railway wagons, conveyors, chutes, tanks and walkways in sectors such as road and rail transport, water distribution, power generation and mining. However, these steels have also been considered in other sectors such as the oil and gas industry, as reported by SILVA et al. (2007) and MACHADO et al. (2006).

The lower application of ferritic stainless steels in the industry is related to the metallurgical problems arising from the fusion welding of these steels. When subjected to thermal welding cycles, these materials undergo metallurgical changes, which compromise their weldability and the mechanical response of the welds. SILVA et al. (2008), evaluating the heat-affected zone (HAZ) of AISI 444 steel observed, in addition to grain growth, the precipitation of chromium nitrides and carbonitrides and the

formation of secondary phases such as Laves, chi (χ) e sigma (σ), that can compromise both the mechanical strength of welded joints and make the weld susceptible to corrosion.

However, in recent decades friction welding (FSW), a solid-state welding process developed by The Welding Institute (TWI) in Cambridge, England, THOMAS et al. (1991) revolutionized the union of materials considered non-weldable or with low weldability. MISHRA and MA, (2005) report that this process uses a non-consumable tool that rotates and penetrates the joint, resulting in heating and plastic deformation of the materials to be joined, which can be heated to temperatures below those experienced in fusion welding.

Among the advantages commonly attributed to the FSW process, stand out: minimal residual stress and distortion, absence of defects related to the material's melting, smaller heat-affected zone and microstructure with refined grains that increase the tensile strength and fatigue life as proposed by BILGIN e MERAN, (2012), DEBROY e BHADESHIA, (2013) and SATHIYA et al., (2006). LIU et al., (2018) report that FSW welding of steels exhibits great advantages compared to traditional fusion welding processes due to efficient control of welding temperature and cooling rate. This aspect helps to avoid unwanted phase transformations, which usually occur during traditional welding, and favorable phase fractions can be maintained in the weld zone, thus avoiding the typical property degradations associated with fusion welding.

SHASHI KUMAR; MURUGAN and RAMACHANDRAN, (2019), applying the FSW process in the production of similar joints of 316L austenitic stainless steel proved that with the correct adjustment of the process parameters, it is possible to reduce secondary phases and produce an intensely refined stir zone with a positive influence on the joint tensile strength limit, reaching peaks of 618 ± 1,1 MPa. This optimization is associated with the tool rotation speed, tool traverse speed and axial force used, which have a significant interaction effect on the UTS of the joints. HAN et al. (2014) evaluating the microstructure and mechanical properties of similar joints of a ferritic stainless steel 18Cr-2Mo, with a chemical composition similar to AISI 444 steel, proved that the FSW process is capable of producing a stir zone with refined equiaxed ferritic grains enabling a high hardness in the stir zone ranging from 186 to 222HV and a good impact resistance of the welded joints, compared with the average toughness of base metal (78 J), the impact values of the FSW joint exhibit only a slight drop and at the level of 61–71 J . Caetano et al. (2021) analyzing a similar weld AISI 444 ferritic stainless steel by the FSW process,

produced joints without defects, with high mechanical resistance and excellent resistance to intergranular corrosion, in the welds were not found any chromium carbides and embrittlement phases capable of compromising the excellent results of resistance to intergranular corrosion in the SZ, HAZ and TMAZ e the mechanical tests showing good results in relation to the ductility, yield strength, tensile strength and elongation of the joints welded, reaching a bending angle of 130°, an elongation of 37.9% and equivalent to that obtained for the base metal and a tensile strength of 512.5 MPa ± 0,6, with all samples tested by the shear test fracturing in the base metal.

When AISI 316L and AISI 444 steels are welded in dissimilar joints, by fusion welding processes, such as those performed by BARROS, (2013) with GTAW autogenous (without filler metal) with pulsed current, the resulting mechanical properties presented problems regarding their performance. One of them was despite having an average elongation of 24% and higher than the base metal of AISI 444 steel. All specimens evaluated failed the bending test, which indicates the presence of cracks and/or fissures in the weld beads when they are subjected to more severe mechanical stresses. According to KOU (2003), grain growth in ferritic stainless steels, which can occur both in the molten zone and in the HAZ when subjected to arc welding, is mainly responsible for compromising the mechanical performance with a decrease in hardness, ductility and tenacity.

Despite the absence of works in the literature that explore the dissimilar welding of AISI 316L/444 joints by the FSW process, some works already highlight the potential of steels, both in similar joints and in dissimilar joints with other materials. HE et al. (2019), evaluating the high-temperature tensile behaviours of the dissimilar joint of 9Cr-1W steel and AISI 316L steel by FSW, concluded that the grain size and dislocation density of the SZ of AISI 316 L were critical for high-temperature tensile behaviour of the joint, and reducing the rotational speed to 300 RPM could enhance the grain refining, and the dislocation density is increased, being the joint more likely to be fractured at AISI 316 L base metal, reaching an elongation of 17.7%, however lower than that observed for the base metal of AISI 316L steel also at 550°C. SENTHILKUMAR and RAMAKRISHNAN, (2021) evaluated the impact of the FSW process parameters on the mechanical properties of dissimilar welds between the FSS AISI 430, which has a chemical composition similar to AISI 444, with the FSS AISI 410. The authors emphasise that the tensile strength of the joint obtained is 8.41% greater than that presented by the

base metal of AISI 430 steel and that among the parameters of the FSW process analysed, the adjustments made in the rotation speed were the ones that contributed most to this improvement.

Despite advances, the combination of these aspects in FSW welding dissimilar between ferritic stainless steel AISI 444 and austenitic AISI 316L are still incipient and more detailed information on the influence of process parameters on the mechanical properties of these joints becomes an essential topic with a significant scientific and technological appeal. Thus, this work aims to evaluate the effect of FSW welding parameters on the mechanical properties of dissimilar joints between austenitic stainless steel AISI 316L and ferritic stainless steel AISI 444, evaluating the performance of welded joints through bending, microhardness tests, uniaxial tensile and shear testing.

9.3 Materials and Methods

The welds were carried out with plates of ferritic stainless steel AISI 444, 2 mm thick and austenitic stainless steel AISI 316L, with thicknesses of 4 mm or 3 mm depending on the joint configuration used. The chemical composition of the materials was determined by optical emission spectroscopy (Shimadzu model PA7000 Japan) and is presented in the Table 9.1.

Table 9.1 - Chemical composition of the base metals (% weight).

Material	Elements											
	C	Si	Mn	P	S	Cr	Ni	Mo	Cu	Co	N	Fe
316L	0.026	0.56	0.84	0.029	<0.010	17.1	9.97	1.96	0.32	0.20	0.056	Bal.
444	0.017	0.53	0.16	0.47	<0.010	17.8	0.24	1.75	0.57	----	----	Bal

Source: The author.

The samples were joined by the FSW process in the Helmholtz-Zentrum Geesthacht (HZG), Germany. All welds, evaluated for mechanical properties, were made using the HZG Gantry System with two different joint configurations. The first was a butt joint with 4 mm of thickness, with AISI 316L steel on the retreating side and AISI 444 steel on the advancing side as shown in Fig. 9.1 (a) and the other in overlap joint configuration with the AISI 316L steel at the top and 5 mm of thickness in the stir zone, showing an overlapping region of 70 mm in length, as can see in Fig. 9.1 (b). An inert gas (Air)

injection system was used to protect the material during the process, as at temperatures above 535 °C these stainless steels react with the atmosphere. Welds were performed in load control mode with an integrated system to record process data, such as penetration depth, rotational speed, torque, forces applied to the tool and tool position over time.

A polycrystalline cubic boron nitride (PCBN) tool with a conical diameter of 25 mm and a conical pin with a diameter of 9.2 mm and a length of 3.7 mm were used. The pin has a conical surface with negative recesses in the form of a spiral in relation to the axis of symmetry of the tool.

Figure 9.1 – Different configurations of welded joints (a) Butt joint with AISI 316L steel on the retreating side (b) Overlap joint with AISI 316L steel on the top.

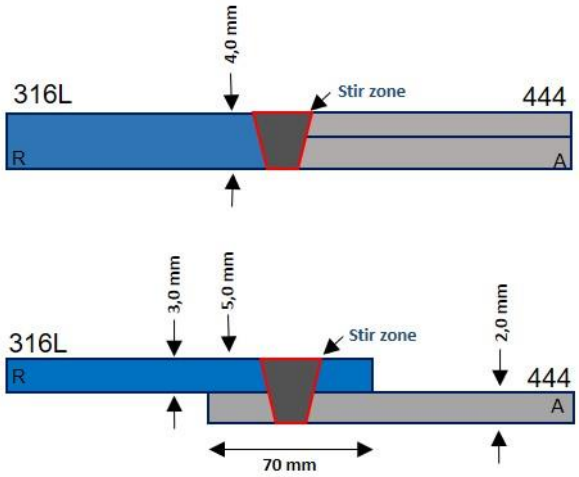

Source: The author.

To define the welding parameters, the best set of parameters found by CAETANO et al. (2018) in similar FSW welding of AISI 444 ferritic stainless steel and AISI 316L austenitic stainless steel. Thus, the butt joints were welded with two levels of rotation speed, 350 and 450 rpm, and two levels of axial force, 25 and 30 kN, as shown in Table 9.2. In the overlap joints, with the austenitic stainless steel AISI 316L at the top, the rotation speed variation from 350 to 450 rpm was also performed, but increasing the axial force to 45 and 50 kN, as shown in Table 9.3. For all 6 conditions welded, the welding speed was kept constant at 1 mm/s and the tool inclination angle at 0º.

Table 9.2 – Welding Parameters for Dissimilar FSW Butt Welding of AISI 316L/444 Steels

Condition	Rotation Speed (rpm)	Axial Force (kN)	Advancing Side	Retreating Side
1	350	30	444	316L
2	450	25	444	316L
3	450	30	444	316L

Source: The author.

Table 9.3 - Welding Parameters for Dissimilar FSW Overlap Welding of AISI 316L/444 Steels

Condition	Rotation Speed (rpm)	Axial Force (kN)	Advancing Side	Retreating Side
4	350	50	316L	444
5	450	45	316L	444
6	450	50	316L	444

Source: The author.

Mechanical tests were performed in order to determine the mechanical properties and correlate them with the microstructural characteristics observed along the joints. For this, bending, microhardness Vickers and uniaxial tensile and shear tests were performed. All tests were performed at room temperature. The bending was performed as a qualitative test to analyse the samples' ductility. This is the first step in evaluating the quality of the FSW weld and selecting the samples that will go to the following mechanical test. The expected answer for this test is that the sample tilts more than 90 degrees without propagating any fault at the root. The distance between brackets was based on ASTM E290-09 standard.

The microhardness Vickers maps were traced in the cross-section of the welded joints according to ASTM E384-99 standard to evaluate the changes in the material microhardness resulting from the welding process. The microhardness lines were drawn so as to cover all regions of the weld. The distance between each indentation was 500 μm, by applying a load of 0.1 Kgf (HV 0.1) for 13 s. The Leco LM110AT microhardness tester was used in the measurements, which features a fully automatic system integrated with the Comerstone AMH55 software for obtaining data.

The specimens were produced for the tensile and shear tests with the dimensions established by the ASTM E8M-04 standard for metallic materials. The weld joint is located precisely in the middle of the specimen. The specimens were duly fixed in a universal mechanical testing machine Zwick/Roell, integrated into the TestXpert

operational platform to obtain data. The tests were carried out with three repetitions for each welding condition and the base material. The equipment used for tensile test included a screw-driven Zwick/Roell testing machine with a load capacity of 200 KN. Tests were carried out at room temperature, with a constant speed of 1mm/min. A 50 mm MTS strain gauge measured the deformation.

9.4 Results and Discussion

9.4.1 Bending Test

The bending test was used to evaluate the quality of dissimilar welds produced with AISI 316L austenitic stainless steel and AISI 444 ferritic stainless steel, by the FSW process as a function of ductility, showing its ability to resist the propagation of cracks in the root of the welds during the bending. From Figure 9.2, it is possible to verify for the butt joints that the combination of parameters used in Condition 1, welded maintaining the axial force at 30 kN and reducing the rotation speed to 350 rpm, supported the most significant bending angle until crack propagation at the root of the joint. As verified in the defect analysis carried out in Chapter 03, Condition 1 was the only condition without internal voids, showing that the material flow reached an adequate state of plasticization due to the heat intensity obtained by the combination of the parameters used.

However, for Conditions 2 and 3, welded with an axial force of 25 kN and 30 kN and rotation speeds of 450 rpm, it is observed the presence of small voids in the stir zone in a region closer to the weld root and the interface between AISI 316L and AISI 444 steels, being considered critical defects for concentrating stresses internally in the material, leading to nucleation and crack propagation. Defects, such as the observed voids, affect the joint's stress distribution, resulting in an increase in the stress concentration in the vicinity of the discontinuity, which can exceed the critical stress intensity factor (KIC), leading to crack propagation. These voids were more prominent for the welded condition with the lowest axial force, so in this condition, there is a higher concentration of stresses close to these defects and lower stress is required for crack propagation, thus supporting a lower bending angle.

Figure 9.2 – Conditions of dissimilar butt joints of AISI 444/316L steels, produced by the FSW process, submitted to bending test.

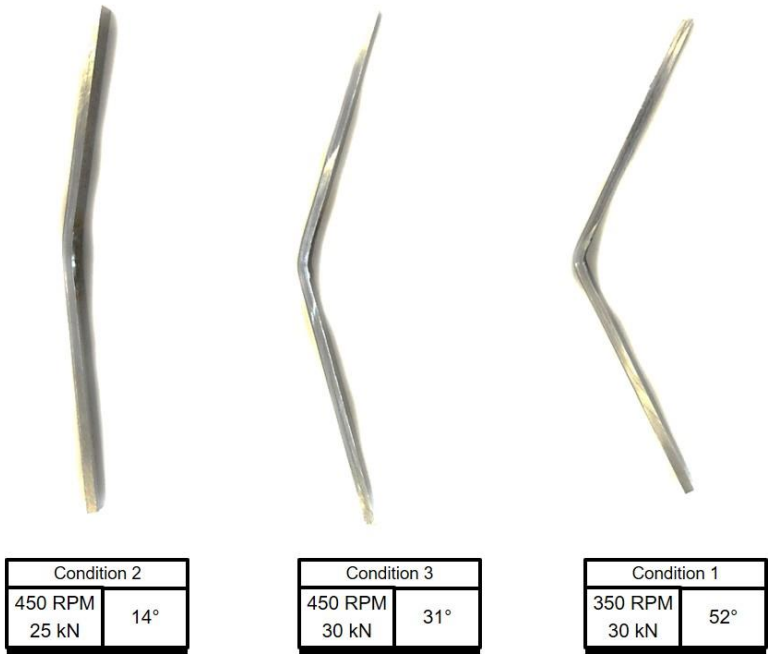

Source: The author.

The worst performance in the bending test between butt joints occurred for Condition 2. According to TONGNE et al. (2015), this low resistance to crack propagation in Condition 2 may be associated with less interaction between the tool and the material, due to the low axial force and consequent reduction in frictional force, generating insufficient heat to reach a plasticizing state suitable for the flow material during the FSW process. According to DOUDE et al. (2015), these voids in the stir zone in regions close to the weld root, as observed in Condition 2 and 3, indicate the use of parameters such as axial force and rotation speed below the ideal recommended to generate adequate heating and plasticization for the consolidation of a defect-free FSW joint with good mechanical properties.

In addition to the presence of voids, another factor detrimental to the low bending angle of butt joints in conditions 2 and 3 was the occurrence of root flaws. In Condition 2, welded with axial force of 25 kN, a root flaw was found with the observation of a line, referring to the interface between the two butt joint plates and a lack of coalescence between the two steels, as can be seen in Figure 9.3 a and Figure 9.3 b, acting as a stress concentrator for the joint, potentiating the efforts and leading to nucleation and

propagation of cracks in the root. This type of defect is associated with insufficient penetration of the tool, as reported by EDWARDS e RAMULU, (2015).

As the axial force increases to 30 kN and the rotation speed is maintained at 450 rpm in Condition 3, an excess of penetration is observed with the presence of grooves from the removal of the backplate joint, introducing another type of root flaw in the weld joint, as seen in Figure 9.3 c and Figure 9.3 d. CAETANO et al. (2018), observed different morphologies of root flaws investigating FSW welds. According to the authors, this type of defect occurs under different mechanisms. It can be formed by both excessive or insufficient axial force application. When excessive axial force is applied, the tool pin tends to pass close to the backplate caused by the excessive penetration, as seen in Condition 3. Therefore, none of the three conditions evaluated in the butt joint reached the expected response for the bending test with the sample leaning more than 90º, without propagating any fault in the weld root.

Figure 9.3 - (a) Cross-section macrograph of the Condition 2 (b) Root flaws due to lack of penetration in Condition 2. (50x) (c) Root flaws due to excess penetration in Condition 3 (50x) and (d) Cross-section macrograph of the Condition 3.

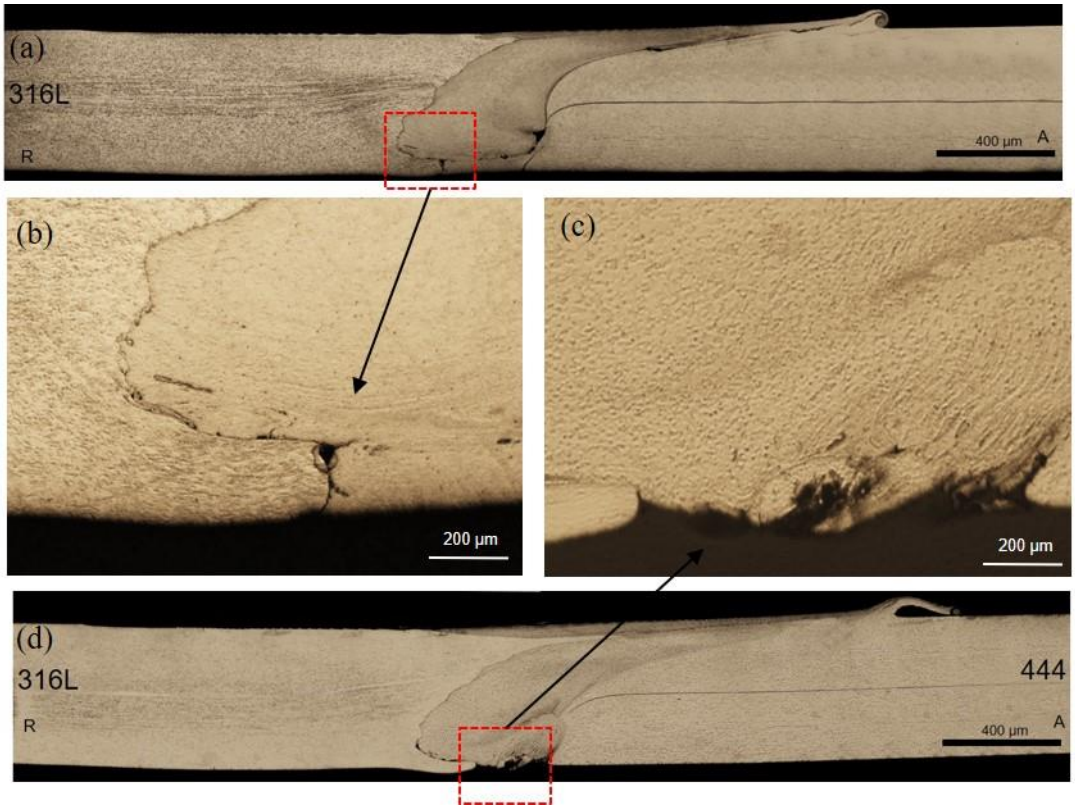

Source: The author.

Through the bending tests to analyze the ductility of the joint, which is affected by the presence of defects that induce the propagation of cracks, the overlap joints, which have AISI 444 ferritic stainless steel positioned at the bottom of the joints. It can be seen in Figure 9.4 that as the axial force increases from 45 kN to 50 kN, between conditions 5 and 6, have an increase in the bending angle from 15° to 73°, as the axial force increases it allowed an increment in the heat input and the consolidation of an adequate plasticization state of the material, reducing the voids and eliminating the tunnel defect presented in condition 5, as can be seen in Figure 9.5 .

However, the condition that supported the largest bending angle among the three conditions evaluated in overlap joint was Condition 4, welded maintaining the axial force at 50 kN and decreasing the rotation speed to 350 rpm, supporting a total angle of 87 °, 14° higher than that observed in Condition 6. According to DOUDE et al. (2015) the location and intensity of the volumetric defect depends on the material flow which can be affected by the rotational speed of the tool and voids, as observed in Condition 5, indicate

a rotational speed above the optimal parameters for an adequate flow. Thus, among the factors that led to this improvement in Condition 4, welded with the lowest rotation speed, the absence of voids and tunnel defects in the stir zone can be highlighted, contributing to a better ductility of the welded joint and a greater bending angle until crack propagation.

Figure 9.4 - Condiditon of dissimilar overlapping joints of AISI 316L/444 steels, produced by the FSW process, submitted to bending test.

Source: The author.

Figure 9.5 - Cross-section macrograph of overlap joint with AISI 316L austenitic stainless steel on top. (a) Condition 4 without defects (b) Condition 5 with voids in the stir zone and (c) Condition 6 without defects.

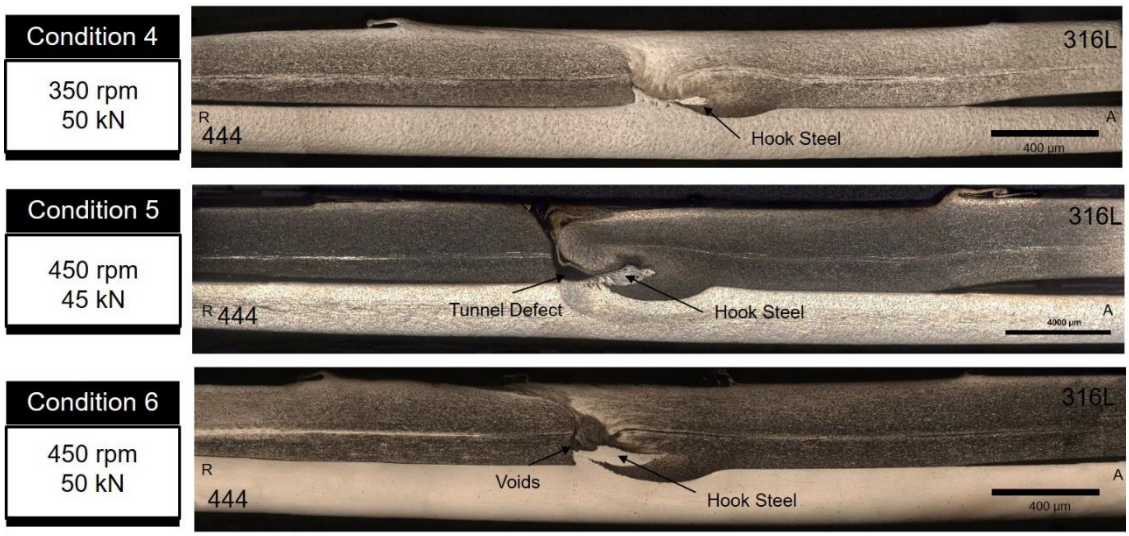

Source: The author.

Thus, among the conditions evaluated by the bending test, the best condition of the butt joint supported an angle of 52° until crack propagation in the joint root, while the best condition of the overlap joint supported an angle of 87°. Therefore, none of the six conditions evaluated reached the expected response for the bending test with the sample bending more than 90º, without propagation of any fault in the root.

9.4.2 Microhardness Test

Based on the result of the bending tests, which was the first method applied in the mechanical evaluation of dissimilar FSW welds produced by the union of AISI 316L austenitic stainless steel with AISI 444 ferritic stainless steel, Condition 1 was selected between conditions welded with butt joint configuration and the Condition 4 between conditions with overlap joint configuration, which presented a better relationship between surface finish, absence of defects and bending angle and, therefore, able to be subjected to microhardness tests.

The microhardness maps shown in Figure 9.6 indicate for both conditions a base metal zone on the retreating side of Condition 1 and on top of the joint of Condition 4 composed of AISI 316L steel with an average microhardness around 190 HV ± 10 and on the advancing side of Condition 1 and in the lower position of the overlap joint of Condition

4 a base metal zone composed of AISI 444 steel with an average microhardness also of 190 HV ± 12, according to the ASTM A240 standard, these materials have microhardness values similar and approximate to 200 HV.

Figure 9.6 - Microhardness maps of dissimilar joints of AISI 316L/444 steels, produced by the FSW process. (a) Condition 1 (b) Condition 4.

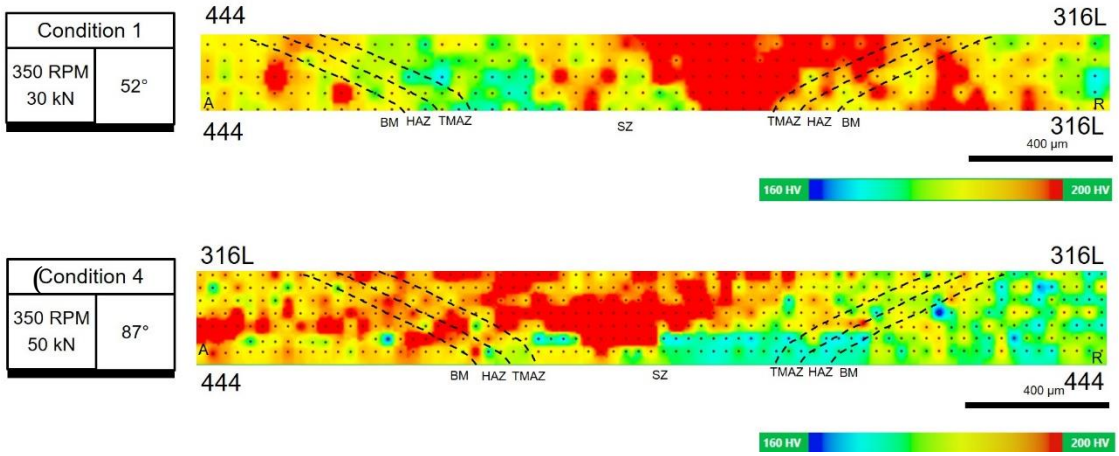

Source: The author.

Evaluating the changes in microhardness values for Condition 1, shown in Figure 9.6a, welded with AISI 316L steel on the retreating side and AISI 444 steel on the advancing side in butt joint configuration, it is possible to observe between base metal (BM), -heataffected zone (HAZ), thermomechanically affected zone (TMAZ) and the stir zone (SZ) on the retreating side, where the AISI 316L steel is positioned, the most significant changes and the highest microhardness values with peaks of 227 HV, a fact not observed on the advancing side for the AISI 444 steel.

The grain refinement is one fundamental aspect to be observed in the FSW for similar and dissimilar steel joints. It was proposed that the grain refinement in FSW is different from the other severe plastic deformation processes, such as equal channel angular pressing (ECAP), high-pressure torsion (HPT), as noted by NENE et al. (2017). According to VALIEV and LANGDON (2006), the fine grain structure obtained from FSW is mainly related to the dynamic recrystallization caused by the severe hot plastic deformation and the limited grain growth is suppressed in the subsequent cooling process. According to CAETANO (2016), the microstructural characteristics of the different regions of an FSW welded joint are determined by the degree of deformation and the maximum temperature reached, resulting from the process parameters combination.

However, as highlighted by ÇAM, (2011) another critical feature in the formation of these regions is the stacking fault energy (SFE) of each welded material, as this determines the metal's tendency to dynamically recover or recrystallize.

Recrystallization is the generation of new grains in a deformed metal, through the formation and migration of high-angle grain boundaries (HAGB). These grain boundaries are formed by the energy stored in the material during deformation in the form of dislocations. While the recovery is the entire softening process that occurred in the deformed metal without involving HAGB migration; the driving force for this transformation is the reduction of the energy accumulated during the deformation, through the rearrangement of the dislocations. This process leads to the formation of low-angle grain boundaries (LAGB), as noted by PORTER; EASTERLING and SHERIF, (2009). According to HEIDARZADEH et al. (2021) recovery and recrystallization are competing processes since both are driven by the stored energy associated with the increased dislocation density.

In the microstructural analysis carried out in Chapter 8, no relevant phase transformations that justify changes in microhardness values for AISI 316L and AISI 444 steels were evidenced. Thus, the microstructural changes that determined the increase in microhardness values on the retreating side of Condition 1 are the intense grain refining observed in the SZ and TMAZ of AISI 316L steel, resulting from the greater dynamic recrystallization that occurred, as can be seen in Figure 9.7 a, through a quantitative analysis of ASTM grain size.

Figure 9.7 - ASTM grain size measurements in different weld zones (a) Condition 1 (b) Condition 4.

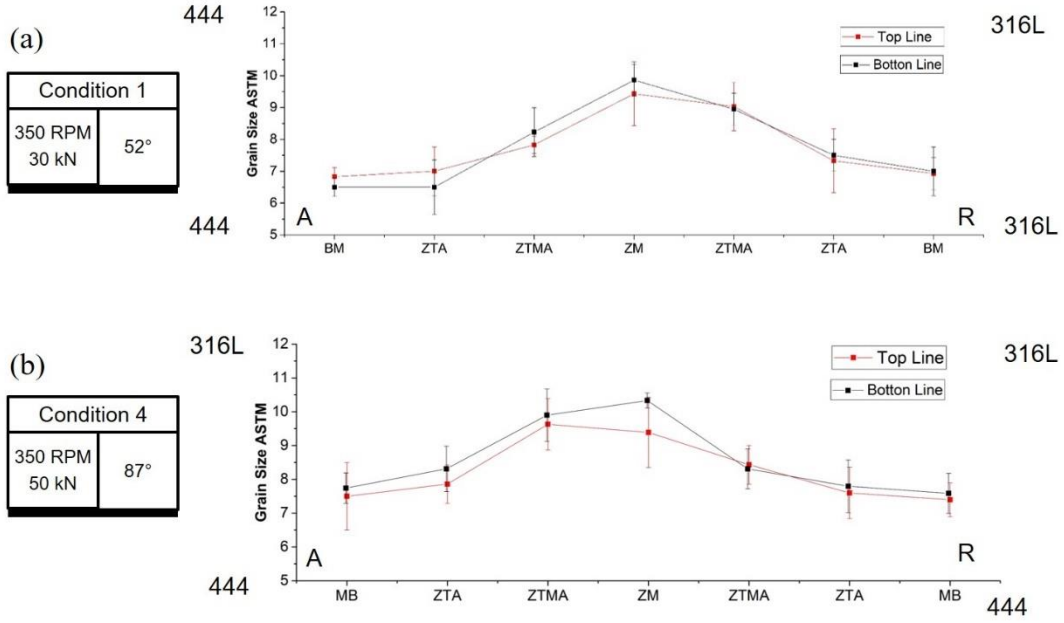

Source: The author.

As observed by ÇAM, 2011 e PARK et al. (2003), austenitic stainless steels are more easily recrystallized and refined by the FSW process than ferritic stainless steels because of the stack failure energy (SFE) differences between ferritic (bcc) and austenitic (fcc) structures. As highlighted by HEIDARZADEH et al. (2021), high-SFE metals usually exhibit extensive cross-slip and dislocation climb; thus, the microstructural behaviour in such materials is often dominated by recovery even at relatively high temperatures. In contrast, low-SFE materials typically experience almost no recovery. According to PADILHA (2000), materials with low stacking energy, such as austenitic stainless steels, produce a higher density of disagreements and higher accumulated deformation energy, favouring dynamic recrystallization and consequently the refining of grain and not the rearrangement of these disagreements leading to material softening as occurs in high-energy stacking materials.

Changing the joint configuration by placing AISI 316L steel at the top and AISI 444 steel at the bottom, forming a 70 mm overlapping zone and increasing the axial force to 50 kN in Condition 4, as can be seen in Figure 9.6 b. The evaluation of changes in microhardness values between BM, HAZ, TMAZ, SZ also shows the highest microhardness peaks for the ASS concerning the FSS, however different from what occurred in Condition 1, with the increase of the axial force, the advancing side started to

present higher microhardness values concerning the retreating side, both for the AISI 316L positioned at the top and for the AISI 444 at the bottom. MISHRA and MA (2005), reports that in the FSW process the highest temperatures and the highest intensity of plastic deformation are found on the advancing side, where the travel direction is the same rotation direction of the tool. Therefore, even in joints with the same material extending on the retreating side to the advancing side, the greatest intensity of dynamic recrystallization and consequent grain refining is found on the advancing side. This effect has been intensified with the increase in axial force, as observed in Condition 4.

According to ÇAM (2011), dynamic recrystallisation in ferritic steels does not occur as quickly as in the austenitic stainless steels because the ferrite phase has high stacking fault energy. However, dynamic recrystallisation also takes place in the SZ of these steels due to the intense plastic deformation and accompanying frictional heating during FSW, especially when there is an increase in axial force and the consequent intensity of plastic deformation.

Another peculiarity of Condition 4 is that it is possible to observe a difference between the microhardness values in the SZ between the upper part close to the shoulder and the central part close to the tool pin. This difference is associated with the highest temperature peaks reached in the upper region of the joint due to the heat generated by the intense friction between the tool shoulder and the welded material, determining lower cooling rates.

According to HE et al. (2019), the thermal distribution of the dissimilar welds in FSW is significantly asymmetrical, the welding peak temperature is found in SZ, beneath the tool shoulder and around the tool probe. Therefore, this asymmetry of temperature peaks leads to different cooling rates, which can determine different microstructural changes between the upper and lower part of the SZ, as seen in Condition 4. MILES et al. (2019) report that in FSW austenitic stainless steel joints, the heat input influences the grain size of SZ more significantly than the variation of strain rate. Thus, to reduce the grain size of SZ by increasing the strain rate, the increased proportion of heat input should be relatively low compared with the strain rate increase, as noted by MISHRA et al., 2018. From Figure 9.7 b, it is possible to observe that the grain refining in the central region of the stir zone is more significant than that found in the upper region. These differences can be associated with the cooling rates. The quantitative analysis of ASTM grain size also proves the more significant refining of grain for the Condition 4 on the advancing side

compared to the retreating side. The grain size results can be correlated with microhardness values, as they exhibit a general law of variation according to the Hall-Patch relationship. It is the smaller the grain size is, the higher hardness value.

9.4.3 Tensile Test

Condition 1, welded in a butt joint configuration, was subjected to the uniaxial tensile test and condition 4, welded in an overlap joint configuration, to the shear test, with the load applied transversely to the weld and, consequently, the rolling direction. Based on the results of the tensile test and shear test presented in Table 9.4, it is possible to verify that Condition 1 initially presented a behaviour, in terms of mechanical properties, close to that observed in the base metal of AISI 316L steels, with a yield limit around 14% higher than those observed in the base metal of AISI 316L steel, however with a tensile strength limit and elongation similar to that stipulated by ASTM A240 for AISI 444 steel.

Table 9.4 - Mechanical properties obtained from tensile tests for dissimilar joints of AISI 316L/444 steels, produced by the FSW process.

Condition	Yield Strength (MPa)	Tensile strength (MPa)	Elogation (%)
1	364.23 ± 8.3	414.45 ± 4.8	23.12 ± 1.31
4	436.95 ± 1.0	526.21 ± 1.2	20.09 ± 2.16
MB 444	375.9 ± 4.7	504.7 ± 1.6	37.8 ± 3.4
MB 316L	309.6 ± 1.9	628.0 ± 8.9	45.65 ± 19.4
ASTM A240 444	205	415	22
ASTM A240 316L	170	485	40

Source: The author.

The behavior of the test specimens from Condition 1 in the stress versus strain graph was quite different from that observed for the base metals and for Condition 4, as can be seen in Fig. 9.8, as initially, the curve had a high yield strength and tensile strength, which led to a partial rupture of the specimen in the stir zone, in a region close to AISI 316L steel and at the bottom of the joint. After the initial break, the stress dropped to 250 MPa and the behavior becomes similar to that found for the AISI 444 base metal until the final rupture of the specimen in the base metal on the advancing side, where it is positioned

AISI 444 steel, as can be seen in the Fig. 9.10 (a). The cause of this behaviour was associated with a small failure in the joint root for Condition 1, as shown in Fig. 9.9 . Although this defect is not a root flaw as expressive as those found in other butt joint conditions, it was possible to observe a small opening in the region referring to the interface between the two butt joint plates, caused due to a lack of coalescence between the two steels, similar to that observed in Condition 2.

In the shear test, in which Condition 4 was submitted, and whose results are presented in Table 9.4. The samples displayed a higher yield strength than those observed for the base metals of AISI 444 and AISI 316L steels, and better to that stipulated by the ASTM A240 standard for the base metals. The tensile strength is above that observed in the base metal of AISI 444 steel and only 16% less than that observed in the base metal of AISI 316L steel. The elongation of Condition 4 was close to that established by the ASTM A240 standard for AISI 444 steel, considering the standard deviation of ± 2.1 occurred. The fracture of the test specimens of Condition 4 occurred entirely on the advancing side and, therefore, in the base metal of the AISI 444 steel, as can be seen in Fig. 9.10 (b). Therefore, the Condition 4 was the one that presented the best evaluation in the stress-strain curve, as it was the condition that best combined good results in yield strength, tensile strength and elongation.

As revealed in the results of microhardness test, the dissimilar joint of AISI 316 L/444 has an obvious heterogeneity on the microstructures and mechanical properties. As reported by HE et al. (2019) in stainless steel FSW joints, when entering the plastic section in tensile test, strain hardening effect might occur in the BM and SZ, thus the position of yielding and necking of the tensile sample is close related to the strain hardening rate of these regions. Thus, if the SZ is strong enough and has higher strain hardening rate during the tensile process, necking and plastic instability would occur in BM, which may, in some cases, delay necking and enhances the elongation.

In the fine grained steels, the uniform elongation decreases with grain size and can be explained in terms of plastic instability or necking in the tensile test. The strain at which necking occurs or the true uniform strain (ε_u) is related to the strain hardening exponent (n) by the formula as $\varepsilon_u = n$ presented by DIETER, (1988). With the decrease in grain size, the mean distance of dislocation motion decreases, and soon pile-up of dislocations start at grain boundaries. Thus, the strain hardening exponent (n) increases when dislocation motion's mean free path (MFP) decreases. Consequently, by decreasing the

grain size, the uniform elongation (ε_u) decreases, and necking occurs at the early stage of the tensile test, as also observed by JAFARZADEGAN et al. (2013). For this reason, they are common in stainless steel FSW welds, submitted to high intensity of dynamic recrystallization and consequent grain refining, high tensile strength values and low elongations.

In dissimilar FSW joints, the heterogeneous microstructure and properties make the situation more complicated than homogeneous materials. MONTEIRO et al. (2018) report that some other aspects regarding the strengthening of stainless steels, which may influence the fracture modes in the dissimilar welded joint, should be noted, such as dynamic strain ageing during tensile deformation, dislocation density and dislocation structures, deformation temperatures and strain rate.

Figure 9.8 - Engineering tensile stress-strain diagram comparing the curve for Condition 1 and Condition 4, both dissimilar joints of AISI 316L/444 steels, produced by the FSW process.

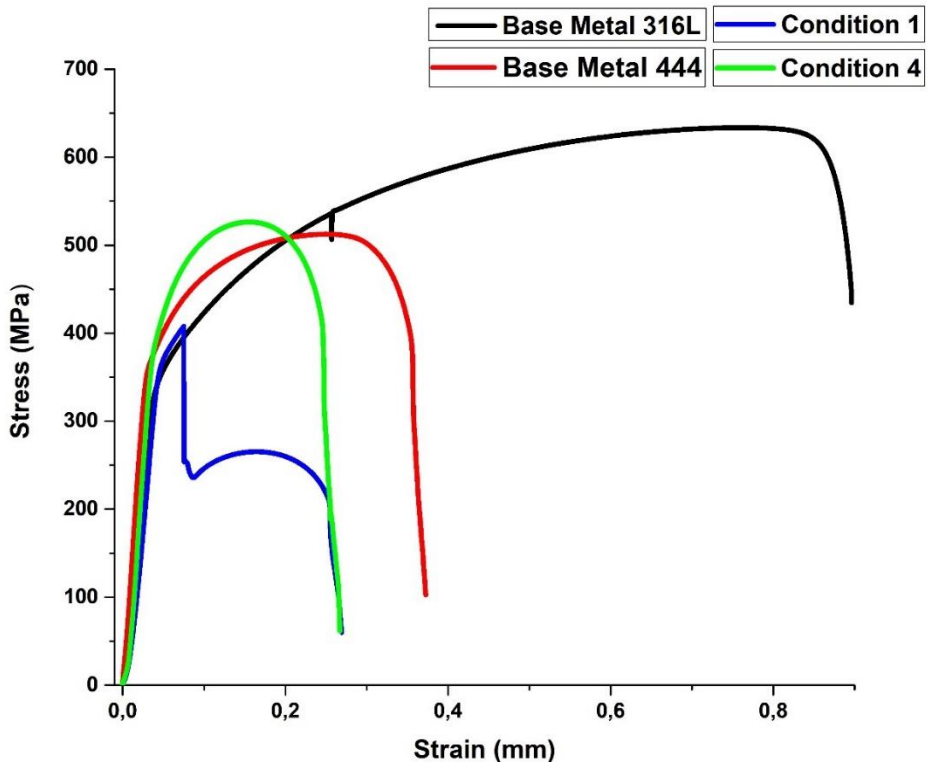

Source: The author.

Figure 9.9 – a) Stir zone of Condition 1 (b) Root flaw found in Condition 1 at the interface zone between AISI 316L and AISI 444 steels.

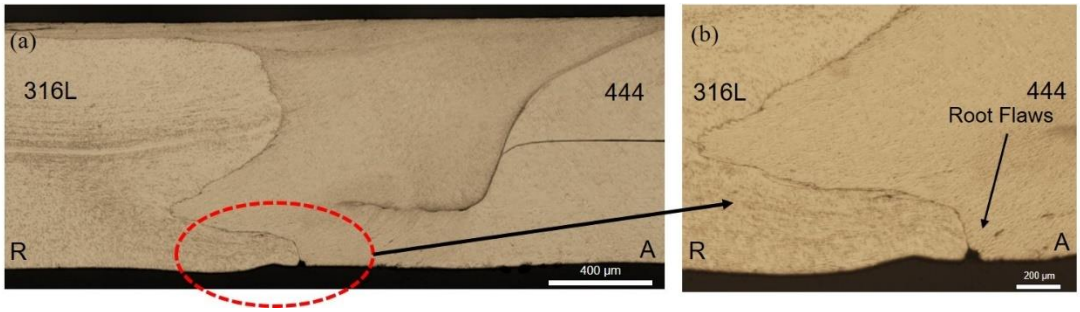

Source: The author.

Figure 9.10 - Specimens after the uniaxial tensile test and shear test (a) Condition 1 (b) Condition 4.

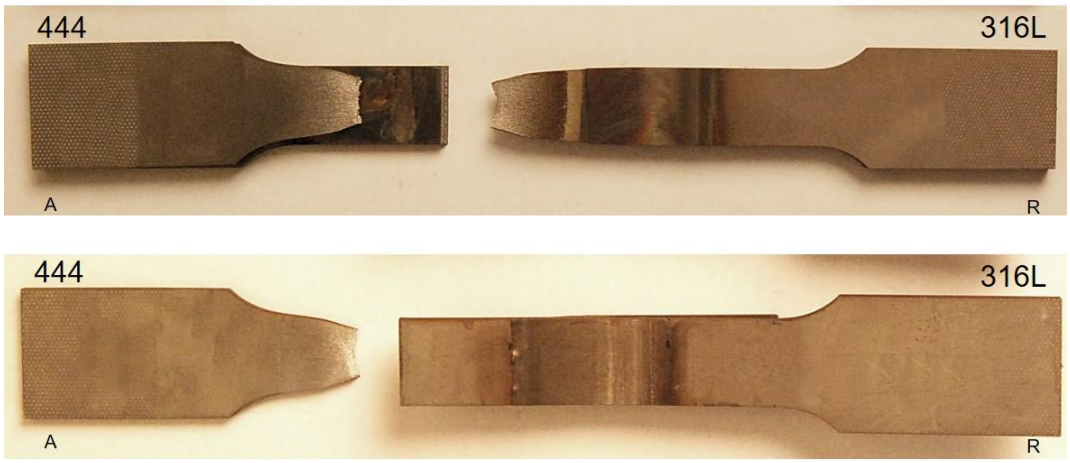

Source: The author.

Therefore, the analysis of the different weld conditions shows that it is possible to produce dissimilar joints of AISI 444 ferritic stainless steel and AISI 316L austenitic stainless steel by the FSW process with mechanical properties superior to those found in the base metal and those determined by the ASTM A240 standard for AISI 444 ferritic stainless steel. The Condition 4 welded in the overlap joint with the positioning of AISI 316L steel at the top with the reduction of the rotation speed to 350 rpm and increased axial force for 50 kN was the best-rated, being the condition that best combined good results in the bending test, yield strength, tensile strength and elongation concerning the base metals of AISI 444 steel and AISI 316L.

9.5 Conclusions

Based on the experimental results of the evaluation of the mechanical properties of dissimilar joints between ferritic stainless steel AISI 444 and austenitic stainless steel AISI 316L, produced by the FSW process, it was possible to conclude that:

1. The analysis of the different weld conditions shows that it is possible to produce dissimilar joints of ferritic stainless steel AISI 444 and austenitic stainless steel AISI 316L by the FSW process with mechanical properties superior to those found in the base metals of AISI 444 e AISI 316L.
2. Among the conditions evaluated by the bending test, the best condition was the butt joint, which supported an angle of 52° until the propagation of cracks in the root of the joint. In comparison, the best condition of the overlapping joint supported an angle of 87° due to the absence of voids and tunnel defects in the stir zone and root flaws, contributing to a better consolidation of the joint root and better ductility of the welded joint.
3. The most significant changes in microhardness values between BM, HAZ, TMAZ and SZ, both for the best butt joint condition and for the best overlapping joint condition, occurred in the austenitic stainless steel AISI 316L, because the austenitic stainless steels are more easily recrystallized and refined by the FSW process compared to ferritic stainless steels.
4. In the tensile test, of the Condition 1 welded in butt joint, initially presented in the stress versus strain curve a high yield strength and tensile strength, leading to partial rupture of the specimen in the stir zone, in a region close to AISI 316L steel, then the tension dropped and the behavior of the graph became similar to that found in the base metal of AISI 444 steel, until the final breakage of the specimen in the base metal on the advancing side, where the AISI 444 steel is positioned.
5. The Condition 4 welded in the overlap joint with positioning of AISI 316L steel at the top with the reduction of the rotation speed to 350 rpm and increased axial force for 50 kN was the best rated, being the condition that best combined good

results in the bending test, yield strength, tensile strength and elongation in relation to the base metals of AISI 444 steel and AISI 316L.

9.6 Acknowledgments

The authors are grateful for the support given by the following Institutions: Universidade Federal do Ceará, Laboratório de Pesquisa e Tecnologia em Soldagem (LPTS), in Brazil, and the Solid State Joining Processes, Helmholtz-Zentrum Geesthacht (HZG), in Germany. This study was financed in part by the Coordenação de Aperfeiçoamento de Pessoal de Nível Superior - Brasil (CAPES) - Finance Code 001, Brazilian funding agencies CNPq (Universal 472185/2011-0), and FUNCAP and CAPES (Project CI1-0050-00049.01.00/11 – International Cooperation).

9.7 References

BARROS, I. F. DE. **Soldagem dissimilar do aço inoxidável ferrítico AISI 444 e do aço inoxidável austenítico AISI 316L por meio do processo TIG autógeno utilizando corrente pulsada**. 2013. Dissertação de Mestrado, Universidade Federal do Ceará, Fortaleza, 2013.

BELLEZZE, T. et al. Improvement of pitting corrosion resistance of AISI 444 stainless steel to make it a possible substitute for AISI 304L and 316L in hot natural waters. **Materials and Corrosion**, [s.l.], v. 59, p. 727–731, 2008.

BILGIN, M. B.; MERAN, C. The effect of tool rotational and traverse speed on friction stir weldability of AISI 430 ferritic stainless steels. **Materials & Design**, [s.l.], v. 33, p. 376–383, jan. 2012.

CAETANO, G. DE Q. et al. Influence of rotation speed and axial force on the friction stir welding of AISI 410S ferritic stainless steel. **Journal of Materials Processing Technology**, [s.l.], v. 262, p. 430–436, 1 dez. 2018.

CAETANO, G. Q. Soldagem Similar de aços Inoxidaveis Ferríticos e Austenícios pelo Processo “Friction Stir Welding”. Dissertação de Mestrado—Fortaleza: Universidade Federal do Ceará - UFC, 2016.

ÇAM, G. Friction stir welded structural materials: beyond Al-alloys. **International Materials Reviews,** [s.l.], v. 56, n. 1, p. 1–48, 1 jan. 2011.

CASHELL, K.; BADDOO, N. **Ferritic stainless steels in structural applications**. [s.l.]: [s.n.], 2014.

COSTA, R. J. G. et al. Comparative Study of Microstructure, Texture, and Formability Between 11CrTi and 11CrTi+Nb ASTM 409 Ferritic Stainless Steel. **Materials Research**, [s.l.], v. 20, p. 1593–1599, 31 ago. 2017.

DEBROY, T.; BHADESHIA, H. Friction stir welding of dissimilar alloys–a perspective. **Science and Technology of Welding & Joining**, [s.l.]: [s.n.], 2013.

DIETER, G. E. Mechanical metallurgy. London: McGraw-Hill Book Company, 1988.

DOUDE, H. et al. Optimizing weld quality of a friction stir welded aluminum alloy. **Journal of Materials Processing Technology**, [s.l.], v. 222, p. 188–196, 2015.

DU, W. et al. Microstructure, Texture, and Formability of Nb+Ti Stabilized High Purity Ferritic Stainless Steel. **Journal of Iron and Steel Research International**, [s.l.], v. 17, n. 6, p. 47–52, 1 jun. 2010.

EDWARDS, P. D.; RAMULU, M. Material flow during friction stir welding of Ti-6Al-4V. **Journal of Materials Processing Technology**, [s.l.], v. 218, p. 107–115, 2015.

HAN, J. et al. Microstructure and mechanical properties of friction stir welded 18Cr–2Mo ferritic stainless steel thick plate. **Materials & Design**, [s.l.], v. 63, p. 238–246, 1 nov. 2014.

HE, B. et al. The metallurgical bonding and high temperature tensile behaviors of 9Cr-1W steel and 316L steel dissimilar joint by friction stir welding. **Journal of Manufacturing Processes**, [s.l.], v. 44, p. 241–251, 1 ago. 2019.

HEIDARZADEH, A. et al. Friction stir welding/processing of metals and alloys: A comprehensive review on microstructural evolution. **Progress in Materials Science**, [s.l.], v. 117, p. 100752, 1 abr. 2021.

JAFARZADEGAN, M. et al. Microstructure and Mechanical Properties of a Dissimilar Friction Stir Weld between Austenitic Stainless Steel and Low Carbon Steel. **Journal of Materials Science & Technology**, [s.l.], v. 29, n. 4, p. 367–372, 1 abr. 2013.

KOU, S. **Welding metallurgy**. New Jersey. USA: John Wiley & Sons, 2003.

LIU, F. C. et al. A review of friction stir welding of steels: Tool, material flow, microstructure, and properties. **Journal of Materials Science & Technology**, [s.l.], v. 34, n. 1, p. 39–57, 1 jan. 2018.

LO, K. H.; SHEK, C. H.; LAI, J. K. L. Recent developments in stainless steels. **Materials Science and Engineering: R**: Reports, [s.l.], v. 65, n. 4, p. 39–104, 29 maio 2009.

MACHADO, J. P. S. E. et al. Effect of temperature on the level of corrosion caused by heavy petroleum on AISI 304 and AISI 444 stainless steel. **Materials Research**, [s.l.], v. 9, n. 2, p. 137–142, 2006.

MILES, M. P. et al. Predicting recrystallized grain size in friction stir processed 304L stainless steel. **Journal of Materials Science & Technology**, [s.l.], v. 35, n. 4, p. 491–498, 1 abr. 2019.

MISHRA, M. K. et al. On the microstructure evolution in friction stir processed 2507 super duplex stainless steel and its effect on tensile behaviour at ambient and elevated temperatures. **Materials Science and Engineering: A**, [s.l.], v. 719, p. 82–92, 14 mar. 2018.

MISHRA, R. S.; MA, Z. Y. Friction stir welding and processing. **Materials Science and Engineering: R**: Reports, [s.l.], v. 50, n. 1–2, p. 1–78, 31 ago. 2005.

MONTEIRO, S. N. et al. High temperature work hardening stages, dynamic strain aging and related dislocation structure in tensile deformed AISI 301 stainless steel. **Journal of Materials Research and Technology**, [s.l.], v. 7, n. 4, p. 571–577, 1 out. 2018.

NENE, S. S. et al. Enhanced strength and ductility in a friction stir processing engineered dual phase high entropy alloy. **Scientific Reports**, [s.l.], v. 7, n. 1, p. 16167, 23 nov. 2017.

PADILHA, A. F. **Materiais de engenharia: microestrutura e propriedades**. Edição Eletrônica ed. São Paulo: Hermus, [s.l.], v.1, 2000.

PARK, S. H. C. et al. Rapid formation of the sigma phase in 304 stainless steel during friction stir welding. **Scripta Materialia**, [s.l.], v. 49, n. 12, p. 1175–1180, dez. 2003.

PORTER, D. A.; EASTERLING, K. E.; SHERIF, M. **Phase Transformations in Metals and Alloys**, Third Edition (Revised Reprint). [s.l.] CRC Press, 2009.

RODRIGUES, D. G. et al. Evaluation of Intermediate Annealing on Nb-Stabilized Ferritic Stainless Steel. **Materials Research**, [s.l.], v. 20, p. 298–303, 7 ago. 2017.

RODRIGUES, D. G. et al. The effect of grain size and initial texture on microstructure, texture, and formability of Nb stabilized ferritic stainless steel manufactured by two-step cold rolling. **Journal of Materials Research and Technology**, [s.l.], v. 8, n. 5, p. 4151–4162, 1 set. 2019.

SAMANTA, S. K.; MITRA, S. K.; PAL, T. K. Effect of rare earth elements on microstructure and oxidation behaviour in TIG weldments of AISI 316L stainless steel. **Materials Science and Engineering: A**, [s.l.], v. 430, n. 1–2, p. 242–247, 25 ago. 2006.

SATHIYA, P.; ARAVINDAN, S.; HAQ, A. N. Effect of friction welding parameters on mechanical and metallurgical properties of ferritic stainless steel. **The International Journal of Advanced Manufacturing Technology**, [s.l.], v. 31, n. 11–12, p. 1076–1082, 21 jan. 2006.

SENTHILKUMAR, G.; RAMAKRISHNAN, R. A study of individual and interaction effect of process parameters on friction welded AISI 410 and AISI 430 joint. Materials Today: Proceedings, International Conference on Materials, **Manufacturing and Mechanical Engineering for Sustainable Developments** (ICMSD 2020). [s.l.], v. 46, p. 3233–3239, 1 jan. 2021.

SHASHI KUMAR, S.; MURUGAN, N.; RAMACHANDRAN, K. K. Identifying the optimal FSW process parameters for maximizing the tensile strength of friction stir welded AISI 316L butt joints. Measurement, [s.l.], v. 137, p. 257–271, 1 abr. 2019.

SILVA, C. C. et al. High-temperature hydrogen sulfide corrosion on the heat-affected zone of the AISI 444 stainless steel caused by Venezuelan heavy petroleum. **Journal of Petroleum Science and Engineering**, [s.l.], v. 59, n. 3–4, p. 219–225, nov. 2007.

SILVA, C. C. et al. Microstructural characterization of the HAZ in AISI 444 ferritic stainless steel welds. Materials Characterization, [s.l.], v. 59, n. 5, p. 528–533, maio 2008.

SIQUEIRA, R. P. et al. Composition and orientation effects on the final recrystallization texture of coarse-grained Nb-containing AISI 430 ferritic stainless steels. **Materials Science and Engineering**: A, [s.l.], v. 528, n. 9, p. 3513–3519, 15 abr. 2011.

SMITH, W. F. **Structure and Properties of Engineering Alloys**. n. 2, [s.l.], McGraw-Hill (New York), 1993.

THOMAS, W. M. et al. Friction stir butt welding. Cambridge, TWI, 1991.

TONGNE, A. et al. Banded structures in friction stir welded Al alloys. **Journal of Materials Processing Technology**, [s.l.], v. 221, p. 269–278, 2015.

VALIEV, R. Z.; LANGDON, T. G. Principles of equal-channel angular pressing as a processing tool for grain refinement. **Progress in Materials Science**, [s.l.], v. 51, n. 7, p. 881–981, 1 set. 2006.

VIEIRA BRAGA, F. et al. Recrystallization of niobium stabilized ferritic stainless steel during hot rolling simulation by torsion tests. **Journal of Materials Research and Technology,** [s.l.], v. 5, n. 1, p. 92–99, 1 jan. 2016.

10 CHAPTER 10: Assessment of corrosion resistance of dissimilar AISI 316L and AISI 444 stainless steel joints by the friction stir welding using DL-EPR technique and oil immersion test.

10.1 Abstract

The corrosion resistance of conditions welded by the FSW process between AISI 444 and AISI 316L steels in butt and overlap joints were evaluated through the DL-EPR test and immersion in high salinity oil. Ir/Ia values between 0.02 and 0.04 were observed under all conditions. However, the highest concentration of Ir/Ia values, close to 0.04 was observed on the forward side of conditions 3 and 6. These values are concentrated in regions with more significant heat input and where AISI 444 steel is positioned, which has a lower intergranular corrosion resistance than AISI 316L steel, with lower levels of Cr, Mo and Ni. Despite this higher Ir/Ia concentration, the observed values do not characterise the impairment of intergranular corrosion resistance. In the immersion test, surface pits were not observed in oil at high temperature and pressure. However, Condition 3 presented a corrosion rate similar to that found in the base metal of AISI 444 steel. Condition 6, welded in an overlap joint and with crevices along its entire cross-section, showed an average corrosion rate 64.7% higher than Condition 3. Thus, it can be concluded that the parameters used in the dissimilar FSW process, with AISI 316L and AISI 444 steels, did not determine the impairment of the intergranular corrosion resistance of the joints. However, the overlap joint configuration provided the formation of crevices and high corrosion rates in the oil immersion test. Thus, condition 3, welded in a butt joint, presents the best results in terms of resistance to intergranular corrosion and crevice corrosion.

Keywords: Friction stir welding; Stainless steel; DL-EPR; Oil Immersion

10.2 Introduction

Exploration of oil reserves in the pre-salt layer in Brazil raised the Brazilian economy to a new level of oil reserves and production, giving Petrobras a prominent position in the world ranking of large energy companies, as portrayed POTTMAIER et al. (2013). Although, BELTRAO et al. (2009) highlight that the production of this oil requires more

remarkable technological development, mainly concerning the corrosion resistance of steels for the construction of oil extraction wells. For the oil and gas industry, corrosion on steels is a severe problem when in the presence of an aqueous medium and in contact with dissolved gases (CO_2, H_2S e O_2). The occurrence of CO_2 in the presence of water produces carbonic acid (H_2CO_3), which reduces the pH of the medium and can cause uniform and localised corrosion in steels. In the case of pre-salt, corrosion control is even more critical, as pre-salt oil is produced with high salinity water and high CO_2 content at high pressures and temperatures; these conditions are quite favourable to produce high levels of corrosivity.

The steels used in oil and gas transport pipelines are specified following the Standard API 5L (2000). These are high strength low alloy (HSLA) a chemical composition similar to carbon steel with the addition of alloying elements in small amounts. The steels used for lining oil extraction wells are specified following the Standard API 5CT (2005) and are carbon steels, micro-alloyed steels, low-alloyed steels and high-alloyed steels. Steels with high chromium content, such as austenitic stainless steels AISI 316L and ferritic stainless steels AISI 444, present a higher initial investment for the oil industry than carbon steel. However, as noted by LIN et al. (2015), this disadvantage balances out when there are operating expenses when using carbon steel in highly corrosive environments, and there is a need to use chemical inhibition or replacement of tubes due to failure/corrosion. In many cases, the economy presented in these operational applications leads to the financial advantages of high alloy steels with high chromium contents over carbon steel and inhibitors.

Good weldability is one of the most essential attributes of austenitic stainless steel. As a result, these steels have gained more widespread applications compared to other stainless steels. They are used in automotive industries, nuclear power plants and high-temperature components, as heat exchangers, and chemical reactors, among others, due to their excellent mechanical properties and corrosion resistance, how to report ABIGAIL RODRÍGUEZ et al. (2010). On the other hand, ferritic stainless steels (FSSs) despite their lower ductility, toughness and weldability when compared to austenitic stainless steels can be used in a wide variety of applications where pitting and stress corrosion resistance is more important than mechanical strength as noted by LIPPOLD e KOTECKI, (2005). Thus, LAKSHMINARAYANAN and BALASUBRAMANIAN (2013a) highlight that FSS is typically used in a mildly corrosive atmosphere for chemical processing

equipment, furnace parts, heat exchangers, oil burner parts, petroleum refining equipment, protection tubes, recuperates, storage vessels, electrical appliances, solar water heaters, and household appliances.

The lower application of ferritic stainless steels in the industry is related to the metallurgical problems arising from the fusion welding of these steels. When subjected to the thermal welding cycles of traditional processes, these materials undergo metallurgical changes, which compromise their weldability and the corrosion resistance of the joints. SILVA et al. (2007) evaluated the effect of fusion welding on the corrosion resistance of the heat-affected zone (HAZ) of the AISI 444 ferritic stainless steel in a medium containing Venezuelan heavy oil and concluded that the temperature of treatment has a direct influence on the level of material corrosion and that the increase in the welding heat input contributes to a higher level of corrosion.

However, in recent decades considerable progress has been made in the welding of stainless steels by the friction stir welding (FSW) process, mainly in aspects related to microstructural control and consequently in the corrosion resistance properties of these welded joints. Compared to traditional fusion welding, FSW welding has unique advantages, according to MISHRA e MA (2005), this process uses a non-consumable tool that rotates and penetrates the joint, resulting in heating and plastic deformation of the materials to be joined, which can be heated to temperatures below those experienced in fusion welding. LIU et al. (2018) report that compared to traditional fusion welding, the FSW process of steel exhibits great advantages due to the efficient control of the welding temperature and cooling rate, providing that unfavourable phase transformations that usually occur during traditional welding can be avoided, and favorable phase fractions can be maintained in the weld zone, thus avoiding the degradations of typical properties associated with fusion welding such as corrosion resistance.

In evaluating the microstructure of AISI 316L austenitic stainless steel similar friction stir welded joints, KUMAR; MURUGAN and RAMACHANDRAN (2018) observed non-existence of secondary phases in the weld zone was owing to lower peak temperatures in FSW process. The base steel and the FSW joints depict a stable pitting potential after the activation controlled the anodic region. The weld joints had marginally better pitting corrosion resistance than the base steel. Evaluating ferritic stainless steels, KIM et al. (2017) proved that 430M2 ferritic stainless steel FSW joints have a significant decrease in sigma phase precipitation compared to arc welding processes and

LAKSHMINARAYANAN; BALASUBRAMANIAN (2012) proved a lower susceptibility to intergranular corrosion of AISI 409M steel when welded by the FSW process, as the fast cooling rates achieved to prevent the diffusion of chromium, in addition to the reduction of the HAZ, which is a region that favours the precipitation of carbides.

Different industrial segments use dissimilar welding joints of different metals to bring together different properties, seek to minimise costs, and maximise the performance of equipment and machinery with different welding processes. SILVA et al. (2013) point out be promising to join different stainless steels in dissimilar joints in the petroleum distillation towers in the gas and petroleum industries through fusion welding processes. MUKHERJEE and PAL (2012) claim that the dissimilar joints between ferritic and austenitic stainless steels are efficient for prolonging metals' service life due to improved toughness, mechanical strength, and corrosion resistance.

According to MURR (2010), when the FSW process is applied to the weld of dissimilar joints, the asymmetry between the retreating and advancing sides is intensified, because there in HAZ, TMAZ, and SZ different behaviours in terms of thermal conductivity and plastic deformation, due to differences in the physical and chemical properties of the materials involved, which support in the asymmetry of heat generation and material flow.

Despite advances, the combination of these aspects in FSW welding dissimilar between ferritic and austenitic stainless steels are still developing and more detailed information on the influence of process parameters on the corrosion resistance of these joints has become a subject of the strong scientific and technological appeal. Thus, this work aims to evaluate the corrosion resistance of dissimilar FSW joints between the austenitic stainless steel AISI 316L and the ferritic stainless steel AISI 444, evaluating the corrosion resistance of welded joints through a non-destructive and quantitative technique called the double loop electrochemical potentiokinetic reactivation (DL-EPR) technique to determine the degree of sensitisation of stainless steels and the behavior of these dissimilar FSW joints when in contact with high salinity oil at high temperature and pressure.

10.3 Materials and Methods

The welds were carried out with plates of ferritic stainless steel AISI 444, 2 mm thick and austenitic stainless steel AISI 316L, with thicknesses of 4 mm or 3 mm, depending on the joint configuration used. The chemical composition of the materials was determined by optical emission spectroscopy (Shimadzu model PA7000 Japan) and is presented in Table 10.1.

Table 10.1 - Chemical composition of the base metals (% weight).

Material	Elements											
	C	Si	Mn	P	S	Cr	Ni	Mo	Cu	Co	N	Fe
316L	0.026	0.56	0.84	0.029	<0.010	17.1	9.97	1.96	0.32	0.20	0.056	Bal.
444	0.017	0.53	0.16	0.47	<0.010	17.8	0.24	1.75	0.57	----	----	Bal

Source: The author.

The samples were joined by the FSW process in the Helmholtz-Zentrum Geesthacht (HZG), Germany. All welds, evaluated for mechanical properties, were made using the HZG Gantry System with two different joint configurations. The first was a butt joint with 4 mm of thickness, with AISI 316L steel on the retreating side and AISI 444 steel on the advancing side, as shown in Figure 10.1a and the other in overlap joint configuration with the AISI 316L steel at the top and 5 mm of thickness in the stir zone, showing an overlapping region of 70 mm in length, as can see in Figure 10.1b. An inert gas (Air) injection system was used to protect the material during the process, as at temperatures above 535 °C these stainless steels react with the atmosphere. Welds were performed in load control mode with an integrated system to record process data, such as penetration depth, rotational speed, torque, forces applied to the tool and tool position over time.

A polycrystalline cubic boron nitride (PCBN) tool with a conical diameter of 25 mm and a conical pin with a diameter of 9.2 mm and a length of 3.7 mm was used. The pin has a conical surface with opposing recesses in the form of a spiral about the axis of symmetry of the tool.

Figure 10.1 – Different configurations of welded joints (a) Butt joint with AISI 316L steel on the retreating side (b) Overlap joint with AISI 316L steel on the top.

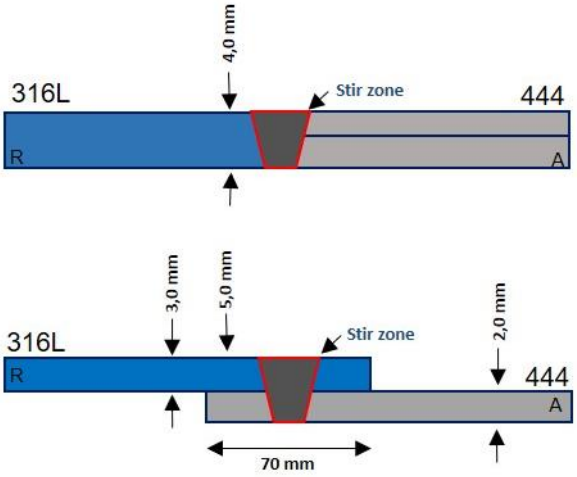

Source: The author.

To define the welding parameters, the best set of parameters found by CAETANO et al. (2018) in similar FSW welding of AISI 444 ferritic stainless steel and AISI 316L austenitic stainless steel. Thus, in the butt joint, the rotation speed varied between 350 and 450 rpm and the axial force from 25 to 30 kN, as shown in Table 10.2. In the overlap joints, with the austenitic stainless steel AISI 316L at the top, the rotation speed variation from 350 to 450 rpm was also performed, but increasing the axial force to 45 and 50 kN, as shown in Table 10.3. For all six welded conditions, the welding speed was kept constant at 1 mm/s and the tool inclination angle at 0º.

Table 10.2 – Welding Parameters for Dissimilar FSW Butt Welding of AISI 316L/444 Steels

Condition	Rotation Speed (rpm)	Axial Force (kN)	Advancing Side	Retreating Side
1	350	30	444	316L
2	450	25	444	316L
3	450	30	444	316L

Source: The author.

Table 10.3 - Welding Parameters for Dissimilar FSW Overlap Welding of AISI 316L/444 Steels

Condition	Rotation Speed (rpm)	Axial Force (kN)	Advancing Side	Retreating Side
4	350	50	316L/444	316L/444
5	450	45	316L/444	316L/444
6	450	50	316L/444	316L/444

Source: The author.

These parameters were related to the heat input generated during FSW welding. Eq. (1) shows the equivalent heat input total required for the joint consolidation among the different ways to calculate the heat generated during the FSW process. The coefficient of friction of the material, the pressure exerted by the tool, the rotational speed, and the geometry of the tool used in welding are the inputs needed to determine that heat input. They are calculated according to the equation formulated by DEQING et al., (2004):

$$E_t = \pi \,.\, \mu \,.\, Ps \,.\, Vr \,.\, \frac{D^2 + D\,.d + d^2}{45\,.(D+d)} \quad (1)$$

Where E_t is the equivalent total heat input (kJ/mm), μ is the coefficient of friction of the material, Ps is the pressure exerted by the tool on the material (Pa), Vr is the speed of rotation (rad/s), D is the shoulder diameter and d is the pin diameter (m). Another way to calculate the heat input to the FSW process is by using Eq. (2) to determine the equivalent heat input per unit length per second, proposed by LIENERT et al. (2002):

$$E_l = \eta \,.\, \frac{T\,.Vr}{Vs} \quad (2)$$

Where E_l is the heat input per unit length (kJ/mm), η is the efficiency of the FSW process for steels, T the Torque (Nm), Vr the rotational speed (rad/s), and Vs the welding speed. (mm/s).

In the analysis of temperature achieved during the FSW process were used 24 thermocouples were divided into 4 different zones separate by 110 mm, with 3 thermocouples positioned on the advancing side and 3 on the retreating side in each zone. To help understand the metallurgical transformations resulting from the different temperatures reached during the process. For microscopic analysis, the welds were initially cut with a diamond abrasive disc on a Struers Discotom-6 cutter. Sandpapers with a grain size between 120 and 2500 mesh were used for sanding. The polishing step was carried out on a universal polishing machine (Buehler Phoenix 4000) with 3μ, 1μ and 1/4μ diamond pastes and 150 rpm rotation speed. As the joints are composed of AISI 316L and AISI 444 steels, the combination of 10% oxalic acid and 10% chromic acid reagents was efficient in creating contrasts in the phases and microconstituents present in the sample, enabling a complete analysis of its microstructure. Optical microscopy (OM) analysis was used using a Carl Zeiss optical microscope integrated with the AxioVision

SE64 software to assess the disposition and characteristics of the different zones; however, for a more detailed investigation of possible precipitates and the constitution of the interfaces between the AISI 316L/444 steels, analyses were carried out by scanning electron microscopy with an FEI Quanta 250.

The double loop electrochemical potentiokinetic reactivation (DL-EPR) tests of the welds produced by FSW were performed at room temperature, about 30 °C, using a portable electrochemical cell. This cell is formed by a platinum counter electrode and a reference electrode consisting of a silver wire immersed in KCl. Two working solutions were used according to the analysed steel: a solution containing 2,0 mol/l H_2SO_4 + 1000 mg/l KSCN to steel AISI 316L and a solution containing 0,5 mol/l H_2SO_4 + 1000 mg/l KSCN to steel AISI 444. The cell was in contact with the sample surface using a flexible nozzle adhering to the material, and the contact area was approximately 0.8 mm^2. A total of 24 different points were used for the analysis. This allowed all the different welding zones, from the advancing side where the direction of travel is the same as the direction of rotation of the tool to the retreating side with the opposite directions, to be evaluated as shown in Figure 10.2, enabling a scan of all the different zones. The current versus the potential curve was acquired with the PalmSensPc software loaded with the parameters, after stabilising the potentiostat and using a constant scan speed of 3 mV/s.

Figure 10.2 – a) The 24 different points for DL-EPR analysis in conditions with a butt joint configuration b) The 24 different points for DL-EPR analysis in conditions with overlap joint configuration.

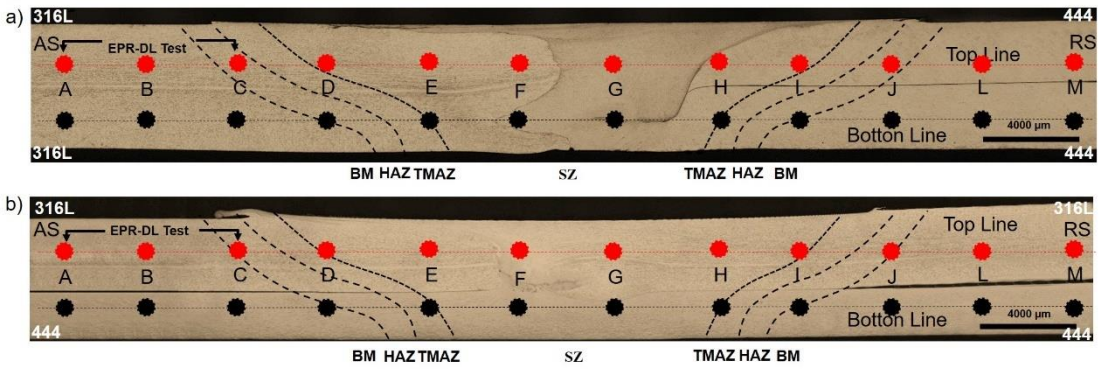

Source: The author.

The conditions with the highest reactivation peaks in the EPR-DL graphs and consequently with the highest Ir/Ia values were evaluated using an oil immersion test in

a high temperature and pressure corrosion cell. To carry out the test, the steel samples were cut and sanded under running water, starting with 220-mesh sandpaper and subsequently passing through 320, 400, 600 and 1200 mesh sandpaper, dipped in acetone in an ultrasound bath for 5 minutes, dried with hot air and weighed on a scale with an accuracy of 0.0001 g. The dimensions obtained from the samples were approximately 20 mm wide, 50 mm high and 4 mm thick for the butt joints and 20 mm wide, 50 mm high and 5 mm thick for the overlap joint samples.

The immersion test was carried out to simulate conditions similar to that of an oil reservoir with high salinity. For this, a synthetic saline solution with a chemical composition similar to the aquifers with high salinity was used. In the search for a more aggressive condition for the test, four different types of oil were evaluated, three supplied by the Repsol company and one from the Campos Basin. Each of these oils was mixed with deionised water with NaCl concentrations of 120 g/l and 240 g/l, formulated at 9,000 rpm for 5 min. Then, samples were immersed in the solution and subjected to a temperature of 60ºC for 24h. After performing the first tests to determine which combination of oil and NaCl concentration would be the most aggressive, the welded samples were subjected to a temperature of 60° at a pressure of 35 MPa. In all assays, the same solution/sample volume ratio was maintained.

The choice of temperatures and pressures for the oil immersion test at high temperature and pressure was based on literature data with those presented by HONARVAR NAZARI; ALLAHKARAM and KERMANI (2010) and CHOI et al. (2014) and also depending on the characteristics of the reactors available (material and maximum working pressure). However, these pressures and temperatures can be found in pre-salt fields. According to VAN DER MEER (2005), the temperature where the pre-salt layer is located is high, reaching from 80ºC to 100ºC, as well as the pressure exceeding 50 MPa. In addition, mass loss assessments were carried out every 100h of exposure time to investigate the kinetics of the reactions involved. After the pre-established period of confinement of the samples in each test had elapsed, the reactors were cooled, depressurised and opened for the removal of the samples, which were later washed with Mili-Q water, acetone and dried with hot air.

To calculate the corrosion rates in mm/year, the standard ASTM G1-03 (Standard practice for preparing, cleaning, and evaluating corrosion test specimens) was used to perform the mass loss test by pickling the corrosion products. A solution of hydrochloric

acid (HCl), distilled water (1:1 by volume) and 3.5 g/L of hexamethylenetetramine were used as pickling agents; the samples were immersed in the pickling solution for 30 seconds, washed with distilled water, dried with acetone and weighed, respectively, in 20 cycles, totalling 10 minutes of immersion of the samples in the pickling solution. With the data obtained, a graph of mass loss versus a number of cycles was constructed for each sample, presented in Figure 10.3, to determine the point "B", considered the point corresponding to the loss of mass due to corrosion, the posterior points (between "B" and "C") correspond to the corrosion of the metal after the removal of the corrosion product, as specified in the standard ASTM G1 – 03, (2010).

Figure 10.3 - Mass loss graph of the corroded sample after repetitive pickling cycles

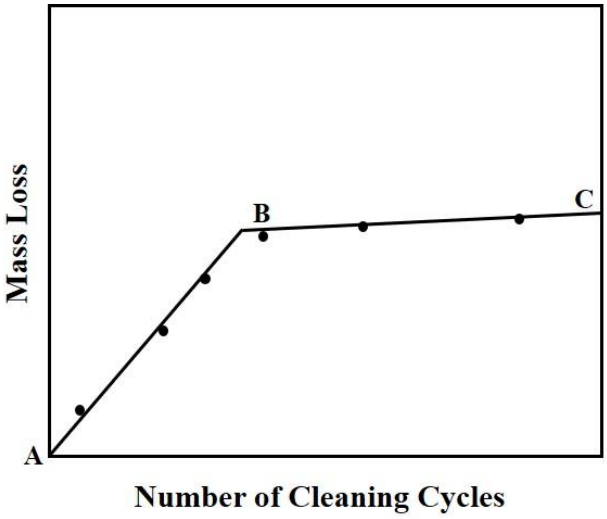

Source: ASTM G1 – 03, (2010).

After the determination of point "B", the corrosion rate was determined following Eq. (3) below:

$$\mathbf{r} = \frac{\mathbf{8{,}76 \times 10^4 \times W}}{\mathbf{A \times D \times t}} \qquad (3)$$

Where r is corrosion rate in (mm/year), w is the weight loss in g; A is the surface area of the specimen in cm2; D is the density of the material in g/cm3; and t is the corrosion time in h.

10.4 Results and Discussions

10.4.1 Heat input and Temperature Analysis

The process parameters directly affect the heat input, which strongly influences the heating and cooling rates of the thermal cycle and, consequently, the resulting microstructure. However, the heat input calculated based on the process parameters corresponds to the equivalent heat input and not precisely to the heat input generated during the process since there are losses that are not considered, being the main ones by conduction and convection in the weld region. The rotational speed is the main parameter related to the friction force at the interface between the base metals and the tool. It is directly linked to heat generation during the welding process, as reported by BILGIN and MERAN, (2012) and LAKSHMINARAYANAN and BALASUBRAMANIAN (2013). Frictional coupling of the tool surface with the base metal governs the heating mechanism and tool rotation, allowing stirring and mixing of the material around the pin. Thus, the higher the rotational speed, the higher the process temperature, and this is due to increased friction heating as proposed by COLEGROVE et al. (2007), SHIRI et al. (2013), and UDAY et al. (2010).

The strong influence of the rotational speed on heat generation was observed among similar welds of AISI 410S ferritic stainless steel produced by FSW, as pointed out by CAETANO et al. (2018), which observed that the reduction in rotational speed from 800 to 450 rpm generates a drop-in equivalent heat input total and equivalent heat input per unit length around 0.4 kJ/mm, keeping the axial force constant. Observing Fig. 2, in the dissimilar FSW welding between ferritic stainless steel AISI 444 and austenitic AISI 316L, it is possible to observe the influence of both the rotation speed and the axial force in the heat generation. Thus, between conditions 1 and 3, where the rotation speed is kept constant at 450 rpm and the axial force is increased from 25 to 30 kN, a variation of the equivalent heat input per unit length of around 0.16 kJ/mm is obtained. In conditions 5 and 6, where the axial force was kept constant at 50 kN, and the increase in rotation speed from 350 to 450 rpm varied the equivalent heat input per unit length to around 0.12 kJ/mm, which demonstrates the welded conditions, the more significant influence of the rotation speed in the heat generation concerning the axial force.

Figure 10.4 - Equivalent heat input per unit length and total heat input calculated for the different conditions of AISI 316L/444 steels dissimilar welding performed by the FSW process.

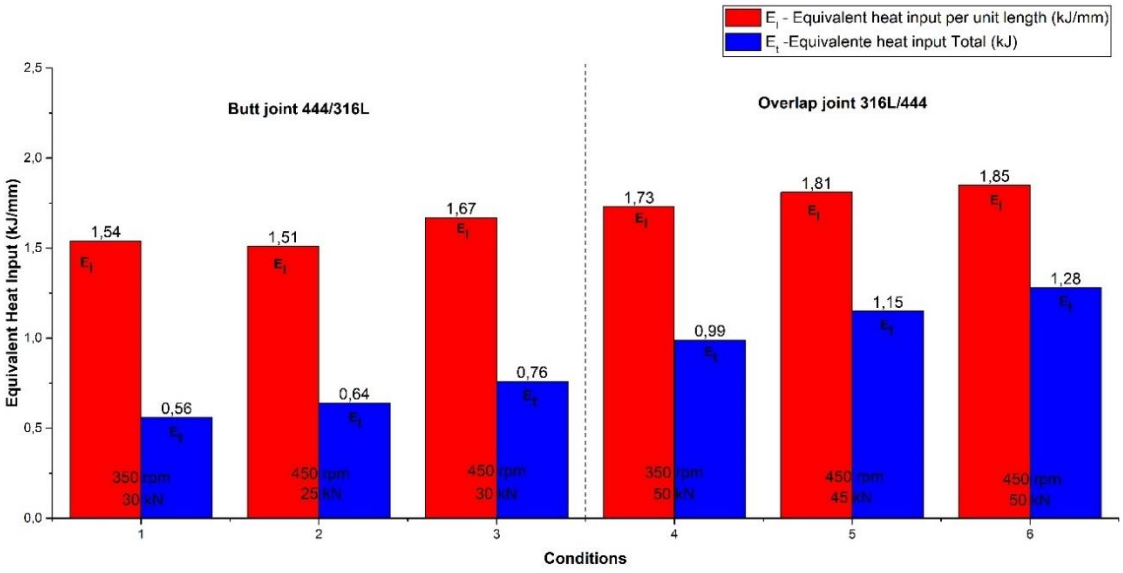

Source: The author.

The temperature analysis produced by using 24 thermocouples divided in 4 different zones of condition 6, welded with the highest axial force, proved the thermal asymmetry between the advancing and retreating sides of the dissimilar FSW joints AISI 316L/444. DARVAZI and IRANMANESH (2014), have already proved this thermal asymmetry by showing that in the cross-section of the FSW process along transverse direction and perpendicular to the weld line, the temperature distribution is toward the advancing side and the maximum temperature distribution is in the back half of shoulder region and toward advancing side. In dissimilar FSW joints, in addition to the characteristics of the FSW process, the difference in properties of the welded materials also contributes to this asymmetry in the temperatures reached and in the heat distribution.

Several studies show there is a more significant generation of heat on the advancing side of the FSW welds, as reported by NANDAN, DEBROY and BHADESHIA (2008) and SANTOS, IDAGAWA and RAMIREZ (2014) show the heat intensity produced in the upper part of the FSW weld is high, mainly due to the greater contact of the material with the tool shoulder, promoting a greater generation of heat. Thus, the upper of the advancing side becomes a region critical to the occurrence of precipitates, as it is subjected to the effects of recrystallisation and higher heat input. By Figure 10.5, it can be seen that, on average the temperatures on the advancing side are 10° higher than those

observed on the retreating side. This temperature difference between advancing and retreating sides is much smaller than that observed for butt joints between AISI 304L and AISI 410S steels, presented in Chapter 4. This fact occurs because Condition 6 is welded in an overlap joint configuration, allowing the participation of both materials on the advancing and retreating sides, reducing the asymmetry of the process.

Figure 10.5 - Thermal analysis for the four different zones showing the temperature peaks of Condition 6, welded in overlap configuration with a rotation speed of 450 rpm and an axial force of 50 kN.

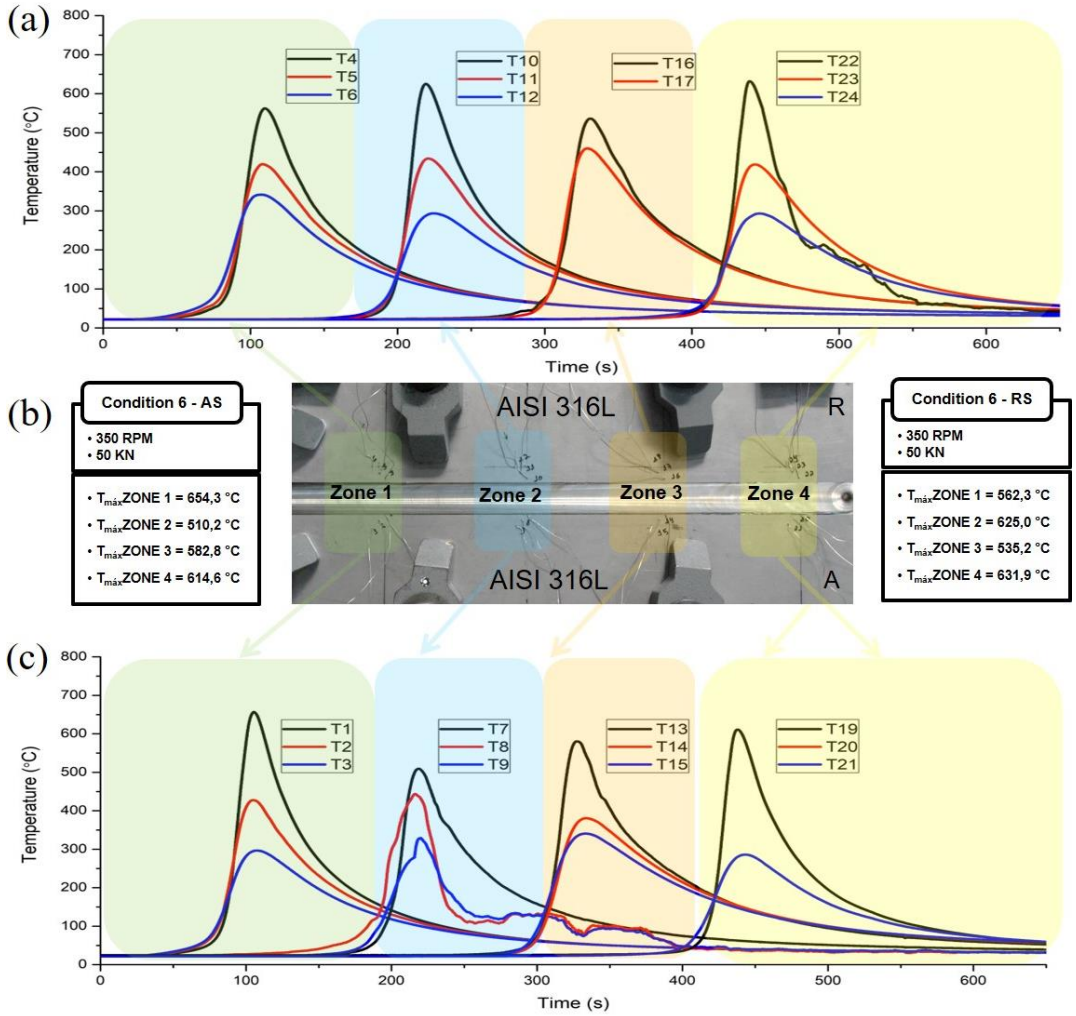

Source: The author.

According to the temperatures observed on the advance side of Condition 6, welded with greater heat input and with temperature peaks of 654 °C in regions located 15 mm from the weld centre, and the analysis performed by SILVA (2021) that reports that

conditions with a rotation speed of 450 rpm and axial force of 35 kN or more, keeping the welding speed at 1 mm/s, some tests reached temperatures above 85% of the melting point. The results verified that the heat generated by the increased rotation, axial force and low welding speed contribute to a temperature very close to the melting point in a zone close to the contact surface between the tool shoulder and the steel. Thus, it is proved that the temperatures reached in SZ, TMAZ and HAZ of AISI 316L and AISI 444 steel are sufficiently high to subject these steels to sensitising temperatures. Evaluating the upper region of the stir zone of butt joints by scanning electron microscopy in chapter 8, it is possible to observe in some conditions, that on the advancing side, where the AISI 444 steel is positioned, the presence of corrosion in the grain boundaries of the ferrite, in a thin layer close to the surface. However, the cooling rates, for AISI 316L steel, must be fast enough for the non-precipitation of $M_{23}C_6$ carbides, as portrayed in Chapter 8 about the equilibrium phase diagram simulated using the Thermo-Calc software and TTT (Transformation–Time–Temperature) diagram using the JmatPro software for AISI 316L austenitic stainless steel and AISI 444 ferritic stainless steel.

10.4.3 EPR-DL Test

The sensitisation phenomenon in stainless steels is related to the chromium segregation in the grain boundaries of the material, mainly in the form of complex chromium carbides, providing a simultaneous depletion of chromium in the surroundings. As highlighted by PARVATHAVARTHINI et al. (2009) this process, if the local chromium content drops below 12% by weight, then the chromium depleted zones become prone to localised corrosion. Research to determine the degree of sensitisation of stainless steels led to the development of a simple, non-destructive and quantitative technique called the double-loop electrochemical potentiokinetic reactivation test (DL-EPR). In this test, the polarisation curve in the anodic direction, called the activation curve, promotes the formation of a passive layer in the material. This curve is compared with the reactivation curve, which evaluates the integrity of the layer formed when applying the reverse potential. Furthermore, RAHIMI; ENGELBERG and MARROW, (2011) claims that the presence and intensity of the reactivation peak in the reverse polarization and the relationship between the reactivation current (Ir) and the activation current (Ia) directly reflect the susceptibility of the material to corrosion. Thus, the DL-EPR test has been consolidated over the years as a simple and efficient technique to

analyse the susceptibility of stainless steels to intergranular corrosion after being subjected to different types of processing, such as heat treatments and welding processes, as can be seen, observed in studies of TAJI; MOAYED and MIRJALILI, (2015) and KIM et al. (2009).

Thus, based on the analysis of current versus voltage graphs obtained by the technique (DL-EPR) and by the Ir/Ia ratios of conditions 1, 2 and 3, welded in butt joint configuration, it is possible to observe low values of Ir/Ia both for the retreating side, where the AISI 316L steel is positioned, and for the advancing side, where the AISI 444 steel is positioned. Under all conditions welded in butt joint configuration, peak Ir/Ia values are between 0.02 and 0.04, as shown in Figure 10.6a, Figure 10.6c and Figure 10.6e. Despite being noticeable in conditions 1 and 3, welded with higher heat input, a concentration of Ir/Ia value around 0.04, in the stir zone (SZ) and in the thermomechanically affected zone (TMAZ), where the AISI 444 steel is positioned. None of these regions' current versus voltage graphs showed reactivation peaks, as shown in the Figure 10.6b and Figure 10.6f. This fact proves the low impact on the corrosion resistance of possible precipitates, observed in chapter 8, which are concentrated in a thin layer near the surface in the stir zone of the butt joint weld conditions with the highest heat inputs. In similar FSW welding of AISI 444 steel CAETANO (2016) also observed, even under higher heat input, the absence of reactivation peaks for all EPR-DL tests performed during the sample scan. This demonstrates the high performance in terms of corrosion resistance of FSW welds produced with this material.

The Ir/Ia values found on the advancing side of Condition 3 are also lower than those observed by CAETANO et al. (2019) in similar welds of ferritic stainless steel AISI 410S, with heat input similar to that applied in Condition 3. This considerable improvement in the intergranular corrosion resistance of ferritic stainless steel AISI 444 compared to the results shown for steel AISI 410S occurs due to the considerable increase in the chromium content from 12.8% to 17.8%, in addition to the reduction of carbon from 0.25% to 0.17%. In this way, there is less carbon to combine with chromium to form chromium carbide $Cr_{23}C_6$ and avoid a greater incidence of its precipitation at the grain boundaries, in addition to the contribution of the stabilisation of AISI 444 steel with titanium and niobium.

Nonetheless, SILVA et al. (2007) evaluated the effect of welding on the corrosion resistance of the heat-affected zone (HAZ) of AISI 444 ferritic stainless steel, using the

shielding metal arc welding (SMAW) process, verified that even in welded conditions with the lowest heat input, Ir/Ia values greater than 0.05 were observed. They are reaching Ir/Ia values close to 0.14 under conditions subjected to the highest heat input. These Ir/Ia values characterise the formation of a dual structure, where some of the precipitates are observed but do not entirely surround the grain and a ditch structure, with grains completely surrounded by chromium carbides. Thus, AISI 444 steel, despite having a higher intergranular corrosion resistance than AISI 410S steel, can be easily subjected to sensitising temperatures when welded by traditional fusion processes.

Figure 10.6 – (a) Ir/Ia ratio for Condition 1 (b) Current versus voltage graphs to point I in the top line of Condition 1 (c) Ir/Ia ratio for Condition 2 (d) Current versus voltage graphs to point I in the top line of Condition 2. (e) Ir/Ia ratio for Condition 3 (f) Current versus voltage graphs to point I in the top line of Condition 3.

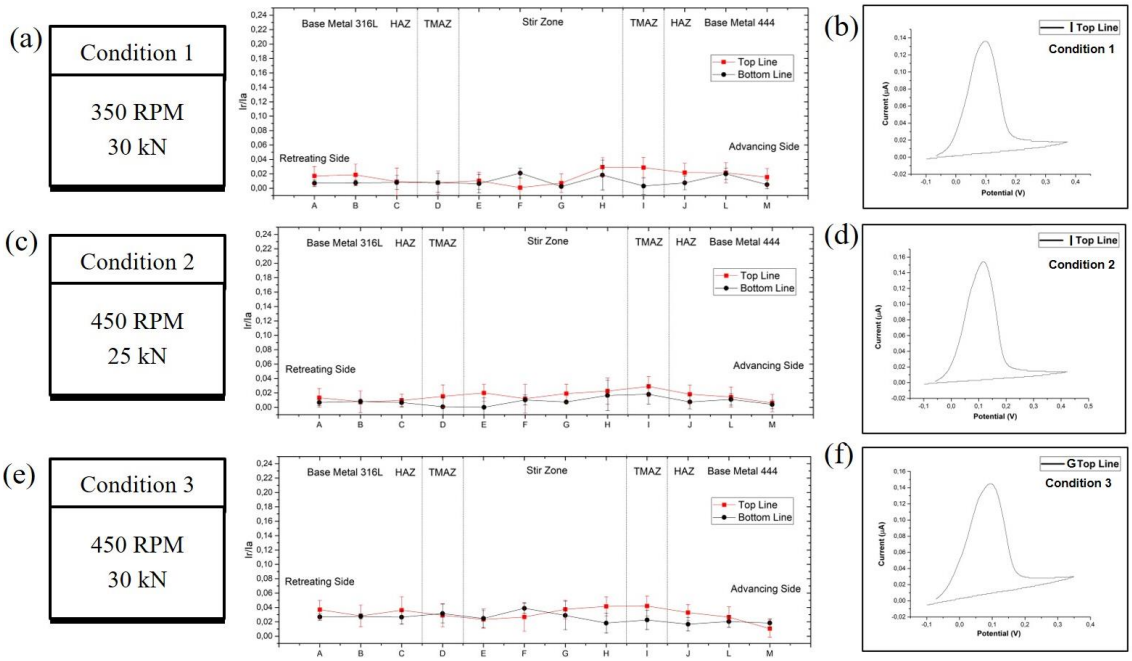

Source: The author.

In conditions 4, 5 and 6, welded in an overlap joint, the Ir/Ia values also varied between 0.02 and 0.04, as can be seen in Figure 10.7a, Figure 10.7c and Figure 10.7e. The main difference from the butt joint welded conditions, is the fact that in the overlap joints the upper scan line corresponds to AISI 316L steel. The lower scan line corresponds to AISI 444 steel, both on the advancing and retreating side. Although all conditions welded in overlap joints, the lower scan line has Ir/Ia values more significant than the

upper scan line. As the rotation speed increases from 350 rpm to 450 rpm and the axial force to 50 kN and, consequently, the heat input generated, an approximation of the values of Ir/Ia between the upper and lower lines can be observed. However, even with this increase in heat input, the Ir/Ia values remain close to 0.04 because in none of the conditions welded in overlap joints were observed reactivation peaks in the voltage versus current graphs, as can be seen in Figure 10.7b, Figure 10.7d and Figure 10.7f. Even with the application of an axial force of 50 kN in Condition 6 and a heat input per unit of length 10% higher than that observed in Condition 3, the Ir/Ia values for the lower line were higher than those observed in the upper line. This fact occurs because in the upper region of the advancing side, where the highest temperatures are observed, the AISI 316L steel is positioned, which has a higher intergranular corrosion resistance than AISI 444 steel, with higher levels of Cr, Mo and Ni. In the studies of PULI and JANAKI RAM, (2012) evaluating the behavior of corrosion resistance, using the DL-EPR technique, of AISI 316L stainless steel coatings made by friction surfacing process, verified that, even in high heat input, none of the samples showed a reactivation peak in the current versus potential graphs, proving the high resistance to intergranular corrosion of AISI 316L steel.

Figure 10.7 - (a) Ir/Ia ratio for Condition 4 (b) Current versus voltage graphs to point I in the top line of Condition 1 (c) Ir/Ia ratio for Condition 5 (d) Current versus voltage graphs to point I in the top line of Condition 2. (e) Ir/Ia ratio for Condition 6 (f) Current versus voltage graphs to point I in the top line of Condition 3. (g)

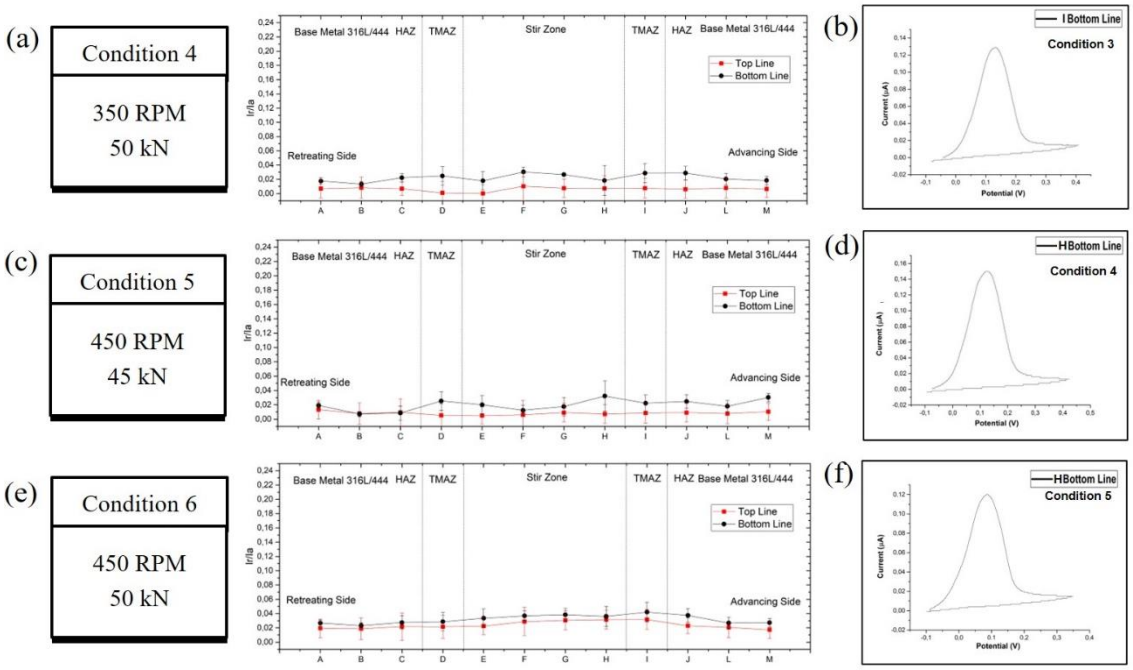

Source: The author.

Stainless steels have different sensitisation levels, represented in the EPR-DL test by different intensities of reactivation peaks. Thus, low reactivation peaks may represent the initial stages of this sensitisation process, with probable low intensity of precipitation of chromium carbides and grains not entirely surrounded by these precipitates, as observed by ABIGAIL RODRÍGUEZ et al. (2010) and LAKSHMINARAYANAN and BALASUBRAMANIAN, (2012b), for ferritic and austenitic stainless steels. CAETANO et al. (2019), analysing similar FSW joints of AISI 410S steel, it was observed that from conditions subjected to an axial force of 20 kN and a rotation speed of 450 rpm, low intensities of reactivation peaks are present on the advancing side of the weld joint. In the dissimilar welds between AISI 304L and 410S steels, presented in Chapter 6, under conditions subjected to a rotation speed of 450 rpm and axial forces greater than 25 kN, reactivation peaks in the current versus potential graphs are also observed. However, in Condition 3 and Condition 6, welded with AISI 316L and AISI 444 steels, with the application of high axial forces, not even low reactivation peaks are observed on the advancing side, which shows the absence of initial stages of the sensitisation process.

Through microstructural evaluation of these conditions carried out in Chapter 08 and presented in Figure 10.8, It is possible to observe that on the advancing side of Condition 3, where the Ir/Ia peaks close to 0.04 are concentrated, between the BM and the TMAZ, no significant microstructural changes were observed, only the presence of slightly larger ferritic grains than those found in MB, making it challenging to limit between the regions of BM and TAZ. In the TMAZ, it is possible to observe intensely deformed ferritic grains following the direction of rotation of the tool, as shown in Figure 10.8c. In the stir zone, deformed and refined grains at the top, close to the region of contact with the tool shoulder, as shown in the Figure 10.8b, in addition to the possible precipitates presented in Chapter 8. Therefore, these possible precipitates did not determine significant impacts on the intergranular corrosion resistance of these conditions, a fact that proves the low values of Ir/Ia observed in the EPR-DL tests. In the work of SILVA et al. (2007), in the HAZ of AISI 444 steel, welded by shielded metal arc welding (SMAW) process, reactivation peaks in voltage versus current graphs and Ir/Ia values greater than 0.04 were observed. However, it was not possible to identify the types of precipitates in the microstructure analysis, as their highly reduced dimensions made it challenging to identify by SEM and EDX analysis. The authors believe that the precipitates observed are chromium carbides and nitrides derived from the welding process because in these areas, the temperatures experienced were above 1000 °C, which, according to the literature, favours the precipitation of chromium carbide in ferritic stainless steel.

In Figure 10.8d and Figure 10.8f, it is possible to observe the upper part of the TMAZ and SZ on the advancing side of Condition 6, where the AISI 316L steel is positioned and where the highest concentrations of Ir/Ia close to 0.04 were observed for this material. The positioning of AISI 316L austenitic stainless steel in the upper part of the joint, as well as the increase in the axial force to 50 kN, provided an intensification in the recrystallisation of the upper regions of the joint. Thus, the upper SZ of Condition 6 presents intensely refined and recrystallised austenitic grains, while in the ZTMA, these austenitic grains are refined and deformed following the tool rotation direction. As observed by ÇAM (2011) and PARK et al. (2003), austenitic stainless steels are more easily recrystallised and refined by the FSW process compared to ferritic stainless steels because of the stack failure energy (SFE) differences between ferritic and austenitic structures. Therefore, in both regions, no carbide precipitation or formation of undesirable

phases was observed that could compromise the intergranular corrosion of AISI 316L steel, which justifies the maintenance of Ir/Ia values close to 0.04 in this region.

Figure 10.8 - (a) Cross-section macrograph of the Condition 1 (b) BM of AISI 304L steel, Condition 1, welded with an axial force of 25 kN (200x). (c) HAZ of AISI 304L steel, Condition 1, welded with an axial force of 25 kN (200x). (d) BM of AISI 304L steel, Condition 4, welded with an axial force of 40 kN (500x). (e) HAZ of AISI 304L steel Condition 4, welded with an axial force of 40 kN (200x). (f) Cross-section macrograph of Condition 4.

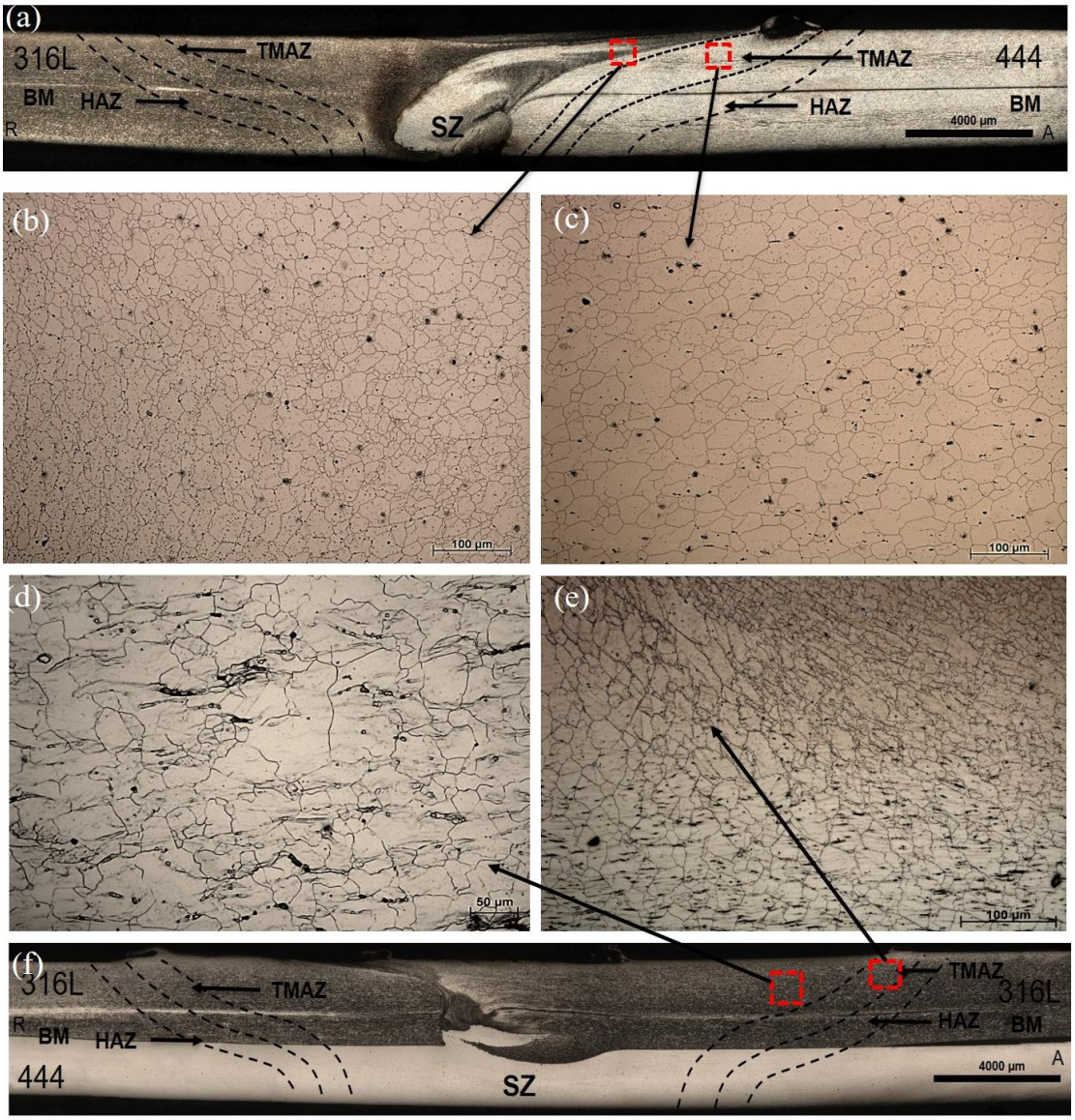

Source: The author.

Thus, the DL-EPR tests, carried out for the different welding conditions, could show whether the thermal welding cycle can promote microstructural changes capable of making some areas of the weld susceptible to corrosion. The test also showed that the difference in heat input caused by the increased axial force applied to the dissimilar 316L/444 welds produced by FSW did not compromise the susceptibility to intergranular corrosion on the advancing side where the highest temperatures are experienced.

10.4.4 Oil Immersion Test

Studies, such as OSSAI, BOSWELL and DAVIES (2015) show that more than 60% of oil fields are being developed in highly corrosive environments with high salinity, pressures, and temperatures. The electrochemical processes involved in corrosion are accelerated with increasing temperature. Therefore, the tendency is for the temperature to negatively influence corrosion rates, as reported by LÓPEZ; PÉREZ and SIMISON (2003).

The oil fields found in the last decades are at great depths, and the pressure and temperature increase with the depth of the reservoir. According to VAN DER MEER (2005), assuming an average geothermal gradient of 30°C/km and a hydrostatic gradient of 10 MPa/km, the temperature and pressure in a reservoir can reach 175°C and 70 MPa, respectively. However, the maximum temperature recorded in wells was about 280°C, at a depth of 7800 m, and the maximum pressure was about 140 MPa. In addition, there is also a general increase in water salinity with reservoir depth. Salinity gradients vary between 0.07 and 0.25 g/L.m, although salinity is not linearly related to depth in many cases.

Corrosion is one of the most prevalent causes of pipeline failures in the oil industry. It accounts for between a quarter to two-thirds of the total downtime in the industry, as reported by BRUSCHI et al. (2015). Therefore, understanding the corrosive process is essential for the correct selection of steels and the development of new materials and processing techniques for application in the oil industry, especially considering that operating and exploration conditions are increasingly critical. In this context, there is great interest in obtaining corrosion data under conditions that simulate high corrosion severity. Thus, seeking the most aggressive condition for carrying out an oil immersion test at high temperature and pressure of the welded joints, preliminary tests with the ferritic stainless steel AISI 410S were carried out. This steel, as it has a lower corrosion

resistance than ferritic stainless steel AISI 444, was used to present a faster response to the environment's corrosivity. As shown in Table 10.4, Preliminary tests were carried out with four oils from different sources, one from the Campos Basin and three supplied by Repsol. These oils were mixed with deionised water with a NaCl concentration of 240 g/l, a water/oil ratio of 30%/70% and formulated at 9,000 rpm for 5 min. Then, the samples of AISI 410S steel were immersed and subjected to a temperature of 60ºC for 24h.

Table 10.4 – Preliminary tests to determine the corrosivity of different types of oil.

Samples	Oil	Temperature	Time	Water/oil ratio
A	Repsol 01	60º C	24h	30% - 70%
B	Repsol 02	60º C	24h	30% - 70%
C	Repsol 03	60º C	24h	30% - 70%
D	Campos Basin	60º C	24h	30% - 70%

Source: The author.

Through optical microscopy analysis of the cross-section of these samples, presented in Figure 10.9, a more significant number of pits is observed in sample D, subjected to oil from the Campos Basin. Sample D also presented the highest mass loss among the analysed samples in addition to the greater quantity and volume of pits formed. These pits were distributed along the entire cross-section, which proves the best homogenisation of the water/oil mixture with the oil from the Campos Basin. SIMÕES; SANTO, and MOREIRA, (2007) evaluated the effectiveness of internal corrosion monitoring techniques in an active pipeline that receives oil through two other pipelines in the Campos Basin. The techniques used to evaluate the internal corrosion of the pipeline under study were mass loss coupons, electrical resistance corrosimetric probes, biocoupons and waste and fluid sampling. The authors concluded that a combination of factors gives the oil transported from the Campos Basin a moderate to severe corrosion potential, including its high salinity.

Figure 10.9 – (a) Sample of AISI 410S steel immersed in Repsol 01 oil at 60°C for 24h, with a NaCl concentration of 240 g/l (b) Sample of AISI 410S steel immersed in Repsol 02 oil at 60°C for 24h, with a NaCl concentration of 240 g/l (c) Sample of AISI 410S steel immersed in Repsol 03 oil at 60°C for 24h, with a NaCl concentration of 240 g/l and (d) Sample of AISI 410S steel immersed in oil from Campos Basin at 60°C for 24h, with a NaCl concentration of 240 g/l.

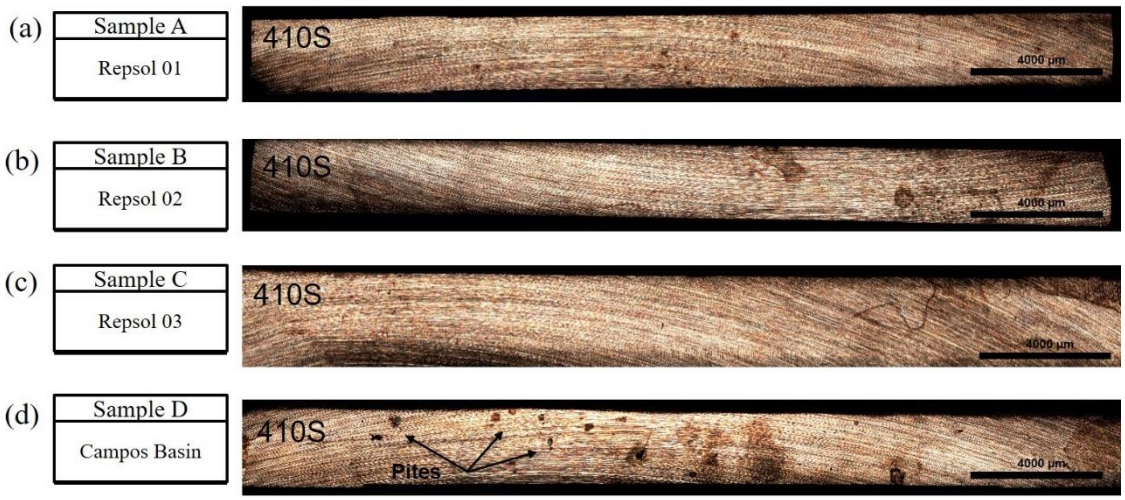

Source: The author.

After carrying out the first tests, that led to the conclusion that the oil from the Campos basin is the most suitable for the test due to its high corrosivity, the base metals used in the dissimilar FSW welds and the conditions with the highest heat input evaluated in the thermal analysis and the highest concentration of peaks of Ir/Ia values in the EPR-DL test were subjected to the immersion test at a temperature of 60° C and 35 MPa. Thus, two samples of base metals AISI 316L and AISI 444 and two samples of Condition 03, welded in butt joint, and two samples of Condition 06, welded in an overlap joint, were adequately prepared to be inserted, along with the oil from the Campos Basin, in a high temperature and pressure cell. Before the start of the test, the initial mass, area and density of each of the samples were duly evaluated, as shown in Table 10.5, for the determination of corrosion rates according to Eq. 01 and the standard ASTM G1 – 03 (2010).

Every 100h, samples were removed and properly weighed to determine mass loss and corrosion rate. As can be seen, in the Table 10.6, Condition 3, welded in a butt joint, after 100h of immersion in oil at high temperature and pressure, showed an average corrosion

rate 54.1% higher than the base metal of AISI 316L steel however, compared to AISI 444 steel the corrosion rate of Condition 3 in 100h was only 17.4%. With the increase in test time to 200 hours, the difference between the average corrosion rate of base metal AISI 444 and Condition 3 drops to only 13.7%, while the corrosion rate of Condition 3 concerning base metal AISI 316L remains constant. According to HATAMI et al. (2016), the corrosion rate in oil media depends on the type of steel, the corrosive media and many environmental variables such as temperature, CO_2 partial pressure, pH and exposure time. However, NEŠIĆ (2007) shows that the properties of corrosion product films formed on the surface of the steel, which is generally made up of iron carbonate or mixed carbonates, are determinants in the corrosion rate. Since they can limit the transport of chemical species involved in electrochemical reactions, their protective properties vary with immersion time and temperature. This phenomenon may explain the tendency of the corrosion rate to decay in Condition 3 in 200h since the longer the immersion time of the sample in oil, the longer the time for the production of corrosion products at the sample/medium interface, serving as a barrier to spread of corrosion. In addition to the immersion time, another factor that interferes with this corrosion rate is the temperature. The studies of NAZARI, ALLAHKARAM and KERMANI, (2010) show that the protection of $FeCO_3$ improves with an increase in temperature above 60° C, as this results in the formation of a dense and thick layer of iron carbonate, which reduces the corrosion rate. However, studies of YIN et al. (2009) reported a reduction in the thickness and compression of the $FeCO_3$ film with increasing temperature, showing that there is a temperature limit for the constitution of this protection.

Table 10.5 - Correlation between Massa Initial, Sample Area Exposed to the Medium and Density to Base Metals AISI 316L, AISI 444, Condition 3 and Condition 6.

Sample	Massa initial, g	Area, cm^2	Density, g/cm^3
BM - 316L	34.525 ± 0.41	30.375 ± 2.10	7,81 ± 0.04
BM - 444	16.044 ± 0.21	25.01 ± 0.14	7,71 ± 0.08
Condition 3	26.170 ± 3.39	27.425 ± 0.24	7,42 ± 0.39
Condition 6	29.692 ± 8.94	24.715 ± 6.38	7,58 ± 0.36

Source: The author.

Table 10.6 - Correlation between Oil Immersion Duration, Average Mass Loss and Rate Corrosion to base metals AISI 316L, AISI 444, Condition 3 and Condition 6.

Sample	Test Duration, h	Average Mass Loss, g	Rate Corrosion, mm/year
BM - 316L	100	$0.0014 \pm 2.1\ 10^{-4}$	$0.0053 \pm 4.2\ 10^{-4}$
	200	$0.0025 \pm 3.5\ 10^{-4}$	$0.0047 \pm 9.8\ 10^{-4}$
BM - 444	100	$0.0020 \pm 1.4\ 10^{-4}$	$0.0090 \pm 6.4\ 10^{-4}$
	200	$0.0044 \pm 3.6\ 10^{-4}$	$0.0101 \pm 8.5\ 10^{-4}$
Condition 3	100	$0.0025 \pm 3.5\ 10^{-4}$	$0.0109 \pm 8.5\ 10^{-4}$
	200	$0.0058 \pm 2.8\ 10^{-4}$	$0.0124 \pm 2.1\ 10^{-4}$
Condition 6	100	$0.0050 \pm 5.7\ 10^{-4}$	$0.0237 \pm 23.3\ 10^{-4}$
	200	$0.0158 \pm 19.1\ 10^{-4}$	$0.0376 \pm 33.9\ 10^{-4}$

Source: The author.

According to the graph in Figure 10.10, it is possible to observe the lowest corrosion rate for the base metal of AISI 316L steel, which, as shown in Table 10.1, presents the highest levels of Cr and Ni. WU et al. (2014) studied the effect of adding Cr to P110 steel on oil immersion corrosion. Therefore, corrosion induction tests were carried out on P110 steels with four different chromium contents (0.5%, 1%, 2% and 3%) at a pressure of 0.1 MPa and 60ºC. The corrosion rates obtained were 2.025, 1.616, 0.793 and 0.367 mm/year, which indicates that the higher the Cr content, the lower the steel corrosion rate. The base metal of AISI 444 steel, both at 100 h and 200 h, showed a higher corrosion rate than the base metal of AISI 316L steel because although AISI 444 steel has a chromium content similar to AISI 316L steel, the Ni contents are lower, contributing to a lower performance of steel in corrosion resistance in environments with high salinity, as observed by LOTO, (2019).

Figure 10.10 - Corrosion rate concerning the oil immersion test duration time for Condition 3, Condition 6 and base metals AISI 444 and AISI 316L.

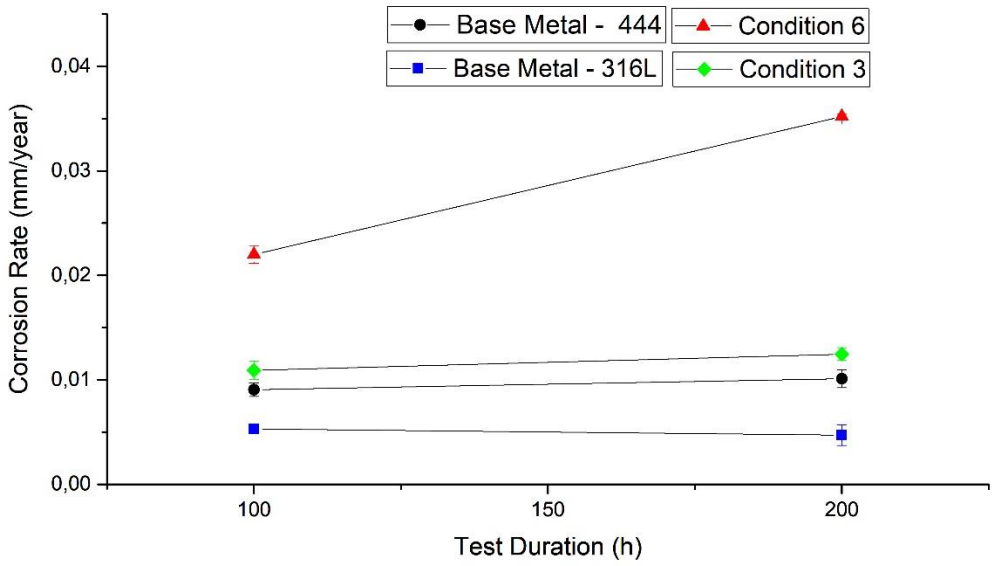

Source: The author.

Among the conditions welded by the FSW process, while Condition 3, welded in a butt joint, with a rotation speed of 450 rpm and an axial force of 30 kN, showed a corrosion rate similar to that found in the base metal of AISI 444 steel. Condition 6, welded in an overlap joint, with the same rotation speed and increasing the application of axial force to 50 kN, presented an average corrosion rate 50.4% higher in 100h than Condition 3. After 200h of testing, a considerable increase in the corrosion rate for Condition 6 was observed, this increase being 64.7% higher than the average corrosion rate for Condition 3 in 200h of testing. According to the thermal and microstructural analysis carried out in Chapter 3 and Chapter 5, the difference in equivalent heat input per unit length between conditions 3 and 6 is only 0.18 kJ/mm. Thus, as observed in the EPR-DL analysis, the possible precipitates concentrated in a thin layer at the top of the stir zone of Condition 3, had no significant impact on the oil immersion test. Therefore, the decisive factor for the highest corrosion rates observed in Condition 6 was the configuration of the sample in an overlap joint, allowing in Condition 6 the formation of crevices along almost the entire cross-section of the samples.

As can be seen in Figure 10.11, the samples of Condition 3 and Condition 6, submitted to the immersion test in oil at high temperature and pressure, after 200h of test, did not show the formation of pits in their cross sections, as shown in Figure 10.11a for Condition

3 and Figure 10.11e for Condition 6, as well as pits are not observed on their upper and lower faces, as shown by the Figure 10.11b and Figure 10.11c for Condition 3 e a Figure 10.11f and Figure 10.11g for Condition 6. However, in Condition 3, the positioning of two sheets of 2 mm thick AISI 444 steel on the advancing side allowed the formation of crevices only in a short cross-sectional region. In Condition 6, the configuration of the joints in an overlap joint, with a 3 cm thick AISI 316L steel plate at the top and a 2 mm thick AISI 444 steel plate at the bottom, allowed the formation of crevices in almost the entire cross-section of the joint, the opening of these crevices being much more extensive for Condition 6, as shown in the Figure 10.11h, than for Condition 3, as shown in Figure 10.11d.

Figure 10.11 - (a) Cross-sectional macrograph of Condition 3 subjected to 200h to oil immersion test (b) Upper surface of Condition 3 subjected to 200h to oil immersion test (c) Lower surface of Condition 3 subjected to 200h to oil immersion test (d) Crevices of Condition 3 subjected to 200h to oil immersion test (e) Cross-sectional macrograph of Condition 6 subjected to 200h to oil immersion test (f) Upper surface of Condition 6 subjected to 200h to oil immersion test (g) Lower surface of Condition 6 subjected to 200h to oil immersion test (h) Crevices of Condition 6 subjected to 200h to oil immersion test.

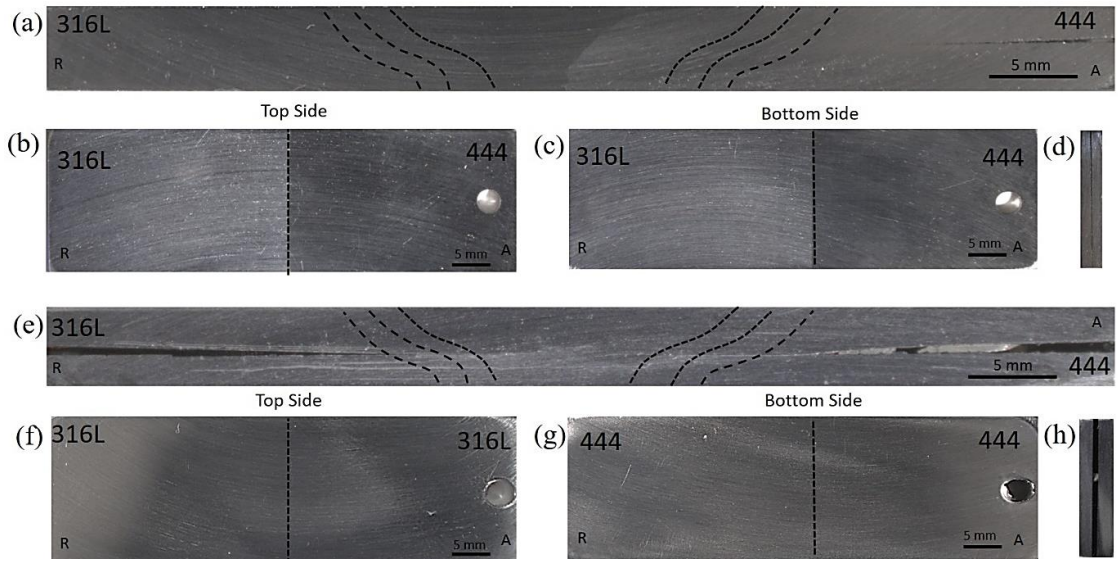

Source: The author.

According to MCCAFFERTY, (2010), crevice corrosion starts due to the operation of a differential oxygen cell, as when O2 molecules are consumed inside the crevice gap, they are not easily replaced due to the long and narrow diffusion path formed by the crevice. Therefore, the metal exposed to a lower oxygen concentration has a more negative potential for oxygen reduction than the metal exposed to a higher oxygen concentration. Differences in electrode potential between the open metal and the crevice may only amount to tens of millivolts, but this difference is enough to initiate corrosion within the crevice. Thus, crevice corrosion is propagated by changes in electrolyte composition within the crevice. In particular, the crevice electrolyte will become acidic and also contain concentrated amounts of cations discharged from the metal or alloy. In solutions containing chlorides, the internal electrolyte within the crevice will also be concentrated in chloride ions. As noted by PARK and LEE (2004), in chloride-containing media, the internal electrolyte becomes more aggressive enough to break the passive film of steels such as AISI 444 and initiate crevice corrosion, the higher the concentration of chlorides in the electrolyte. According to ZHU et al. (2021) the increase in pressure and tensions in oil and gas exploration environments accelerates the anodic dissolution of stainless steels inside the crevice under these conditions.

WU et al. (2021) state that all types of metals that rely on passive films are prone to crevice corrosion, one of the most common corrosion failures of stainless steels and even more dangerous than pitting corrosion when exposed to chloride-containing solutions or marine atmospheres, as noted by HORNUS et al. (2017). Among the solutions to this corrosive process MCCAFFERTY (2010) cites the use of corrosion inhibitors, cathodic protection, material selection and design considerations to minimise the existence of crevices, such as the use of butt joint welds rather than overlap joints. This fact is decisive for the lowest corrosion rates observed in Condition 3, welded in butt joint and with the depreciation of crevices.

10.5 Conclusions

Based on the experimental results of the evaluation of the corrosion resistance of dissimilar joints between ferritic stainless steel AISI 444 and austenitic stainless steel

AISI 316L, produced by the FSW process, using the EPRP-DL technique and oil immersion test, it was possible to conclude that:

1. It is possible to weld AISI 444 ferritic stainless steel and AISI 316L austenitic stainless steel in a dissimilar joint by the FSW process without sensitization and with corrosion rates in the oil immersion test similar to the base metal of AISI 444 steel.

2. The heat input and temperature analysis prove the increase in heat input with the increased application of axial force. The thermal asymmetry between the advancing and retreating sides of dissimilar FSW joints AISI 316L/444 was also verified, showing average temperatures on the advancing side are 10° higher than observed on the retreating side.

3. The DL-EPR tests, performed for the different weld conditions, could show whether the welding thermal cycle may promote microstructural changes capable of making some areas of the weld susceptible to corrosion.

4. In all welded conditions in butt joint configuration, the Ir/Ia values are between 0.02 and 0.04, although it is noticeable in Condition 3, welded with higher heat input, an Ir/Ia value concentration around 0.04, in the SZ and TMAZ on the advancing side, where the AISI 444 steel is positioned.

5. In the butt and overlap joints, even with the increase in heat input, the Ir/Ia values remained close to 0.04, because in none of the welded conditions were reactivation peaks observed in the voltage versus current graphs

6. The preliminary tests carried out with the four oils from different sources proved by the more significant number of pits and loss of mass observed, that the oil from the Campos basin is the one that presents the best water/oil homogenisation and greater corrosivity.

7. Condition 3, welded in a butt joint, after 200h of immersion in oil at high temperature and pressure, showed an average corrosion rate close to that observed in the base metal of AISI 444 steel.

8. The Condition 6, welded in an overlap joint and with the presence of crevices in the cross-section, after 200h of immersion test in oil at high temperature and pressure, showed a considerable increase in the corrosion rate, being this increase 64.7% higher the average corrosion rate for Condition 3.

9. The higher corrosion rates in Condition 6 were attributed to the greater amount of crevices in the cross-section and the development of a greater difference in electrode potential between the external metal and the crevice, causing the development of crevice corrosion.

10. After 200 hours of testing, the welded conditions with higher heat input and submitted to the oil immersion test at high temperature and pressure did not present the formation of pits in their cross sections and upper and lower faces.

10.6 Acknowledgments

The authors are grateful for the support given by the following Institutions: Universidade Federal do Ceará, Laboratório de Pesquisa e Tecnologia em Soldagem (LPTS), in Brazil, and the Solid State Joining Processes, Helmholtz-Zentrum Geesthacht (HZG), in Germany. This study was financed in part by the Coordenação de Aperfeiçoamento de Pessoal de Nível Superior - Brasil (CAPES) - Finance Code 001, Brazilian funding agencies CNPq (Universal 472185/2011-0), and FUNCAP and CAPES (Project CI1-0050-00049.01.00/11 – International Cooperation).

10.7 References

ABIGAIL RODRÍGUEZ, N. et al. Analysis of sensitization phenomenon in friction stir welded 304 stainless steel. **Frontiers of Materials Science in China**, [s.l.], v. 4, n. 4, p. 415–419, 1 dez. 2010.

API 5CT. **Specification for Casing and Tubing,** D.C, Washington (EUA), 2005.

API 5L. **Specification for pipeline,** D.C, Washington (EUA), 2000.

ASTM G1 – 03. **Standard practice for preparing, cleaning, and evaluating corrosion test specimens.**ASM International, [s.l.], 2010.

BELTRAO, R. L. C. et al. **SS: Pre-salt Santos basin - Challenges and New Technologies for the Development of the Pre-salt Cluster, Santos Basin, Brazil**. . Em: OFFSHORE TECHNOLOGY CONFERENCE. OnePetro, 4 maio 2009. Disponível em: <https://onepetro.org/OTCONF/proceedings/09OTC/All-09OTC/OTC-19880-MS/35954>. Acesso em: 1 abr. 2022

BILGIN, M. B.; MERAN, C. The effect of tool rotational and traverse speed on friction stir weldability of AISI 430 ferritic stainless steels. **Materials & Design**, [s.l.], v. 33, p. 376–383, jan. 2012.

BRUSCHI, R. et al. Pipe technology and installation equipment for frontier deep water projects. **Ocean Engineering**, [s.l.], v. 108, p. 369–392, 1 nov. 2015.

CAETANO, G. DE Q. et al. Influence of rotation speed and axial force on the friction stir welding of AISI 410S ferritic stainless steel. **Journal of Materials Processing Technology**, [s.l.], v. 262, p. 430–436, 1 dez. 2018.

CAETANO, G. DE Q. et al. Intergranular corrosion evaluation of friction stir welded AISI 410S ferritic stainless steel. **Journal of Materials Research and Technology**, [s.l.], fev. 2019.

CAETANO, G. Q. **Soldagem Similar de aços Inoxidaveis Ferríticos e Austenícios pelo Processo "Friction Stir Welding"**. Dissertação de Mestrado—Fortaleza: Universidade Federal do Ceará - UFC, 2016.

ÇAM, G. Friction stir welded structural materials: beyond Al-alloys. **International Materials Reviews**, [s.l.], v. 56, n. 1, p. 1–48, 1 jan. 2011.

CHOI, Y.-S. et al. Corrosion Behavior of Deep Water Oil Production Tubing Material Under Supercritical CO. Environment: Part 1—Effect of Pressure and Temperature. **CORROSION**, [s.l.], v. 70, n. 1, p. 38–47, jan. 2014.

COLEGROVE, P. A.; SHERCLIFF, H. R.; ZETTLER, R. Model for predicting heat generation and temperature in friction stir welding from the material properties. **Science and Technology of Welding and Joining**, [s.l.], v. 12, n. 4, p. 284–297, 1 maio 2007.

DARVAZI, A. R.; IRANMANESH, M. Thermal modeling of friction stir welding of stainless steel 304L. **The International Journal of Advanced Manufacturing Technology**, [s.l.], v. 75, n. 9–12, p. 1299–1307, dez. 2014.

DEQING, W.; SHUHUA, L.; ZHAOXIA, C. Study of friction stir welding of aluminum. **Journal of materials science**, [s.l.], v. 39, n. 5, p. 1689–1693, 2004.

HATAMI, S. et al. On the prediction of CO2 corrosion in petroleum industry. **The Journal of Supercritical Fluids**, [s.l.], v. 117, p. 108–112, 1 nov. 2016.

HONARVAR NAZARI, M.; ALLAHKARAM, S. R.; KERMANI, M. B. The effects of temperature and pH on the characteristics of corrosion product in CO2 corrosion of grade X70 steel. **Materials & Design**, [s.l.], v. 31, n. 7, p. 3559–3563, 1 ago. 2010.

HORNUS, E. C. et al. Comparative study of the crevice corrosion resistance of UNS S30400 and UNS S31600 stainless steels in the context of Galvele's model. **Corrosion**, [s.l.], v. 73, n. 1, p. 41–52, 2017.

KIM, J. K. et al. Intergranular segregation of Cr in Ti-stabilized low-Cr ferritic stainless steel. **Scripta Materialia**, [s.l.], v. 61, n. 12, p. 1133–1136, dez. 2009.

KIM, K. H. et al. Joint properties of ultra thin 430M2 ferritic stainless steel sheets by friction stir welding using pinless tool. **Journal of Materials Processing Technology**, [s.l.], v. 243, p. 381–386, 1 maio 2017.

KUMAR, S. S.; MURUGAN, N.; RAMACHANDRAN, K. K. Microstructure and mechanical properties of friction stir welded AISI 316L austenitic stainless steel joints. **Journal of Materials Processing Technology**, [s.l.], v. 254, p. 79–90, 1 abr. 2018.

LAKSHMINARAYANAN, A. K.; BALASUBRAMANIAN, V. Assessment of sensitization resistance of AISI 409M grade ferritic stainless steel joints using Modified Strauss test. **Materials & Design**, [s.l.], v. 39, p. 175–185, 2012a.

LAKSHMINARAYANAN, A. K.; BALASUBRAMANIAN, V. Sensitization resistance of friction stir welded AISI 409 M grade ferritic stainless steel joints. **The International Journal of Advanced Manufacturing Technology**, [s.l.], v. 59, n. 9, p. 961–967, 1 abr. 2012b.

LAKSHMINARAYANAN, A. K.; BALASUBRAMANIAN, V. Use of DL-EPR Test to Assess Sensitization Resistance of AISI 409M Grade Ferritic Stainless Steel Joints. **Journal of materials engineering and performance**, [s.l.], v. 22, n. 8, p. 2293–2303, 2013a.

LAKSHMINARAYANAN, A. K.; BALASUBRAMANIAN, V. Process Parameters Optimisation for Friction Stir Welding of AISI 409M Grade Ferritic Stainless Steel. **Experimental Techniques**, [s.l.], v. 37, n. 5, p. 59–73, 2013b.

LIENERT, T. J.; STELLWAG JR, W.; LEHMAN, L. Comparison of heat inputs: friction stir welding vs. arc welding. **American Welding Society**, [s.l.], p. 1–3, 2002.

LIN, X. et al. Effect of O2 on corrosion of 3Cr steel in high temperature and high pressure CO2–O2 environment. **Applied Surface Science**, [s.l.], v. 329, p. 104–115, fev. 2015.

LIPPOLD, J. C.; KOTECKI, D. J. **Welding Metallurgy and Weldability of Stainless Steels**. 1 edition ed. Hoboken, NJ: Wiley-Interscience, 2005.

LIU, F. C. et al. A review of friction stir welding of steels: Tool, material flow, microstructure, and properties. **Journal of Materials Science & Technology**, [s.l.], v. 34, n. 1, p. 39–57, 1 jan. 2018.

LÓPEZ, D. A.; PÉREZ, T.; SIMISON, S. N. The influence of microstructure and chemical composition of carbon and low alloy steels in CO2 corrosion. A state-of-the-art appraisal. **Materials & Design**, [s.l.], v. 24, n. 8, p. 561–575, 1 dez. 2003.

LOTO, R. T. Corrosion resistance and morphological deterioration of 316Ti austenitic, GX4CrNiMo16-5-1 martensitic and 444 ferritic stainless steels in aqueous corrosive environments. **Results in Physics**, [s.l.], v. 14, p. 102423, 1 set. 2019.

MCCAFFERTY, E. **Introduction to Corrosion Science**. New York, NY: Springer New York, 2010.

MISHRA, R. S.; MA, Z. Y. Friction stir welding and processing. **Materials Science and Engineering: R: Reports**, [s.l.], v. 50, n. 1–2, p. 1–78, 31 ago. 2005.

MUKHERJEE, M.; PAL, T. K. Influence of Heat Input on Martensite Formation and Impact Property of Ferritic-Austenitic Dissimilar Weld Metals. **Journal of Materials Science & Technology**, [s.l.], v. 28, n. 4, p. 343–352, 1 abr. 2012.

MURR, L. E. A Review of FSW Research on Dissimilar Metal and Alloy Systems. **Journal of Materials Engineering and Performance**, [s.l.], v. 19, n. 8, p. 1071–1089, 1 nov. 2010.

NANDAN, R.; DEBROY, T.; BHADESHIA, H. K. D. H. Recent advances in friction-stir welding – Process, weldment structure and properties. **Progress in Materials Science**, [s.l.], v. 53, n. 6, p. 980–1023, ago. 2008.

NEŠIĆ, S. Key issues related to modelling of internal corrosion of oil and gas pipelines – A review. **Corrosion Science**, [s.l.], v. 49, n. 12, p. 4308–4338, 1 dez. 2007.

OSSAI, C. I.; BOSWELL, B.; DAVIES, I. J. Pipeline failures in corrosive environments – A conceptual analysis of trends and effects. **Engineering Failure Analysis**, [s.l.], v. 53, p. 36–58, 1 jul. 2015.

PARK, C.-J.; LEE, Y.-H. Initiation and repassivation of crevice corrosion of type 444 stainless steel in chloride solution. **Metals and Materials International**, [s.l.], v. 10, n. 5, p. 447, 1 out. 2004.

PARK, S. H. C. et al. Rapid formation of the sigma phase in 304 stainless steel during friction stir welding. **Scripta Materialia**, [s.l.], v. 49, n. 12, p. 1175–1180, dez. 2003.

PARVATHAVARTHINI, N. et al. Sensitization control in AISI 316L (N) austenitic stainless steel: defining the role of the nature of grain boundary. **Corrosion Science**, [s.l.], v. 51, n. 9, p. 2144–2150, 2009.

POTTMAIER, D. et al. The Brazilian energy matrix: From a materials science and engineering perspective. **Renewable and Sustainable Energy Reviews**, [s.l.], v. 19, p. 678–691, 1 mar. 2013.

PULI, R.; JANAKI RAM, G. D. Corrosion performance of AISI 316L friction surfaced coatings. **Corrosion Science**, [s.l.], v. 62, p. 95–103, 1 set. 2012.

RAHIMI, S.; ENGELBERG, D. L.; MARROW, T. J. A new approach for DL-EPR testing of thermo-mechanically processed austenitic stainless steel. **Corrosion Science**, [s.l.], v. 53, n. 12, p. 4213–4222, 2011.

SANTOS, T. F. A.; IDAGAWA, H. S.; RAMIREZ, A. J. Thermal history in UNS S32205 duplex stainless steel friction stir welds. **Science and Technology of Welding and Joining**, [s.l.], v. 19, n. 2, p. 150–156, 1 fev. 2014.

SHIRI, S. G. et al. Diffusion in FSW Joints by Inserting the Metallic Foils. **Journal of Materials Science & Technology**, [s.l.], v. 29, n. 11, p. 1091–1095, 1 nov. 2013.

SILVA, C. C. et al. High-temperature hydrogen sulfide corrosion on the heat-affected zone of the AISI 444 stainless steel caused by Venezuelan heavy petroleum. **Journal of Petroleum Science and Engineering**, [s.l.], v. 59, n. 3–4, p. 219–225, nov. 2007.

SILVA, C. C. et al. Austenitic and ferritic stainless steel dissimilar weld metal evaluation for the applications as-coating in the petroleum processing equipment. **Materials & Design**, [s.l.], v. 47, p. 1–8, 1 maio 2013.

SILVA, Y. C. DA. **Modeling and simulating of stainless steel joints by the Friction stir welding**. [s.l.]: [s.n.], 2021.

SIMÕES, A. V.; SANTO, V. M. E.; MOREIRA, A. P. E. **A eficácia da aplicação das técnicas de monitoração da corrosão interna em um duto real**. Salvador, [s.l.], v. 1, p 1-10. Trabalho apresentado na 9º Conferência sobre Tecnologia de Equipamentos - COTEQ. 2007, Salvador

TAJI, I.; MOAYED, M. H.; MIRJALILI, M. Correlation between sensitisation and pitting corrosion of AISI 403 martensitic stainless steel. **Corrosion Science**, [s.l.], v. 92, p. 301–308, 2015.

UDAY, M. B. et al. Advances in friction welding process: a review. **Science and Technology of Welding & Joining**, [s.l.], v. 15, n. 7, p. 534–558, 2010.

VAN DER MEER, B. Carbon dioxide storage in natural gas reservoir. **Oil & gas science and technology**, [s.l.], v. 60, n. 3, p. 527–536, 2005.

WU, H. et al. Influence of Chromium on Mechanical Properties and C02/H2S Corrosion Behavior of P110 Grade Tube Steel. **Journal of Iron and Steel Research International**, [s.l.], v. 21, n. 1, p. 76–85, jan. 2014.

WU, X. et al. A discussion on evaluation criteria for crevice corrosion of various stainless steels. **Journal of Materials Science & Technology**, SI: Advanced Corrosion-Resistant Materials and Emerging Applications. [s.l.], v. 64, p. 29–37, 20 fev. 2021.

YIN, Z. F. et al. Effect of temperature on CO2 corrosion of carbon steel. **Surface and Interface Analysis**, [s.l.], v. 41, n. 6, p. 517–523, 2009.

ZHU, G. Y. et al. Corrosion behavior of 13Cr stainless steel under stress and crevice in high pressure CO2/O2 environment. **Journal of Materials Science & Technology**, [s.l.], v. 88, p. 79–89, 20 out. 2021.

11 CHAPTER 11: The summary of the thesis

11.1 Conclusions

Based on the results obtained and presented in this thesis on processing, microstructure, mechanical properties and corrosion susceptibility of ferritic/austenitic dissimilar welds produced by FSW, it was possible to conclude that:

Operational Aspects

- With the right combination of welding parameters, a dissimilar joint can be successfully welded between AISI 410S ferritic stainless steel and AISI 304L austenitic stainless steel, producing a stable and defect-free joint.
- Due to the differences in the AISI 410S and AISI 304L steels' physical and chemical properties and the different phenomena that occur on the advancing and retreating side, the reduction in flash production and voids in the stir zone occurs when AISI 410S ferritic stainless steel is placed on the advancing side.
- The dissimilar joints' production between the AISI 410S/304L stainless steels welded by the FSW process without root flaws was achieved, keeping the rotational speed at 450 rpm and increasing the axial force to 40 kN, consolidating an appropriate balance between rotation speed, axial force, and tool angle.
- It is possible to produce good dissimilar welds of AISI 444 ferritic stainless steel and AISI 316L austenitic stainless steel by the FSW process through a butt joint with AISI 316L austenitic stainless steel on the retreating side, with an axial force of 30 kN and speed of 350 rpm rotation.
- Dissimilar FSW joints of AISI 444 ferritic stainless steel and AISI 316L austenitic stainless steel are also satisfactorily consolidated through an overlap joint with AISI 316L austenitic stainless steel on top, increasing the axial force to 50 kN and maintaining the rotation speed at 350 rpm.

Metallurgical Aspects

- It is possible to weld dissimilar FSW joints between the AISI 410S ferritic stainless steel located on the advancing side and the AISI 304L austenitic stainless steel on the retreating side, with no grain growth on TMAZ and HAZ, intense grain refining in SZ and with significant interaction between the two steels and consequently a good consolidation of the joint.
- In dissimilar FSW joints between the AISI 410S and AISI 304L, on the retreating side, where is the AISI 304L austenitic stainless steel, as the applied axial force increases and consequently an increase in heat input, there is an increase in ferrite-δ intensity uniformly distributed in HAZ and TMAZ. On the advancing side, where the AISI 410S ferritic stainless is positioned, in the HAZ and TMAZ, as the axial force increases, there are more favourable conditions for the growth of austenite grains that will be transformed into martensite during cooling, consuming the ferrite grains and providing its refining.
- In the stir zone of joints AISI 304L/410S, differences in intensity of recrystallised fraction are observed for AISI 304L and AISI 410S steels due to different dynamic recrystallisation (DRX) mechanisms. The DRX type on the FSS AISI 410S side, with high SEF, is dominated by a continuous DRX mechanism (CDRX), and in the case of the ASS AISI 304L side with low SFE, the dominant mechanism is the discontinuous DRX (DDRX).
- In dissimilar FSW joints between the AISI 444 and AISI 316L, with the proper combination of welding parameters, it is possible to successfully weld a dissimilar joint between ferritic stainless steel AISI 444 and austenitic stainless steel AISI 316L, producing a joint without harmful microstructural changes in the HAZ, with intense grain refining in the TMAZ and a refined stir zone with high cohesion between the two materials.
- The contact interface between the two steels is strongly modified by increasing the axial force. In butt joints, the increase in axial force causes tipped inserts to appear. In the overlap joints, with AISI 316L steel at the bottom, the reduction of central hooks steels and the complete nullification of the existing voids in the

interface region occurs. In overlap joints, with AISI 316L steel at the top, it causes the appearance of hooks composed of regions interleaved between the two steels.

Performance Aspects

- In dissimilar FSW joints between the AISI 410S and AISI 304L, by increasing the axial force to 35 kN and 40 kN and keeping the rotation speed at 450 rpm, it is possible to produce a dissimilar FSW joint between AISI 410S ferritic stainless steel and AISI 304L austenitic stainless steel with high bending angle, high values of microhardness and good tensile strength properties.
- In dissimilar FSW joints between the AISI 410S and AISI 304L, the TMAZ and SZ on the advancing side, where the AISI 410S steel is located, have regions with microhardness values greater than 340 HV and more remarkable than those found on the retreating side, due to the excessive amount of martensite and refined ferritic grains in both regions, due to the intense dynamic recrystallisation and the cooling rates achieved.
- It is possible to weld AISI 410S ferritic stainless steel and AISI 304L austenitic stainless steel in a dissimilar joint by the FSW process with low sensitisation levels and corrosion rates in the salt spray test lower than the base metal of AISI 410S steel.
- Macroscopically evaluating the upper and lower surfaces of the samples AISI 410S/304L by conditions 3 and 4, after being submitted to 1000h in the salt spray test, it is possible to observe that for all conditions, the base metal of the AISI 410S steel presents a large formation of macroscopic pits, with this surface degradation being more intense in regions close to HAZ for condition 4, welded with higher heat input.
- The analysis of the different weld conditions shows that it is possible to produce dissimilar joints of ferritic stainless steel AISI 444 and austenitic stainless steel AISI 316L by the FSW process with mechanical properties superior to those found in the base metals of AISI 444 e AISI 316L.
- It is possible to weld AISI 444 ferritic stainless steel and AISI 316L austenitic stainless steel in a dissimilar joint by the FSW process without sensitisation and

with corrosion rates in the oil immersion test similar to the base metal of AISI 444 steel.

- In dissimilar FSW joints between the AISI 444 and AISI 316L, Condition 3, welded in a butt joint, after 200h of immersion in oil at high temperature and pressure, showed an average corrosion rate close to that observed in the base metal of AISI 444 steel. Condition 6, welded in an overlap joint and with the presence of crevices in the cross-section, after 200h of immersion test in oil at high temperature and pressure, showed a considerable increase in the corrosion rate, being this increase 64.7% higher than the average corrosion rate for Condition 3.
- In joints AISI444/316L, after 200 hours of testing, the welded conditions with higher heat input and submitted to the oil immersion test at high temperature and pressure did not present the formation of pits in their cross sections and upper and lower faces.